NASA Technical Memorandum 78275

Space Processing Application Rocket Project

SPAR V Final Report

AUGUST 1980

NASA

NASA Technical Memorandum 78275

Space Processing Application Rocket Project

SPAR V Final Report

Compiled by F. Reeves and D. Schaefer
George C. Marshall Space Flight Center
Marshall Space Flight Center, Alabama

National Aeronautics
and Space Administration

Scientific and Technical Information Office

1980

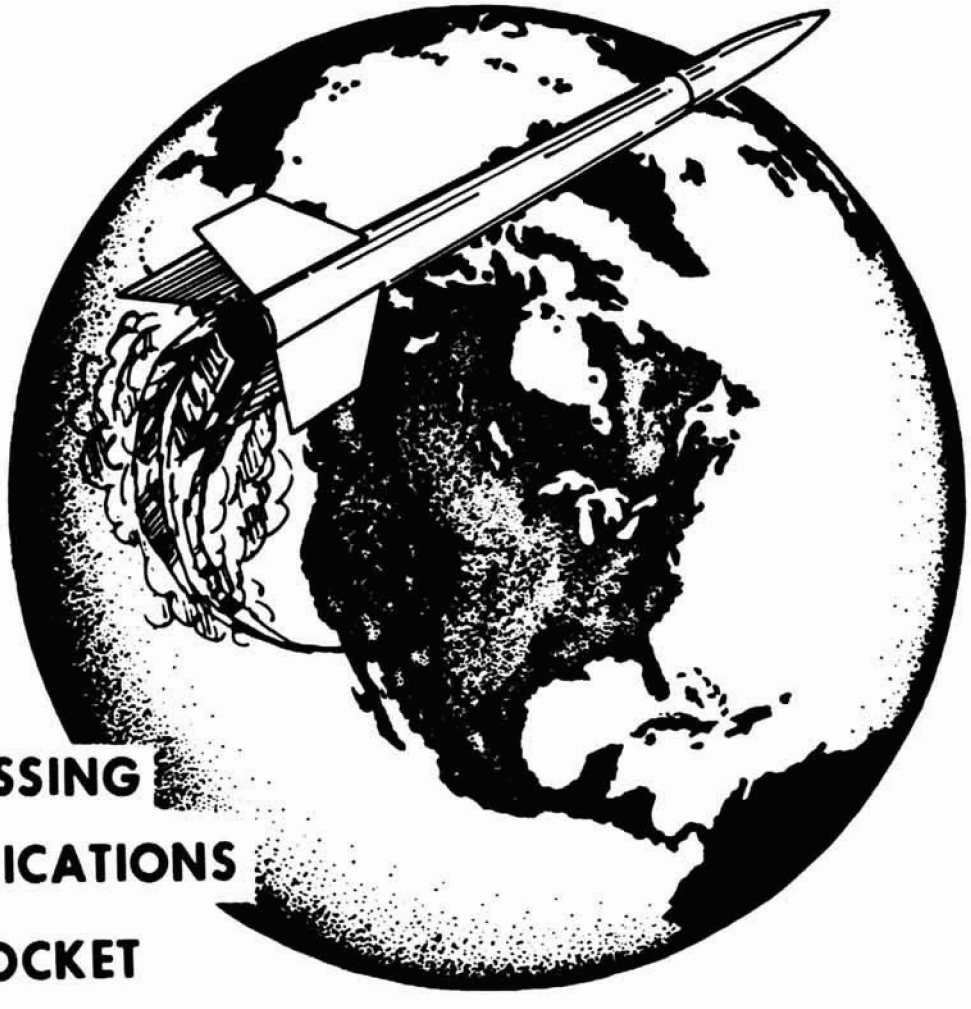

SPACE PROCESSING APPLICATIONS ROCKET

TABLE OF CONTENTS

SPACE PROCESSING APPLICATION (SPAR) PROJECT

SPAR V - FINAL REPORT

INTRODUCTION

The unique low-g environment of space affords an opportunity for exploring and developing techniques for processing a variety of materials without the constraining gravitational influences as evidenced with the processing of liquid phase materials or melts on Earth. The Materials Processing in Space (MPS) program is directed toward the stimulation and development of the associated science and technology required to pursue these investigations. This NASA activity is undertaken in cooperation with the scientific community and includes follow-on studies of specific areas of scientific research emphasizing those selected investigations of materials and processes which best demonstrate potential benefit from the enhanced sensitivity of the controlled processing in a low-g environment. Examples of interest to the program are the reduction and/or elimination of adverse thermal effects such as convection, sedimentation of heavy particles, buoyancy rise and positioning aspects of bubbles in liquids or melts, and the stratification effects of particulate of variable density in solution. These and similar studies are considered to be the expansion of a limiting frontier in the development of new materials and processes which are envisioned ultimately to be of immeasurable benefit to mankind. As complementary to the research and technological nature of the investigations, the evolving emphasis is being directed, with the advent of the Shuttle and increased payload potential, toward commercialization and the development of self-sustaining programs yielding direct product benefit.

The initial precursory zero-g demonstrations and investigations associated with this family of scientific experiments were proposed and developed for the Apollo flights beginning in the late 1960's and continuing with Skylab and Apollo-Soyuz flights through the mid-1970's. During the period between the close of that era and the orbital space flights on the Space Shuttle in the 1980's, the Space Processing Application Rocket (SPAR) Project has provided the only viable flight opportunity for low-g scientific investigations for experimenters and is serving in a precursory role for planned and approved Shuttle investigations. It is also anticipated that sounding rocket flights could satisfy a continuing need and a complementary role for the establishment and definition of future precursory Shuttle experiments.

The SPAR Project is part of the Materials Processing in Space (MPS) program of the Office of Space and Terrestrial Applications which is responsible for directing research into the scientific effects of materials processing in the unique environment of space. This effort involves participation and interaction from various disciplines of the scientific community, governmental agencies, universities, and industrial organizations, in addition to foreign participation.

The Black Brant VC (BBVC) sounding rocket series, which is currently the carrier vehicle for the scientific payloads, with a Nike-boosted configuration available for heavier payloads, provide the opportunity to process materials in a low-g environment for periods up to 5 minutes in duration during a suborbital flight.

The rocket flights, which are conducted at the White Sands Missile Range, afford experimentors and apparatus developers a flight opportunity for a proof-of-concept verification and/or refinement of equipment operation and procedures prior to the longer duration, more sophisticated Shuttle flights.

This SPAR flight, which is fifth in a planned series of rocket flights, occurred on September 11, 1978, and carried four experiments. The investigations for the experiments comprising the payload manifest were managed and coordinated by the MPS Projects Office of the Marshall Space Flight Center. Two such experiments were proposed and devised by industrial firms, one by university participation and one by a government agency.

Previous experiments flown on the first four SPAR flights included the measurement of liquid mixing due to spacecraft motions and the dispersion of normally immiscible materials in the area of fluid dynamics. Solidification experiments involving the gravitational effects on dendritic growth, epitaxial growth, and eutectic determination on materials with widely differing densities have flown previously, in addition to solidification studies of interactions between second-phase particles and an advancing crystal-liquid interface and gravity-induced convection on cast microstructures. In the area of multiphase particle interaction, various experiments were conducted on the migration and coalescence of bubbles and particles, closed-cell metal foam, and dispersion strengthening of composites.

The SPAR Project has been increasingly active in supporting research in the promising area of containerless processing with previous flights, including experiments on cast beryllium and the processing of amorphous ferro-magnetic materials in an electromagnetic field, and control of liquid droplets by an acoustic field in the furtherance of state-of-the-art of acoustic containerless processing technology.

The SPAR V flight has, through an evolutionary program, addressed experiments of increasing complexity and refinement and has afforded additional flight opportunities consistent with the maturity of each investigation. The payloads selected for this flight manifest were based on the advanced state-of-preparedness of their ground-based research activity.

The following experiments are included in this selection: Uniform Dispersions by Crystallization Processing (Experiment No. 74-15) which addresses the interaction between second-phase particles and an advancing crystal growth interface during solidification; Contained Polycrystalline Solidification in Low-g (Experiment No. 74-37) which deals with understanding the role of gravity induced convection and thermal conditions on the columnar-to-equiaxed microstructural transition during solidification; The Direct Observation of Dendrite Remelting and Macrosegregation in Casting (Experiment 74-21) which investigates the gravity-driven effects on dendrite and interface growth during columnar and unidirectional solidification process in castings; and Agglomeration in Immiscible Liquids at Low-g (Experiment No. 74-30) which is an attempt to determine composition, cooling rates, and gravitational effects on the microstructures of miscibility gap materials.

The post-flight results and analyses of each experiment flown on SPAR V as prepared by the respective flight investigators, in addition to an engineering report on the performance of the SPAR Black Brant rocket,are contained in separate sections of this Technical Memorandum. With the successful completion of this flight and subsequent data analysis, much useful data and information was accumulated for directing and developing experimental techniques and investigations toward an expanding, commercially beneficial program of materials processing in the coming Shuttle era.

National Aeronautics and
Space Administration

George C. Marshall Space Flight Center
Marshall Space Flight Center, Alabama 35812

SPACE PROCESSING APPLICATION ROCKET PROJECT

SPAR V

ENGINEERING REPORT

DECEMBER 1979

SCIENCE AND ENGINEERING
OFFICE OF THE ASSOCIATE DIRECTOR FOR ENGINEERING

MSFC - Form 454 (Rev. October 1976)

SPACE PROCESSING APPLICATION ROCKET PROJECT

SPAR V

ENGINEERING REPORT

K. L. Reed
SPAR V Experiment Engineer

Date

R. C. Edwards
MPS Chief Engineer

12/19/79
Date

R. P. Chassay
SPAR Project Manager

Date

TABLE OF CONTENTS

LIST OF FIGURES

LIST OF TABLES

SPAR V POST-FLIGHT ENGINEERING REPORT

1.0 SUMMARY

The SPAR V Black Brant VC rocket lifted off the launch pad at WSMR Monday, September 11, 1978, at 1600:00:00 G.m.t. (10 a.m., m.d.t.). The launch was successful and the payload was recovered intact.

Payload power was applied to all experiments as planned, and all experiments operated within the predicted near zero gravity. All MSFC flight support requirements to each experiment were met as indicated by the reduced flight data. Power to the payload experiments was removed at T+728 seconds as programmed.

2.0 SPAR V PAYLOAD CONFIGURATION

The SPAR V payload consisted of four experiments, a General Purpose Rocket Furnace (GPRF) containing two of the four experiments, the Experiment Support Module (ESM) and the Abbreviated Measurement Module (AMM). The SPAR V experiments are:

74-21/2R and 3R	Dendrite Remelting and Macro Segregation
74-15/2R	Uniform Dispersions of Crystallization Processing
74-37/2R	Contained Polycrystalline Solidification in Low-G
74-30/1R and 2	Agglomeration in Immiscible Liquids

The orientation of the experiments within the SPAR V rocket is shown in Figure 1.

3.0 ROCKET PERFORMANCE

3.1 Flight Sequence

The SPAR V flight profile is shown in Figure 2. The predicted and actual sequence of events are shown as a function of flight time.

3.2 Low Gravity

The predicted low-g (10^{-4} or less) time was based upon an all-up payload weight of 881.8 pounds. The science payload (MSFC furnished) weighed 565.5 pounds.

SPAR PROJECT
BLACK BRANT PAYLOAD V CONFIGURATION

1260-79

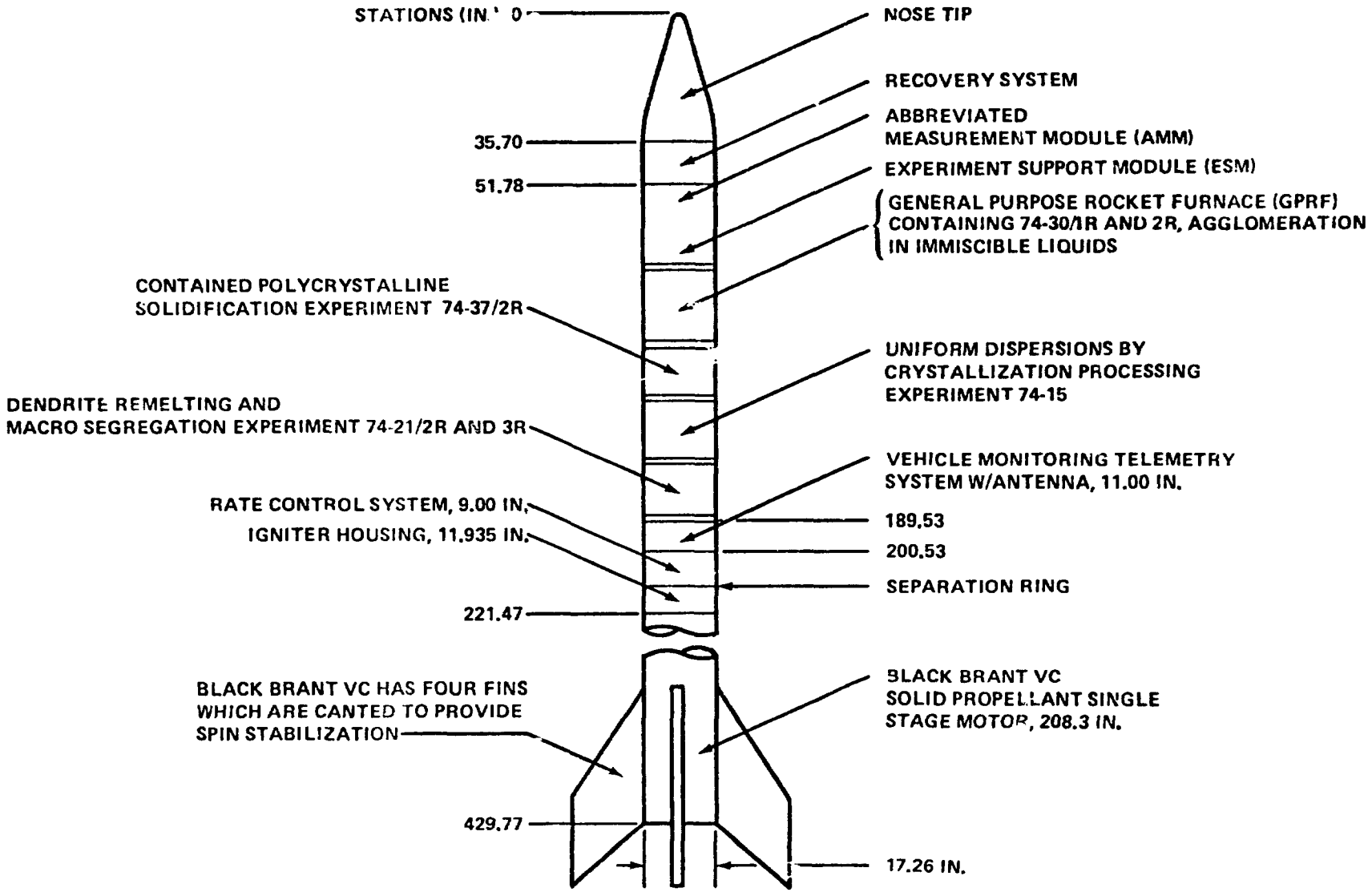

FIGURE 1 LAUNCH VEHICLE AND PAYLOAD CONFIGURATION

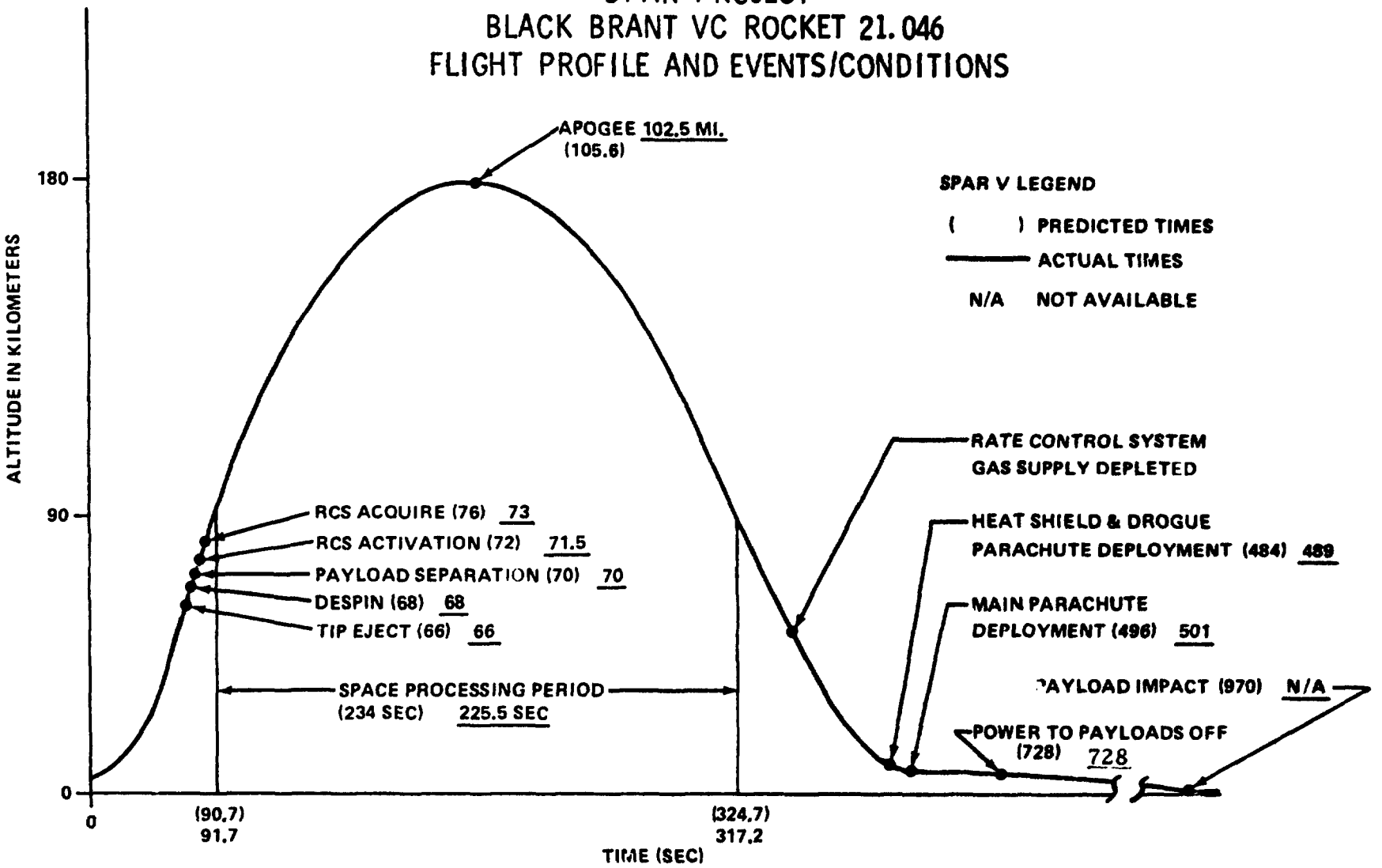

FIGURE 2. FLIGHT PROFILE AND EVENTS

The measurement module low-g accelerometer measurements indicated that the low-g period on all three axes began at T+91 seconds and ended at T+317 seconds, giving a low-g period of 226 seconds. Minimum low-g period expected for experiments was 234 seconds. The eight-second deficit is not considered detrimental to the performance of any SPAR V experiment.

4.0 PAYLOAD SUPPORT

4.1 Payload Sequence of Events

Experiments 74-15 and 74-37 and the GPRF required preheat prior to launch that was supplied by ground power. At T-0, a lift-off signal was given which activated a timer within each experiment and the GPRF, for control of events during the flight. These events are shown in Figure 3.

The actual timelines were well within the acceptable limits of each experiment. The planned power removal to experiments at T+728 seconds occurred as planned.

4.2 Payload Power

Transfer of electrical power from ground support equipment to the flight battery was accomplished at T-3 minutes. The Experiment Service Module battery supplied power to all experiments. Battery voltage measurement (M01-SM) indicates that the battery voltage was 32.5 volts at lift-off and remained essentially constant until power cut-off at T+728 seconds. The battery current measurement (M39-SM) was inoperative during the SPAR V flight. This condition was discovered during the Horizontal Testing at WSMR and was documented in Test Discrepancy Report (TDR) W-SPAR-5-625-6. The decision was made to launch without the battery current measurement, since it was not considered to be essential and troubleshooting and repair of the circuit would have delayed the launch.

5.0 EXPERIMENTS

5.1 Experiment 74-15 - Uniform Dispersions of Crystalline Processing

The experiment consisted of investigating interaction between second phase particles and an advancing crystal-liquid interface. The flight operation first applied heat to the specimens, then cooling was allowed while photographs were taken. Figure 3 shows the flight sequence timelines.

The lamp current monitor (M32-15) indicates that heating and camera operation began at T+92 seconds. These events are verified by the camera exposure monitor (K44-15) which shows the first exposure to have occurred at T+95 seconds. The experiment temperature monitors (C84-15 through C98-15) show cooling to have begun at about T+121 seconds.

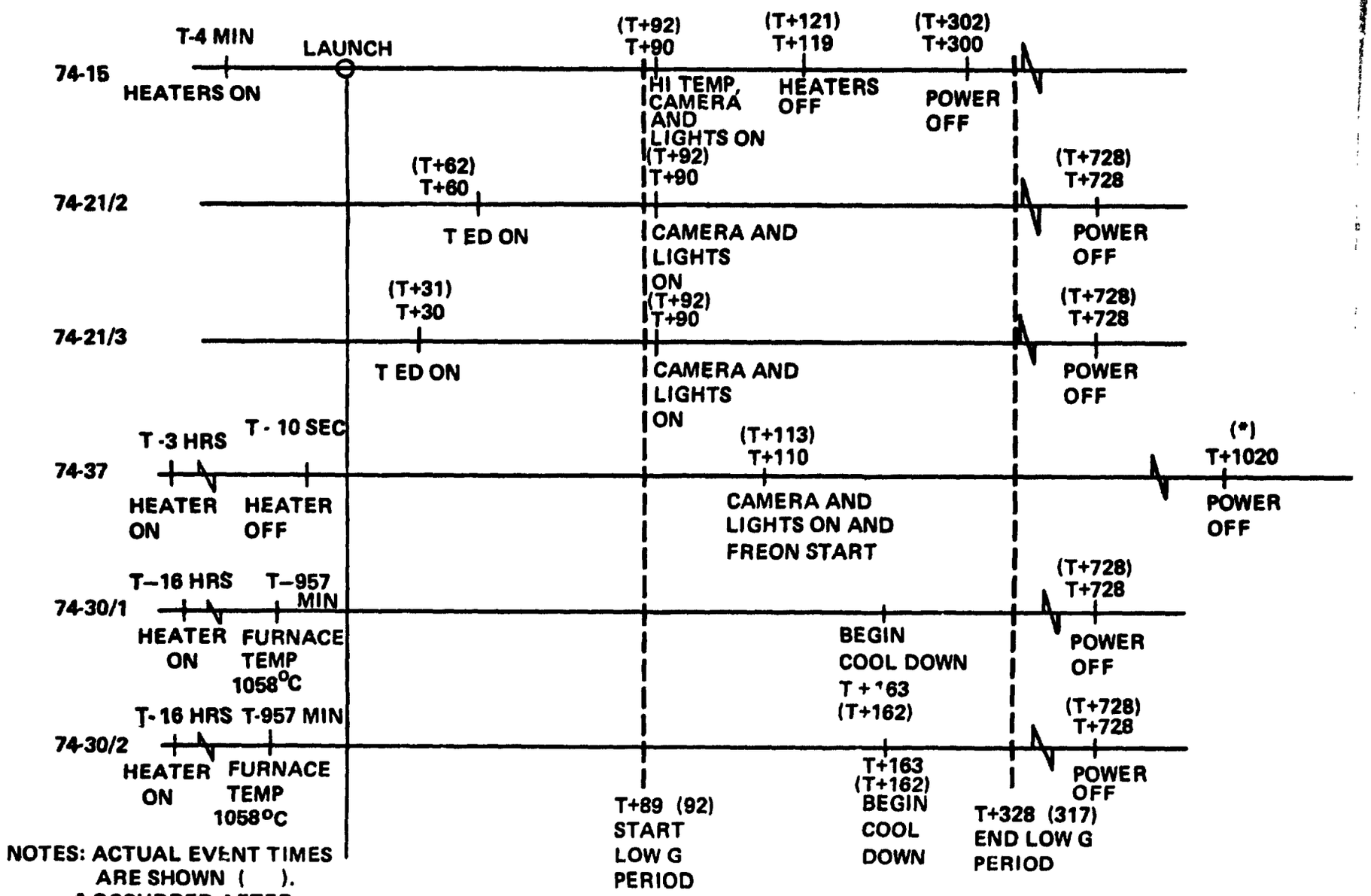

NOTES: ACTUAL EVENT TIMES ARE SHOWN ( ).
* OCCURRED AFTER LOSS OF TELEMETRY COVERAGE

FIGURE 3 SPAR V EXPERIMENT TIMELINE

The +28 Vdc monitor (M63-15) indicates that the experiment received +28 Vdc until cutoff by the experiment timer at T+302 seconds. The clock counting monitor (K47-15) indicates that the ESM timer removed the +28 Vdc experiment power at T+728 seconds. The camera exposure monitor (K44-15) indicates that the camera shutter operated until T+387 seconds. No 74-15 anomalies could be determined by examination of the SPAR V flight data.

5.2 Experiment 74-37 - Contained Polycrystalline Solidification in Low-G

This experiment's purpose was to determine if a low-g condition affects the superheat temperature at which transition occurs between equiaxed and columnar grain structure in metallic castings. The samples required 3 hours of preheat prior to launch. This was accomplished by GSE power. At 113 seconds into the flight, freon was injected into the sample area for cooling, and the camera and lights were activated as indicated by the lamp monitor (M27-37). The camera exposure monitor (K48-37) indicates that the first exposure was made at T+113 seconds, and that the camera shutter operated until loss of telemetry coverage at T+795 seconds. The reference voltage monitor (M26-37) remained at a steady 2.6 Vdc throughout the flight from lift-off until loss of telemetry. The experiment temperatures (C100-37 through C106-37) indicate that cooling began at T+113 seconds and continued until loss of telemetry. Cooling rates varied from 3°/minute (C100-37 and C101-37) to 69°/minute (C106-37) for the first minute of cooling. No 74-37 anomalies could be determined by examination of the SPAR V flight data.

5.3 Experiment 74-21/2 - Dendrite Remelting and Macro Segregation

This experiment consisted of the solidification of an ammonium chloride solution by cooling with thermo electric devices (TED's) and photographing the solidification.

The timer output TED power on monitor (K28-SM) shows that the TED was commanded on at T+62 seconds. The camera and lights were commanded on at T+92 seconds, according to the timer output monitor for this event (K31-SM). The camera shutter monitor (K12-22) indicates that the camera began exposure at T+93 seconds and continued operation until experiment power was removed at T+728 seconds. The scientific temperatures (C60-22, C61-22, and C62-22) dropped from 20°C at lift-off to 7°C, 11.5° and 17°C respectively when powered down at T+728 seconds. No 74-21/2 anomalies could be determined by examination of the SPAR V flight data.

5.4 Experiment 74-21/3 - Dendrite Remelting and Macro Segregation

This experiment consisted of the solidification of an ammonium chloride solution by cooling with thermo electric devices (TED's) and photographing the solidification.

The timer output TED power on monitor (K29-SM) shows that the TED was commanded on at T+31 seconds. The camera and lights were commanded on at T+92 seconds, according to the timer output monitor for this event (K30-SM). The camera shutter monitor (K13-23) indicates that the camera began exposure at T+93 seconds and continued operation until experiment power was removed at T+728 seconds. The scientific temperatures (C16-23 through C18-23) dropped from 20°C at lift-off to 4°C, 4°C and 5°C respectively when powered down at T+728 seconds. The fourth scientific temperature (C19-23) dropped from 20°C at lift-off to 4°C at approximately T+100 seconds and then increased to 22°C when powered down at T+728 seconds. This condition indicates the probable failure of a thermo electric device at approximately T+100 seconds. Otherwise, no known anomalies occurred during the experiment 74-21/3 operation on the SPAR V flight.

5.5 Experiment 74-20/1 - Agglomeration in Immiscible Liquids

This experiment consisted of processing Al-In samples in the General Purpose Rocket Furnace (GPRF) in order to investigate the evolution of micro structures in miscibility gap materials and to relate this to the influence of gravity. The GPRF was preheated for 16 hours to 1059°C in order to maintain the sample temperature at 970°C. The GPRF cavity 1 temperature measurement (C12-RF) indicates that the temperature was 1036°C at lift-off. The 23°C difference between the telemetry and landline temperatures was known prior to shipment from MSFC, and was due to the fact that at lift-off, the furnace control voltage is shifted from a ground voltage source to the flight battery. From cooldown initiation at T+162 to the end of low-g environment, T+317 seconds, the average cooling rate was about 5.4°/second. The cavity temperature was 180°C at low-g end and 72°C at T+728 seconds. The sample temperature (C15-31) was lost during launch countdown and was not replaced due to cost involved with a launch scrub. Therefore, no valid sample temperature data is available for the 74-30/1 experiment processing on the SPAR V flight. No 74-30/1 anomalies could be determined by examination of the SPAR V flight data.

5.6 Experiment 74-30/2 - Agglomeration in Immiscible Liquids

This experiment was the same as experiment 74-30/1 except that the sample compositions were different. The GPRF was preheated for 16 hours to 1059°C in order to maintain the sample temperature at 970°C. The GPRF cavity 2 temperature (C13-RF) indicates that the temperature was 1044°C at lift-off. The 15°C difference between the telemetry and landline measurements was known prior to shipment from MSFC, and was due to the

fact that at lift-off, the furnace control voltage is shifted from a ground voltage source to the flight battery. From cooldown initiation at T+162 seconds, to the end of low-g environment, T+317 seconds, the average cooling rate was about 5.7°C/second. The cavity temperature was 159°C at low-g end and 47°C at power cut-off at T+728 seconds. No 74-30/2 anomalies could be determined by examination of the SPAR V flight data.

6.0 INSTRUMENTATION

6.1 Low-G Measurements

The low-g data indicates that a low-g environment considerably less than 1×10^{-4}g was achieved in all 3 axes. The X-axis linear acceleration measurement (A02-MM) indicates that low-g entry was at about 90 seconds and exit at about 317 seconds with the g level during this period ranging from $+0.2$ to -0.4×10^{-4}g. The Y-axis linear acceleration measurement (A03-MM) indicates the same low-g entry and exit times with the g levels ranging from 0 to 0.3×10^{-4}g. The Z-axis linear acceleration measurement (A04-MM) indicates the same low-g entry and exit times with the g levels ranging from -0.2 to $+0.2 \times 10^{-4}$g.

A large spike of 0.29×10^{-4}g occurred on the Z-axis plot in the -Z (flight) direction at T+159 seconds. The exact duration of the spike is unknown since the low-g measuring system integrates over a 1-second increment between samples, but the data shows that the g level immediately preceding (T+158 seconds) was 0.1×10^{-4}g in the +Z direction (opposite flight direction) and immediately following (T+160 seconds) was 0.11×10^{-4}g in the -Z direction. The cause of this spike is unknown since the GPRF quench was initiated some 3 seconds later at T+162 seconds, and no programmed function occurred at this time.

A second spike of 0.47×10^{-4}g in the +Z direction occurred at T+289 seconds. This was immediately followed by a spike of 0.5×10^{-4}g in the -Z (flight) direction at T+290 seconds. The data immediately preceding (T+288 seconds) shows that the g level was 0.13×10^{-4}g in the +Z direction and immediately following (T+291 seconds) was 0.08×10^{-4}g in the -Z direction. Again, the cause of this spike is unknown since no programmed function occurred at this time and the next function occurred 12 seconds later (74-15 power cut-off).

6.2 Engineering Temperatures

Engineering thermistors were located on the SPAR V Science Payload (SPL) in the following locations (see Figure 4).

C28-SM	Transmitter Plate Temperature
C30-RF	GPRF External Temperature
C31-RF	GPRF Z Ring Temperature
C33-MM	Linear Accelerometer Block Temperature

FIGURE 4
SPAR V ENGINEERING MEASUREMENT LOCATIONS

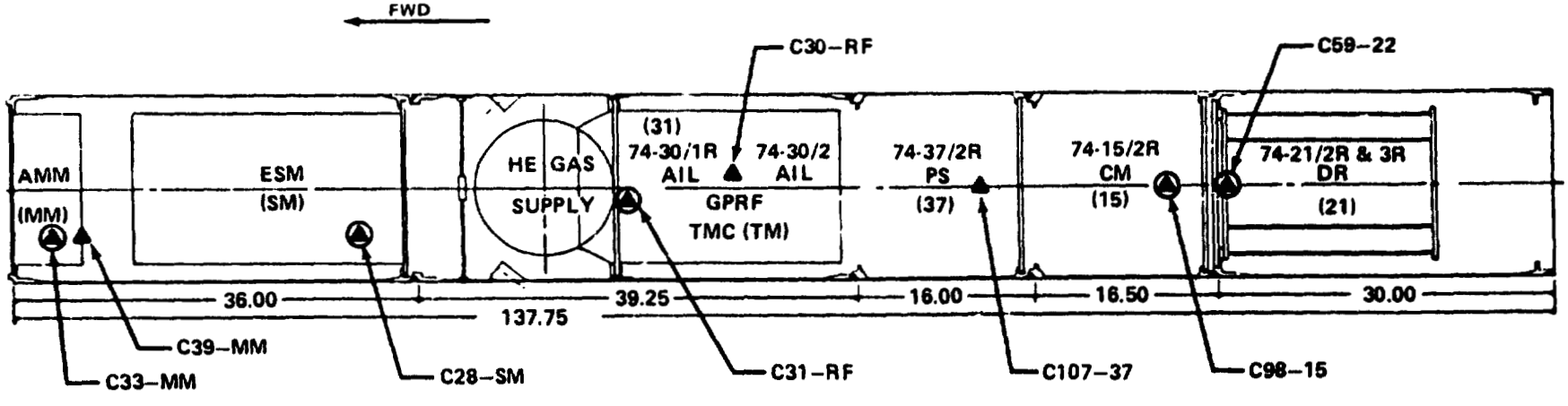

C39-MM	AMM External Temperature
C59-22	74-21/2 Camera Plate Temperature
C98-15	74-15 Cell Chassis Temperature
C107-37	74-37 External Temperature

The engineering temperature thermal analysis (Fig. 5) was performed by Joseph Sims, EP41, MSFC. The data shows that the SPAR V payload was warmer during flight than SPAR IV. The temperature at the forward end of the SPL (C39-MM) is very similar to that measured on SPAR III. The rapid temperature rise seen in the C39-MM data during both ascent and re-entry may be explained by: a) the sensor location on the AMM case, and b) the influence from aerodynamic heating during ascent and re-entry.

3530-79EE

FIGURE 5 ENGINEERING MEASUREMENTS, SPAR V

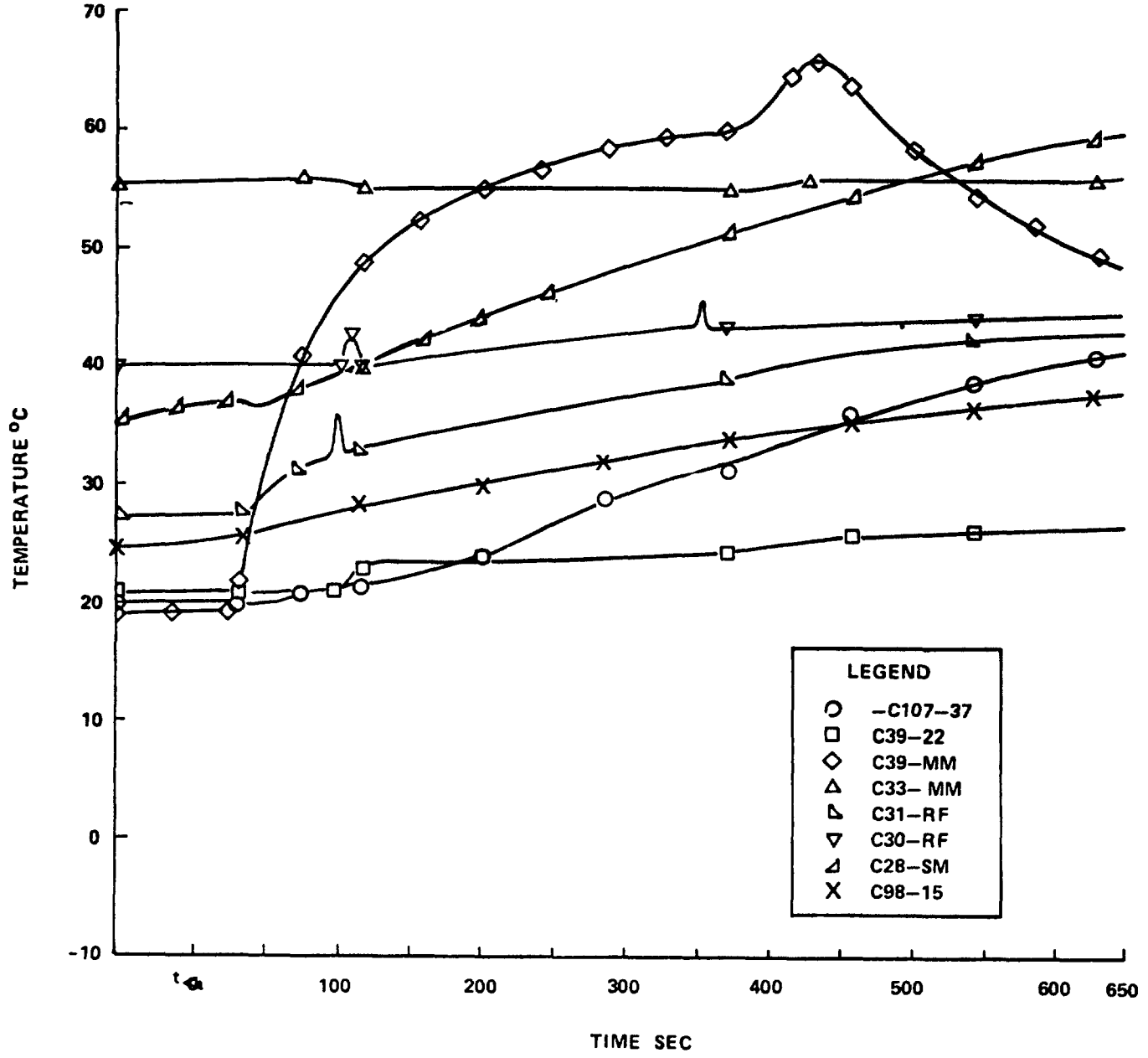

6.3 Pressures

Ambient pressure in the AMM (D01-MM) was 13.4 psia at lift-off, and 0.6 psia (≈ 30 torr) at T+67 sec. The AMM ambient pressure measuring device (D06-MM) was also located in the AMM, and was capable of monitoring from 30 to 10^{-4} torr in six ranges. It indicated that the ambient pressure continued to decrease until a minimum of 8 torr was reached at approximately T+360 seconds. From this point, the pressure rose rapidly to 30 torr at T+367 seconds and then dropped to 21 torr at T+372 seconds as the payload reentered the atmosphere; this pressure drop is not harmful and is probably due to erratic repressurization of the irregular payload configuration. From this point, the pressure continued to increase rapidly and reached 8 psia at T+489 seconds when the heat shield and drogue chute were deployed. From this point, the pressure increased steadily until it reached 12.8 psia when telemetry contact was lost at T+780 seconds.

The GPRF H_e sphere pressure (D02-RF) data indicates that the sphere pressure was 2080 psia at lift-off, and began decreasing at T+162, about 15 seconds after initiation of GPRF cooldown was programmed to begin. The pressure decreased to about 30 psia at T+780 seconds when loss of telemetry coverage occurred.

6.4 Vibration and Shock

No vibration data from the X, Y, and Z vibration measurements (E02-MM, E03-MM, and E04-MM) are available for evaluation, due to the loss of SPAR V data. However, this type of data is no longer significant since the vibration environment on SPAR is well characterized from previous flights.

Nine impact-o-graphs, capable of measuring shock levels from 100 G's to 750 G's, were mounted on the forward side of the GSFC Telemetry Module Extension (Figure 6). The impact-o-graph results are tabulated in Table I. The shock level experienced upon impact seems to be between 550 and 600 G's. Since SPAR V was the first flight to use impact-o-graphs capable of measuring levels greater than 120 G's, no comparison can be made with shock data from previous payloads.

6.5 Thermal Mapping Cartridge

The Thermal Mapping Cartridge (TMC) was an instrumented cartridge in the third GPRF cavity. Its function was to measure the temperatures at the top and bottom of the cartridge and the differential temperature between them in order to determine GPRF cartridge isotherms during sample quench.

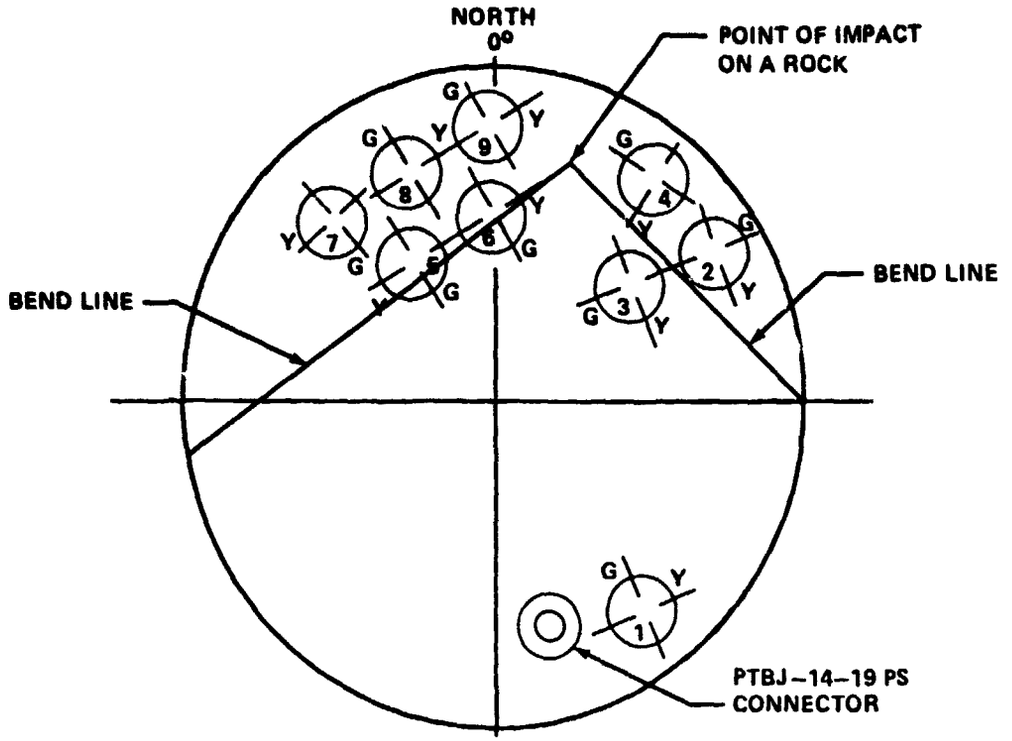

FIGURE 6 LOCATION OF THE IMPACT-O-GRAPHS ON THE FORWARD SIDE OF GSFC'S SPAR RATE CONTROL SYSTEM EXTENSION

IMPACT-O-GRAPH		SPRINGS AND BALLS FOUND UNSET AFTER LANDING		REMARKS
NO	Gs ± 5G	G (GREEN) AXIS	Y (YELLOW) AXIS	
1	700	NO	NO	
2	350	YES	YES	
3	400	YES	YES	
4	550	YES	YES	
5	300	NO	YES	
6	450	YES	YES	
7	750	NO	YES	
8	600	NO	YES	
9	100	YES	YES	

TABLE I LOCATION, NOMINAL G - LEVELS AND THE RESULTS ON SPAR V.

The Cavity 3 temperature (C! ·RF) indicates that the cavity temperature was 750°C at lift-off, and remained stable until the H_e quench began at T+162 seconds. The average cooling rate was 4.0°C/min. from the beginning of quench until the end of the low-g period, T+317, and the temperature at low-g end was 124°C. The TMC top temperature (C02-TM) indicates that the top TMC temperature was 380°C at lift-off, and increased to 416°C at quench initiation. These temperatures are much lower than anticipated, and the thermocouple for this measurement is believed to have failed. The TMC bottom temperature (C04-TM) was 700°C at lift-off, and increased to 711°C at quench initiation. The average cooling rate was 3.8°C/sec. from quench initiation to low-g end, at which time the temperature was 121°C. The differential temperature, between the top and bottom (C05-TM), indicates a constant 31°C for the entire flight. This reading is due to the failure of the top thermocouple, and indicates that the difference between the top and bottom temperatures was greater than the 31°C maximum range capability of measurement C05-TM.

7.0 RECOVERY

The payload landing/recovery site was a gentle sloping rock-covered foothill of the San Andres Mountains which bordered the West side of the range. The payload landed on its aft end as planned, and then fell over in the uphill direction. It did not appear to have moved down the slope after impact or to have been dragged by the parachute. More specifically, the payload landed on a rock which deformed the aft end plate of the rate control system (RCS), as shown in Figure 6. The nine impact-o-graphs attached to the forward side of the RCS aft end plate recorded the decelerations shown in Table I.

A helicopter was used to transport the payload from the hillside to a level area for loading into a second helicopter. The method selected for transporting the payload from the landing site to the loading area was to pick it up at the top of the parachute canopy. To prepare for this, the lines and canopy of the parachute were taped together at approximately two-foot intervals.

The payload was loaded into the second helicopter as a single piece, as opposed to being disassembled into two pieces, for ease of handling. It is recommended that future payloads of this size or larger have provisions for disassembly in the field, e.g., that the GSFC ORSA cable have connectors installed in it at the station line where the planned field break is to be made.

8.0 CONCLUSION

In conclusion, the flight data and post-flight analysis shows the launch, flight, and recovery of SPAR V to have been highly successful.

TECHNICAL REPORT

on

EXPERIMENT 74/15

flown on

SPAR 5

SEPTEMBER 11, 1978

Principal Investigator:

Professor Donald R. Uhlmann
Department of Materials Science
and Engineering
Massachusetts Institute of Technology
Cambridge, Mass. 02139

January 29, 1980

I. INTRODUCTION

This report describes Experiment 74/15 which was flown on SPAR 5 on September 11, 1978. Experiment 74/15 was designed to study the behavior of second-phase particles at a solidification front. In general, a solidification interface as it approaches a second-phase particle will either engulf the particle, or reject the particle and push it ahead of the interface. Whether the solidification front pushes or entraps the particle depends on the speed at which the solidification front is advancing, the size and shape of the particles, and the characteristics of the particle-interface interactions. The objective of the experiments was to measure the critical velocity--that is, the maximum velocity at which a particle is pushed by the interface--as a function of a variety of parameters.

Our interest in the behavior of second-phase particles at a solidification front and in studying this behavior in a microgravity environment was motivated by two principal considerations. First, such behavior seems certain to be important for the fabrication in space of many composite materials having unique microstructures. It already seems clear that uniform and unique dispersions of solid or liquid phases in matrix liquids can be obtained in the space environment. In nearly all attempts to achieve uniform dispersions by crystallization processing, the crystallization of the matrix liquid upon cooling can substantially change the initially uniform distribution of second phase material due to rejection of the second-phase materials at the solidification front.

Second, and perhaps more important for the overall program of space applications, the understanding and insight gained in the study of particles-at-interfaces in space can be used to provide improved understanding and control of many processes and phenomena on earth.

In previous work (1-5, e.g.) it was found that at sufficiently small growth rates, particles of nearly all materials are rejected by a moving crystal-liquid interface; i.e., they are pushed ahead into the liquid, traveling along with the interface as it advances. Particles can thus be pushed for long distances (thousands of times the particle diameters).

It is apparent that the pushing of a particle or pile-up of particles by an interface demands both a force preventing incorporation of the particle in the crystal and feeding of fresh material to the region of the interface immediately behind the center of the particle. The interaction of the particles with the interface, which is responsible for their rejection from the growing solid, can be represented in terms of a short-range repulsion which exists between the particle and the solid. The particle becomes incorporated into the solid when liquid cannot diffuse sufficiently rapidly to the growing solid behind the particle.

The present investigation was concerned broadly with developing improved understanding of the interaction between second-phase particles and an advancing solidification front, and with developing criteria for the solidification processing of many two-phase composite materials in space. The elimination in space of the effects of density differences between particles and matrix offered the opportunity for systematically determining the factors which are important to the phenomenon of particle

rejection and incorporation.

In addition to obtaining appropriate experimental data, the investigation was also concerned with developing a satisfactory theoretical description of the behavior of second phase particles at a solidification front. In this work, the forces of interaction between particles and interfaces have been computed from the refractive indices, characteristic absorption frequencies and static dielectric constants following the approach suggested by Lifshitz (6). This description of the interaction was combined with a description of the relevant transport phenomena to obtain theoretical predictions of the critical velocities.

With this background, let us consider the SPAR 5 experiment and the results of the ground-based studies.

II. GROUND-BASED STUDIES, CRITICAL VELOCITY

The single most important parameter used to evaluate the interaction of second-phase particles with a solidification front is the critical velocity. As indicated above, the critical velocity is the solidification rate below which the particles are rejected by the advancing interface and above which they are incorporated into the growing crystal. The critical velocity can conveniently be measured on earth by carrying out solidification in either of two geometries: (1) a horizontal geometry in which the sample is contained within a thin chamber, with the particles resting (because of gravity) on the bottom support of the chamber, and the solidification behavior observed through a microscope as the interface advances horizontally; and (2) a vertical geometry in which the particles rest on the interface (because of gravity) as the interface advances vertically upward. In this case, the behavior has usually been characterized by measuring the distribution of particles after solidification rather than by direct observation during the solidification. In both cases, the effects of gravity introduce a significant complication into the measurement.

In the majority of the work carried out to data in our laboratory, the horizontal solidification geometry was employed. Selected particles were mixed into a molten sample contained between a glass support and a cover glas; and the sample was cooled and crystallized rapidly. The resulting sample was typically in the range of 50-200 microns in thickness, and was confined between two glass plates. The sample was then located in a controlled temperature gradient and was traversed through the temperature gradient by a motor-driven screw to provide the desired rate

of solidification. When viewed through a microscope at magnifications in the range of 100 X, particles as small as 2-5 microns in diameter could easily be seen, and their behavior could be followed individually as solidification proceeds. By varying the solidification rate, the critical velocity for each type (and size) of particle could be measured.

While this geometry has the disadvantage that the particles rest on the bottom supporting glass plate and are subjected to unspecified frictional forces, the thin horizontal geometry has the advantage of simplicity and ease of viewing the sample at high magnification over a range of readily controlled growth rates.

The apparatus used for the measurements with a vertical geometry was the single cell version of the flight apparatus, which was discussed in detail in our SPAR 4 report. The single cell apparatus was used with a microscope to permit visual observation of the particles during the experiment. Hence the observational technique was the same as that employed with the horizontal geometry apparatus.

Previous measurements of critical velocities have been carried out for a number of particle-matrix combinations. In all cases, the matrix materials have been characterized by entropies of fusion which are large in Jackson's sense (7). Since the entropy of fusion has been demonstrated to have significant effect on the crystal-liquid interface morphology as well as upon many characteristics of the crystallization process, it seemed highly desirable to explore the behavior of second-phase particles in matrix materials characterized by low entropies of fusion. In addition to the intrinsic interest in such behavior, our concern in this regard was prompted by the fact that metals are

characterized by small entropies of fusion. For this reason, carbon tetrabromide (CBr_4), which has a small entropy of fusion, was chosen as the first matrix material for the SPAR 1 flight. Ground-based measurements of the critical velocity for various particles in CBr_4 were carried out. The particles which were investigated included zinc, tungsten, oxide glasses of two compositions, aluminum oxide, ferric oxide, and zinc sulfide. No particle was observed to be pushed at the lowest growth rate measurable on our equipment (0.1 micron sec^{-1}). CBr_4 could therefore not be used in subsequent experiments.

For this reason, a survey of the critical velocities of low entropy of fusion organic materials was undertaken. The results are given in Table I along with a few of the high entropy of fusion organic materials which were also studied. The other low entropy of fusion materials identified by Jackson (8) were not available in sufficient purity to be usable.

As seen in Table I, d-camphor is the only low entropy of fusion material which exhibits particle pushing at reasonable solidification rates. The critical velocities for particle pushing were measured for camphor with a variety of second-phase particles. Some of the results are summarized in Table II.

Besides the interaction between the particle and the solidification interface, the drag force on the particle is also important in determining the critical velocity. The drag force arises from the difficulty of feeding fluid behind the particle to the growing interface. The drag force can be approximately calculated if the shape of the interface near the particle is known. The shape of the interface behind the

Table I

Critical Velocities of Zinc and Glass Particles in Various Organic Matrix Materials

Name	Formula	Growth Morphology	Critical Velocity (μm/s) Zn (2-8 μm)	Glass (2-10μm)
1. Low Entropy of Fusion Organics				
Camphene	$C_{10}H_{16}$	dendritic	Too impure	
Succinonitrile	$CN-CH_2-CH_2-CN$	flat front	<.3	<.3
Carbon tetrabromide	CBr_4	flat front	<.3	<.3
d-camphor	$C_{10}H_{16}O$	flat front	6	1.5
2. High Entropy of Fusion Organics				
Eicosane	$CH_3-(CH_2)_{18}-CH_3$	prismatic	≥13	>2
Thymol	$C_{10}H_{14}O$	flat front below 2μm/s	4	4-5
Bibenzyl	$C_6H_5-CH_2-CH_2-C_6H_5$	prismatic above 15μm/s	>15	
Chalcone	$C_6H_5-CH-CH-CO-C_6H_5$	prismatic sluggish growth (glass former)	1.3-1.6	(3-4μm) 1.32-1.51 (9 μm) .76-1.32
o-Terphenyl	$C_6H_5-C_6H_4-C_6H_5$	prismatic	0.25-0.30	
Cyclododecane	$C_{12}H_{24}$	flat below 2.2 μm/s needles above	1.3-2.1	.4-1
3-4 Dimethyl phenol	$(CH_3)_2C_6H_3OH$	prismatic	5	
3-5 Dimethyl phenol	$(CH_3)_2C_6H_3OH$	needles	1	
Coumarin	$C_9H_6O_2$	large prisms	≥30	5-8

Table I (Cont'd.)

Name	Formula	Growth Morphology	Critical Velocity (m/s) Zn (2-8 μm)	Critical Velocity (m/s) Glass (2-10μm)
1-10 Decanediol	$OH-(CH_2)_{10}-OH$	needles	>4	2-5
Hexatriacontane	$CH_3-(CH_2)_{34}-CH_3$	needles	No?	No?
Durene	$1,2,4,5\ (CH_3)_4\ C_6H_2$	flat front	$\geq$35	8
Biphenyl	$C_6H_5C_6H_5$		.5	
Naphthalene	$C_{10}H_6$	flat front	>35	10
Vanillin	$C_8H_8O_3$		<.2	<.2
α-phenyl o-cresol	$C_6H_5CH_2C_6H_4OH$		1.5	$_$2
9-Fluorenone	$C_{13}H_8O$		12	6-8
3-Hydroacetophenone	$HOC_6H_4\ COCH_3$	needles	1.5	
Benzil	$C_6H_5COCOC_6H_5$	prismatic	5	$\geq$6.5
Acenaphtene	$C_{12}H_O$		∿.3	∿.3
Phenanthrene	$C_{14}H_{10}$		1	.3
Pyrocatechol	$1,2(OH)_2-C_6H_4$	prismatic	10	1.5
2-Naphtyl benzoate	$C_6H_5\ COOC_{10}H_7$	glass former spherulitic growth	<.2	<.2
Resorcinol	$C_6H_4-1,3(OH)_2$		∿.4	∿.3
Iodoform	CHI_3	needles	<.2	<.2
Cholesteryl Acetate	(liquid crystal)	needles	∿.2	∿.2

Table II

Critical Velocities in Camphor

	D-Camphor
T_M(°C)	179.8
$\Delta S_M/R$	1.4
η(cpoise)	.4-.6
Particles	
Glass	4-5
	.8-1
	<.2
Zn(ZnO)	30-40
	8
	.4
	4-6
Cu(CuO)	30-40
Cu	25-30
	.15
Ni	12-20
	3
	1-3
Au	0.2-0.8
	0.1-0.2
Ge	14-20
Mica	12

particle may be strongly affected by the relative thermal properties of matrix and particle. If the particle is much more conductive than the matrix, as is most often the case for organic matrix materials, the front will curve behind the particle, and the drag force will be considerably increased. To study this problem in more detail, we carried out an analysis of the shape of the interface in the vicinity of the particle using finite element methods. The results will be described in the final report.

In summary, we made extensive ground based measurements of the critical velocities of particles of different thermal conductivities, size, roughness, etc. in a variety of organic matrix materials. We sought to understand the results of these measurements by formulating a new treatment of the phenomenon based on the Lifshitz treatment of the particle-interface interaction coupled with a more accurate description of the drag force based on a knowledge of the shape of the solidification front.

III. FLIGHT EXPERIMENT

It was necessary to design a scientifically valuable experiment which would meet the design requirements of the sounding rocket environment: (1) high acceleration and vibration levels; (2) only a short microgravity experiment period; and (3) power, size, and weight limitations. As detailed above, d-camphor was chosen as the organic matrix material. Unfortunately camphor is a difficult material with which to work; it has a melting point of 178°C, a narrow liquid temperature range, and a high vapor pressure.

The ground based experimentation coupled with the results of the SPAR 1 experiment detailed the following design considerations for the apparatus flown on SPAR 4 and SPAR 5.

(1) It was necessary to control carefully the shape and speed of the solidification front to achieve a useful experiment. Since the telemetry was not sufficiently accurate to measure the position and speed of the front, it was necessary to build an apparatus which would precisely repeat the same cycle for each experiment. The telemetry was used only to detect malfunctions in the apparatus.

(2) The solidification process should at least in some cases be photographed at sufficiently high magnification such that individual particles can be seen at the interface.

(3) The sample chamber must be transparent with flat walls to permit effective photographic recording. Extensive finite element thermal calculations indicated that control of the solidification conditions and the interface shape can be best achieved with a thin

sample (but thick relative to the diameter of the largest particles being studied). This choice was also required to obtain short thermal time constants for melting and solidification.

(4) The sample must only be melted in the microgravity environment to avoid the particles settling out of their initial dispersion.

Based on the above design criteria, fused silica (quartz) was chosen as the sample cell material. It might be noted that plastics could not be used because of the temperature at which camphor melts, 178°C, and its corrosive character.

The sample cell assembly is shown schematically in Figure 1. The quartz sample cell is 3.4 cm high with a 5 mm long fill tube extending from it. The sample thickness is 0.008 inch (200 um). The wall thickness of the quartz cell is 1.5 mm. The cell is 1.3 cm wide. Separately controlled aluminum heater blocks at each end of the cell control the temperature profile in the cell. An expansion reservoir with a Teflon diaphragm compensates for volume changes in the camphor upon solidification or melting. The sample cell is sealed to the volume compensating chamber with a filled Teflon o-ring machined with a square cross section from Rulon H257. The entire sample cell assembly is enclosed in a gold plated copper can which re ·es the temperature of the bottom heater block. The gold plated can reduces the radiational cooling of the exposed quartz cell and isolates each sample cell from its surroundings. The plated can for the photographed sample has infrared reflective windows manufactured by Corion Corporation.

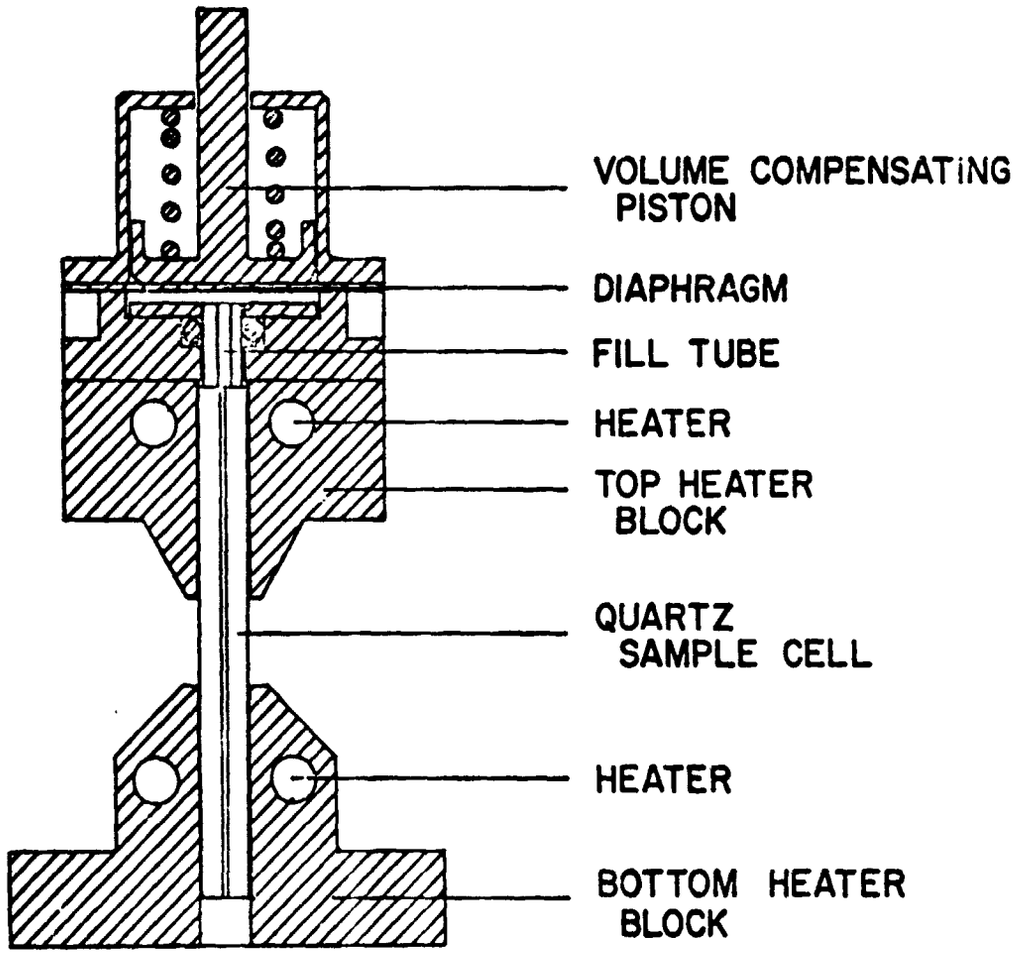

Figure 1 - Sample cell assembly

A sample cell assembly as shown in Figure 1 was also used in the "single cell apparatus" for the ground based testing and measurement of the critical velocities.

The approximate experiment cycle for each cell is shown in Figure 2. At four minutes before launch, the heaters are turned on to bring the cells to their preheat temperature of 175°C at the top and bottom heater block. At 89 seconds after launch when the microgravity portion of the flight has been reached, the sample is melted by raising the temperature of the top heater block to 193°C and lowering the temperature of the bottom heater block to 163°C. Thus a stable solidification interface is created in a temperature gradient of about 55°C cm^{-1}. At 140 seconds, the slow controlled solidification of the sample begins by changing the set point of both the top and bottom temperature controllers at a constant rate. This rate is, of course, set by the desired growth rate of the solid but is about 1°C min^{-1}. At 300 seconds, the experiment is over and the heaters are turned off to solidify the sample before reentry occurs.

The flight apparatus consists of seven sample cell assemblies, a temperature controller for both top and bottom of each of the seven cells, the necessary control electronics, and a camera and lens assembly to photograph one of the seven cells. A Nikon camera with a 250 exposure back is used to photograph one cell at 17.7 X using a 19 mm Nikkor lens at approximately 50 frames $minute^{-1}$.

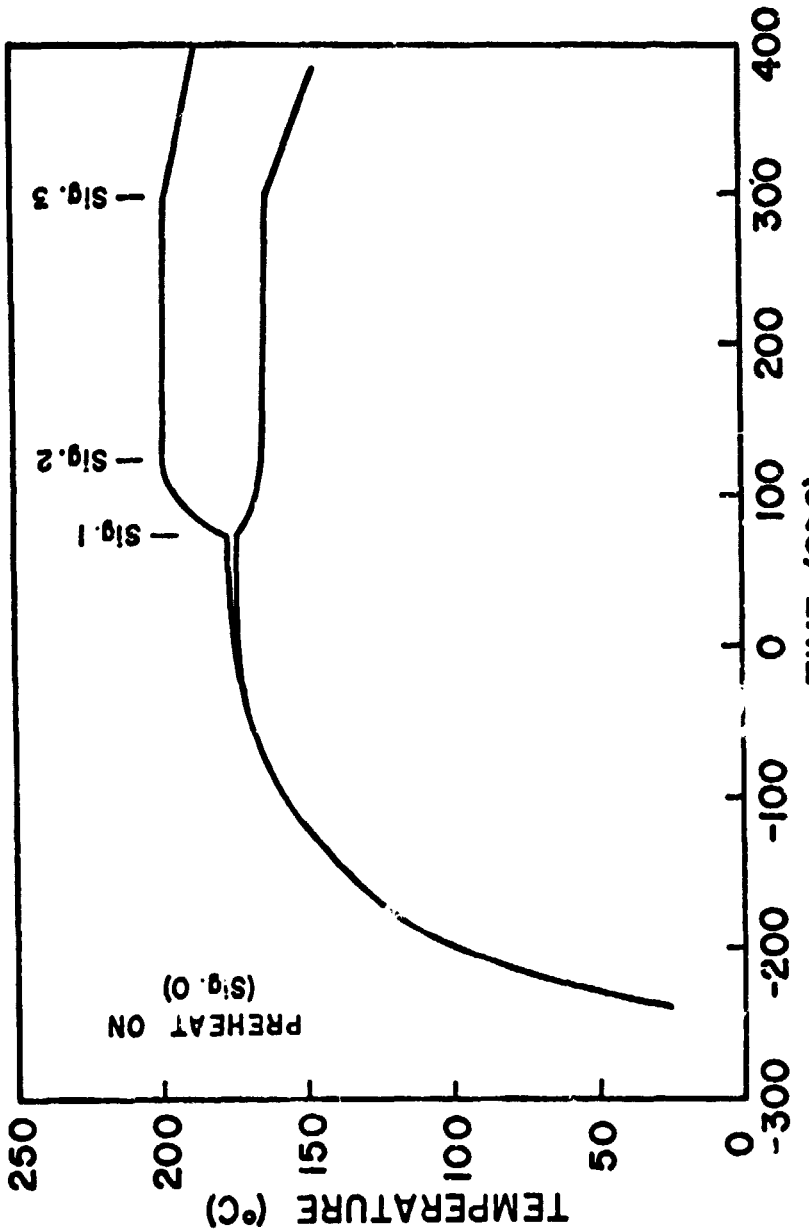

Figure 2 - Approximate temperature cycle of both top and bottom heaters of the sample cell assembly.

IV. MANUFACTURE OF GLASS CELLS AND FILLING PROCEDURE

Because of the fracture of the cell being photographed in the SPAR 4 flight, particular attention was directed to the fabrication of glass cells for the SPAR 5 flight. After much experimentatior, the following procedure was adopted.

1. Two plates of fused silica, 0.4 x 1.22 x 0.06 inch were held in a fixture on a glass lathe; and a fused silica tube was fused coaxily onto one end of the plates.

2. The lathe fixture was removed; the cell was supported by the tube; and fusion of the plates along the bottom, sides and top (where the tube was attached) was affected.

3. The cell was then ground just enough that the width of the cell was 0.500 inch (+0.005, - 0.010), so it would fit into the next lathe fixture.

4. The bottom of the cell was heated in the center with a small torch, and a dimple was blown out and broken off. The fused silica tube that would be the sample neck was fused to the hole in the bottom of the cell.

5. The original tube was snapped off from the cell, and the hole was closed. This rather complicated procedure reduced the necking of the tube which would make the cell impossible to seal with the o-ring.

6. The cell was then placed in another lathe fixture to center the neck and make sure that the cylindrical axes of the neck coincided with

the center line of the cell. If this were not done, the neck would break when the cell was assembled. The neck was left about 1 - 1.5 inches long at this state.

7. The cell was then ground by hand with a sharpening stone to remove the ridges at the edge of the cell so it could be fitted to the aluminum heater blocks. The target clearance was 0.001 inch; but in some cases the actual clearance was about 0.002 inch. The neck was covered with masking tape to keep dust and water out of the cell during this operation.

8. The cell was then fire polished.

9. The neck was cut to length using a scribe-and-break technique. A special jig was used to measure the length prior to cutting.

10. The cell was then ready for installation in the sample assembly.

The procedure for assembling the cell in the sample assembly was as follows:

1. The inside of the sample assembly heater blocks was liberaly coated with thermal grease.

2. The top o-ring assembly was attached to the sample cell. For the SPAR 5 flight, the o-ring was machined from Rulon 257, a filled Teflon. This attachment provided an interference of about 0.001 inch. The o-ring was inserted into the o-ring groove, and the lower plate was screwed down. The inside opening on the o-ring was enlarged with a tapered tool from both sides until the neck of the cell could be inserted. The cell was then inserted and the screws tightened, thereby

compressing the o-ring. Since the filled Teflon used here (for thermal reasons) does not seal well, the o-ring required tightening after every thermal cycle.

3. Holding the seal by the top assembly, the seal was coated with thermal grease and inserted into the cell assembly. Special attention was directed to providing thermal grease around the neck near the o-ring.

4. The bottom of the cell was shimmed with Teflon pieces so that a small leaf spring action forced the cell up against the top cover and o-ring assembly.

5. The cell was then pressure tested and vibration tested. A non-leaking cell was defined as one with a negligible or extremely slow leak rate from 15 psi with just the cell and 1/8 inch ID connecting tube volume. Viton tubing was used so that the cell could be operated hot during the vibration testing.

The cells were filled using the following procedure:

1. The camphor was cleaned by vacuum sublimation at 100°C in a fixture.

2. The particles were put into the cell using the corner of a jeweller's screw driver.

3. The purified camphor was placed inside the filling fixture, and the fixture was assembled into the cell.

4. The fixture was brought to 190°C, with the top and bottom heater blocks at 185°C, using the single cell apparatus to control manually the heater blocks and a Variac to control the temperature of the filling fixture.

5. After the cell was filled, the camphor was further degassed by melting and recrystallization four times.

6. The expansion reservoir Teflon diaphgram, spring load piston, and cover were installed. The nuts were torqued to 58 in-oz.

7. The camphor was again completely remelted with special care taken to ensure the sample being melted from the top down (to avoid cell breakage).

8. While the sample was being continuously inverted back and forth, the power was turned off and the center of the cell was quenched with a jet of air to ensure that the particles were dispersed.

V. CALIBRATION PROCEDURE AND PRE-FLIGHT TESTING

After much experimentation, it was found that the most accurate and reliable calibration technique employed fourteen thermocouples attached to an external data logger to monitor the temperature of both heater blocks. By calibrating the system in its flight configuration in a vacuum, problems associated with transfer of the calibration conditions between the single cell apparatus and the flight apparatus could be avoided. The temperature set points and cooling rates were determined by fixed resistors soldered into the controller boards. Hence the calibration procedure specified the replacement of these resistors to achieve the desired experimental conditions.

The samples in positions 6 and 7 were designed to have the same experimental conditions. Hence should the sample or temperature controller in position 7 fail, the sample and its associated controller from position 6 could be shifted to position 7 without requiring that the system be recalibrated. This flexibility was in fact required for the SPAR 5 flight due to a cell failure caused by mechanical misalignment during the fill procedure.

Two cell failures were observed during the filling of the cells for the SPAR 5 flight (one of which was intended for position 7). In both cases, the failure took the form of the neck snapping off as a result of mechanical misalignment. Two spare cells were available to replace the two broken cells. Unfortunately, one of the spare cells apparently had a very small crack, as a very small leak was observed after the cell was filled with camphor. Since no additional replacement cell was

available, the cell with the very small crack was flown (in position 1).

The interchange of the cells in positions 6 and 7 and their associated temperature controllers invalidated the telemetry data for these cells. It was planned to obtain the appropriate telemetry calibration data after the flight during post-flight testing; but a voltage reference in the telemetry circuits was damaged on impact, which invalidated the telemetry data obtained during post-flight testing. In any case, the telemetry was designed to point out gross malfunctions, rather than to verify correct calibration--for which it was not sufficiently accurate. The absence of telemetry calibration data for positions 6 and 7 was not a significant handicap, since the temperatures of the cells were reproduced within 1°C between the calibration tests and the post-flight tests. The 1°C variation is a product of both the inaccuracy of the system and the measuring technique.

As a result of difficulties observed during integration testing, some concern was expressed about the ability of the system to achieve reproducibly the correct interface location for the photographed cell (cell No. 7). The program manager at Marshall requested that a dummy sample be installed for the horizontal test at the White Sands missile range, so that the calibration procedures could be checked.

In the calibration testing at MIT/Draper Laboratories, carried out using dummy cells, the apparatus functioned as programmed. Following this calibration, the apparatus was hand-carried to White Sands. The apparatus functioned as programmed during the horizontal test with the dummy cells. The photographed cell used in these horizontal tests was

the same as that used in the integration test sequence. A problem was encountered with a light source in the horizontal test, which required an emergency installation of new lamps and photographic testing.

The flight samples were installed for the vertical test, with a thermal shift cable employed to prevent the samples melting. The telemetry output for position 7 was somewhat low, but the lack of exact calibration data made interpretation of the discrepancy difficult. A set of thermocouples was installed on the cell in position 7 to verify the preheat temperature set-point; but the resulting data were inconclusive. Since the apparatus was functioning properly, the decision was made to accept that the temperature controllers were operating correctly and assign the discrepancy to the telemetry channel. This decision was consistent with the overall design philosophy of the experiment, the accuracy of the telemetry data, and the results of many calibration tests run at MIT/Draper Laboratories.

VI. SPAR 5 EXPERIMENT AND RESULTS

The experiments flown on SPAR 5 are shown in Table III. Each experiment was chosen with a solidification rate and a range of particle diameters such that the largest particles are not pushed in the ground based experiments but the smaller particles are pushed. The final distribution of particles is then examined after recovery of the apparatus and analyzed to estimate the critical velocity.

The growth rates shown in Table III are average growth rates during the middle of the controlled growth. Significant deviations from this growth rate can occur during the initial portion of the growth as will be discussed in detail in connection with the flight film. The accuracy of this growth rate is approximately $\pm$ 10%.

The glass particles are fused glass spheres obtained from Potters Industries; the nickel particles are "5 μm spheres" obtained from Ventron-Alfa Products. The particles were sized with sieves, and the diameters were measured with a microscope and calibrated eyepiece.

The d-camphor used in both the ground based experiments and the flight experiments was purified by vacuum sublimation at 100°C three times.

The telemetry indicated that the apparatus functioned correctly during flight. Post-flight testing of the apparatus, carried out under identical conditions employed in the preflight testing with the same set of thermocouples, indicated that the apparatus repeated its temperature cycle within 1°C. The 1°C variation represents the overall accuracy of both apparatus and the test procedure. The design philosophy of this experiment dictated a reliance on this repeatability of the apparatus

Table III

Experiment Set-up (SPAR 5)

Cell No.	Particles	Growth rate in 10^{-6} m/s
1	glass (0-20 µm)	2.2
2	glass (10-30 µm)	1.2
3	glass (0-10 µm)	3.2
4	Ni (0-30 µm)	5.2
5	Ni (0-30 µm)	4.6
6	glass (0-20 µm)	1.3
7	glass (0-20 µm)	1.5

to control the experimental conditions during the flight, since the telemetry was not sufficiently accurate to measure the experimental conditions. Based on this series of tests in vacuum at room temperature, the experimental conditions listed in Table III were verified. Unfortunately, as noted in the previous section, a voltage reference within the telemetry circuits was damaged on impact so that preflight and postflight telemtry could not be compared.

The results obtained on the samples in the various cells may be summarized as follows:

1. Cell No. 7

This cell was photographed during flight. It contained glass spheres and was solidified in the microgravity environment at growth rates between 4 and 2 $\mu m\ sec^{-1}$ during the period of crystallization recorded photographically. From the flight photographs, the following information was noted:

1. The sample was not melted before launch; hence this sample--and inferentially the others as well--retained the initial dispersion of particles prior to melting and recrystallization in the microgravity environment.

2. The matrix material (camphor) was successfully melted in the microgravity environment, leaving the particles dispersed in the liquid.

3. Although the interface melted back to a position in the field of view, it did not melt back as far as desired (and programmed). In particular, the interface melted back to a position about 27% of the frame length into field of view, whereas it was programmed to melt back

to a position in the middle of the field of view.

The difference between the observed melt-back position and the programmed position could be accounted for by either a mechanical misplacement of about 0.022 inch or a shift in temperature of about 3°C. A mechanical misplacement anywhere near as large as 0.022 inch is exceedingly unlikely; and the repeatability and accuracy of the temperature measurements--based on a sizable number of laboratory calibrations--is unlikely to be greater than about 1°C. For this reason, we remain uncertain as to the precise cause of the discrepancy between the observed melt-back position and the programmed position. It is apparent, however, that the top heater heated at a faster rate than the bottom heater cooled--behavior which was not observed in the ground-based work.

Because the interface did not melt back as far as programmed during the melting cycle, a large portion of the recrystallization which was photographed corresponded to the period of relatively rapid growth (3-4 μm sec^{-1}). This is seen as the interface starts to advance in recrystallization following melt-back. During this period of relatively rapid crystallization, the particles were incorporated in the growing crystal rather than pushed ahead by the interface. Near the end of the flight film, the growth rates slowed to values about 2 μm sec^{-1}. In this range of slower growth, rejection of some of the particles at the advancing interface was observed.

From these measurements, a critical velocity of about 2 μm sec^{-1} is estimated for a particle size of approximately 5 μm. Considering

the limited number of particles which were examined and the limited crystal growth which was observed under near-programmed conditions (before the interface grew out of the field of view), we can simply suggest that the critical velocity for the glass spheres in this sample was approximately equal to the critical velocity measured in the vertical geometry in the ground-based experiments. It can also be stated that particles are entrapped in the growing crystal in the absence of external forces with the container walls.

Figures 3-8, taken from the flight film (frames 665, 657, 653, 650, 647 and 646 respectively) show the advance of the interface during the final stages of observed growth (where the growth rate was in the range of 2 $\mu m\ sec^{-1}$). Directing particular attention to the particles in the top left portion of the photographs, rejection of particles at the crystal-liquid interface is seen. At the same time, entrapment of other particles and particularly groups of particles is also seen. Rejection-entrapment behavior of the type seen here was frequently seen in our ground-based studies at growth rates near the critical velocity. That is, some of the particles are pushed while other particles are rejected at the interface.

Postflight examination of sample No. 7 supported this finding. No lines of high particulate density parallel to the interface position during growth were seen in the solidified sample. Apparently, the growth rate did not get quite as low as programmed--very likely for reasons similar to those responsible for the incomplete melt-back of the interface--and at the somewhat higher growth rate, only a modest portion

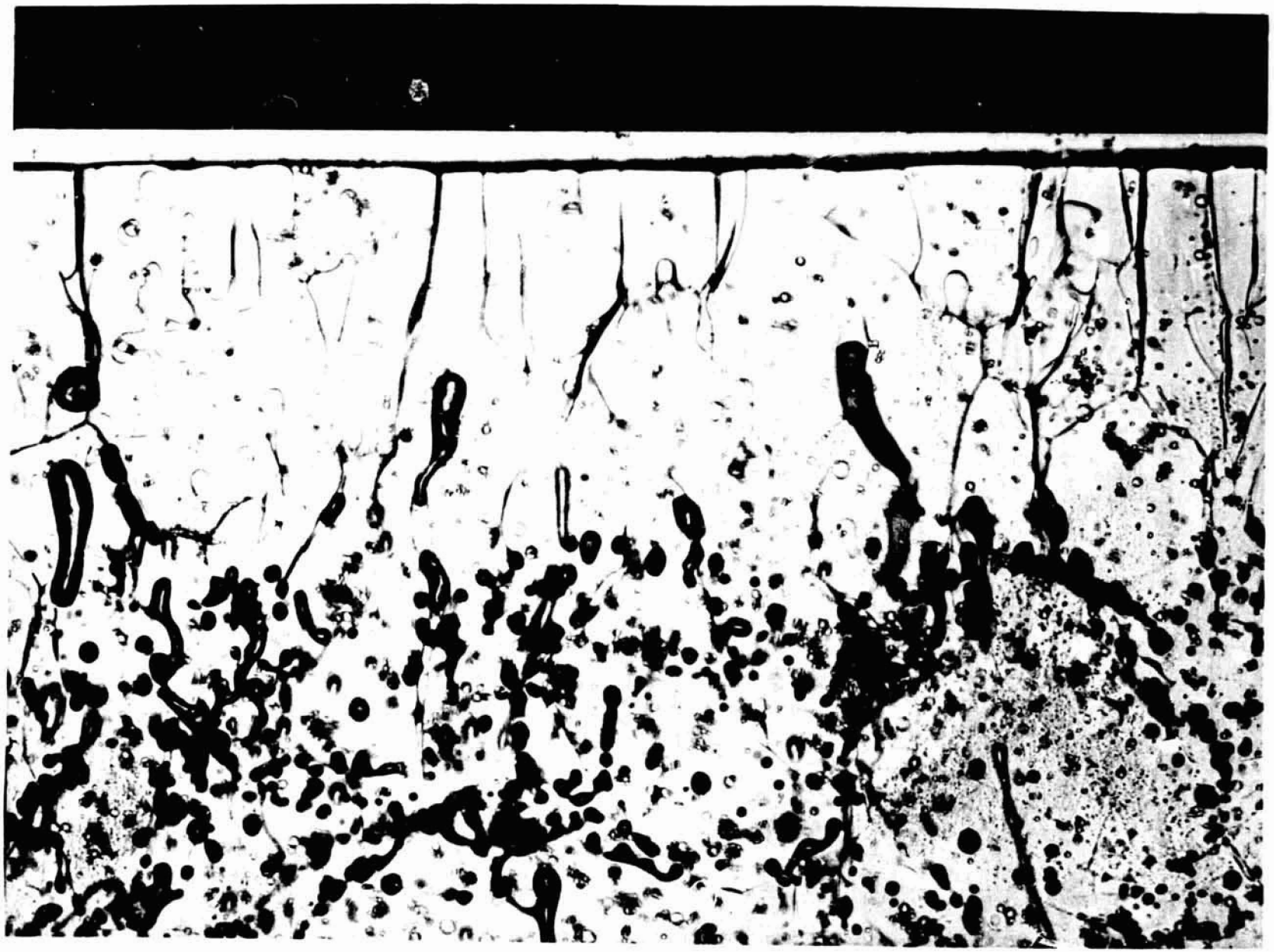

Figure 3 - Photo No. 665 from flight film, Cell No. 7. Magnification x117 .

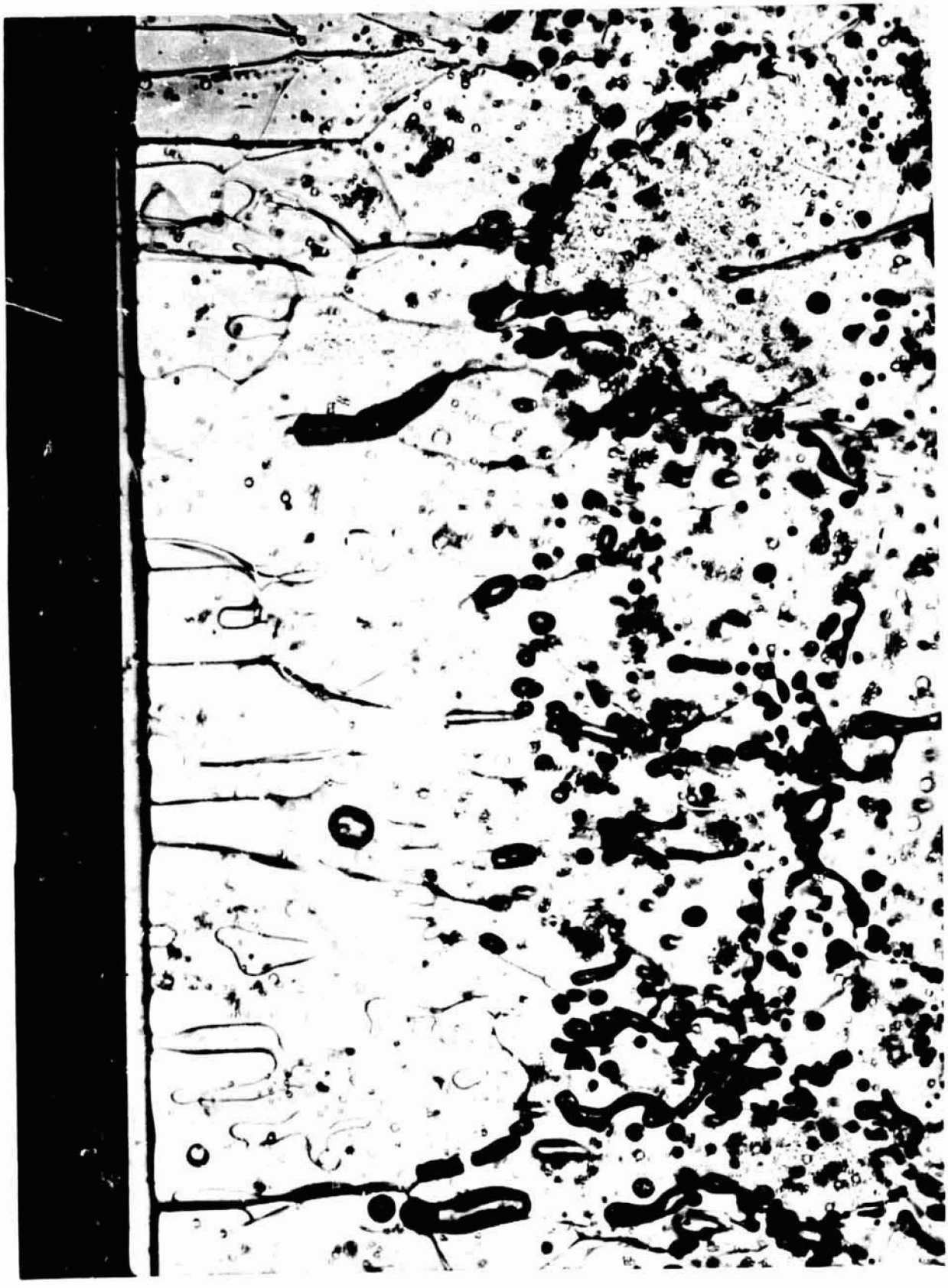

Figure 4 - Photo No. 657 from flight film, Cell No. 7. Magnification ~117 X.

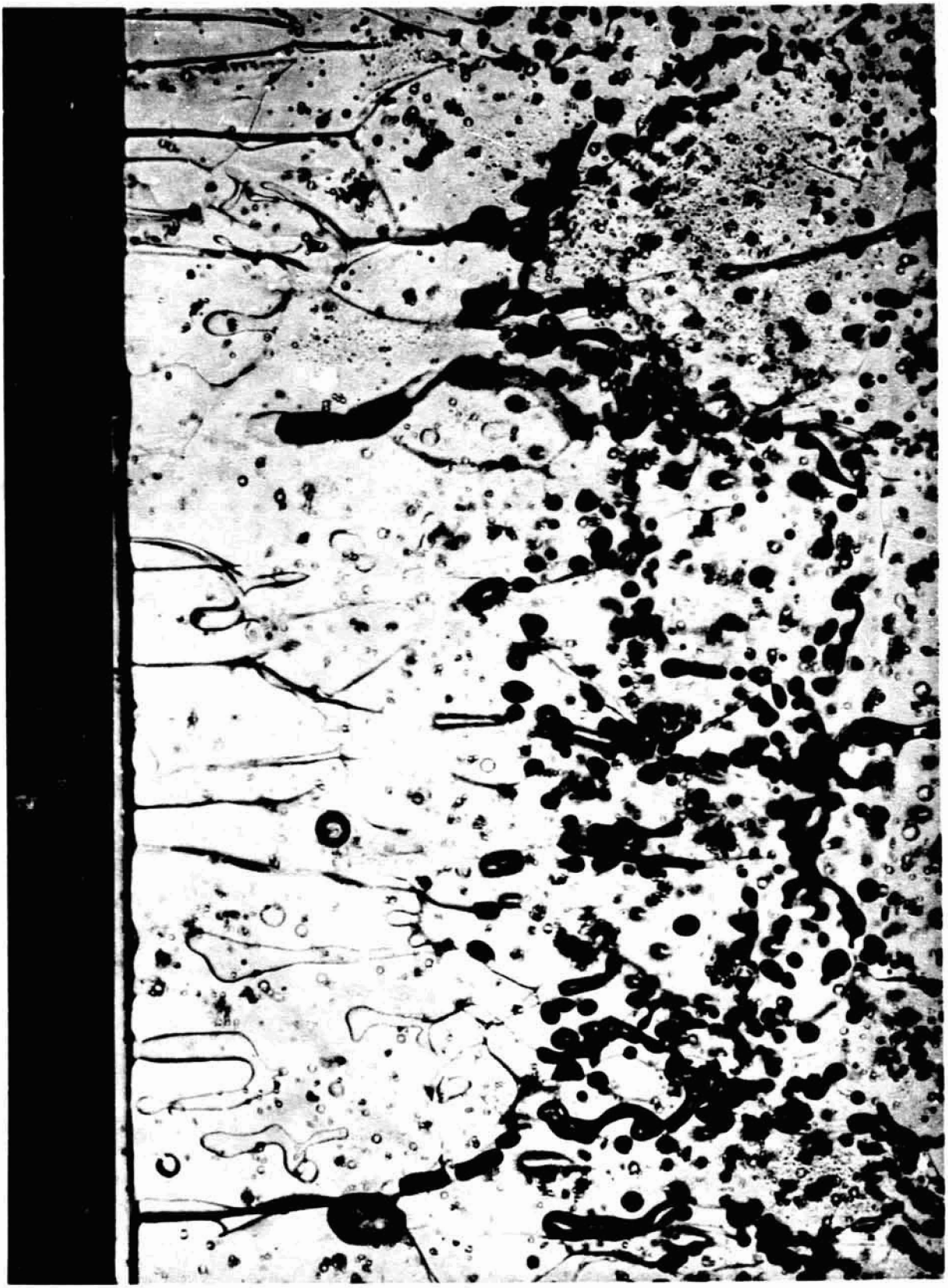

Figure 5 - Photo No. 653 from flight film, Cell No. 7. Magnification ~117 X.

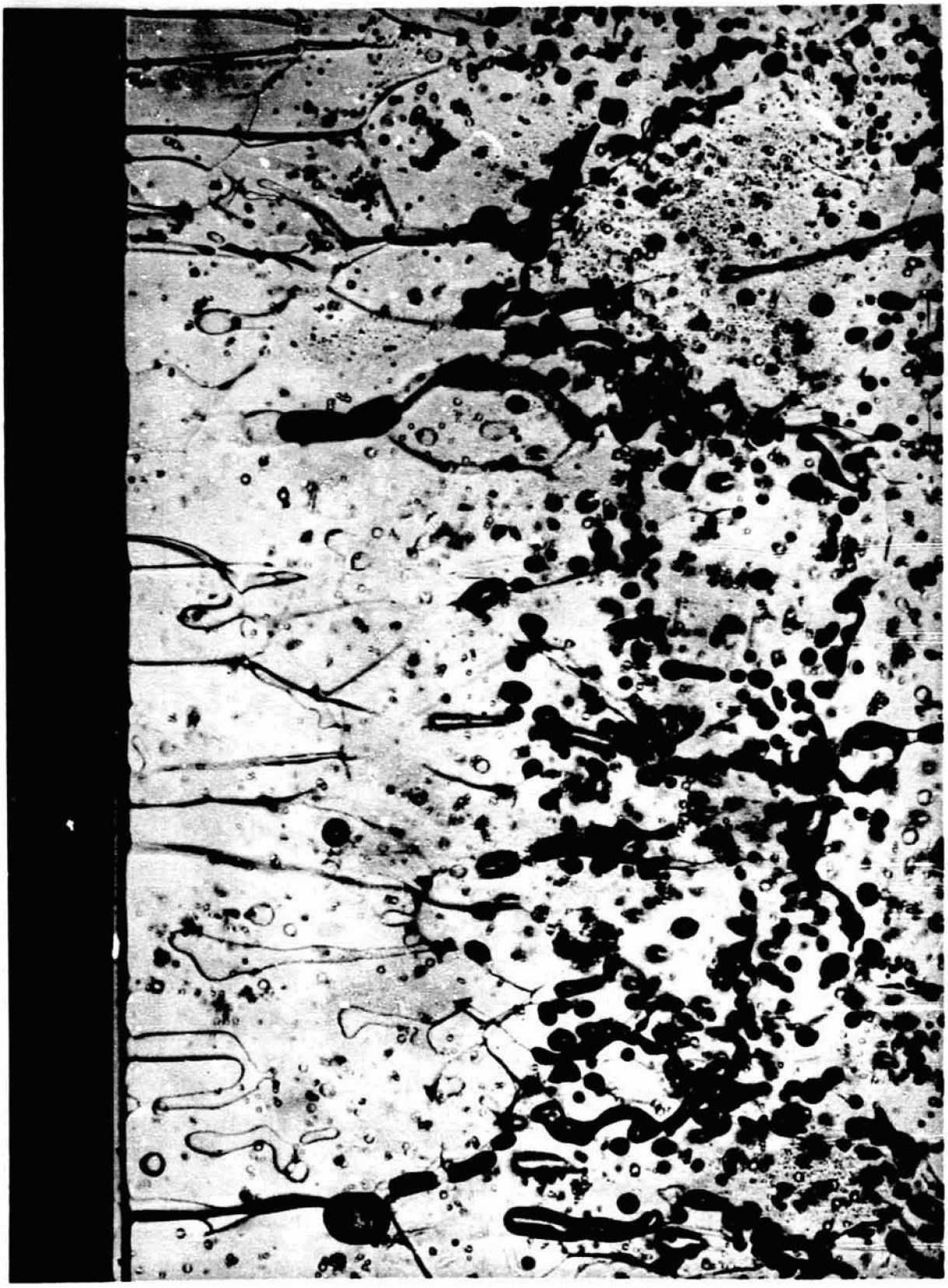

Figure 6 - Photo No. 650 from flight film, Cell No. 7. Magnification ~117 X.

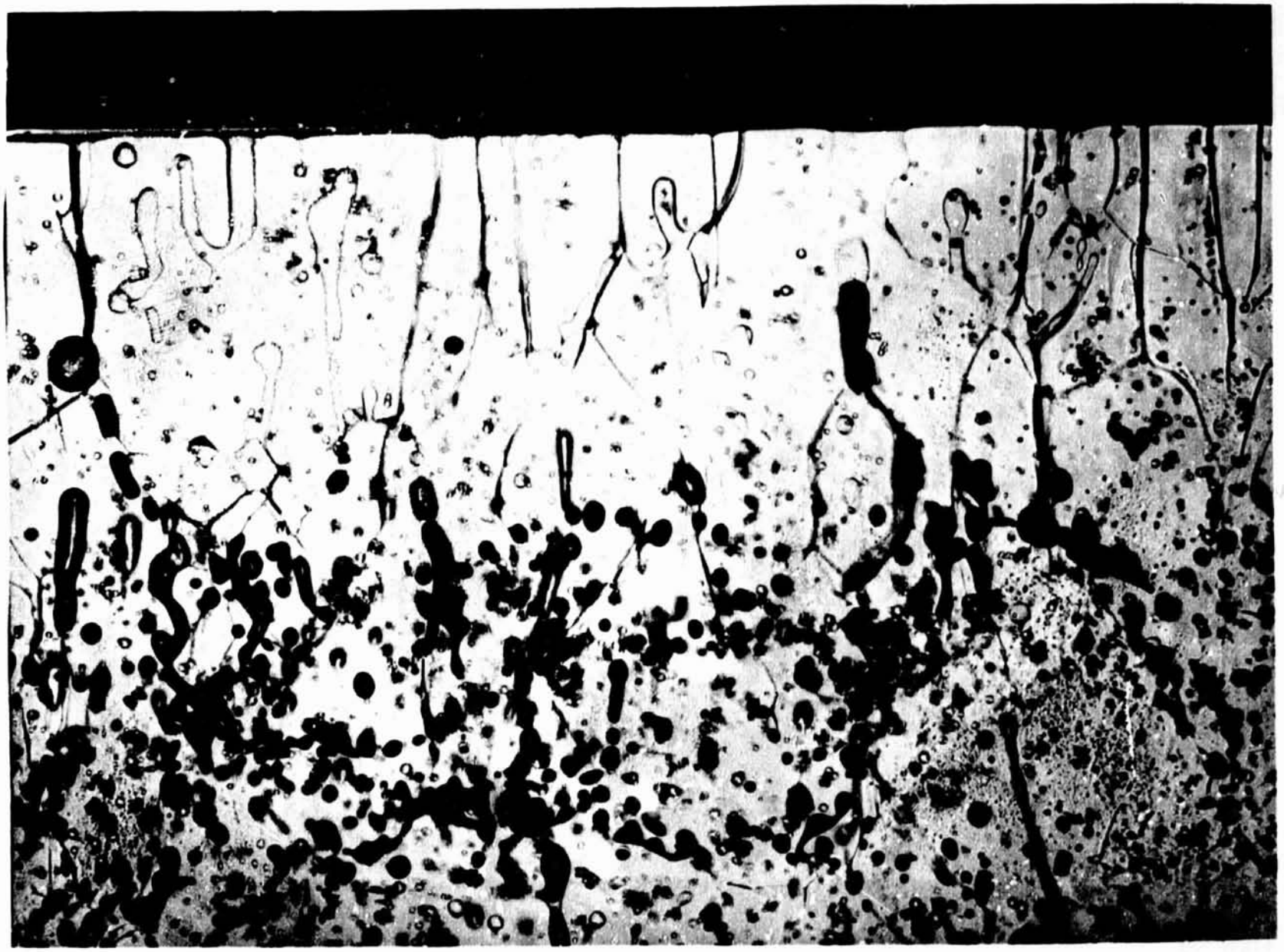

Figure 7 - Photo No. 647 from flight gilm, Cell No. 7. Magnification ∿117 X.

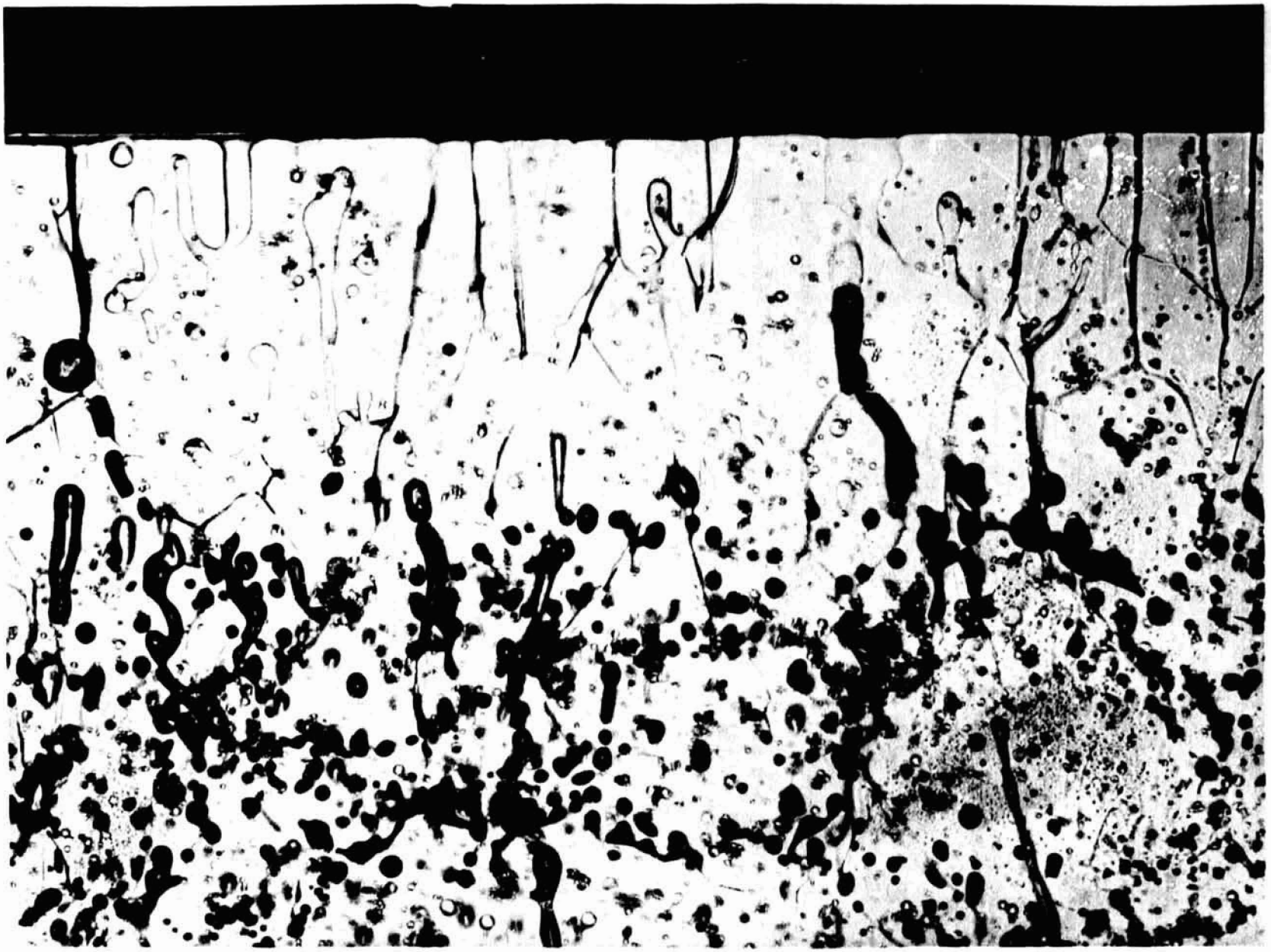

Figure 8 - Photo No. 646 from flight film, Cell No. 7. Magnification ∿117.

of the particles are pushed by the interface; and these are not pushed indefinitely.

Also observed in the flight film, e.g., in the top left region of Figures 6-8, is thermomigration of bubbles in the solid. As expected, the bubbles move through the temperature gradient toward the hot end of the sample.

2. Cell No. 1

This cell, which also contained glass spheres, was empty of camphor when returned to MIT. As indicated in the discussion in the preceding Section, a possible leak in the cell was detected before launch; but an appropriate, calibrated replacement cell was not available (the two spare cells were already in use). It was hoped that rate of leakage would be sufficiently slow that information could be obtained from the sample; but this was not the case.

3. Cell No. 2

This sample also contained glass spheres and was crystallized in the microgravity environment at an average rate of about 1.2 $\mu m\ sec^{-1}$. The post-flight examination indicated the presence of two large bubbles in the sample. These are shown in the overall view of the cell shown in Figure 9. The bubble to the left in the figure was observed in the left-central region of the zone which crystallized slowly in microgravity. The larger bubble in Figure 9 was observed near the end of the controlled-solidification region and in the region of subsequent quench-induced growth. The region of the first bubble is

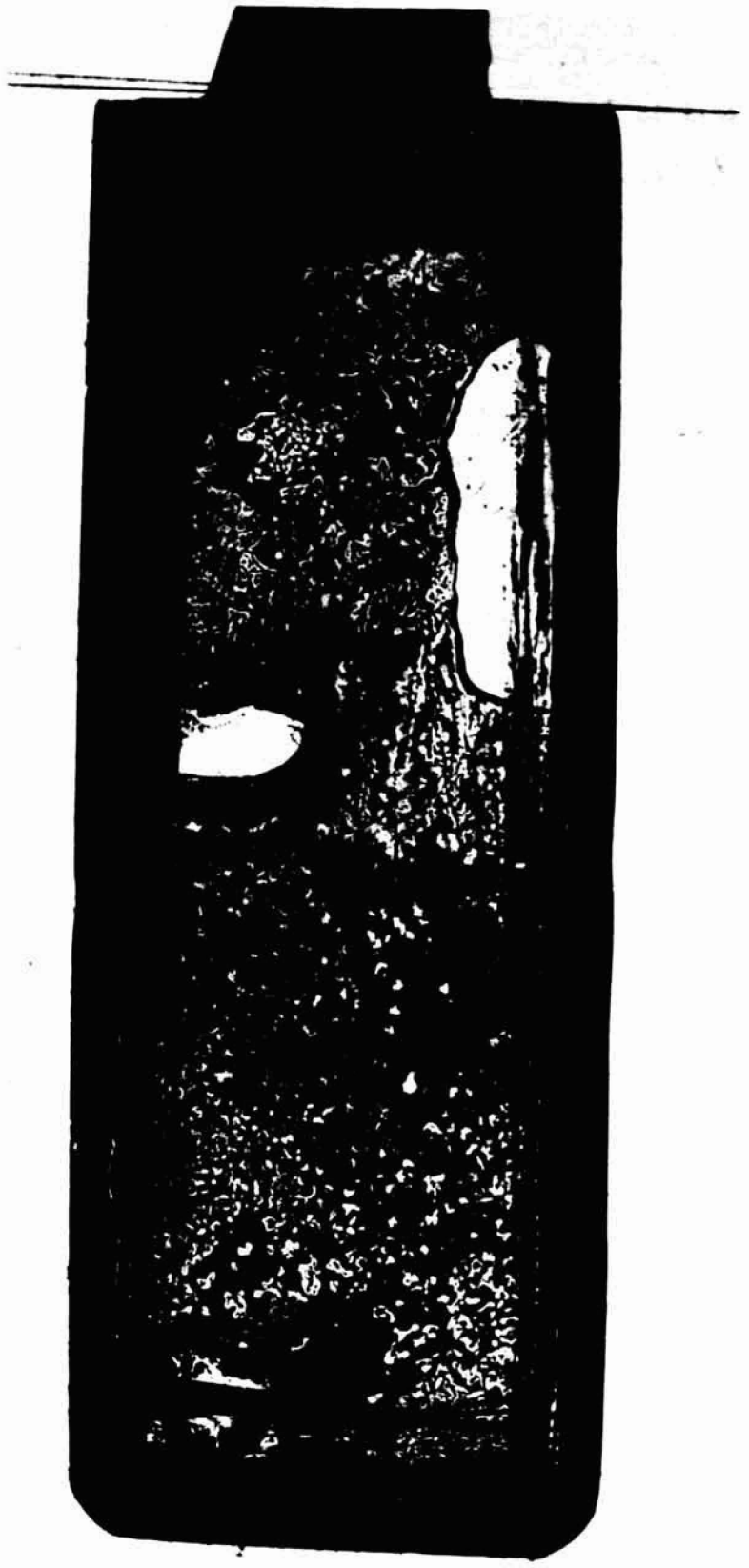

Figure 9 - Overall view, Cell No.2, post-flight.
Cell width is 0.5 inch.

shown in more detail in Figure 10.

Detailed examination of this sample showed no evidence of large-scale rejection of the glass spheres at the interface. The occurrence of the bubbles, particularly the first bubble, and the convection cells in the liquid associated with such bubbles in a temperature gradient, could wipe out any rejection that might have been observed. Such convection cells were sometimes noted in the ground-based experiments; and the rejection-incorporation behavior near the bubbles was found not to be characteristic of behavior elsewhere in the samples. In any case, the programmed growth rate for this cell is only somewhat smaller than that in the photographed cell, where only some of the particles were rejected at the interface, and were pushed only short distances before being incorporated in the solid.

4. Cell No.3

This cell also contained glass spheres, and was programmed to solidify at an average rage of 3.2 μm sec^{-1}. As shown in the overview of the full cell shown in Figures 11 and 12, the solidified zone in this sample lacked the clarity seen in the other samples. The camphor appeared dirty, despite the fact that it was purified like that in the other cells. Detailed post-flight examination of the sample showed no evidence for rejection of particles at the interface during the controlled microgravity solidification. This finding is consistent with the observations made on the photographed sample in Cell No. 7, where all particles were seen to be incorporated in the solid (no rejection at

Figure 10 - Post-flight view of lower portion of recrystallized region in Cell No. 2. Magnification ~35 X.

Figure 11 - Overall view, Cell No. 3, post-flight.
Cell width is 0.5 inch.

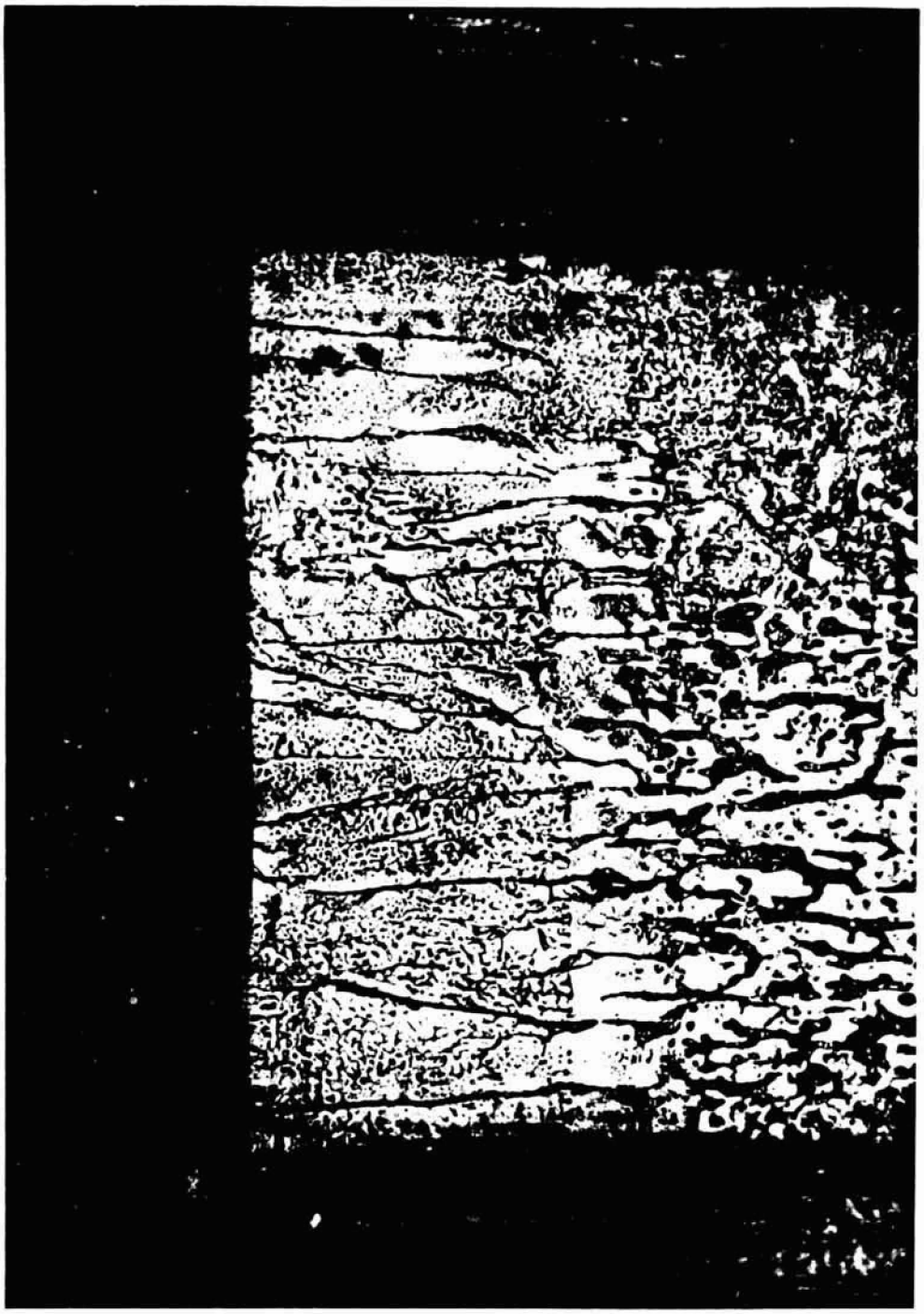

Figure 12 - Post-flight view of recrystallized region in Cell No. 3.
Magnification ~35 X.

the interface) at growth rates of 3 μm sec^{-1}.

5. Cell No. 4

This sample contained nickel particles and was programmed to solidify at an average rate of 5.2 μm sec^{-1}. A sizable bubble was seen in the post-flight analysis, as noted in the overall view of the cell shown in Figure 13. It is not clear if this bubble was present during solidification in microgravity, or whether it formed subsequently by agglomeration of smaller bubbles (perhaps by thermomigration). The distribution of particlesin the cell seems to indicate that at least partial rejection of particles occurred during solidification in microgravity (see Figure 14). Clumps of particles oriented perpendicular to the solidification direction were seen, as were sizable regions devoid of particles.

6. Cell No. 5

This cell also contained nickel particles, and was programmed to solidify at an average rate of 4.6 μm sec^{-1}. The region solidified under microgravity conditions is seen clearly in the overall view of the cell shown in Figure 15. Post-flight examination indicated that the region solidified under microgravity conditions was much cleaner of individual randomly distributed particles than the rest of the cell; and the incidence of clusters of particles oriented perpendicular to the growth direction is greater than in the rest of the cell. These features are seen in Figure 16. It is concluded therefore that many of the individual particles in this sample were pushed at the specified growth rate.

Figure 13 - Overall view, Cell No. 4, post-flight.
Cell width is 0.5 inch.

Figure 14 - Post-flight view of a portion of recrystallized region in Cell No. 4. Magnification ~135 X.

Figure 15 - Overall view, Cell No. 5, post-flight Cell width is 0.5 inch

Figure 16 - Post-flight view of a portion of recrystallized region in Cell No. 5. Magnification ~135 X.

7. Cell No. 6

This cell contained glass particles and was programmed to solidify at an average rate of 1.3 μm sec^{-1}. The region solidified under microgravity conditions in this sample was not clearly visible (see the overall view of the cell in Figure 17 and the higher magnification view in Figure 18). Detailed examination of the cell showed no positive evidence of large-scale rejection of the particles. It is not possible, however, to rule out the local rejection of particles (pushing for a short distance and then trapping) of the type observed for the glass particles in the photographed cell (Cell No. 7).

Figure 17 - Overall view, Cell No. 6, post-flight.
Cell width is 0.5 inch.

Figure 18 - Post-flight view of recrystallized re in Cell No. 6.
Magnification ~15 X.

VII. CONCLUSIONS

The most important objective of this experiment was to ascertain whether redistribution of particles would occur in a microgravity environment, and whether such redistribution could be a significant problem for the solidification of two-phase materials in space, in cases where one of the phases occurs as discrete second phase particles.

While difficulties were encountered with several aspects of the flight experiments, most notably difficulties associated with the interface in the photographed cell not melting back to the programmed position, the results indicate that particle pushing by a crystal-liquid interface does occur under microgravity conditions. The results also indicate that particle pushing in microgravity occurs with similar characteristics to those found by solidifying the same combinations of materials in 1-g.

The SPAR 5 experiment was therefore successful with respect to its principal objectives. Our principal disappointment was the less-than-programmed time photographed solidification in Cell No. 7. While specific problems were found with some of the unphotographed cells, sufficient data were obtained from the cells without problems to provide the desired insight.

REFERENCES

1. A. E. Corte: J. Geophys. Res. 67 (1962) 1085.
2. D. R. Uhlmann, B. Chalmers and K. A. Jackson: J. Appl. Phys. 35 (1964) 2896.
3. G. F. Bolling and J. Cisse: J. Crystal Growth 10 (1971) 56, 67.
4. A. W. Neumann, C. J. Van Oss and J. Szekely: Kolloid Z.u.Z. Polym. 251 (1973) 415.
5. V. H. S. Kuo and W. R. Wilcox: I & EC Process Design and Develop. 12 (1973) 375.
6. E. M. Lifshitz: Soviet Phys. - Theoretical Physics (JETP) 2 (1956) 73.
7. K. A. Jackson: in H. Reiss, ed., Progress in Solid State Chemistry, Vol. 4 (Pergamon Press, New York, 1967).
8. J. D. Hunt and K. A. Jackson: Acta Met. 13 (1965) 1212.

FINAL POST-FLIGHT REPORT

ON

SPAR V
EXPERIMENT NO 74-21
THE DIRECT OBSERVATION OF DENDRITE REMELTING AND MACROSEGREGATION IN CASTING

NATIONAL AERONAUTICS AND
SPACE ADMINISTRATION
GEORGE C. MARSHALL SPACE FLIGHT CENTER
ALABAMA

PRINCIPAL INVESTIGATOR:

DR. M. H. JOHNSTON

CO-INVESTIGATOR:

C. S. GRINER

The Direct Observation of Uni-Directional Solidification As a Function of Gravity Level

M. H. Johnston, C. S. Griner, R. A. Parr, and S. J. Robertson

The NASA Space Processing Program is investigating the application of the low gravity space flight environment to the advancement of materials science and technology. This objective can be met by positive research results which contribute to improving processes on the ground by studying materials processing in space.

The Space Processing Applications Rocket (SPAR) Project offers the investigator conditions of low gravity (10^{-5} g, where g is defined as 980 cm/s^2) for periods up to five minutes. An earlier publication[1] presented the results of a SPAR casting experiment of bidirectional solidification. This experiment was designed to observe the growth of dendrites in the columnar solidification region and to determine the influence of gravity driven flow on the formation of the equiaxed zone. Solidification in low gravity resulted in four nuclei that formed a completely columnar casting. Obviously, the absence of gravity related flow severely altered the final growth morphology. To further study the columnar solidification region, a second experiment was flown that incorporated three-sided solidification, (designated 74-21/3R).

The unidirectional solidification series experiments (designated 74-21/2R) were designed to observe the dendrite and interface growth during unidirectional

solidification and to ascertain the influence of gravity flow on dendrite remelting and hence the occurrence of freckling-type phenomena.

H_2O-NH_4Cl was selected as the transparent metal-model material for the experiment. This system has been used extensively as a metal-model material in the investigation of solidification phenomena[2-4], and was used in the previous SPAR bidirectional solidification study[1]. Experimentation has included such areas as growth morphology[5], dendrite remelting and coarsening[6], and the origin of freckles[7]. The present experiments added to our knowledge of solidification phenomena and in particular further enhanced the earlier space processing studies on metal and metal-model systems.

Experimental Procedures

A solution of NH_4Cl was prepared for the experiments by saturation in H_2O at 22°C. The resultant saturated solution was determined from the phase diagram[7] to be 28.4 pct NH_4Cl.

For experiment 74-21/2R, the solution was then encapsulated in a completely filled quartz cuvette and sealed with a teflon cork and a flat silicone washer. The cuvette was mounted into a cuvette assembly (Figure 1) consisting of one thermoelectric cooling unit, three thermistors, and the mounting bracketry which also provided the heat sink for the thermoelectric device.

In experiment 74-21/3R the solution was encapsulated in a plexiglass cuvette and sealed by glueing a small piece of plexiglass over the fill hole. The cuvette was mounted in a cuvette assembly (Figure 2) consisting of three

thermoelectric units, four thermistors, and the mounting bracketry. Power was supplied by a 28V DC battery regulated to constant 4 amperes. The assemblies were backlighted by tungsten filament lamps. The solidification process was photographed from the front of the cuvette with a 35mm Nikon F2 camera. A total of 240 frames per experiment were taken with a motorized back at 1 fps.

The two experiments were housed in the sounding rocket in the orientations shown in Figure 3. The cooling devices were actuated at 60 sec into the flight for #2 and 30 sec for #3. During the launch phase of the flight, the rocket was spin-stabilized with a spin rate of about 240 rpm. At about 70 sec, the rocket underwent de-spin, and at 90 sec, powered flight ended and the low gravity period begun. The low gravity portion of the flight continued until about 360 sec flight time.

Thermistor temperature measuring devices were attached to the outside of the containers at several locations to permit an analysis of heat transfer throughout the containers and the ammonium chloride solution in the containers. The temperature histories thus determined along the fluid boundaries were then used as boundary conditions for an analysis to determine convective fluid motions. Figure 4 shows the experiment configurations and the locations of the temperature measurements on both the 74-21/2R and 74-21/3R experiments.

The gravity levels during flight as measured by on-board accelerometers are shown in Figure 5 for the components in the vehicle X, Y, Z coordinate directions (see Figure 1 for orientation of experiments with respect to these directions). Zero flight time was taken at 15:59:10 (hrs, min, sec) on the day of launch.

A series of ground based tests (GBT) was made for comparison with the low g experiment. All GBT were run in the flight hardware within a vacuum chamber having a thermally controlled shroud. The gravity vector was oriented perpendicular to the cooled surface, and hence the growing interface. The cuvette temperature versus time curves for GBT and flight are shown in Figures 6 and 7. The cooling rates of 74-21/2R for the two cases were comparable and it should be noted that the flight experiment began below the saturation temperature. As shown in the previous experiment[1], differences in temperature during the two tests are attributable to the respective presence or absence of convective fluid flow. The temperature profiles for 74-21/3R indicate that this flight experiment also began below the saturation temperature. The cooling rate appears to be less than that of the ground based tests.

Thermal analyses were performed to simulate heat transfer in the 74-21/2R and 74-21/3R experiment configurations during both flight and ground test. A Lockheed-Huntsville developed thermal analyzer computer code was used in these simulations. The experiment configurations, including both

container and enclosed ammonium chloride solution were modeled on the thermal analyzer program. Then the cooling rates where the thermoelectric devices contact the container surfaces were systematically adjusted until the temperatures at the thermistor locations satisfactorily matched the measured temperatures. The computed temperatures at the interface between the container and enclosed liquid were then used in an analysis of coupled thermal conduction and convection within the liquid.

Thermal analyzer computed temperatures in the quartz container walls and in the enclosed liquid are shown in Figure 8 for a section of container near the cooled face at various flight times for experiment 71-21/2R. Note that the container wall is substantially cooler than the enclosed liquid during the transient cool-down period. This is due to the higher thermal conductivity of the quartz material (3.3×10^{-3} cal/cm sec C) compared to the ammonium chloride solution (1.2×10^{-3} cal/cm sec C). The effect of the cooler walls will be to induce some side wall cooling of the liquid in addition to the expected longitudinal conduction toward the cooling surface.

The wall temperatures computed over the interior surface of the container by the thermal analyzer program were used as boundary conditions for the LOCAP two-dimensional coupled thermal conduction and convection analyzer code.

Using the temperature boundary conditions obtained from the thermal analyzer program and the gravity conditions calculated from telemetry data,

temperature, density and velocity distributions were computed throughout the liquid as a function of flight time. As expected for the very low gravity conditions, the computed convective velocities were very low, the largest being on the order of 10^{-5} cm/sec. Heat transfer within the liquid, therefore, was essentially by conduction only. Computer generated plots of isotherms, and velocities are given in Figure 9 at different time periods after initiation of cooling at 60 sec flight time. The X and Y dimensions on the computer plots are the short and long container dimensions, respectively. These plots show contours at intervals of one-tenth the difference between extreme values and are intended for a broad indication of gradients and flow patterns. Note that the isotherms are curved near the side walls to indicate side wall cooling as previously shown in Figure 8. The streamline and velocity plots show an initial flow toward the cooling surface, probably due to thermal contraction of the liquid. Later on, circular flow patterns begin to develop and, at the very low velocities computed, the convective flow results probably become meaningless.

A plot of centerline temperatures is shown in Figure 10 as a function of distance from the cooling surface at various flight times. Note that the cooled region is confined to about 2 cm from the cooling surface, with the strongest variation in the region less than about 0.6 cm. The lateral variation in temperatures along a section 0.6 cm from the cooling surface is shown

in Figure 11 for various flight times. The strongest lateral gradients and, hence, sidewall cooling is indicated in the initial cool-down period between about 80 and 180 sec flight time. The longitudinal component of gravity is directed away from the cooling surface, and, therefore, is in the direction opposite the density gradient. For sufficiently high gravity levels, this would be unstable. From Figure 10, the temperature gradient near the surface is seen to be nearly constant at about 10 C/cm during the first 100 sec of cool down. This corresponds to a nearly constant surface heat flux of about -.012 cal/cm^2 sec. Temperature penetration by pure conduction for a constant surface heat flux can be given by:[10]

$$T(y, t) = T_o - \frac{2q\sqrt{\alpha t}}{k} \text{ ierfc } \frac{y}{2\sqrt{\alpha t}}$$

with the surface temperature being

$$T(o, t) = T_o - \frac{2q\sqrt{\alpha t}}{k}$$

where T is temperature, y is distance from the surface, t is time, q is surface heat flux, α is thermal diffusivity and k is thermal conductivity. From the shape of the ierfc function, a characteristic temperature penetration depth is given by

$$\delta \sim 2\sqrt{\alpha t}$$

From Eq. (6), the difference between the surface temperature and the undisturbed temperature at depth is

$$\Delta T = \frac{2q\sqrt{\alpha t}}{k}$$

The effective thermal Rayleigh numbers Ra_T for this experiment configuration can then be defined as:

$$Ra_T = \frac{g \beta_T \Delta T \delta^3}{\nu \alpha}$$

$$= \frac{16 g \beta_T q}{\nu \rho C} t^2$$

where g is gravity level, β_T is the thermal expansion coefficient, ν is kinematic viscosity, ρ is density and C is specific heat. Using $g = 2 \times 10^{-5}$ g_E (.02 cm/sec^2), β ..95 x 10^{-4}/C, q = .012 cal/cm^2 sec, ν = 9.3 x 10^{-3} cm^2/sec, ρ = 1.08 g/cm^3 and C = .74 cal/g C, this becomes

$$Ra_T = 1.5 \times 10^{-4} t^2 \text{ (t is sec)}.$$

The Rayleigh number is seen to be only 1.5 at t - 100 sec after initiation of cooling (160 sec flight time) and 14 at t - 300 sec (360 sec flight time). Convective flow should not be initiated for Rayleigh numbers less than about 1000. The 74-21/2R flight test experiment, therefore, should be stable from the standpoint of thermally driven convection.

A similar analysis was done for experiment 74-21/3R as shown in Figure . The temperature measurements at T_4, T_5, and T_7 were located adjacent to thermoelectric cooling devices on faces being cooled. The thermal analyzer simulation therefore entailed adjusting the surface cooling rates until temperatures computed at the T_4, T_5, and T_7 locations satisfactorily matched

the measurements. The T_6 measurement was located midway between the two cooled surfaces on which the T_4 and T_5 measurements were made. The thermal analyzer simulation indicated that a considerable lag should have been noted in the cooling at T_6 compared to that at T_4 and T_5. Unfortunately, the T_6 measurement closely followed the T_4 and T_5 measurements and failed to compare well with the thermal analyzer simulation. No explanation is available at this time. Possibilities include a thermal or electrical short between the T_6 and T_4 or T_5 measurements.

As with the 74-21/2R flight test data, the thermal analyzer computed interior container wall surfaces were used as boundary conditions in the LOCAP program. The X-component accelerometer data are in the direction of the long (4 cm) container dimension (positive in the direction toward the cooled 1 cm x 1 cm surface) and the Y-component are in the direction of the container axis between the two cooled 1 cm x 4 cm surfaces. The resulting LOCAP generated plots of isotherms, and velocities are shown in Figure 11. The X and Y experiment coordinates shown in Figure 11 correspond to the Y and -X vehicle coordinates, respectively. The temperature measurements shown in Figures 12, 13, and 15 indicate that the T_7 surface started cooling somewhat prior to the T_4 and T_5 surfaces. This is reflected also in the isotherms shown in Figure 11. As with the 74-21/2R experiment, the computed convective velocities were on the order of 10^{-5} cm/sec, indicating heat transfer essentially by pure conduction.

Using analyses similar to 74-21/2R, the surface temperature gradient is seen to be about 30 C/cm, corresponding to a surface heat flux of -.036 cal/cm^2 sec. The longitudinal component of gravity is away from the cooled surface with a magnitude of around 2×10^{-5} g_E (.02 cm/sec^2). The Rayleigh number is

$$Ra_T = 4.5 \times 10^{-4} t^2$$

where t is in sec. As previously found in the 74-21/2R flight test, the Rayleigh numbers are seen to be very low over the low gravity flight period, and, therefore, convective flow is not likely to be initiated by the density gradients at the cooled end. For side cooling, the appropriate parameter for convective flow is the Grashof number:

$$Gr = \frac{g \beta_T \Delta T \delta^3}{\nu 2}$$

where, in this case, ΔT is the temperature difference from the center to an outside surface, and δ is one-half the width of the container. From calculations, ΔT is about 7C, and δ is 0.5 cm. For $g = 2 \times 10^{-5}$ g_E (.02 cm/sec^2), the Grashof number is .009. The maximum velocity in the boundary layer for free convection on a vertical plate is given by:[11]

$$U_{max} = \frac{.766}{\delta} (.952 + \frac{\nu}{\alpha})^{1/2} Gr^{1/2} (\frac{x}{\delta})^{1/2}$$

Assuming x equal to 2 cm, (the cooled distance on the side wall) the maximum velocity would be about .0026 cm/sec, compared to velocities on the order of

10^{-5} cm/sec calculated by the LOCAP program. Apparently, the equation overestimates the convective velocities by up to two orders of magnitude. In either case, the thermal convective velocities for the flight test are very small.

In attempting to simulate chemical diffusion effects using the LOCAP program, we found that the extremely low chemical diffusivity limited significant diffusion effects to a very thin layer adjacent to the solidifying interface. Thus, the LOCAP program would require an extremely fine grid to adequately simulate diffusion within this thin layer. For this reason, we elected to investigate the solutal effects in the thin layer using closed form, rather than numerical, analytical methods.

Mass flow diffusion of a particular species in a moving fluid is described by

$$\bar{q} = C\,\bar{v}_l - D \operatorname{grad} C$$

where $\bar{q}$ is the mass flux of the particular species, C is concentration, $\bar{v}_c$ is fluid velocity and D is chemical diffusivity. At the interface, the mass flux q_o is:

$$q_o = \rho_s v_s$$

where ρ_s is the density of the crystal and v_s is crystal growth rate. From photographs taken during flight test, the crystal was observed to grow at an overall rate of about 1.28×10^{-2} cm/sec. Based on a density of 1.527 g/cm^3 for the NH_4Cl crystal, this corresponds to a mass flux at the interface of .0195 g/cm^2 sec. Neglecting fluid motion, the diffusion equation for a constant

flux at the interface is:

$$C(x,t) = C_o - 2 \frac{q_o\sqrt{Dt}}{C} \text{ierfc}\left(x/2\sqrt{Dt}\right)$$

where x is distance from the interface, t is time from the initiation of solidification and C_o is the initial concentration. The behavior is such that the concentration C (o, t) at the interface will decrease down to zero, and beyond that time the relationship is no longer applicable. At the interface (x = 0), the equation becomes

$$C(o,t) = C_o - \frac{2\,q_o}{D}\sqrt{\frac{Dt}{\pi}}$$

and the time t_o required for the concentration to reach zero is

$$t_o = \pi D \left(\frac{C_o}{2\,q_o}\right)^2$$

For an initial concentration C_o of 0.302 g/cm^3 (28 percent mass fraction), chemical diffusivity D of 1.8×10^{-5} cm^2/sec and mass flux q_o of .0195 g/cm^2 sec, t_o is .003 sec. Thus, the concentration at the interface drops down to zero almost immediately. Thereafter, the concentration is given by

$$C(x,t) = C_o \text{ erf}\left(x/2\sqrt{Dt}\right)$$

The diffusion distance δ from the interface is indicated by

$$\delta \sim 2\sqrt{Dt}$$

Thus, the diffusion distance is only 0.08 cm after 100 sec and 0.14 cm after 300 sec.

The solutal Rayleigh number Ra_s is defined as:

$$Ra_s = \frac{g \beta_s \Delta C \delta^3}{\nu D}$$

where β_s is the solute expansion coefficient and ΔC is the concentration difference over the distance δ.

During the 74-21/2R flight test, the gravity vector is directed away from the solidification interface. For the ammonium chloride solution, the solutal expansion coefficient β_s is negative ($\beta_s = -0.281$ per unit mass fraction), and the decrease in concentration near the interface results in a decreased density. This is equivalent to heating from above and is thus a hydrostatically stable configuration. Even if the gravity were directed toward the solidifying interface, assuming $g = 2 \times 10^{-5} g_E$ (.02 cm/sec^2) $\Delta C = 0.28$ mass fraction and $\delta = 0.14$ cm, the Rayleigh number would be only about 25, which is well within the stable range. For the ground test, however, gravity is directed toward the solidifying interface and, for sufficiently high Rayleigh numbers, convective motion may be induced. Assuming ΔC - 0.28 mass fraction and $\delta = 0.14$ cm, the solutal Rayleigh number is 1.25×10^6, definitely unstable. A solutal Grashof number Gr_s can be defined as

$$Gr_s = Ra_s/Sc$$

where

$$Sc = \nu/D.$$

The Schmidt number SC for the ammonium chloride solution is 516. The solutal Grashof number for the 74-21/2R ground test, therefore, is about 2422. Using the solutal equivalent for Umax, with x being the width of the bottom surface, 1 cm, the estimated convective velocity is about 0.3 cm/sec, about the same as the thermal convective velocity.

For the 74-21/3R flight experiment, solidification on the side walls can result in some solutal convection. The solutal Rayleigh and Grashof numbers for the 74-21/3R experiment should be about the same as for 74-21/2R. Again using Umax, with x being the length of the cooled surface on the side walls, 2 cm, the convective velocity is 0.06 cm/sec, which is about half that due to thermal convection from the cooling surfaces. The solutal convection is also confined to a much thinner layer than the thermal convection.

Using the same equations, the solutal convection velocities for the 74-21/3R ground test are estimated to be about 0.4 cm/sec, about the same as the estimated thermal convection velocity.

Experiment Results

The solidification was photographed during the low g portion of the rocket flight and since the camera focus was fixed at the center of the cuvette with a depth of field of 1 mm, some degradation is inherent in the quality of the

photographs. Selected photographs from experiment 74-21/2R are shown in Figures 12 through 15 together with photographs of ground based solidification taken during the same time frame. Comparisons of dendrite characteristics and overall growth morphology were made between the two solidification conditions. Figure 16 shows photographs taken during experiment 74-21/3R. Some of the fluid appears to have leaked out of the cuvette prior to flight. The solidification is also severely limited. Since very little information could be obtained from these photographs, the remainder of the discussion is therefore limited to experiment 74-21/3R.

Length versus time measurements of secondary dendrite arms and dendrite array "interfaces" for low g and 1 g growth were taken during the same time period for comparison purposes, and were restricted to those crystals within the plane of focus. The growth rate and orientations are listed in Table I.

The starting dendrites in each environment appeared to have the $[110]$ growth orientation with growth rates ranging from 0.94 to 1.0 cm/min. This corresponds to earlier results which suggest that the $[110]$ orientation is preferred during the more rapid growth rates. Subsequent crystals that appeared ahead of the interface ("Free Floaters-FF") exhibited $[100]$ growth orientation.

There was a difference in the growth rates of the interfaces (interface refers to the unresolved array advancing behind the protruding dendrites and the FF crystals for the two experiment conditions). The low g crystals and interface grew at slower rates than their 1 g counterparts. The 1 g experiment contained sufficient fluid flow to supply fresh solute to the growing interface; hence, the controlling factor for growth rate in 1 g is crystallographic orientation and cooling rate.

Although the orientation of FF crystals appears to be $\left[100\right]$ in both environments, there is a significant difference in growth rates. The low g crystals are stationary and grow at a rate commensurate with their orientation. In contrast, 1 g crystals are in constant movement and grow at twice the low g rate. Since the nuclei for the 1 g crystals are secondary $\left[100\right]$ arms which have broken off from the interface $\left[110\right]$ dendrites, their initial orientation is expected to be $\left[100\right]$. Careful review of the photographs indicated that given sufficient time (the duration of existence of these crystals is generally less than 10 seconds before they fall into the interface) some crystals do exhibit a tendency to branch into the $\left[110\right]$ orientation in the manner reported[9] for more rapid growth rates.

The measured spacings for dendrite arms for 1 g and low g FF crystals are given in Table II. The low g arms spacing is greater than that of the 1 g material. This is contrary to expected results in view of the anticipated

stagnant layer of fluid around the low g crystals. However, this effect would occur if the spacings were determined by growth rate (faster growth rate producing smaller spacings[6]) rather than by availability of solute. It is therefore suspected that the role of fluid flow on the arm spacings is seen only by its second order determination of the growth rates. There is no direct influence on the dendrite arm spacings.

The standard deviation for the arm spacings is larger in the 1 g case, indicating that gravity driven fluid flow is breaking off arms. In some instances, where plumes were visible, it was possible to see the fragmentation or breaking off of arms. Remelting was not observed due to the short duration of the experiment.

An obvious difference between the 1 g and low g solidification is the number of crystallites ahead of the interface. The 1 g photographs show the constant movement of numerous crystals. After separating from the dendrites, the arms continue to grow, rising with the fluid until either the change in flow direction or their increasing weight pulls them back to the interface.

In the low g case, several crystals appear ahead of the interface, and continue to grow in their stationary positions. This phenomenon did not occur in the earlier flight experiment, i.e.; no crystals formed ahead of the interface. In order to determine the cause of these crystals, several possibilities were considered: (1) They nucleated at their observed location either due to a flaw

on the cuvette wall or constitutional supercooling (due to the high temperatures, homogeneous nucleation was not considered). (2) Some form of fluid flow carried crystallites into the liquid where they began to grow as the surrounding temperature decreased.

Since the camera was focussed at the center of the cuvette with a depth of field of 1 mm, it is concluded that they are free floating in the liquid and are not attached to the cuvette surface. Calculations were made to determine the characteristic distance (D/R where D is diffusion coefficient and R is growth rate) for the consitutional supercooled region ahead of the interface. Due to the rapid growth rates of this experiment, the characteristic distance is very small, on the order of 1×10^{-3} cm. It is therefore improbable that constitutional supercooling or nucleation on the cuvette wall could account for the presence of the crystals.

Since the convective velocities during solidification in low g were $\sim 10^{-5}$ cm/sec (thermal) and 0.002 cm/sec (solutal), there was inadequate force or time for these flows to carry crystals into the liquid. It is possible however that crystal nuclei were carried into the fluid by residual flows resulting from the spin-stabilized mode of rocket flight. Although the apparati undergo "de-spin" at 70 sec flight time, the velocities decay slowly over a period of time due to dissipative viscous forces.

A number of spin-up and spin-down studies have been made for cylindrical containers, either full or with a free surface. A comprehensive review of studies prior to 1974 is given by Benton and Clark.[12] McLeod[13] studied laminar flow spin-up and spin-down in circular cylinders during which the effects of the end walls or free surfaces could be neglected. A recent analysis and comparison with the experiment for spin-up and spin-down in circular cylinders[12, 13] included the effects of end walls. In any event, the application of these studies to our rectangular contains will be useful for order-of-magnitude estimates only.

The dimensionless parameters of primary interest to spin-up and spin-down in circular cylinders are the Ekman and Reynolds numbers defined by:

$$E = \frac{\nu}{\Omega h^2}$$

$$R = a\sqrt{\frac{\Omega}{\nu}}$$

where ν is the kinematic viscosity, Ω is the rotational velocity, a is cylinder radius and h is cylinder height. We assumed that both a and h (effective cylinder dimensions) for our rectangular containers are of order 1 cm. For an initial spin-rate Ω=240 rpm and kinematic viscosity $\nu = 9.3\times10^{-3}$ cm^2/sec for the ammonium chloride solution, the Ekman and Reynolds numbers E and R_e, respectively, are found to be $E = 3.88\times10^{-4}$ and $R_e = 50$.

Weidman's analysis is valid only for very small Ekman numbers ($\ll 10^{-4}$ according to a recent telephone conversation with Weidman). Also, the side walls dominate for $E^{1/4} \sim 1$. In our case, $E^{1/4} = 0.14$, which is in the range where side walls should either be dominant or play a major role, and the McLeod analysis should be used. The Reynolds number is low enough in our case that the flow is laminar; thus, McLeod's analysis should be valid.[14]

Residual velocities based on McLeod's theory are plotted in Figure 17 as a function of flight time. The velocity was computed at a radial distance of one-half the cylinder radius. Although the decay is extremely rapid, residual velocities greater than 0.01 cm/sec may be present until about 120 sec flight time, which is the time at which the first free floating (FF) crystals became visible in the photographs. The subsequent crystals appeared at 131, 136, and 150 seconds into the flight. Since the entire solution was below saturation temperature at launch, any crystals which floated into the center would not remelt.

The low g FF crystals exhibited two interesting asymmetry characteristics: secondary arms tended to grow toward the cooler walls and in a direction away from the interface. The latter effect is due to the influence of the thermal field from the advancing interface. Calculations of the thermal diffusion characteristic distance were well within the range of the first crystals to appear and the advancing interface.

Conclusions

Saturated solutions of NH_4Cl-H_2O were solidified on Earth at 1 g and in a suborbital rocket at 10^{-5} g. The unidirectional solidification experiment was successful. The tri-directional solidification experiment failed due to leakage of the fluid. In the 1 g 74-21/2R experiment, extensive fluid flow was apparent, creating plumes which carry numerous cyrstallites vertically above the interface in a manner usually attributed with causing freckling in castings. During growth the single interface grew into the liquid at the same rate as the individual dendrites. In some instances dendrites which protruded ahead of the interface were seen to be asymmetric, exhibiting growth of secondary arms on the side where no flow was apparent. At times, arms in the flow path were broken off or remelted. The crystals which were carried ahead of the interface grew rapidly in the fresh supply of liquid. Several crystals attempted to alter their growth orientation to accommodate the more rapid growth rates.

When solidified in low g the interface grew at a slower rate than the individual dendrites. In general, the interface dendrites grew symmetrically. No plumes of liquid carrying crystals were seen, but several crystals did appear and grow ahead of the interface. These were carried into the super-saturated fluid by residual flows from the rocket de-spin. The growth rates were slower than the 1 g FF crystals, giving a correspondingly greater arm spacing. Total growth was dendritic with no occurrence of freckling-type phenomena. Some effect of the influence of overlapping thermal growth fields was noted in the asymmetry of the FF crystals.

References

1. M. H. Johnston and C. S. Griner: Met. Trans., 1977, Vol. 8A, p. 77.

2. K. A. Jackson and J. D. Hunt: Acta. Met., 1965, Vol. 13, p. 1212.

3. S. D. Sharma and K. Kumar: J. Appl. Phys., 1974, Vol. 45, p. 4120.

4. M. Kahlweit: J. of Crystal Growth, 1970, Vol. 6, p. 125-29.

5. J. D. Hunt and K. A. Jackson: Trans. TMS-AIME, 1966, Vol. 236, p. 843.

6. T. Z. Kattamis, J. C. Conghlin, and M. C. Flemings: Trans. TMS-AIME, 1967, Vol. 239, pp. 1504-11.

7. S. M. Copley, A. F. Giamei, S. M. Johnson, and M. F. Hornbecker: Met. Trans., 1970, Vol. 1, pp. 2193-204.

8. S. J. Robertson, Final Report LMSC-HREC TR D568959, April 1979, Lockheed Missile & Space Company, Inc.

9. S. K. Chan, H. H. Reimer, and M. Kahlweit: J. Crystal Growth, 1976, Vol. 32, pp. 305-15.

10. Carslaw, H. C., and J. C. Jaeger, Conduction of Heat in Solids, Oxford University Press, 1959.

11. Eckert, E. R. G., and R. M. Drake, Jr., Heat and Mass Transfer, McGraw-Hill, New York, 1959.

12. E. R. Benton and A. Clark, Jr.: Annual Review of Fluid Mechanics, Vol. 6, Annual Reviews, Inc., Palo Alto, Califor., 1974.

13. A. R. McLeod: Phil. Mag., 1972, Vol. 44, No. 259.

14. P. D. Weidman: J. Fluid Mech., 1976, Vol. 77, p. 709.

TABLE I. DENDRITE GROWTH RATES AND ORIENTATION

FLIGHT			GROUND BASED (g ⊥ Interface)		
LOCATION	GROWTH ORIENTATION	GROWTH RATE (mm/min)	LOCATION	GROWTH ORIENTATION	GROWTH RATE (mm/min)
Bottom (Initial Crystals)	<110>	9.4 - 10.1	Bottom (Initial Crystals)	<110>	9.6 - 12.6
Ahead of Interface	<100>	0.59 - 0.79	Floating	<100>	1.9
-------	Front	7.7	-------	Front	9.4

TABLE II. DENDRITE ARM SPACINGS

	$X \pm \sigma$ mm	σ Pct
FLIGHT	0.85 ± 0.011	13.2
GROUND BASE	0.38 ± 0.02	42.4

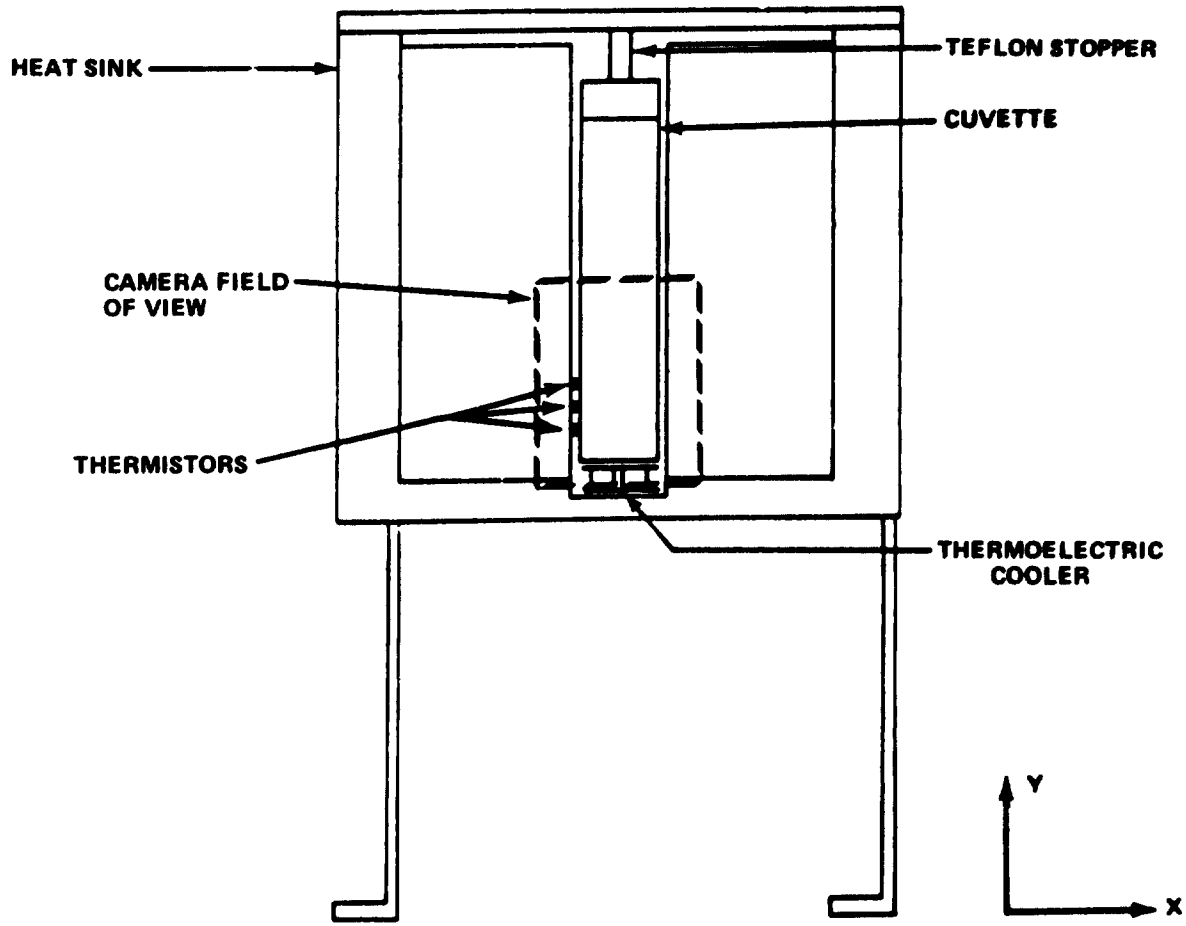

FIGURE 1: CUVETTE ASSEMBLY VIEWED ALONG Z-AXIS

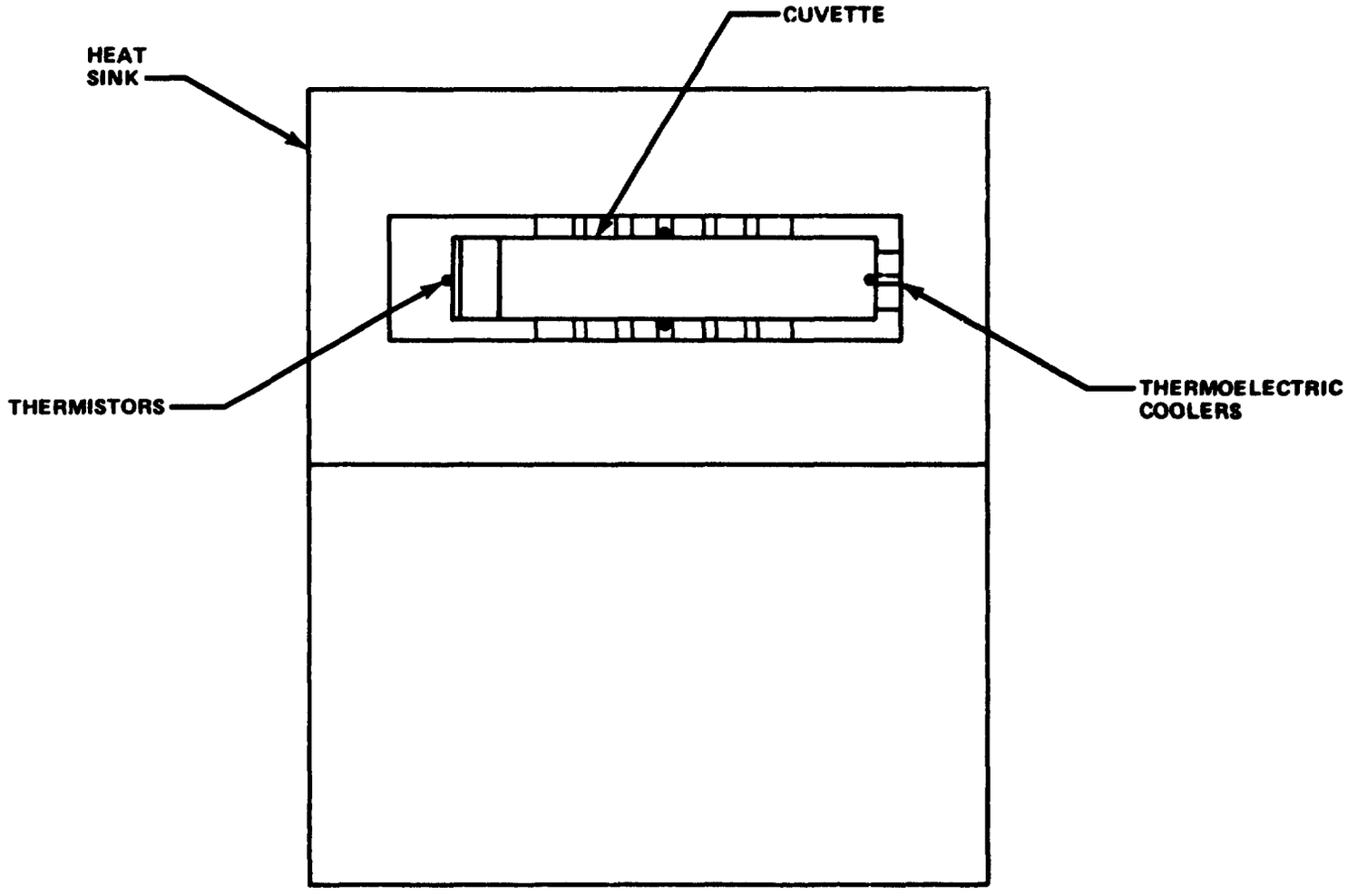

FIGURE 2: CUVETTE ASSEMBLY VIEWED ALONG Z-AXIS

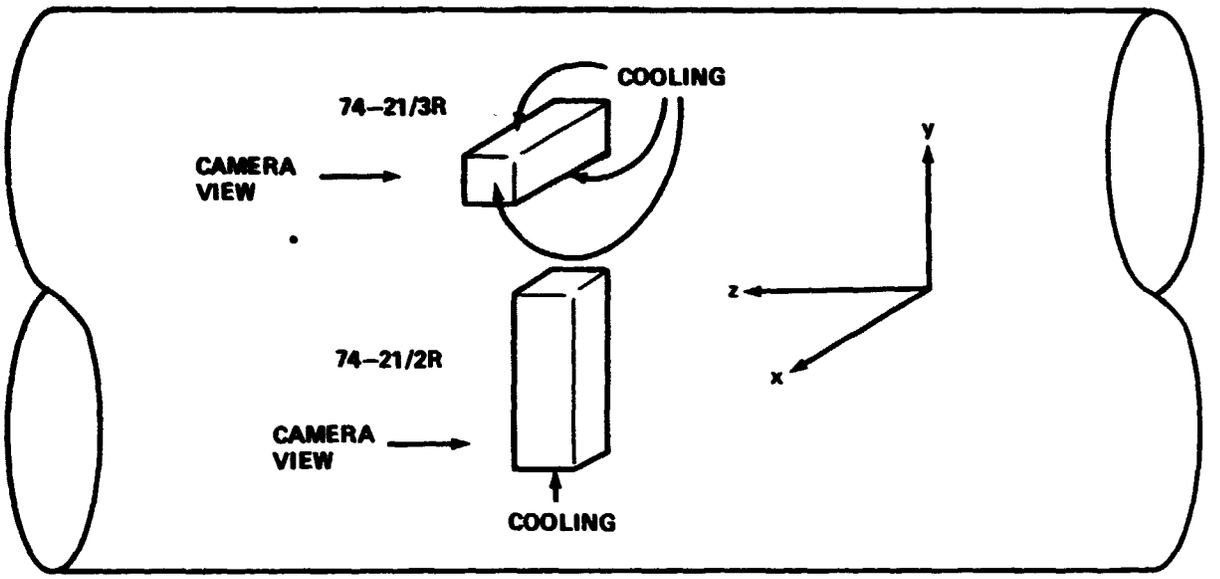

FIGURE 3: ORIENTATION OF EXPERIMENTS 74–21/2R AND 74–21/3R IN SOUNDING ROCKET

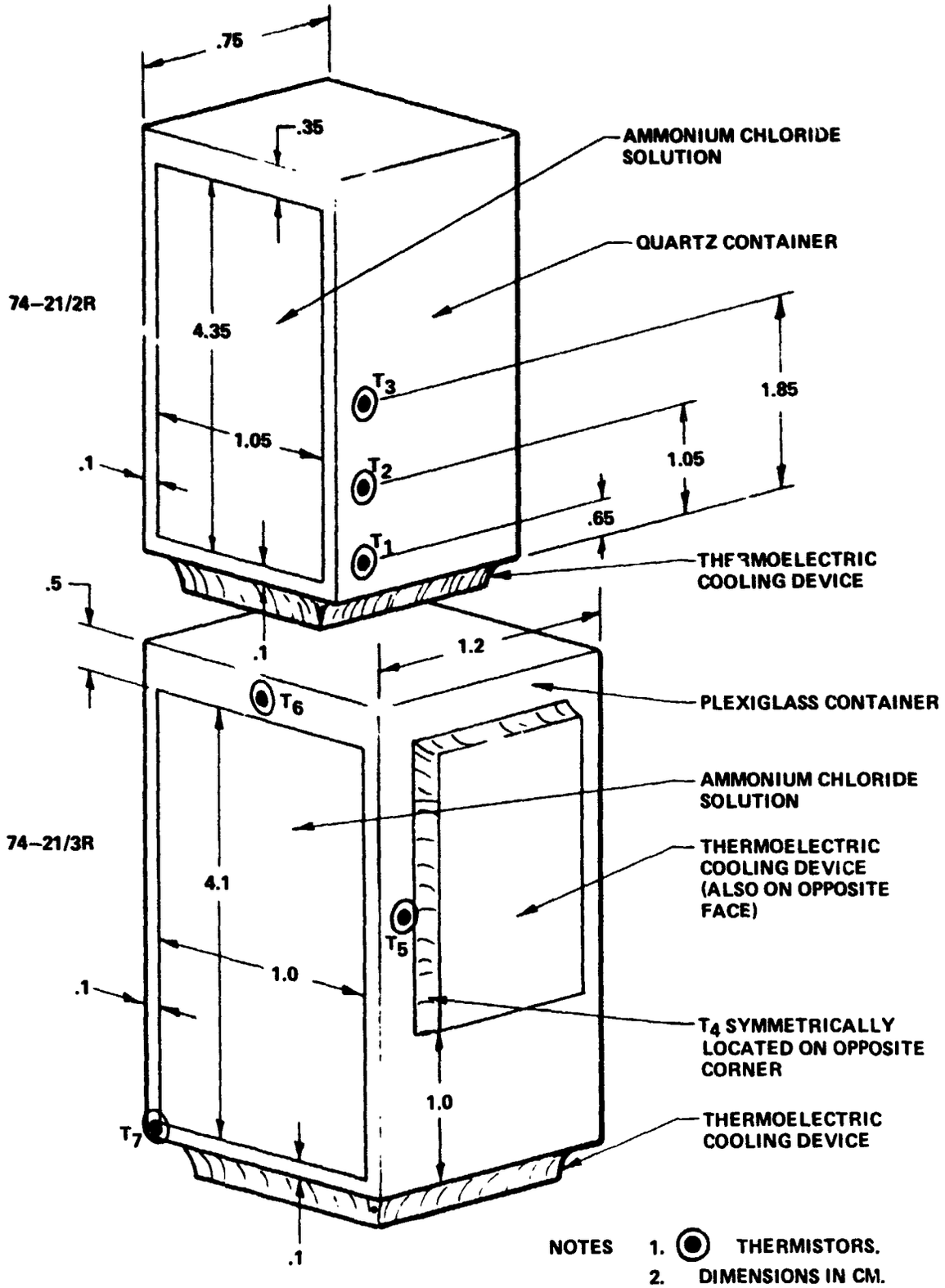

FIGURE 4: GEOMETRY OF EXPERIMENTS 74–21/2R AND 74–21/3R WITH LOCATIONS OF TEMPERATURE MEASUREMENTS

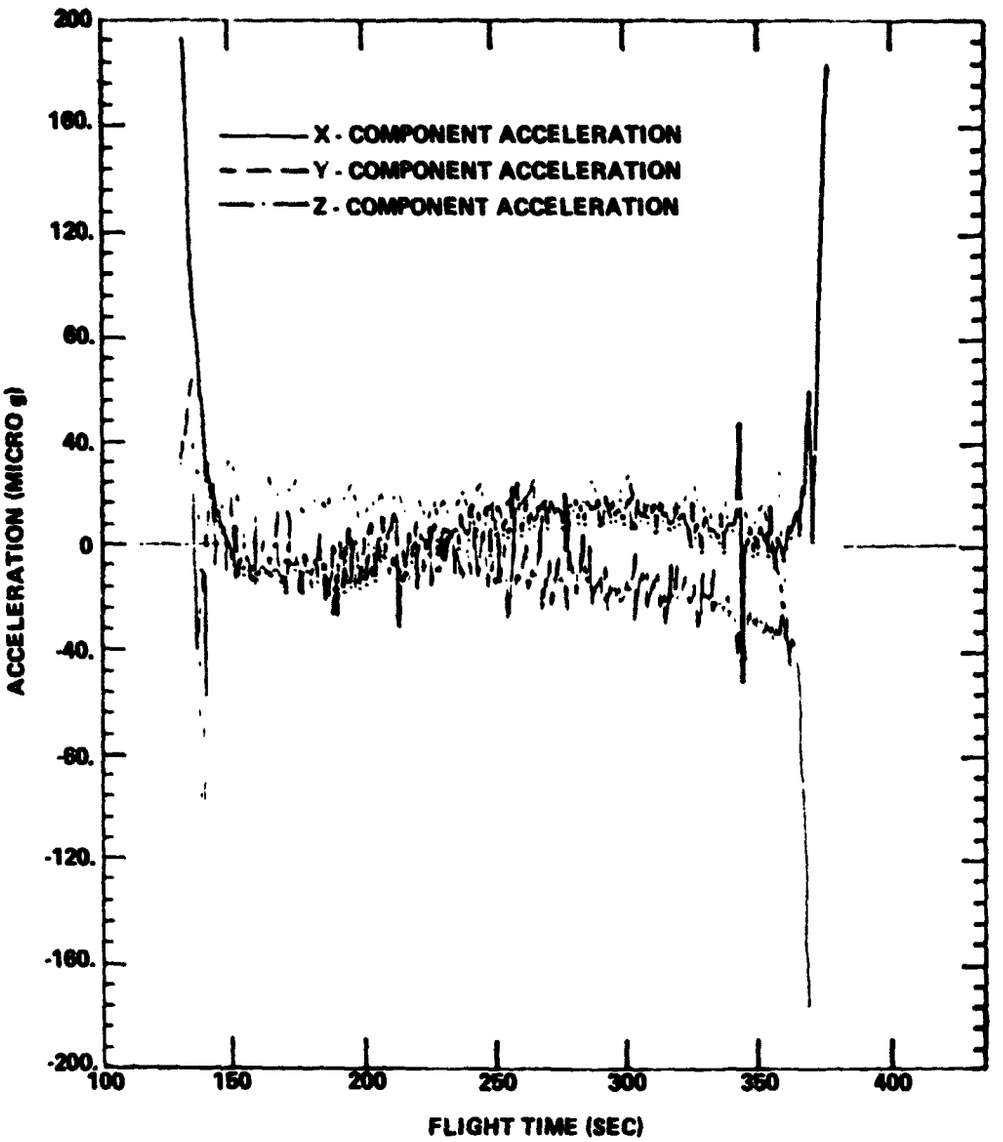

FIGURE 5: GRAVITY LEVEL DURING FLIGHT

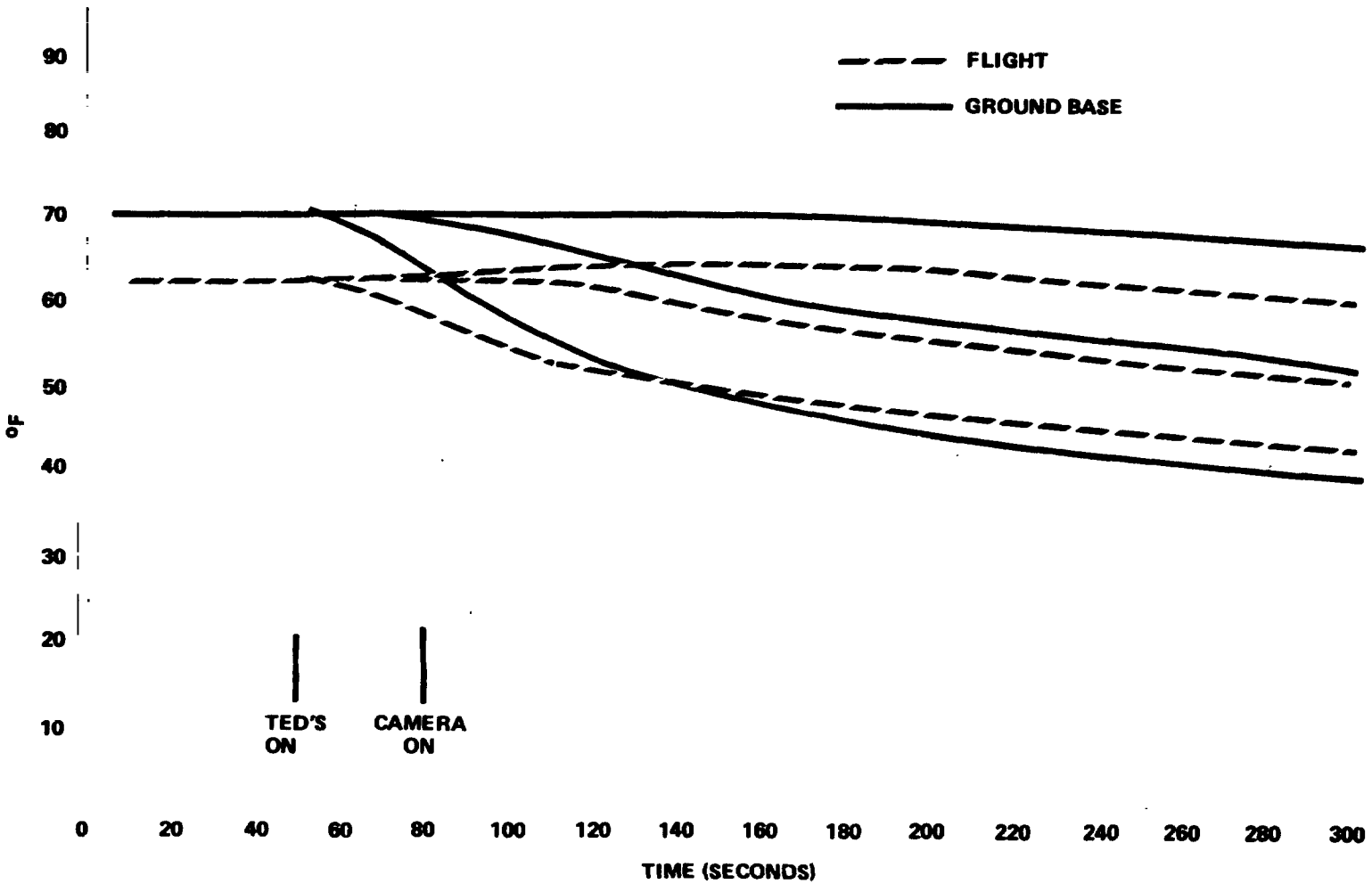

FIGURE 6: MEASURED TEMPERATURES ON 74–21/2R FLIGHT TEST COMPARED TO GROUND TEST.

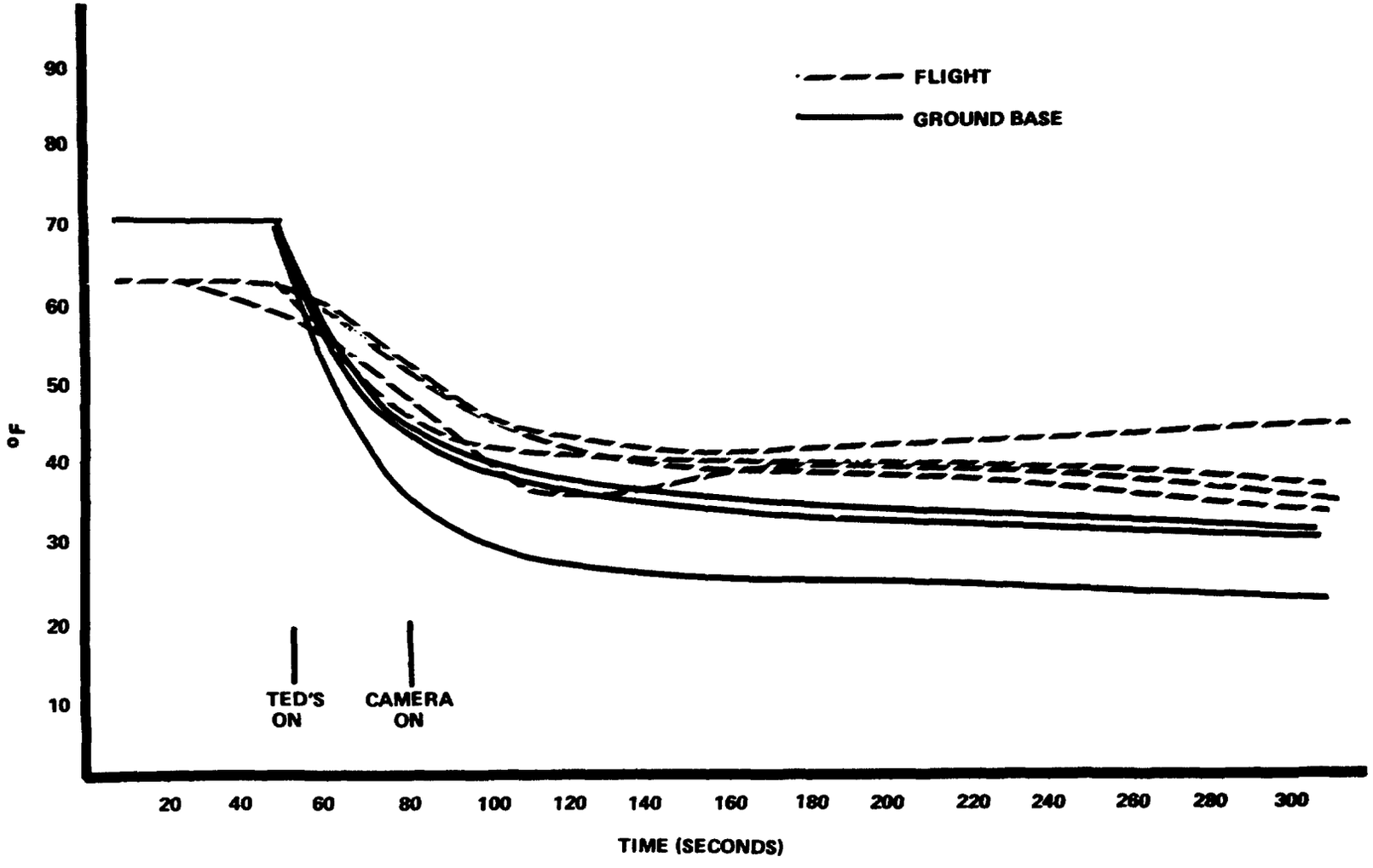

FIGURE 7: MEASURED TEMPERATURES ON 74–21/3R FLIGHT TEST COMPARED TO GROUND TEST.

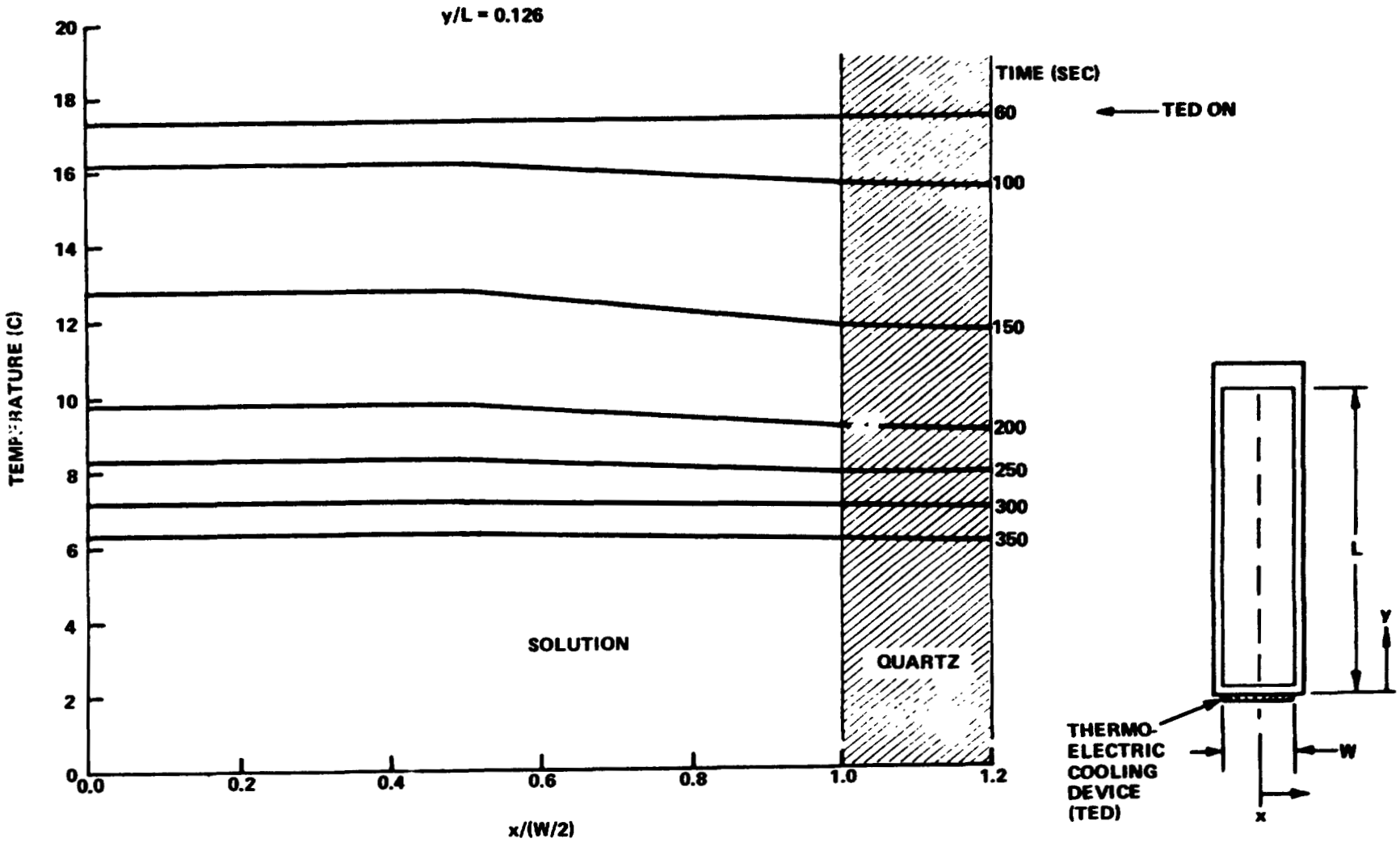

FIGURE 8: THERMAL ANALYZER COMPUTED TEMPERATURES IN 74–21/2R EXPERIMENT AT VARIOUS TIMES DURING FLIGHT TEST

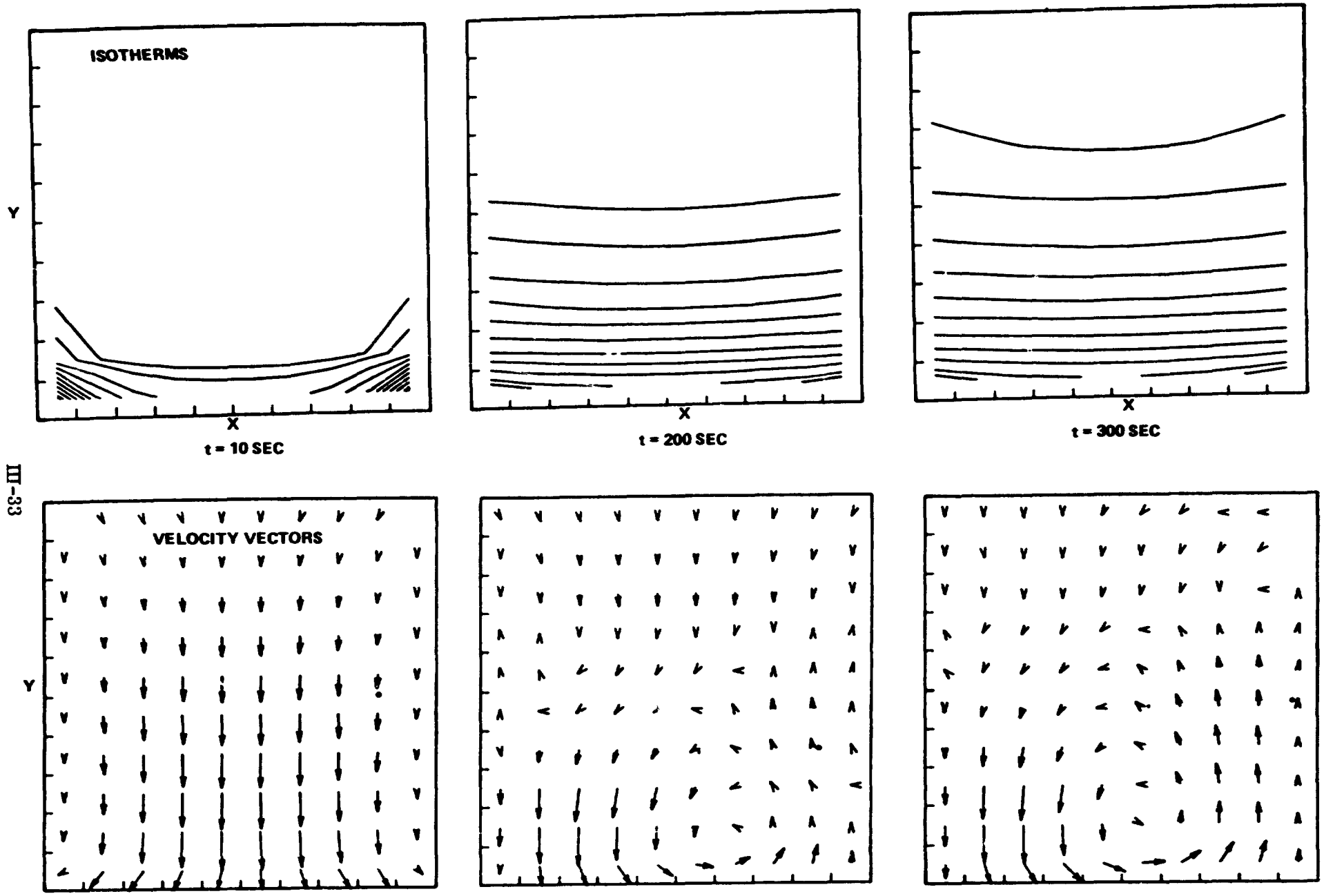

FIGURE 9: TEMPERATURE ISOTHERMS AND VELOCITY VECTORS AT SELECTED TIMES FOR EXPERIMENT 74–21/2R.

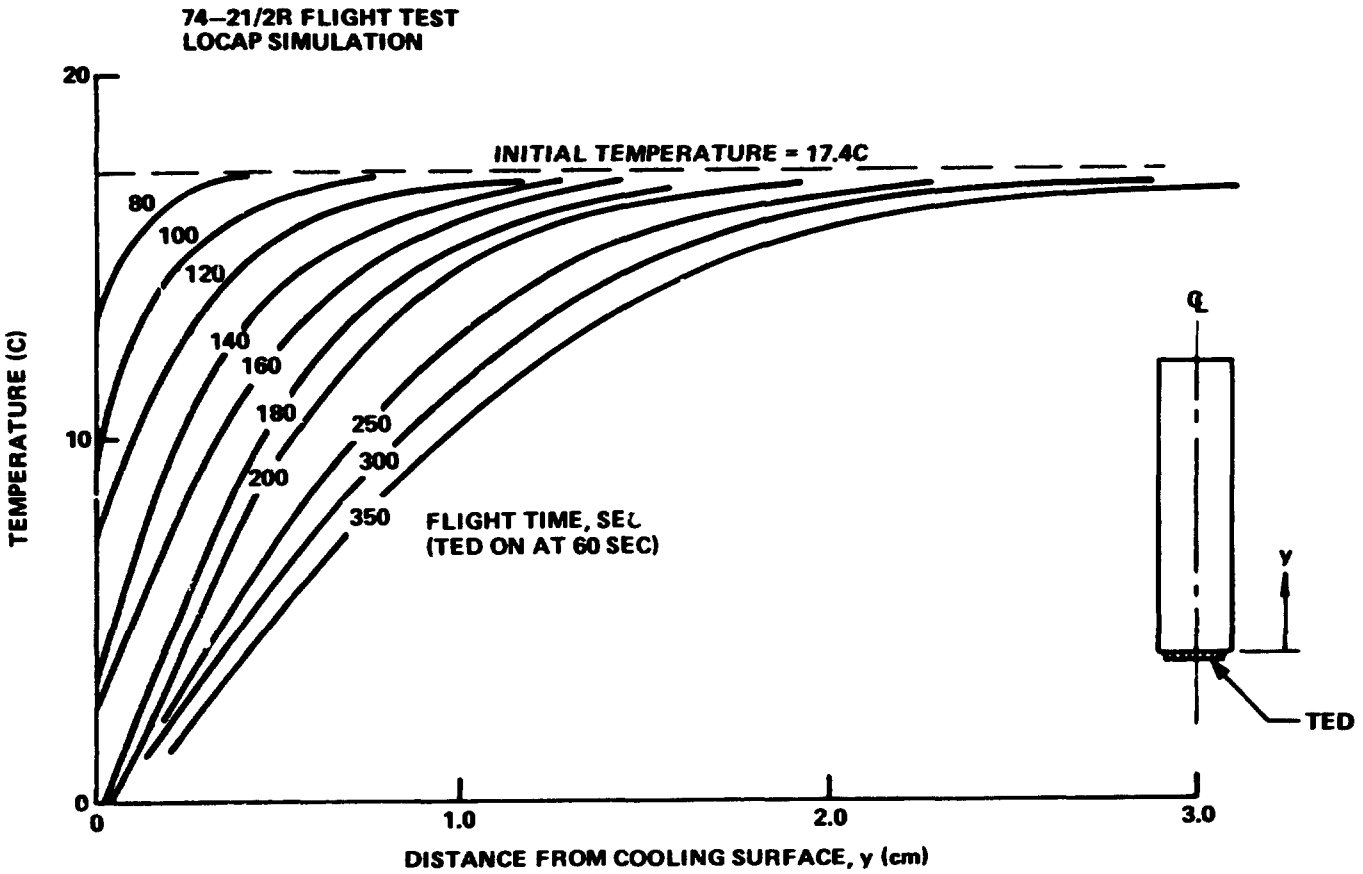

FIGURE 10: CENTERLINE TEMPERATURE DISTRIBUTIONS FOR 74–21/2R FLIGHT TEST FOR VARIOUS FLIGHT TIMES

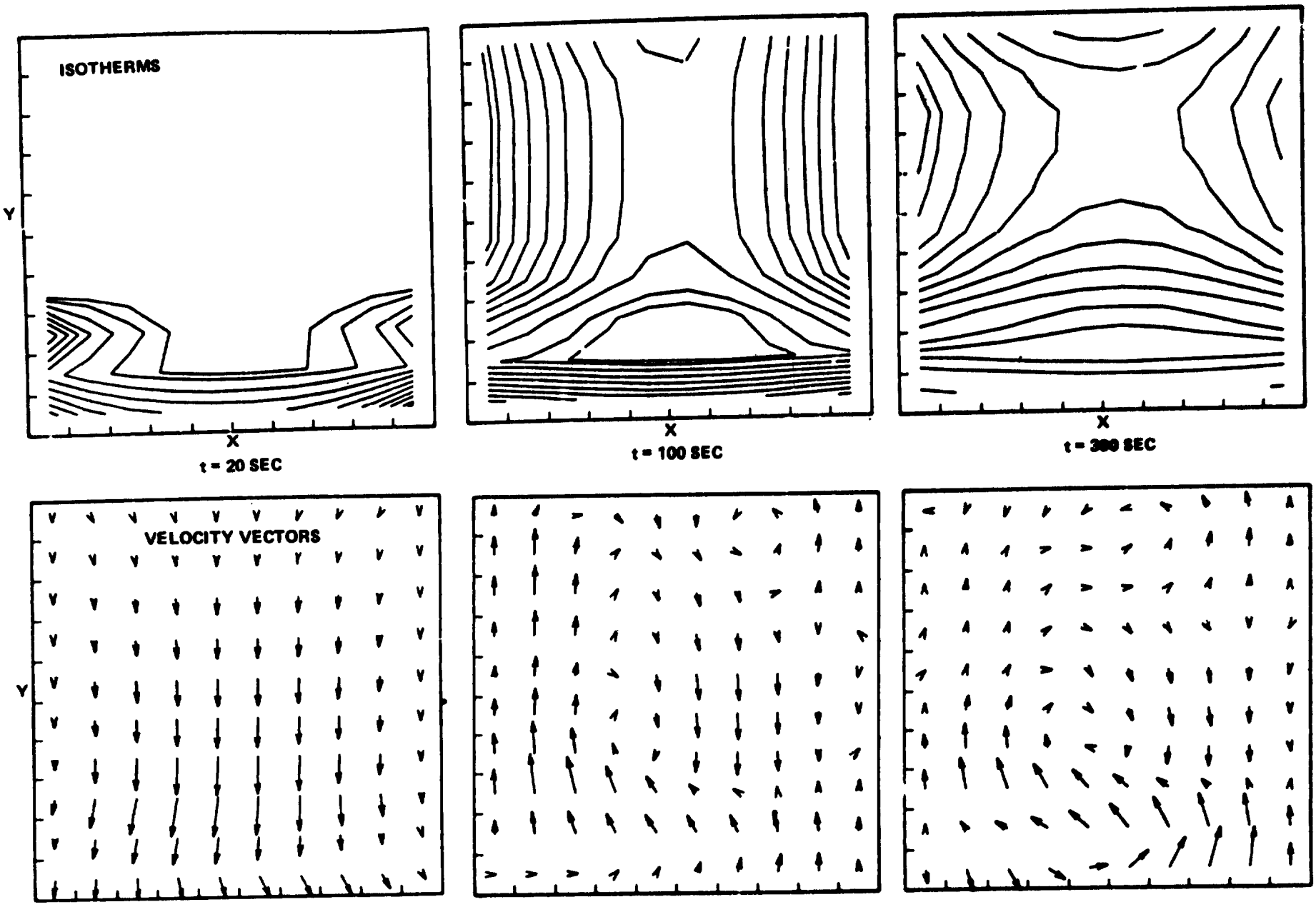

FIGURE 11: TEMPERATURE ISOTHERMS AND VELOCITY VECTORS AT SELECTED TIMES FOR EXPERIMENT 74–21/3R.

Figure 12: Ground Based (a) and Low-Gravity (b) Initial Crystallization

Figure 13: Ground Based (a) and Low-Gravity (b) Solidification, Lapse Time 40 Sec.

Figure 14: Ground Based(a) and Low-Gravity (b) Solidification, Lapse Time 75 Sec.

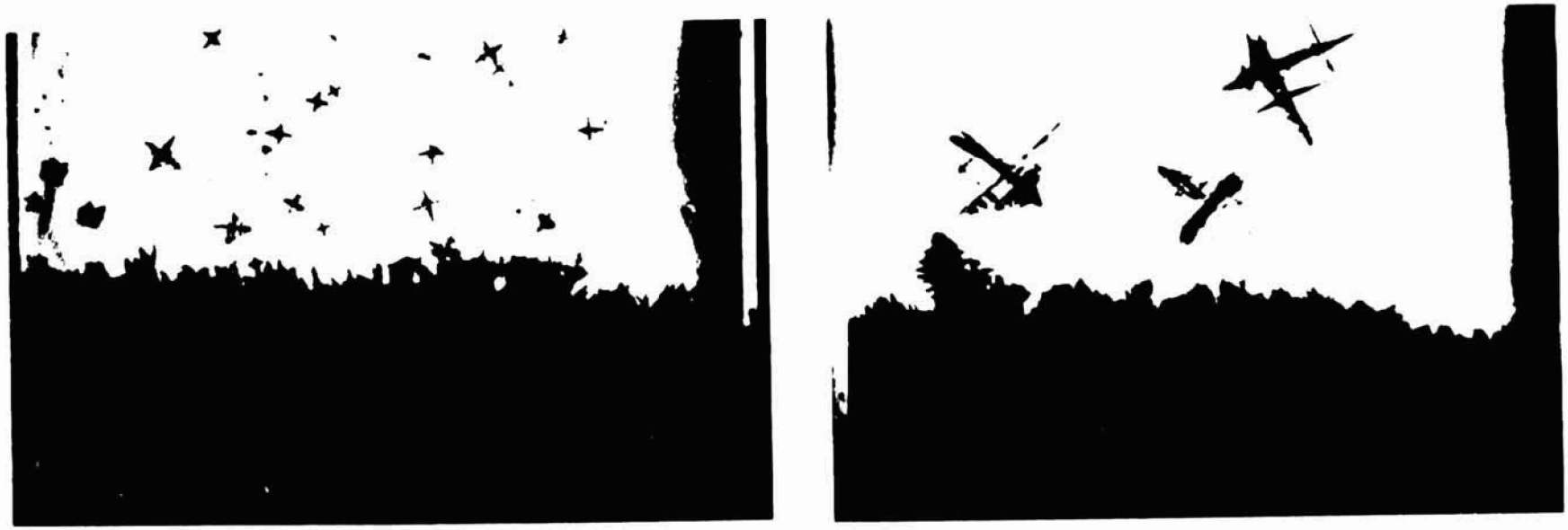

Figure 15: Ground Based (a) and Low-Gravity (b) Solidification, Lapse Time 125 Sec.

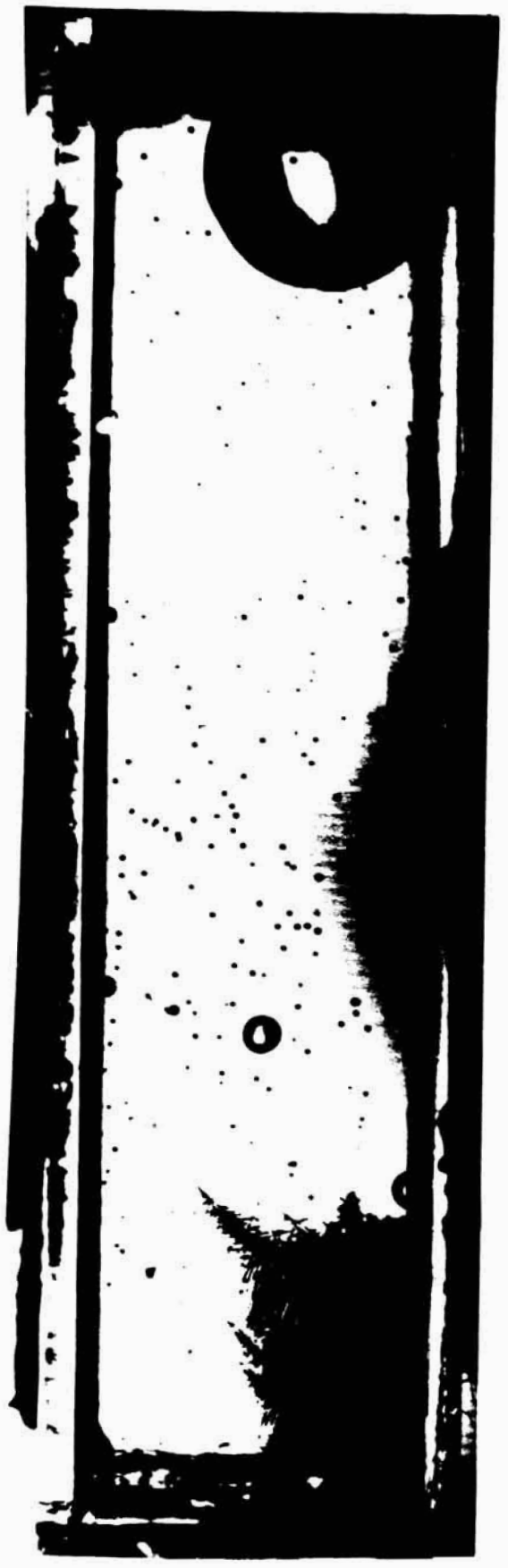

Figure 16 : Photograph of Experiment 74-21/3R Cuvette During SPAR Flight

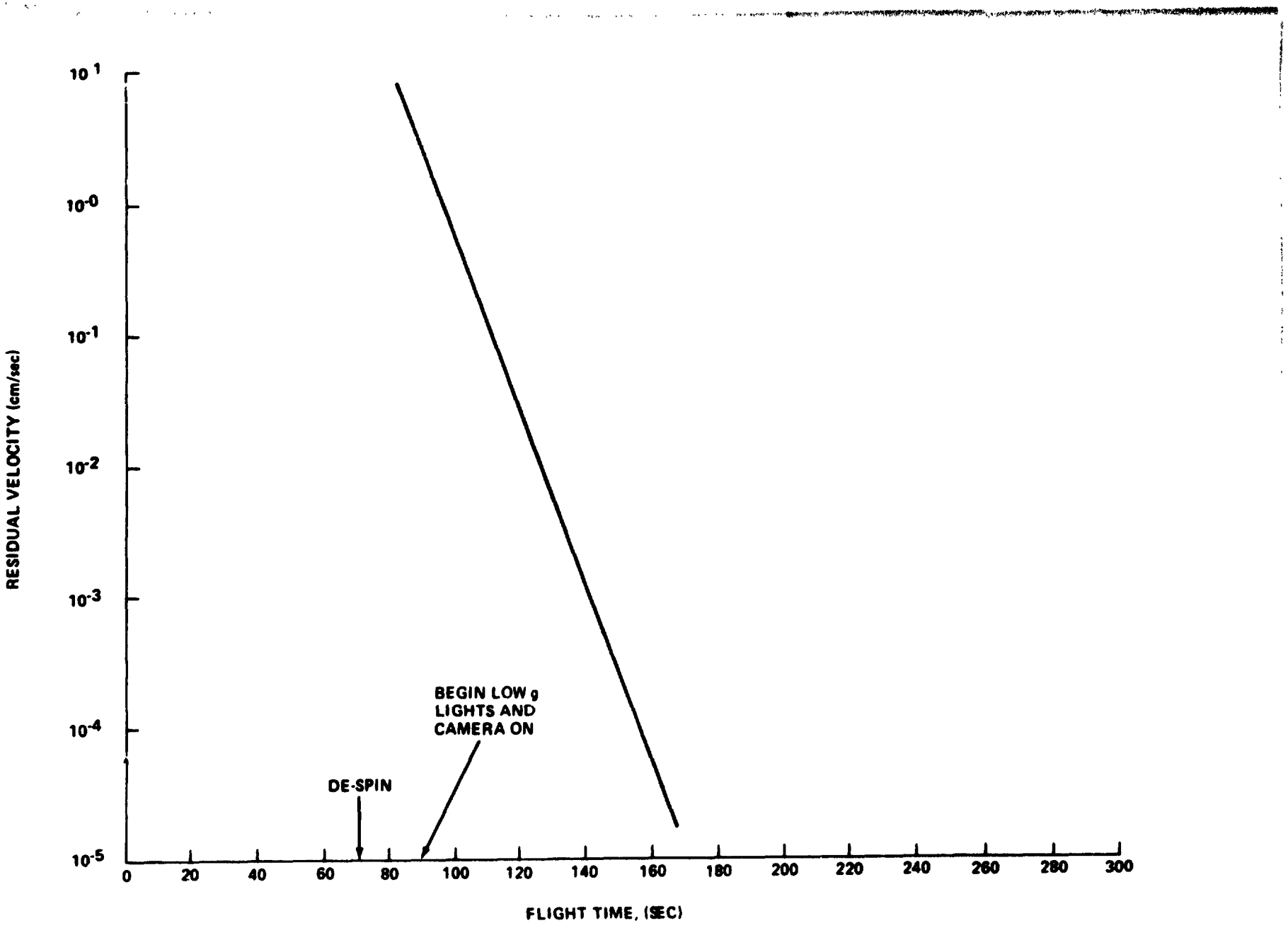

FIGURE 17: RESIDUAL VELOCITIES AFTER DE-SPIN (ESTIMATED FROM REF. 2)

FINAL POST-FLIGHT REPORT

on

SPAR V
EXPERIMENT NO. 74-30
AGGLOMERATION IN IMMISCIBLE LIQUIDS
(Contract No. NAS8-31543)

to

NATIONAL AERONAUTICS AND
SPACE ADMINISTRATION
GEORGE C MARSHALL SPACE FLIGHT CENTER
ALABAMA

July, 1979

Principal Investigators:

S. H. Gelles and
A. J. Markworth

BATTELLE
Columbus Laboratories
505 King Avenue
Columbus, Ohio 43201

FOREWARD

This report was prepared by Battelle's Columbus Laboratories under NASA Contract No. NAS8-31543 entitled "Rocket Experiment 74-30: "Agglomeration in Immiscible Liquids at Low G" for the George C. Marshall Space Flight Center of the National Aeronautics and Space Administration. Mr. Roger Chassay is the principal COR. Data on this program are recorded in Battelle's Columbus Laboratories Research Notebook 32085 and 33314.

ABSTRACT

This report describes a research effort, the overall objective of which is to understand the influence of gravity, cooling rate, and composition on the macro- and microstructure of liquid-phase immiscible alloys. Al-In alloys of compositions 30, 40, 70, and 90 weight percent indium have been processed aboard two sounding rocket flights, SPAR II, and SPAR V. The SPAR II flight experiment capsule included the 40 and 70 weight percent indium alloys and was processed by heating to 970 C, holding at this temperature for 15 minutes, and then rapdily cooling through the miscibility gap and solidification temperatures while in the microgravity environment. Comparative ground-base samples were similarly processed.

Radiographic and metallographic examination of the SPAR II flight and ground-base samples showed the expected separation at 1-g of the ground-base alloys into indium-rich and aluminum-rich layers. The flight alloys, however, produced unexpected results. Instead of the fine uniform structures expected, an aluminum-rich core surrounded by indium-rich metal was found.

A number of possible mechanisms were suggested to explain the origin of the massive separation. One of these, namely the possibility that the alloys were not homogeneous at the start of the cool-down, was made the subject of an extensive ground-base program and the prime motivation for the SPAR V experiments.

The Post-SPAR II ground-base experiments included spin-up/despin simulations and liquid-phase interdiffusion measurements and analyses. The spin-up/despin tests demonstrated the ineffectiveness of this motion in providing measureable mixing and thus supported the inhomogeneity hypothesis. The liquid-phase diffusion measurements and analyses indicated that if diffusion were the only mechanism available for homogenization, the holding time of 15 minutes used in the SPAR II experiment was insufficient.

The SPAR V experiment was primarily design to determine whether suspected inhomogeneity in the liquid phase contributed to the observed

segregation. SPAR V was conducted in a manner similar to SPAR II but incorporated a hold-time of 16 hours at the homogenizing temperature. Four Al-In alloys; 30, 40, 70, and 90 weight percent indium, were processing in this flight and on the ground but with a somewhat slower cooling rate. The results obtained from the SPAR V 40 and 70 weight percent indium alloys were essentially identical to those from SPAR II. The 30 and 90 weight percent indium alloys also showed massive separation into configuration similar to the 40 and 70 weight percent indium alloys. The 90 weight percent indium alloy showed additional important evidence that surface-tension induced droplet migration had occurred in this alloy which could at least in part account for the observed structures.

Because of the similarity between the SPAR II and SPAR V results, it was concluded that the SPAR II specimens must have been homogeneous at the start of cool-down. This conclusion, coupled with observation of wave-like structures and oscillatory convection occurring during DTA experiments, indicate that surface-tension drive fluid motion was probably present during the processing of these alloys. Recommendations for further work to confirm some of the suggested mechanisms are included in the report.

TABLE OF CONTENTS

TABLE OF CONTENTS
(Continued)

LIST OF FIGURES

LIST OF FIGURES
(Continued)

LIST OF TABLES

LIST OF TABLES
(Continued)

FINAL POST-FLIGHT REPORT

on

SPAR-V EXPERIMENT NO. 74-30
AGGLOMERATION IN IMMISCIBLE LIQUIDS

to

NATIONAL AERONAUTICS AND SPACE ADMINISTRATION

from

BATTELLE
Columbus Laboratories

by

S. H. Gelles and A. J. Markworth

July, 1979

INTRODUCTION AND SUMMARY

Background

Immiscible liquid systems as defined in this study are those material systems containing a liquid-phase misicibility gap, i.e., a field in the phase diagram representing an equilibrium between two liquids of different composition. At a sufficiently high temperature, the two-phase equilibrium is replaced by a single-phase liquid field. The present study is primarily devoted to metallic liquid immiscible systems and in particular to a model system, Al-In.

The Al-In phase diagram as determined by Predel[1] and checked in the present study is shown in Figure 1. The miscibility gap extends from above the monotectic temperature of 640 C to the upper consolute temperature of ∿820 C. The composition extremes range from the monotectic composition of 17.5 to 96.8 weight percent indium.

There are a large number of liquid-phase immiscible materials. Reger[2], for example, has listed over 500 systems which contain or were suspected of containing liquid-phase miscibility gaps. A number of these

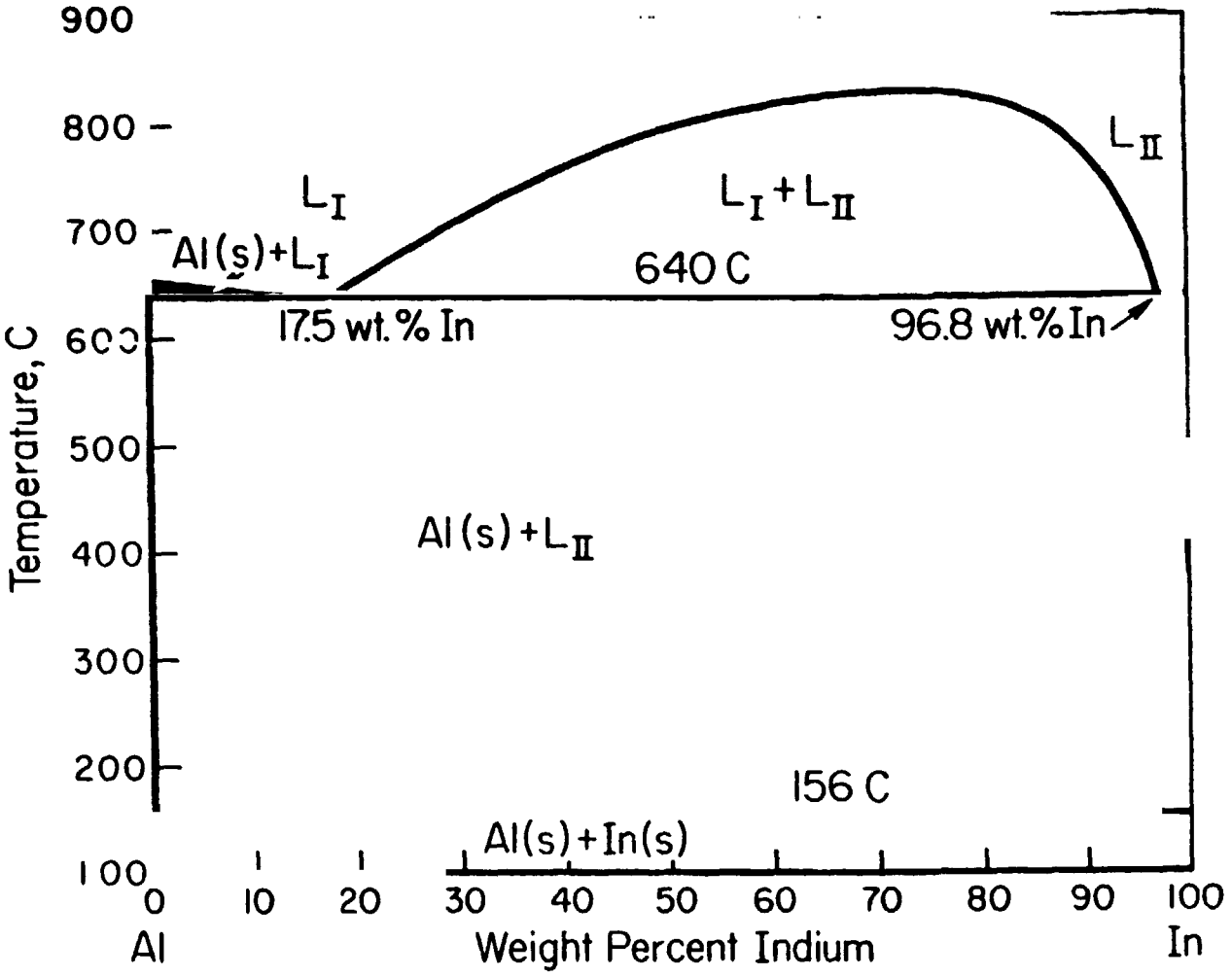

FIGURE 1. Al-In EQUILIBRIUM DIAGRAM[1]

systems are presently being used in such applications as electrical contacts, permanent magnets, and bearings. There are many other potential applications, for example, superconductors, superplastic materials, and catalysts. These applications and the role of processing these materials in space have been the subject of NASA sponsored programs at Battelle's Columbus Laboratories.[3,4]

If the coexisting liquids present within the miscibility gap have measurable density differences, there will be a great tendency for the materials to segregate and coalesce. Since Stoke's flow and convection are minimized in the absence of gravity, it was anticipated that droplet coalescence and segregation resulting from these movements would be virtually eliminated at low g.[5] This fact should, at least in theory, allow the production of materials containing a fine distribution of one phase contained within a matrix of a second phase.

The low-gravity environment also offers an opportunity to study the phase separation process without a major influence from gravitational effects. Thus, effects that may be masked by gravity on earth can likely be studied more efficiently at low g.

Overall Objective

The overall objective of this study is to gain an understanding of the influence of gravity, cooling, rate, and composition on the structure of liquid-phase immiscible systems.

Program Outline

Experiments involving four alloy compositions in the Al-In system were conducted on Sounding Rocket Flights SPAR II and SPAR V. A detailed description of the SPAR II flight and ground base experiments has been previously published[6,7] and is summarized in the present report for the sake of completeness and for the purposes of comparison with the SPAR V results. During the experiments, all of the flight and ground-base specimens were subjected to a homogenizing treatment at 970 C and were then rapidly cooled to room temperature.

The SPAR II experiments provided unexpected results in the form of massive separation of the aluminum-rich and indium-rich phases. After careful analysis of the SPAR II experiments, it was concluded that in all likelihood, the alloys were not homogeneous at the start of cool-down. The suspicion prompted a detailed ground-base study dealing with such subjects as the degree of mixing to be expected from rocket spin-up and despin and the liquid-phase diffusion characteristics of Al-In alloys. The results of these ground-base investigations have shown that little mixing is expected from rocket spin-up and despin. Furthermore, it was determined that the homogenizing time used in SPAR II was insufficient to produce a uniform composition if it is assumed that the only mechanism for available homogenization is diffusion. Accordingly, the SPAR V experiment was designed to insure that the alloys were homogeneous before cool-down by increasing the holding time at 970 C. A summary of the SPAR II and SPAR V experiments as well as the intermediate ground-base research follows.

Review of the SPAR II Experiment

The specific objective of this experiment was to determine the effect of gravitational acceleration on the macro- and microstructure of an Al-40 and Al-70 In alloy cooled through the miscibility gap at a rate of approximately 15 C/second.

The flight experiment, which was processed May 17, 1976, incorporated both alloy samples contained in separate crucibles within a single cartridge. The samples were held at 970 C for 15 minutes on the ground prior to launch. Approximately 154 seconds after launch, the flight samples were cooled at a rate of ∿14.7 C/second. A comparative ground-based sample was processed in a similar way but with an average cooling rate of 17.9 C/second. The flight sample was solidified completely while still at low g.

Post-flight analysis of the macro- and microstructures of the Al-40 and -70 In alloys showed rather unexpected results. Instead of the expected fine dispersion of indium-rich particles within an aluminum-rich matrix, the structures consisted of a massive aluminum-rich core surrounded by indium-rich metal. In the case of the -40 In alloy, the shape of the aluminum-rich phase was constrained by the crucible dimensions. However,

in the -70 In alloy, the aluminum-rich core assumed a roughly spherical geometry. The microstructure of the aluminum-rich portion of the alloys consisted of large drops of indium-rich metal contained in the aluminum-rich host as well as a fine distribution of indium-rich particles (presumably the result of the monotectic decomposition). In the indium-rich material, two types of aluminum-rich phases were found; aluminum-rich spheres which result from droplet precipitation within the miscibility gap and aluminum-rich dendrites which result from the precipitation of solid aluminum within an indium-rich liquid.

A number of mechanisms were suggested and some analyzed to explain how the massive separation might have occurred. Among these were residual fluid motion, conventional convection, surface tension driven flows and non-homogeneous starting material. The last of these items appeared to be highly probable, and was thus made the subject of extensive ground-base research and the SPAR V flight experiment.

Post-SPAR II Ground-Base Experiments

Three types of experiments were carried out for the purpose of assessing the degree of mixing and homogenization that might be expected after a 15-minute hold at 970 C and the spin-up/despin motion occurring during rocket flight. The following experiments were conducted:

(1) Spin-up/despin experiments
(2) Differential thermal analysis (DTA) measurements of equilibrium kinetics
(3) Direct measurements of interdiffusion coefficients in liquid Al-In alloys.

Spin-Up/Despin Experiments

The spin-up/despin experiments simulated the action of the rocket on a single phase liquid having a sharp concentration gradient above the consolute temperature. A layer of water saturated with copper sulphate set below a layer of pure water contained in a transparent vial made up the

system used to simulate the single phase liquid Al-In alloys. The samples were spun-up on a turntable to speeds of 246 RPM (simulating the spin-up to 240 RPM of the rocket while being photographed. The compositional changes occurring during this motion were qualitatively followed by the color variation imparted by the blue copper sulfate solution. The parameters varied in the experiments were (1) the relative amounts of copper sulfate solution and water, and (2) the presence or absence of an air gap or wetting agent.

A major conclusion from the spin-up/despin simulation is that little in the way of mixing occurs as a result of this motion. The major disturbance is confined to the region of highest concentration gradient adjacent to the original interface between the copper sulfate solution and water.

DTA Experiments - Approach to Equilibrium

Differential thermal analysis was used to determine the rate of homogenization of liquid Al-In alloys by measurement of the apparent consolute temperature as a function of holding time at 970 C. These studies were carried out on three alloys, Al-40.1, -70.1, and -76.0 In. The most extensive series of measurements was conducted on the Al -40.1 In alloy. The results show that a holding period of 8 hours is required to produce an equilibrium value of the consolute temperature. This observation corresponds to a value for the interdiffusion coefficient of 8×10^{-5} cm^2/second. Equilibrium values of the consolute temperatures were obtained for the Al- 40.1 and - 76.0 In alloys and were found to agree reasonably well with the values obtained by Predel.[1] It should be noted that some of the DTA curves obtained for these alloys displayed oscillatory behavior which has been attributed to the presence of oscillatory convective flows in the melt.

Liquid Phase Interdiffusion Considerations

A series of computations have been made of the product of interdiffusion coefficient, D, and time, t, to produce a uniform composition for

the geometrical configuration of the SPAR alloys. These calculations are based upon a solution of Fick's diffusion equations for the applicable boundary conditions.[8] Values of Dt equal to 0.5 have been computed for producing homogeneity within 1 percent (absolute) of the intended compositions in the 40 and 70 weight percent indium alloys.

A series of direct measurements of the interdiffusion coefficients of liquid Al-In alloys have been carried out at 970 C in 1 mm inside diameter capillary tubes. Samples have been held at this temperature for 1 or 4 hours and then rapidly cooled. They have then been metallographically polished along a central longitudinal plane and subjected to electron beam microprobe analysis in order to obtain composition as a function of distance along the length of the diffusion couple. The interdiffusion coefficients have been determined from a least-square fit of the data with computed composition-distance curves for various values of D. The computer codes used account for the changes in dimension on cooling from 970 C, where the diffusion occurs, to room temperature, where the electron beam probe measurements are made.

The average obtained from these measurements is 8.1×10^{-5} cm^2/second. This compares reasonably well with the average values of 4.8×10^{-5} cm^2/second calculated from the in situ measurements made by Dr. L. Lacy of Marshall Space Flight Center by a radiographic technique and with the $\sim 8 \times 10^{-5}$ cm^2/second value obtained from DTA measurements. Based on an average value for the diffusion coefficient of 6.4×10^{-5} cm^2/second (average value of present measurements and those of Lacy) and the calculated value for Dt equal to 0.5, a time period of 2.2 hours is anticipated as the required duration for producing homogeniety in the SPAR Al-In alloy samples assuming diffusion is the only process by which homogenization can take place. Hence, it was concluded that an insufficient hold time was used on the SPAR II experiment.

SPAR V Flight Experiment 74-30

The objective of this experiment was to determine whether the concentration gradients thought to be present in the SPAR II samples at the start of cool-down were the cause of the observed massive separation. The hold time of 16 hours at 970 C was chosen as a reasonable homogenizing

time. This represents a safety factor of ∿7 over the 2.2 hour time period calculated on the basis of the measured diffusion coefficient and the solutions to Fick's equations.

Beside the 40 and 70 weight percent In alloys, which were the same composition as used in the SPAR II experiment, two other alloy compositions were processed; 30 and 90 weight percent In. The 30 weight percent In alloy was chosen in order to investigate the effect of lower indium droplet concentrations on phase separation whereas the 90 weight percent In alloy was selected to investigate the propensity of the primary phase to precipitate at the crucible walls.

The cartridge design used in the SPAR V samples was basically the same as that used in SPAR II. The 40 and 70 weight percent In alloys were contained in one capsule while the 30 and 90 weight percent In alloys were contained in a second one. The only deviation in the design was the absence of an internal thermocouple within the capsule containing the 30 and 90 weight percent In alloys.

The SPAR V flight samples were processed on September 11, 1978, but not without some deviations from the original plan in the form of a failed internal thermocouple in the capsule containing the 40 and 70 weight percent In alloys and in a somewhat lower cooling rate (10 C/sec versus the desired 15 C/sec). The latter deviation provided the complication that the alloys were not completely solidified within the lower gravity time period.

After processing, the flight and comparably prepared ground control samples were examined radiographically and by optical microscopy. The results obtained for the 40 and 70 weight percent In alloys were very similar to those previously obtained in the SPAR II experiments. The flight samples, once again, have a structure consisting of a macroscopically sized aluminum-rich core surrounded by an indium-rich alloy. Likewise, the ground control samples had typical layered structures. Some subtle differences in the microstructures of the SPAR II and SPAR V ground control samples could be attributed to differences in cooling rate.

The structures of the 30 weight percent In alloys were quite similar to those of the 40 weight percent In alloys and thus provided little further understanding of the phase separation process. The 90 weight percent In alloy, however, did provide some new insight into the mechanisms that may be contributing to massive phase separation. Most notable among the observations made on the alloy is the presence of an annular zone denuded of aluminum-rich spheres around the massively separated aluminum-rich core. This observation, coupled with the fact that there is an increasing concentration of aluminum-rich spheres close to the central core, has provided evidence supporting the theory that the aluminum-rich spheres have migrated from the outer regions of the alloy into the interior, presumably under the action of surface tension gradients. These observations have been analyzed according to a formulation previously used by Bewersdorff[9] and found to be consistent with that mechanism. An alternative interpretation, that of particle pushing by an advancing indium solidification front, has been ruled out on the grounds that the observed coalescence of the aluminum-rich spheres would not be expected for solid aluminum spheres at the melting point of indium ($\sim$ 155 C). Evidence for particle pushing, however, has been observed elsewhere in the SPAR samples. In this case, agglomeration of the particles has been observed but not coalescence. The particle pushing mechanism does not appear to have contributed significantly to the massive coalescence that has been observed in all the Al-In SPAR II and SPAR V samples.

In addition to the surface tension driven migration of the aluminum-rich spheres, there is mounting evidence to indicate that surface tension driven fluid flows arising at the liquid-gas or liquid-liquid interfaces induce appreciable convection currents within the alloys during the homogenization and phase separation processes. Such flows can originate from temperature or concentration gradients and would contribute significantly to the observed massive separation. Evidence for this behavior has been obtained in the following forms.

(1) A number of wave-like structures have been observed both in the flight and ground base samples.

(2) Oscillatory temperature fluctuations have been observed in DTA samples undergoing phase separation.

(3) The SPAR II samples appear to have been homogenized after a 15-minute hold time even though the theoretical hold time necessary as calculated from diffusion considerations is 2.2 hours.

A number of experiments have been suggested to follow-up on these suggested mechanisms.

DETAILED PROGRAM DESCRIPTION

Review of the SPAR II Experiment

The SPAR II experiment which was flown May 17, 1976, has been described in detail in a Post Flight Summary Report[6] and in an AIAA publication[7]. For the sake of completion, we will include here a brief description of the SPAR II flight and ground-base experiments and a summary of the results.

The specific objective of the SPAR II experiment was to determine the effect of gravitational acceleration on the macro- and microstructure of an Al-40 and an Al-70 weight percent In alloy cooled through the miscibility gap at a rate of $\sim$ 15 C per second.

Sample Configuration

The sample configuration used in the SPAR II experiments (and later used in one of the SPAR V samples) is schematically shown in Figure 2. The alloy components in proper proportion were contained in separate aluminum oxide crucibles especially machined for a close fit with the internal dimensions of the stainless steel cartridge. The samples were carefully prepared by initially melting the components in high vacuum and then by sealing them in the cartridge under a partial pressure of helium. The

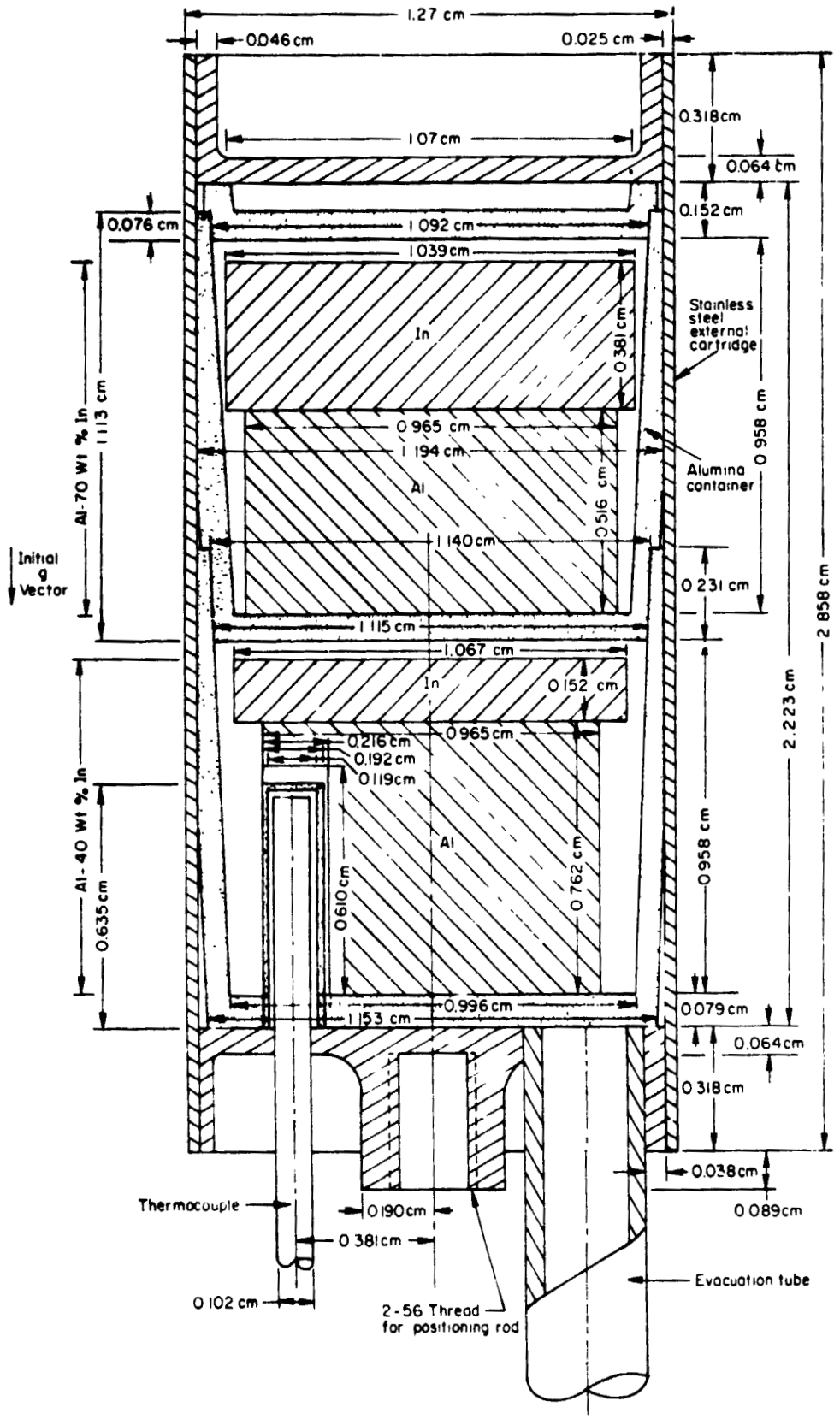

FIGURE 2. SCHEMATIC DIAGRAM OF EXPERIMENT CARTRIDGE

helium pressure level was chosen so that the cartridge contained slightly less than one atmosphere (0.1 MN/m^2) of pressure at the maximum temperature, 970 C. Provision was made for measurement of the sample temperature through introduction of an internal inconel sheathed chromel-alumel thermocouple into the capsule.

Flight Procedure

The stainless steel cartridge containing the two alloys was heated to ∿950 C in the rocket for 15 minutes before launch. This temperature corresponds to positions in the Al-In equilibrium diagram within the homogeneous single phase liquid field above the miscibility gap (See Figure 1). The alloys were allowed to remain at this temperature during launch and for ∿ 154 seconds after launch. Accelerations decreased to $< 4 \times 10^{-5}$ g ∿ 91 seconds after launch so that a time period of ∿ 63 seconds was available for the damping of any residual fluid motion in the specimen. At the end of this stabilization period, the samples were rapidly cooled by means of helium gas which was allowed to flow around the periphery of the stainless steel cartridge. A complete cooling curve was successfully telemetered from the rocket and indicated that the average cooling rate through the miscibility gas was 14.7 C/second. A thermal arrest of approximately 9-second duration corresponding to the monotectic transformation was clearly visible on the cooling curve. Complete solidification at ∿ 156 C, as indicated by the internal temperature of the alloy, took place well within the microgravity time frame. All in all, the experiment appears to have been conducted successfully and according to the original plan.

Ground Base Samples

Prior to the SPAR II flight, two ground base samples had been processed in the General Purpose Rocket Furnace for the purpose of obtaining terrestrial standards for comparison with the flight samples. One of the samples was run in exactly the same way as the flight

sample and had an average cooling rate through the miscibility gap of 17.9 C/second, reasonably close to that of the flight sample. The other ground-base sample which was considered to be a secondary standard was actually subjected to the thermal cycle twice and in an orientation anti-parallel to that of the other two samples. Average cooling rates through the miscibility for the two cycles conducted on this sample were 12.2 and 12.9 C/second.

The flight and ground base samples were examined by X-radiography and by metallographic techniques on a macroscopic and microscopic level.

Results of the SPAR II Experiments

As previously delineated, we expected that the 40 weight percent In alloy flight sample would show a fine dispersion of indium-rich droplets within an aluminum-rich matrix. The expected structure of the 70 weight percent In alloy flight sample was not as clearly defined. One possibility was an interlacing network of aluminum-rich and indium-rich phases on a microscopic level. Alternatively, the expected structure of this alloy might be that resulting from the spinodal decomposition of the homogeneous liquid. If this latter structure was retained during solidification, the sample would be expected to have modulated structure consisting of composition fluctuations having a wavelength on the order of 0.01 to 0.1 μ. The spinodal structures, however, may be extremely unstable in the liquid owing to the relatively high liquid phase diffusion coefficients.

As shown in Figure 3, the expected macro- and microstructures were not observed on the flight sample. Instead the structure of the space processed alloys as determined by X-radiography and macro-examination consisted of an aluminum-rich core surrounded by indium-rich metal. For the Al-70 weight percent In alloy, the aluminum-rich core was approximately spherical; whereas, in the Al-40 weight percent alloy, the aluminum-rich core occupied a larger fraction of the container volume and was roughly the shape of the container. There was a great tendency for the indium-rich material to wet the aluminum container walls.

The expected layering of the indium-rich and aluminum-rich materials in the alloys processed terrestrially was observed.

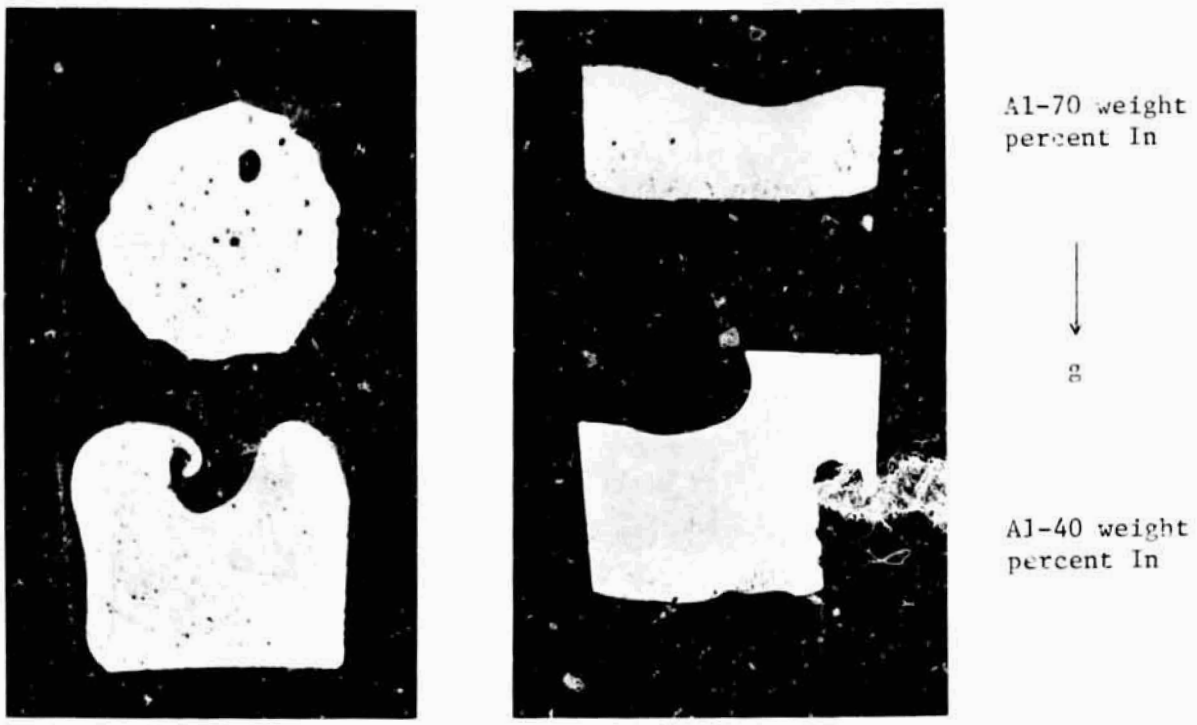

Flight

Ground Base

FIGURE 3. MACROPHOTOGRAPHS OF SPAR II FLIGHT AND GROUND BASE ALLOYS

The microstructural features of all the samples were similar and consisted of the following phases:

(1) Indium-rich droplets in an aluminum-rich matrix
(2) Aluminum-rich spheres showing evidence of the monotectic transformation and aluminum-rich dendrites in an indium-rich matrix

A great difference in the distribution of the dispersed phases was seen between the samples processed at 1-g and those processed in space. In the 1-g processed samples, the effect of gravity could be easily seen by the settling of the indium-rich droplets in the aluminum-rich matrix and by the floating of the aluminum-rich spheres and dendrites in the indium-rich matrix. The same type of particles were seen in the flight sample, and although they were relatively coarse, their distribution was much more uniform than it was in the samples processed on the earth.

Interpretation of SPAR II Results

The unusual distribution of phases in the SPAR II flight sample was considered to have resulted from two causes:

(1) The tendency to form the configuration which has the lowest combination of surface and interfacial energies
(2) Fluid flow mechanisms that provide the means to achieve the lower energy configurations.

As part of the SPAR II analysis, calculations were made to determine the configurations expected at low gravity for mixtures of molten aluminum and indium as a function of the volume fraction of aluminum. The two liquids are assumed to be of spherical geometry and are in a containerless configuration. The results show an overwhelming tendency for the liquid indium to surround the liquid aluminum when the interfacial energy between the aluminum and indium is < 350 ergs/cm^2 as expected.

Insight into the case in which a container is involved was also obtained from published analyses and experiments conducted on liquid-gas mixtures at low g (10,11). Based on these results, the observed macro-

structure of a wetting indium-rich material surrounding an aluminum-rich core is expected.

During the analysis of the SPAR II results, a number of possible mechanisms by which massive separation might occur were suggested. These are summarized in Table 1. Most of them involve fluid motion leading to droplet collisions and subsequent coalescence. Only the first three mechanisms listed in Table 1 were analyzed in any detail and are summarized in the following discussion.

Calculations dealing with residual motion from the rocket spin and despin have shown that the time available at micro-g levels before the quenching operation (94 seconds) is appreciably longer than that required to dampen the residual motion to a very small level (30 seconds for the 40 weight percent In alloy, 55 seconds for 70 weight percent alloy). It was concluded that this source of potential fluid motion can be neglected.

Analysis of conventional convection at low-g arising from density differences in the single phase alloy led to the conclusion that fluid velocities on the order of 0.1 cm/second are possible. Thus, in the 10-second period between initial phase separation and monotectic solidification, fairly substantial fluid flows are possible. Although this was a "worse case" computation since the density differences assumed were those between pure aluminum and pure indium, it was concluded that this mechanism is a probable contributor to the observed massive separation.

An estimate of the likelihood for thermocapillary flow (surface tension drive fluid motion arising from temperature gradients) was obtained through calculation of Marangoni numbers for the Al-In alloys studied. The high values of the Marangoni numbers (Ma = 229 for Al-40 weight percent In, Ma = 500 for Al-70 weight percent In) indicated that at a cooling rate of 15 C/second and with the resulting temperature gradient of 10 C/cm, fluid motion due to surface tension gradients are likely. Another manifestation of the Marangoni effect, the migration of droplets under a thermal or solutal gradient was not considered in the SPAR II post-flight analysis. However, some evidence that this effect may be present in this system is presented in the second of the report "SPAR V Flight Experiment 74-30".

TABLE 1. POSSIBLE MECHANISMS FOR MASSIVE PHASE SEPARATION

Residual Fluid Motion
Surface Tension Drive Flow (Marangoni effect)
Conventional Convection
Capillarity (spreading)
Transformation Segregation
Transformation Volume changes
Nonuniform Starting Composition

Another suggested source of the observed massive separation, the spreading of a liquid onto a solid or another liquid surface was not analyzed. Droplet spreading is usually rapid and thus, could also play a major role in the evolution of the observed structure of SPAR II flight samples.

Another contributor to the observed macrostructure was hypothesised in terms of directional cooling effects during specimen quenching and their relation to phase separation. In this mechanism, the separating phase (indium, in the SPAR II samples) would initially precipitate preferentially at the container walls since this part of the melt is the first to reach theconsolute temperature during cool-down. The local precipitation may be coupled with the spreading phenomenon described above and could, in addition, be associated with the rejection of aluminum into the specimen interior. This mechanism, however, was not a part of the SPAR II post-flight analysis.

Still another source of fluid motion was considered but not analyzed; namely transformational volume changes as a result of the liquid-liquid phase separation or due to the monotectic transformation. It is possible that these volume changes could lead to fluid motion sufficiently large to effect droplet coalescence. Some evidence of volume changes accompanying phase separation has recently been presented by Potard[12].

The agglomeration process itself, wherein two colliding droplets unite to become one larger droplet could also lead to localized fluid motions due to the expulsion of host liquid from between the droplets and due to the shape change from dumb-bell to spherical. It is expected that the more rapid this coalescence process is the more wide-spread will be the fluid motion.

At the conclusion of the SPAR II experimental analyses, the most suspicious source of the unanticipated structures observed was the possible lack of homogeneity in the single phase liquid alloy at the start of cool-down after the relatively short 15-minute hold at 950 C. Accordingly, an extensive ground-base program was initiated to analyze this possibility. The analysis culminated in the design and execution of the SPAR V experiment.

Post-SPAR II Ground Based Experiments

Purpose and Overall Description

In order to explore the possibility that the SPAR II flight and ground base samples were not homogeneous at the time of the cool-down (after the 15-minute hold time), three types of experiments were conducted for the purpose of assessing the degree of mixing that might have occurred during rocket spin-up and despin and to determine the rate of homogenization of the liquid alloy assuming that this process is controlled strictly by diffusion. A simple ground base simulation of the rocket spin-up and despin was conducted to determine the degree of mixing expected from this motion. In addition, two types of experiments were conducted to determine the diffusion characteristics of liquid phase Al-In alloys. The first used a differential thermal analysis (DTA) technique to assess the rate of homogenization of a liquid melt at a temperature above the miscibility gap by monitoring the apparent consolute temperature as a function of hold time. The second set of experiments was designed to provide a direct measurement of the interdiffusion coefficients in the liquid Al-In alloys at 970°C, the approximate hold temperature used on SPAR II and later used on SPAR V.

Spin-up and Despin Experiments

In order to simulate the action of spin-up and despin in a single phase liquid containing a concentration gradient, the apparatus shown in Figures 4 and 5 was fabricated. This equipment consisted of a 61 cm diameter lucite "spin" platform mounted on a two-speed (163 and 246 RPM) polishing wheel. The apparatus included a fixture for holding a sample vial 13-mm inside diameter (see Figure 5) and a bracket for mounting an 8-mm movie camera perpendicular to a line between the spin axis and the vial.

The axis of the vial was displaced $\sim$ 41 mm from the spin axis reproducing the position of the sample relative to the rocket spin axis in SPAR II.

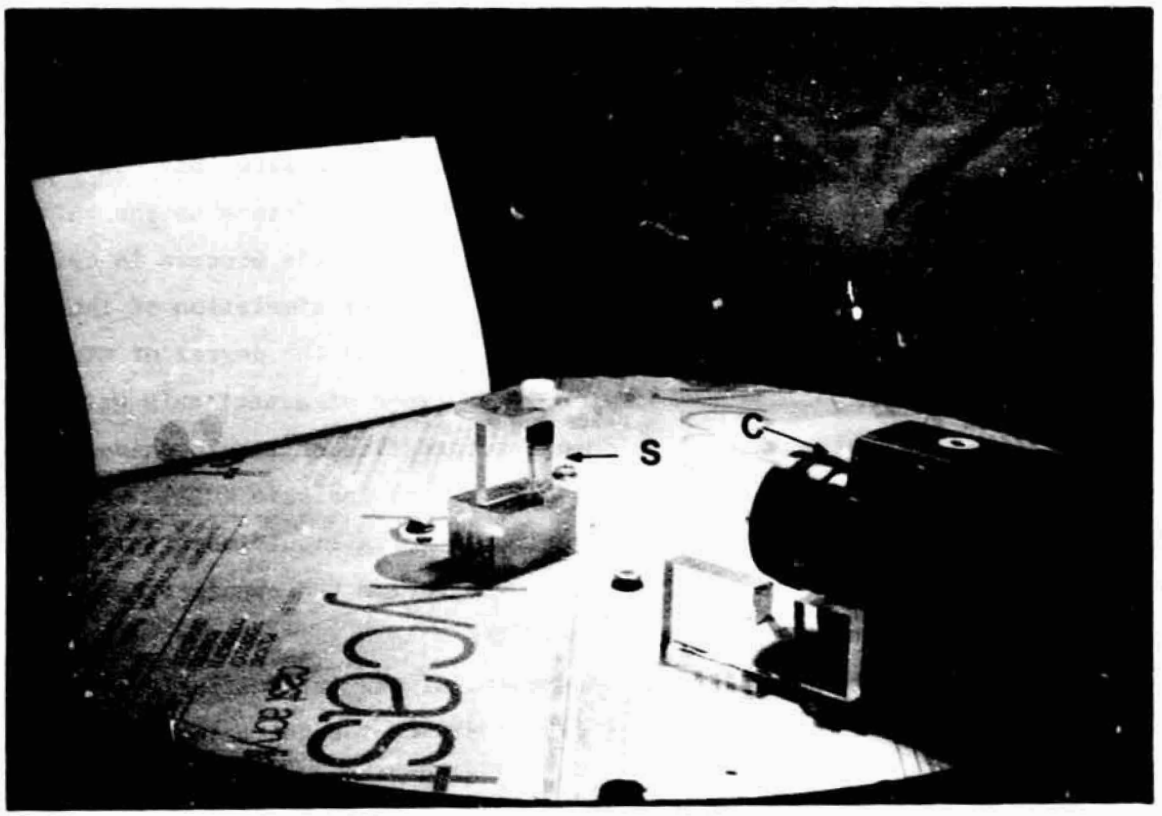

FIGURE 4. PHOTOGRAPH OF SPIN PLATFORM USED TO SIMULATE THE EFFECT OF ROCKET SPIN-UP AND DESPIN ON LIQUID MIXING. THE VIAL CONTAINING THE LIQUID SAMPLE IS DESIGNATED "S" AND THE 8mm MOVIE CAMERA IS MARKED "C".

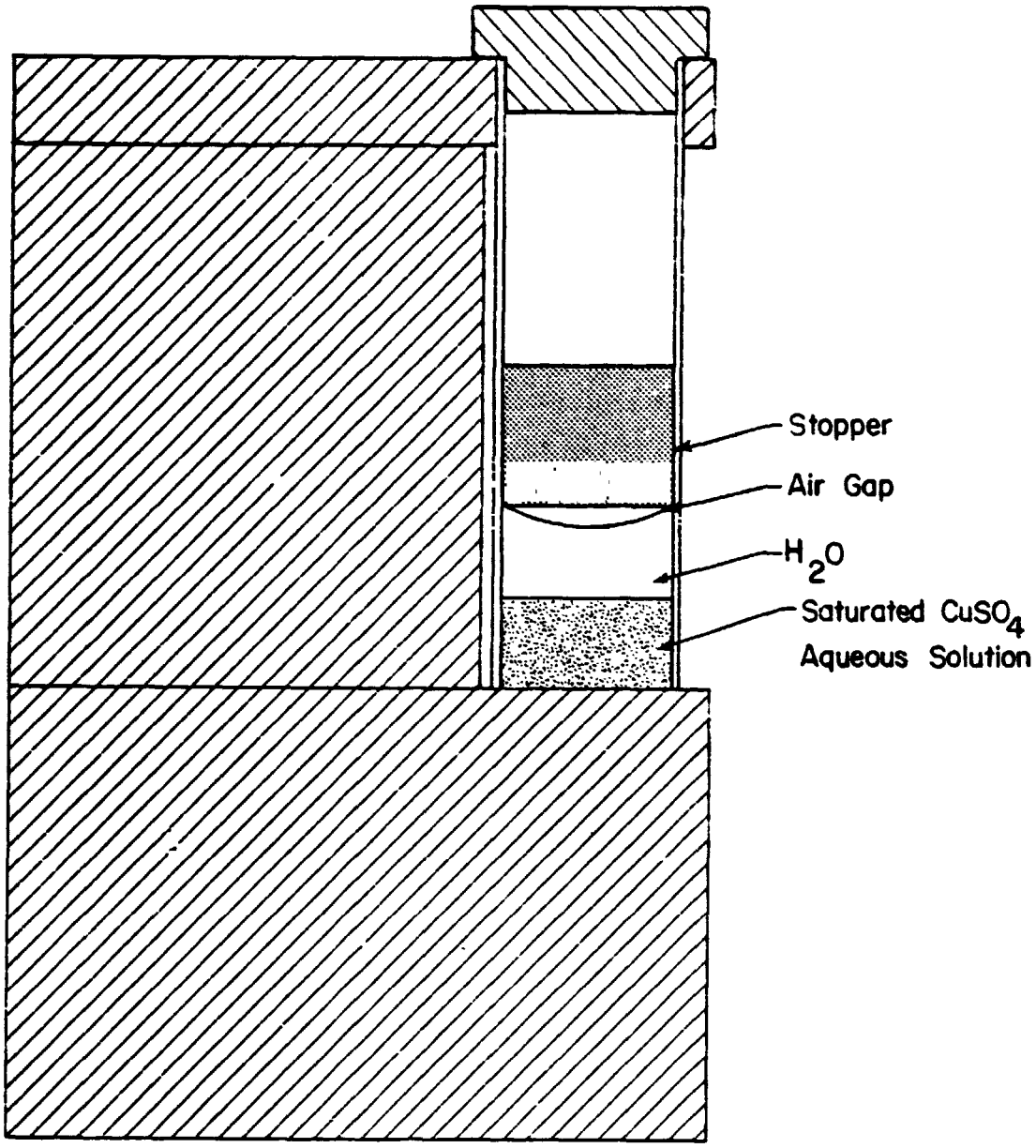

FIGURE 5. SCHFMATIC DRAWING OF SAMPLE AND HOLDER FOR SPIN-UP/DESPIN EXPERIMENTS

An aqueous solution of copper sulfate was chosen as the system to simulate the liquid Al-In alloys. The choice was based on consideration of viscosity level (∿ 1 cp) and ease of photography (the blue colored copper sulfate provides excellent contrast with the colorless water).

In a typical experiment, the bottom of the vial was filled with the saturated aqueous solution of copper sulfate (calculated specific gravity 1.17) and a top layer of pure water was carefully added. A rubber stopper sealed the liquid into the vial either with or without a layer of air at the top of the liquid surface. The specimen was accelerated either directly to a speed of 246 RPM or accelerated to that speed after first pausing at the intermediate speed of 163 RPM. The specimen was continuously photographed at 18 or 36 frames/second during the process.

Among the investigated variables were the relative proportion of the overall height of the liquid occupied by the copper sulfate solution (0.25 and 0.5), the presence or absence of an air gap to simulate the presence of helium gas in the SPAR II experiment and the presence or absence of a wetting agent (1 drop of Kodak photoflow). A summary of the parameters used in the spin-up despin experiments is provided in Table 2.

Frames from Film Roll No. 2 are shown in Figure 6. They illustrate the position of the liquid and gas layers at the start of the experiment (Figure 6a), after acceleration to the intermediate speed of 163 RPM (Figure 6b), after acceleration to the maximum speed of 246 RPM (Figure 6c) and after deceleration to a rest position (Figure 6d). At the intermediate and highest rotational speeds, the higher specific gravity copper sulfate is forced up the vial wall to a height which increases with the rotational speed. The fluid motion produces a paraboloidal gas pocket at the top of the liquid adjacent to the vial surface closest to the spin axis.

The major point to be noted from these film strips is that after the spin-up and despin sequence is completed, the final configuration is altered little from the starting configuration. This demonstrates

TABLE 2. SUMMARY OF SPIN-UP/DESPIN EXPERIMENTS

Film Roll Number	Approximate Ratio of $CuSO_4$ Solution Height to Total	Other Conditions
1	.25	Air gap. No wetting agent.
2	.25	Air gap. No wetting agent.
3	.25	No air gap. Wetting agent present.
4	.25	Air gap. Wetting agent present.
5(a)	.50	Air gap. Wetting agent present.
5(b)	.50	Air gap. No wetting agent present.
6	.50	Air gap. No wetting agent.

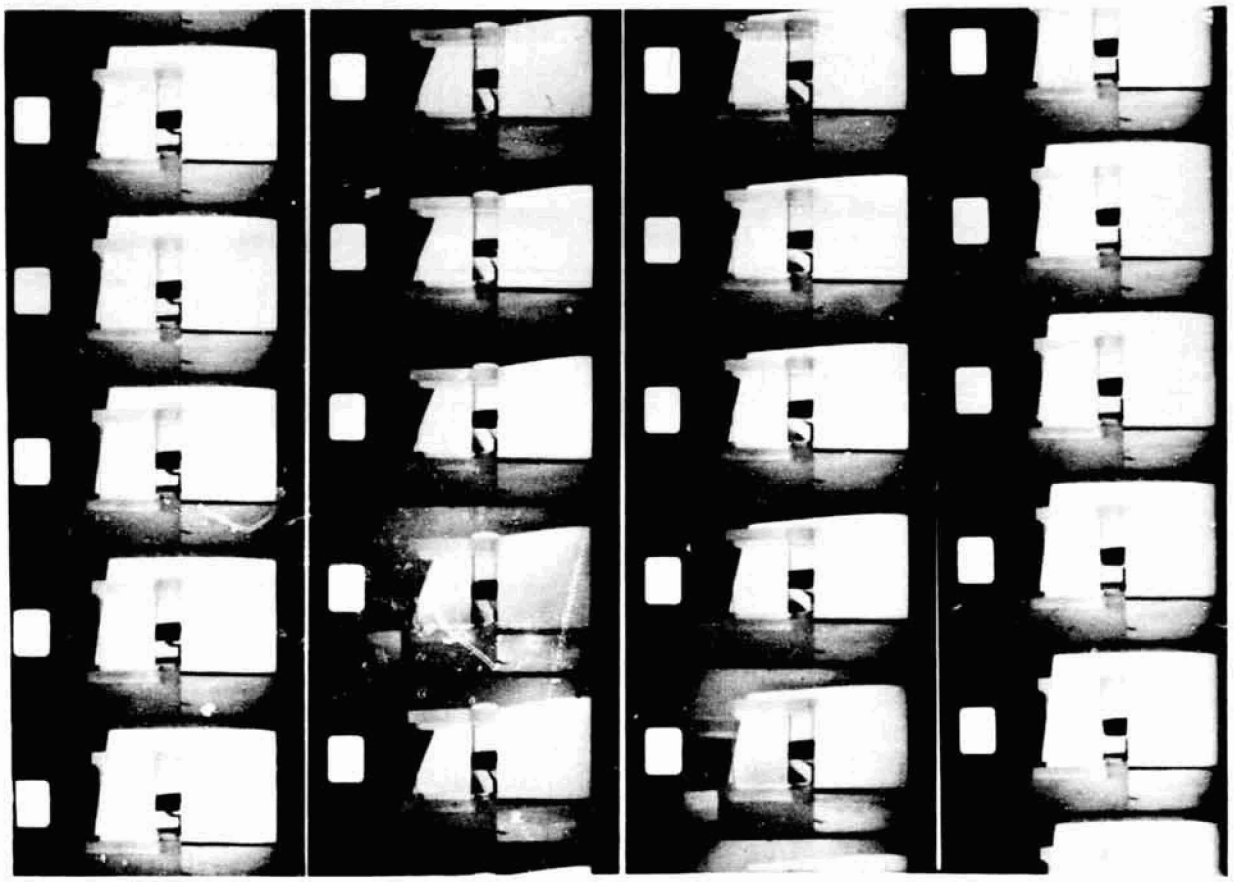

d c b a

FIGURE 6. SELECTED FRAMES FROM FILM NO. 2. (a) At Start (b) Rotating at 163 RPM (c) Rotating at 246 RPM, and (d) At rest after spin-up and despin.

the major conclusion of the experiment, that there is little mixing associated with the spin-up and despin of the rocket. (This conclusion neglects any mixing which may be induced by vibration during the various phases of the rocket flight.)

The following general comments can be made on the basis of all the films taken and analyzed.

(1) Although the liquid is a single phase, the region rich in copper sulfate behaves similarly to that expected in a multiphase material and is centrifugally accelerated up the vial on the side opposite the spin axis. The faster the rotational speed, the higher up the vial wall the copper sulfate is forced. This behavior appears to be independent of whether an air gap is present or not.

(2) When an air gap is present, it assumes a sectional shape which is approximately parabolic at the top surface nearest the spin axis. This is due to the acceleration of the heavier liquids to the outside of the vial. In the absence of a wetting agent, the configuration is stable (except for minor shape changes) even after motion has stopped. The presence of a wetting agent promotes the return of the air gap to its original configuration.

(3) The presence of the wetting agent appears to accelerate the movement of copper sulfate into the pure water portion of the sample either by enhanced diffusional or convective processes.

(4) The major turbulent disturbance of the liquid sample occurs during the rotational speed changes occurring during spin-up or despin and appears to be concentrated at the free

surface and in the area where the concentration gradient is the steepest.

Kinetics of Homogenization

Two methods were used to assess the rate at which homogenization of the pure aluminum and indium components took place at a temperature of 970 C, the target hold temperature for the SPAR II and SPAR V experiments. The first method, which was somewhat indirect, used differential thermal analysis (DTA) to measure the kinetic approach to homogenization by determining the time necessary to obtain a constant and reproducible measure of the consolute temperature for a given Al-In alloy. This technique also had the advantage of providing a check on the published results for the Al-In miscibility gap. The second method provided a direct measure of the interdiffusion coefficient in liquid Al-In alloys above the miscibility gap. Both methods provided sufficiently accurate, self-consistent data to select a hold time which would insure prequench melt homogeneity in the SPAR V experiment.

DTA Measurements

The DTA equipment used in the kinetic measurements is schematically shown in Figure 7. The heart of the apparatus consists of an alumina crucible capped with an alumina lid and containing the aluminum and indium components in the desired proportions. The crucible and its contents are in turn contained in an OFHC copper block which serves primarily as an untransforming standard with which the aluminum-indium alloys are compared. The copper block which has a heat capacity close to that of the alloys also serves to smooth out any non-uniformities in thermal conditions seen by the alloy samples.

The sample temperature and the differential temperature between the sample and the standard are measured by means of 1 mm outside diameter inconel sheathed chromel-alumel thermocouples. The sample thermocouple is positioned in an alumina well fabricated from tubing 1.2 mm ID x 1.9 mm OD cemented in the center of the crucible base and sealed at the top end with an alumina slurry. The crucible containing the

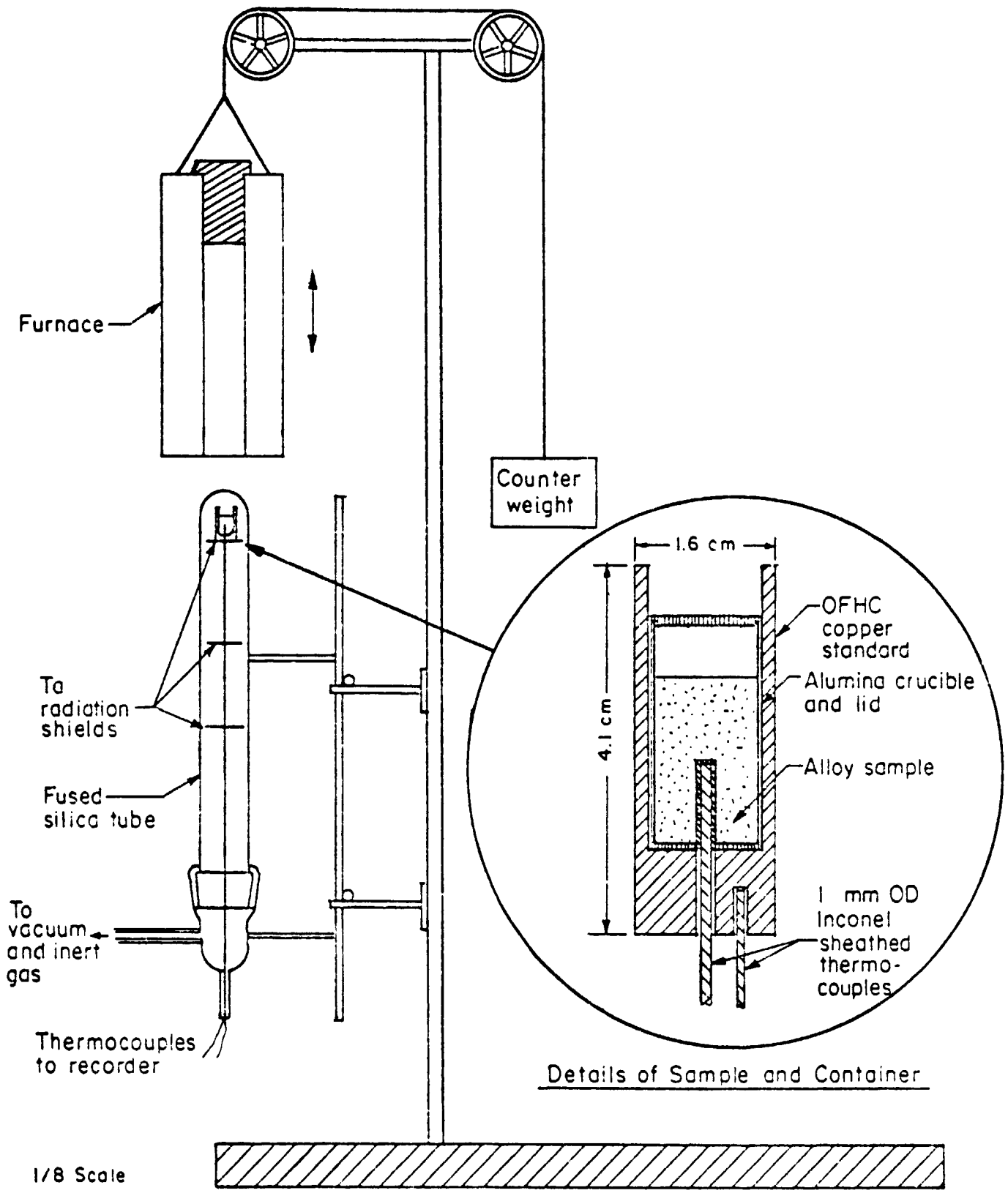

FIGURE 7. SCHEMATIC DRAWING OF THERMAL ANALYSIS EQUIPMENT

thermocouple well is fired at 1200 C before use. The "standard" thermocouple is positioned in a blind hole at the base of the copper block. Thermocouple calibration has been carried out at the melting point of pure aluminum, 660 C.

The direct and differential signals from the thermocouples are recorded on a two-channel millivolt recorder at a sensitivity of either 10 or 4 mV/in. (3.94 or 1.57 mV/cm) for the direct signal and 0.02 mV/in. (0.0079 mV/cm) for the differential signal.

The sample and copper block supported by a tantalum disc and by the thermocouples contained in an alumina tube are sealed in a fused silica tube capable of vacua of better than 1×10^{-5} Torr. Provision for the introduction of helium is also made. A resistance-heated furnace can be lowered around the fused silica tube and sample to provide heating and cooling rates in the temperature range of interest of approximately 7 and 6 C/minute, respectively.

In a typical experiment, the alumina crucible is loaded with pure aluminum and indium components in the proper proportions. The weights of the components are also chosen so as to fill approximately 75 percent of the crucible volume. After insertion of the alumina crucible and its contents into the apparatus, the fused silica tube is evacuated to $\sim 1 \times 10^{-5}$ Torr and the furnace is lowered around the fused silica tube and sample. Heating is carried out until the sample is completely molten (660 C) and any residual dissolved gas eliminated. At this point, helium at just below atmospheric pressure is introduced into the system in order to prevent excessive evaporation of the alloy components. When the sample reaches 970 C, it is allowed to remain at this temperature for a controlled time and then is cooled to below the monotectic temperature ($\sim$ 640) while the direct and differential temperatures are recorded. The sample is then usually reheated to 970 C and, after another hold period, is cooled again while the direct and differential temperatures are recorded as a function of time. The procedure is repeated in order to collect data for a number of hold-times.

The DTA studies were carried out on three alloys, 40.09. 70.06, and 76.02 weight percent In. The results of these studies are summarized in Table 3 and Figure 8. A typical differential temperature trace is shown in Figure 9.

Figure 8 shows the variation of the indicated miscibility gap boundary with hold time for the 40 weight percent In alloy. The data indicates that approximately 8 hours at 970 C is needed to produce a reliable value of the consolute temperature. Values for shorter hold times are presumed to be in error because of a lack of homogeneity in the alloy at the start of the DTA cooling experiment.

DTA data for all the alloys studied is presented in Table 3. All the measurements of consolute temperatures, have been made during cooling. However, measurements of the monotectic temperature have been made both during heating and cooling since this parameter is insensitive to compositional inhomogeneities. A best value for the monotectic temperature based on the present results is 640 C and is the average of the mean value obtained on heating and that obtained on cooling. The data for the 40 weight percent In alloys is by far the most sensitive of the three to hold time. The indicated miscibility gap boundary for the 70 weight percent In alloy still appears to be increasing up to four hours, while the data for the 76 weight percent In alloy does not appear to be at all sensitive to hold time. It should also be noted from Table 3 that there is a tendency for undercooling to occur at the monotectic temperature.

Consolute temperatures measured after 16 hours at 970 C for the 40 and 76 weight percent In alloys agree reasonably well with the equilibrium Al-In phase diagram published by Predel[1]. The data from the present investigation are compared with Predel's data in Table 4.

The DTA trace presented in Figure 9 for the 76 weight percent In alloy held at 970 C and cooled at a rate of 4 C/minute clearly shows the monotectic transformation at 637 C. Curiously, the initial heat effect is followed by temperature oscillations having an amplitude on the order or 0.05 C and a period of $\sim$ 20 seconds. The oscillations are presumably due to oscillatory convection currents which alternatively bring hot and cold fluid into the neighborhood of the measuring thermo-

TABLE 3. SUMMARY OF DTA RESULTS

Hold Time (hr)	Cooling Data: Miscibility Gap Boundary, °C	Cooling Data: Monotectic Temperature, °C	Cooling Data: Degree of Undercooling, ΔT, °C at Monotectic Temperature	Heating Data: Monotectic Temperature, °C
		Al-40.09 Weight Percent		
0	813	--	--	642
0	814	639	9	--
0	813	639	12	--
0	812	639	13	--
0	--	639	18	--
1	813	640	9	--
2.1	788	638	10	642
4.1	782	640	5	--
8.0	764	638	10	641
16.0	761	639	11	642
		Al-70.06 Weight Percent In		
0	812	638	5	641
0	--	638	6	644
1	813	638	3	--
2	--	--	--	--
4	815	639	9	--
		Al-70.02 Weight Percent In		
0	811	638	4	642
0	--	638	8	641
0.5	812	636	9	--
1.0	814	638	3	--
2.1	>812	637	8	641
4.0	813	636	9	--
16.0	811	637	13	644

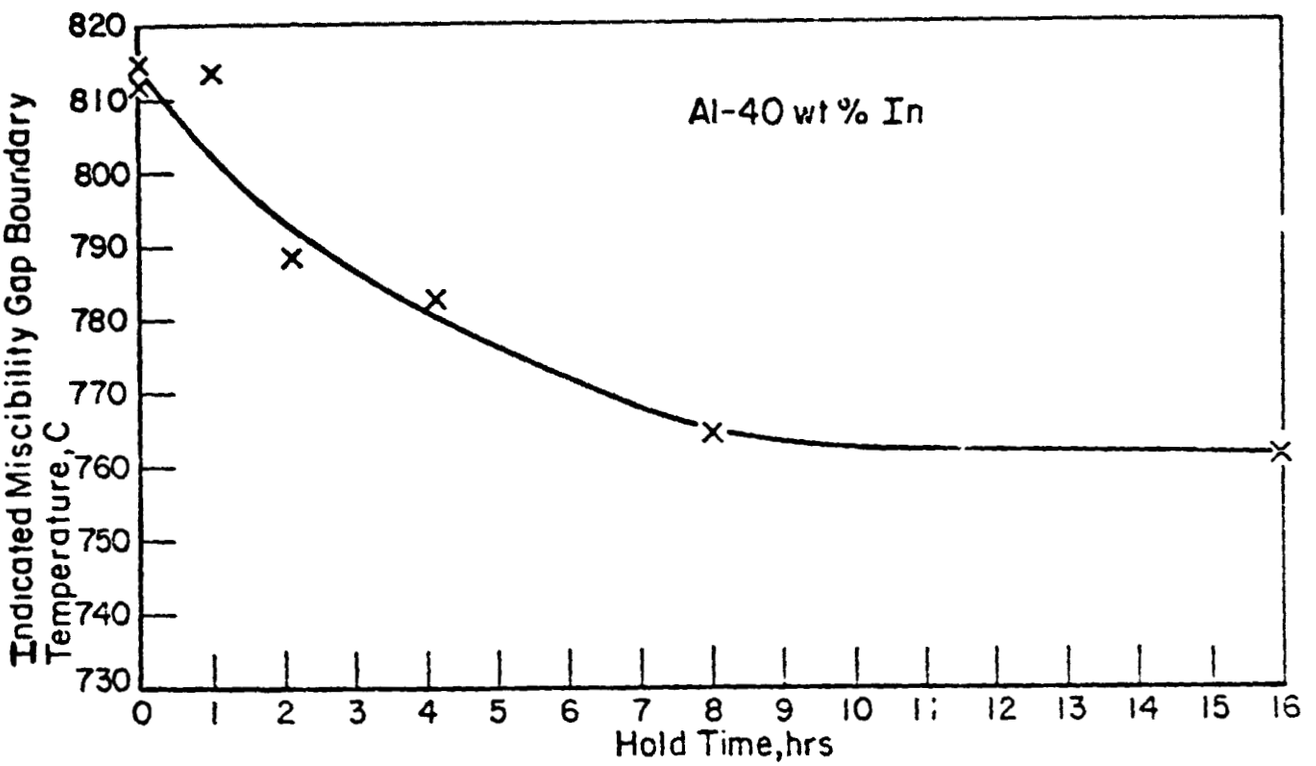

FIGURE 8. THE VARIATION OF INDICATED MISCIBILITY GAP BOUNDARY TEMPERATURE WITH HOLDING TIME AT 970 C

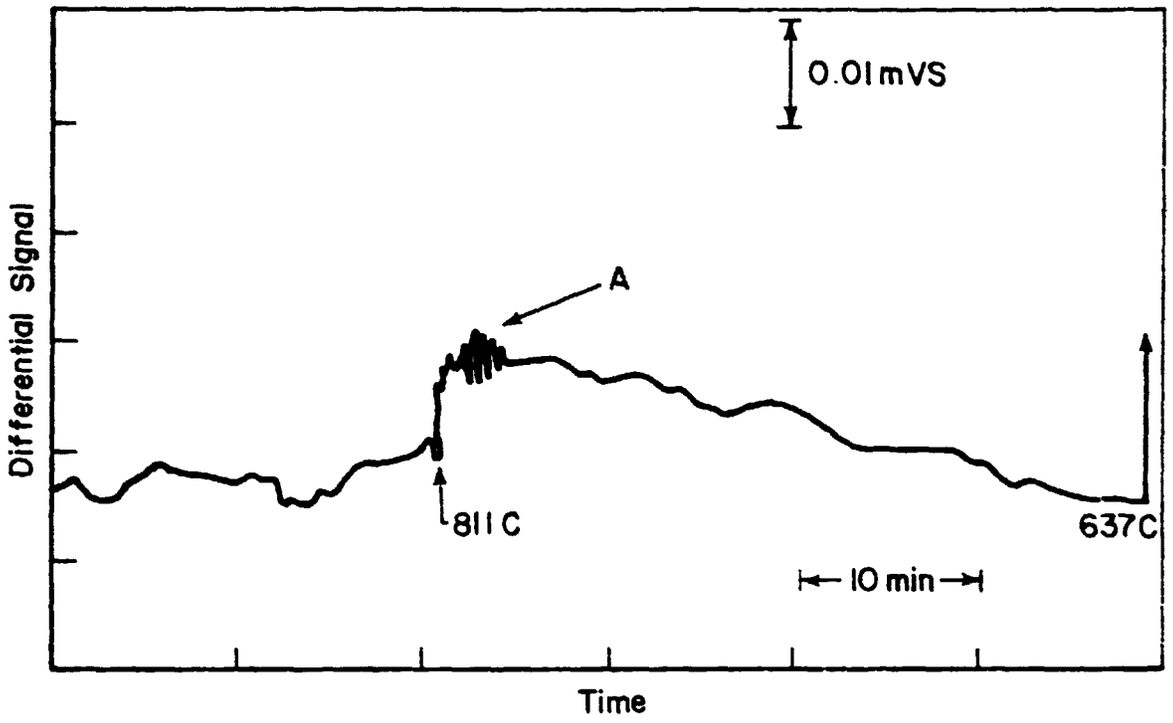

FIGURE 9. DTA TRACE FOR Al-76 WEIGHT PERCENT In ALLOY HELD 16 HRS AT 970 C AND COOLED AT ∿ 5C /MIN

Note cyclic differential signal at A having a maximum amplitude of ∿ 0.002 mv (0.05 C) and of frequency 3 cycles/min.

Table 4. COMPARISON OF DTA DATA FROM PRESENT WORK WITH PUBLISHED DATA OF PREDEL[1]

Predel Data		Present Investigation	
Composition, Wt. Pct.	Consolute Temperature, °C	Composition, Wt. Pct.	Consolute Temperature, °C
39.91	775	40.09	761
75.12	830	76.02	811
	Monotectic Temperature, °C		
	637		640

couple. Oscillations in liquid volume have recently been observed by Potard[12] during the cooling of Al-In alloys into the miscibility gap. His cooling rate was about one-tenth that used in the present investigation and the oscillation period was 600 seconds. Although the two oscillatory effects are possibly related, the relationship between them is not obvious. Oscillatory convection currents have also been observed to result from surface tension gradients arising from temperature variations in a liquid containing a free surface. Much more work is required in this area for a fuller understanding of these phenomena.

The conclusion to be drawn from the DTA experiments is that a hold time of at least 8 hours is necessary to yield a reproducible and equilibrium value of the consolute temperature. It is presumed that this time period is associated with the homogenization of the alloy above the miscibility gap. It should be noted that the homogenization time period for the DTA geometry would be appreciably longer than for the SPAR configuration owing to the longer diffusion distances in the DTA configurations. These factors will be discussed at length in the next section.

Diffusion Analysis

Introduction. In order to assess the results of SPAR II with regard to possible lack of homogeneity in the melt just before the cool-down and to provide design data for the SPAR V experiment, the diffusional characteristic of liquid Al-In alloys above the miscibility gap were assessed analytically and experimentally.

Analytical Calculations. The analytical calculations considered a simple one dimensional boundary-value problem based on Fick's formulation.

$$\frac{\partial C\ (x,t)}{\partial t} = D\ \frac{\partial^2 C\ (x,t)}{\partial x^2} \qquad \text{Equation 1}$$

where

$$C\ (x,0) = \begin{cases} C_o \text{ for } 0<x<h \\ 0 \text{ for } h<x<1,\ 1>h \end{cases} \qquad \text{Equation 2}$$

Here, C (x,t) is the composition at position x and time t, and D is the interdiffusion coefficient.

The solution of this boundary-value problem has been shown by Barrer[8] to be given by

$$C\ (x,t) = C_o \left\{ \frac{h}{\ell} + \frac{2}{\pi} \sum_{n=1}^{\infty} \frac{1}{n} \exp\left[-\left(\frac{n\pi}{\ell}\right)^2 Dt \right] \cos\left(\frac{n\pi x}{\ell}\right) \sin\left(\frac{n\pi h}{\ell}\right) \right\}$$

Equation 3

This expression has been used to describe the kinetics of homogenization, neglecting such effects as the possible concentration dependence of the interdiffusion coefficient and the somewhat undefined boundary conditions actually existing at t = 0.

Illustrated in Figure 10 is the manner in which C (ℓ, t), the composition at position ℓ, increases as a function of Dt from its initial value of zero and approaches its equilibrium level, $C_{eq} = C_o h/\ell$. The cases illustrated in this figure correspond to the three alloys run in the DTA and the two alloys run in the SPAR Rocket Flight configuration.

The principal feature of interest in this figure lies in the relatively strong dependence of C (ℓ, t) upon the value of ℓ itself. Decreasing ℓ from values a little over 2 cm for the DTA configuration to values just under 1 cm for the SPAR configuration results in a pronounced decrease in the time required to attain equilibrium. To further illustrate this fact, Table 5 presents the Dt values required to bring C (ℓ, t)/C_{eq} to within 1 percent of the asymptotic value of unity and the corresponding

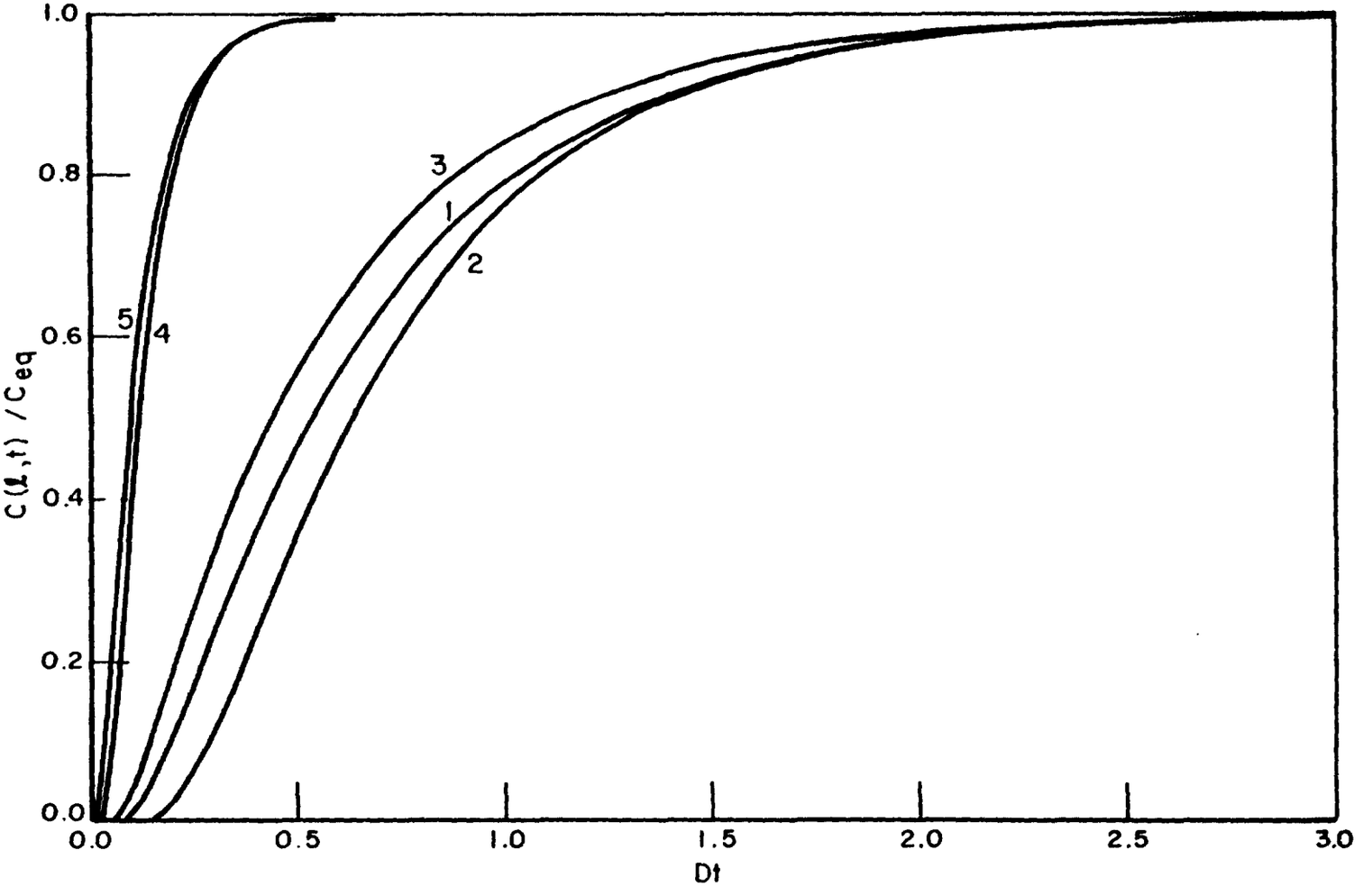

FIGURE 10. APPROACH OF C (ℓ,t) TO ITS EQUILIBRIUM VALUE FOR VARIOUS CONFIGURATIONS OF INTEREST

1--DTA Al-70 weight percent In, h = 1.04, ℓ = 2.29; 2--DTA Al-40 weight percent In, h = 0.421, ℓ = 2.19; 3--DTA Al-76 weight percent In, h = 1.18, ℓ = 2.22, 4--SPAR Configuration Al-40 weight percent In, h = 0.183, ℓ = 0.952; 5--SPAR Configuration Al-70 weight percent In, h = 0.446, ℓ = 0.9817; h and ℓ in units of cm.

times assuming a value of D = 8 x $10^{-5}cm^2$/second*. The more than 8 hours required to attain equilibrium in the DTA configuration is consistent with the experimental results presented in Figure 8. On this basis, ∿ 1.7 hours are required to homogenize the Al-In alloys in the SPAR configuration (see Table 5).

TABLE 5. VALUES FOR Dt REQUIRED TO BRING C (ℓ,t) TO WITHIN 1 PERCENT OF ITS EQUILIBRIUM VALUE

Case	Configuration	Composition Weight Percent In	Dt	$t^{(a)}$ (hr)
1	DTA	70	2.6	9.03
2	DTA	40	2.5	8.68
3	DTA	76	2.4	8.33
4	SPAR	40	0.5	1.74
5	SPAR	70	0.5	1.74

(a) Based on an assumed value of D = 8 x $10^{-5}cm^2$/second.

Finally, in Figure 11, we have presented the concentration gradients calculated for various values of Dt from 0.07 (t = 15 minutes, D = 8 x 10^{-5} cm^2/second) to that required to attain near uniform composition for the 40 and 70 weight percent In alloys in the approximate SPAR and DTA configurations. Based on these calculations and the ground base spin-up and despin studies, it was concluded that the SPAR II alloys were far from homogeneous after the 15-minute hold time assuming that fluid flow had not been induced by rocket vibration, etc.

* This value of D was chosen before measurements of D were made in the present study (see next section). The assumed value of 8 x $10^{-5}cm^2$/second based on measurements reported in the literature on the self diffusion of indium in an In-5 weight percent alloy[13] is somewhat higher than the value measured in the present study, 6.4 x $10^{-5}cm^2$/second. However, the conclusions based on our calculations using the assumed value of D are still valid.

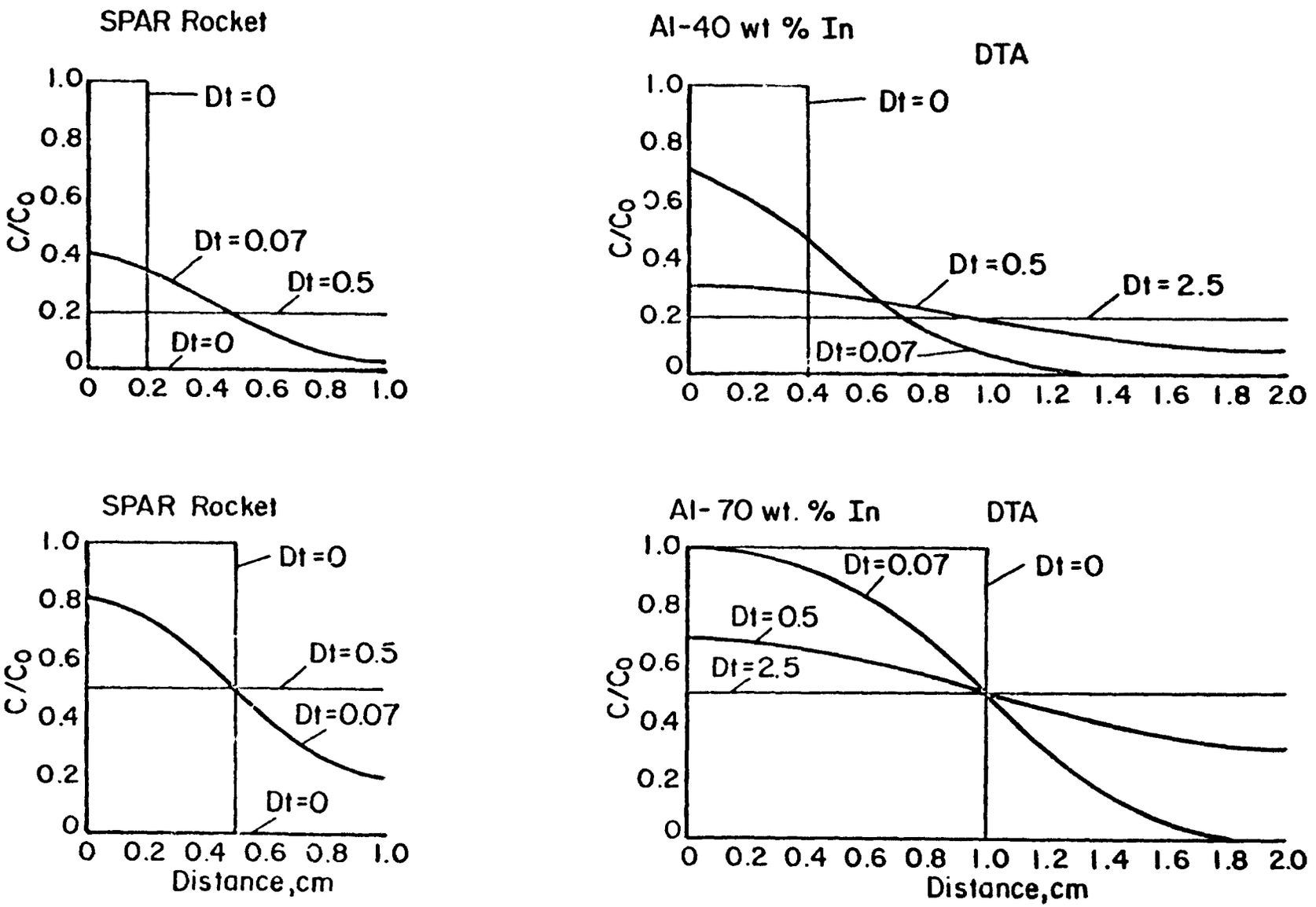

FIGURE 11. CALCULATED CONCENTRATION GRADIENTS IN THE Al-40 WEIGHT PERCENT In AND Al-70 WEIGHT PERCENT In ALLOYS IN THE DTA AND SPAR ROCKET CONFIGURATIONS

Direct Measurement of the Interdiffusion Coefficient, D. The purpose of this set of experiments is to determine the value of the interdiffusion coefficient in liquid aluminum-indium alloys at a temperature of 970 C, in the homogeneous liquid region above the miscibility gap. These measurements were made to check the validity of the conclusions made in the previous section on the basis of an assumed value of D = $8 \times 10^{-5} cm^2/second$.

The results obtained thus far are still considered tentative since there are still some unsolved experimental difficulties associated with the technique. We feel, however, that when the method has been perfected, it will allow us to determine diffusion coefficients as a function of composition in liquid phase alloys. The technique has the added advantage that the microstructure of a continuous series of alloys can be conveniently prepared, examined and related to composition.

Three sets of experiments have been conducted thus far. In all cases two samples were involved, one for a diffusion time of 1 hour and the second for 4 hours.

The specimen design used in these experiments is shown in Figure 12. An alumina capillary tube, one end of which is sealed with a slurry made up of fine alumina in an H_3PO_4/H_2O solution, was utilized. The other end of the capillary incorporated a radial hole for suspending the sample in the furnace. These tubes were then fired by slowly heating in air to 1200 C* in order to drive off moisture and sinter the slurry. High purity In and Al wire, both of which were $\sim$ 1 mm in diameter and 3 cm long, were carefully inserted into the alumina tube after chemical cleaning of the indium and aluminum components in concentrated HCl and a 20 percent aqueous solution of NaOH respectively. After the capillaries were filled, they were suspended in a fused silica tube contained in a furnace as shown in Figure 13. The chamber was then evacuated to 1×10^{-5} torr and the samples heated to 800 - 900 C in approximately 30 minutes. At this temperature, helium was introduced into the system until a pressure level of slightly less than 1 atmosphere (0.1 MPa) was reached

* The tubes used in the first experiment were fired to only 700 C. Some gas evolution during the diffusion experiment is suspected. See text.

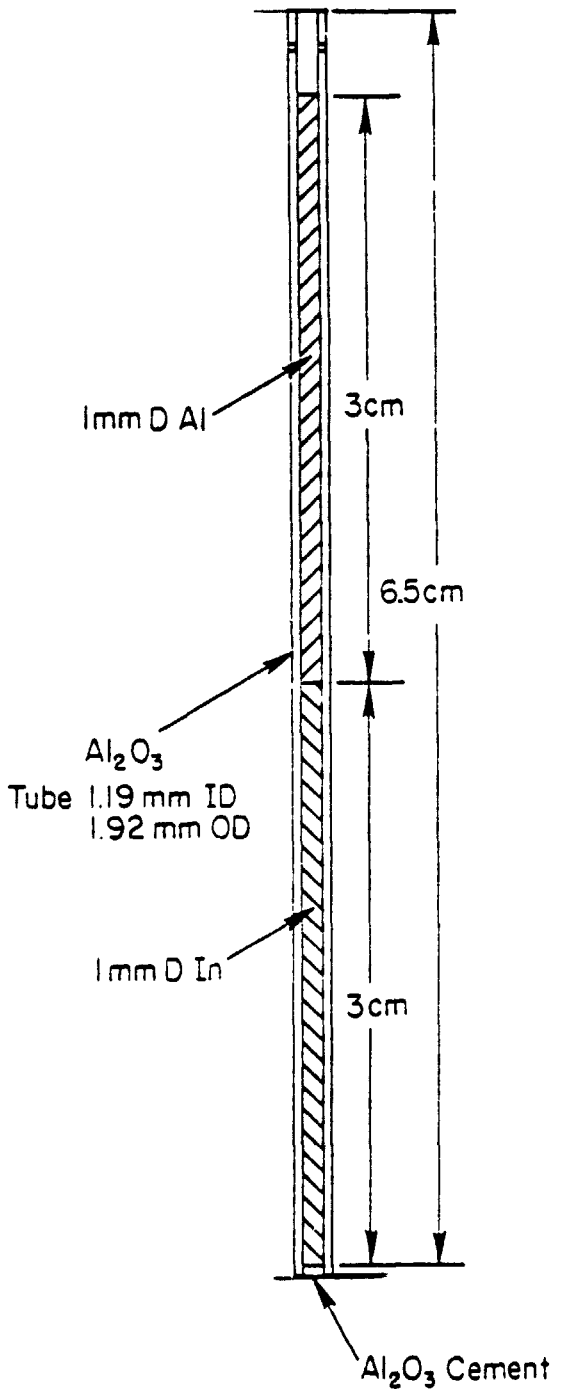

FIGURE 12. SPECIMEN DESIGN FOR Al/In LIQUID PHASE DIFFUSION EXPERIMENTS

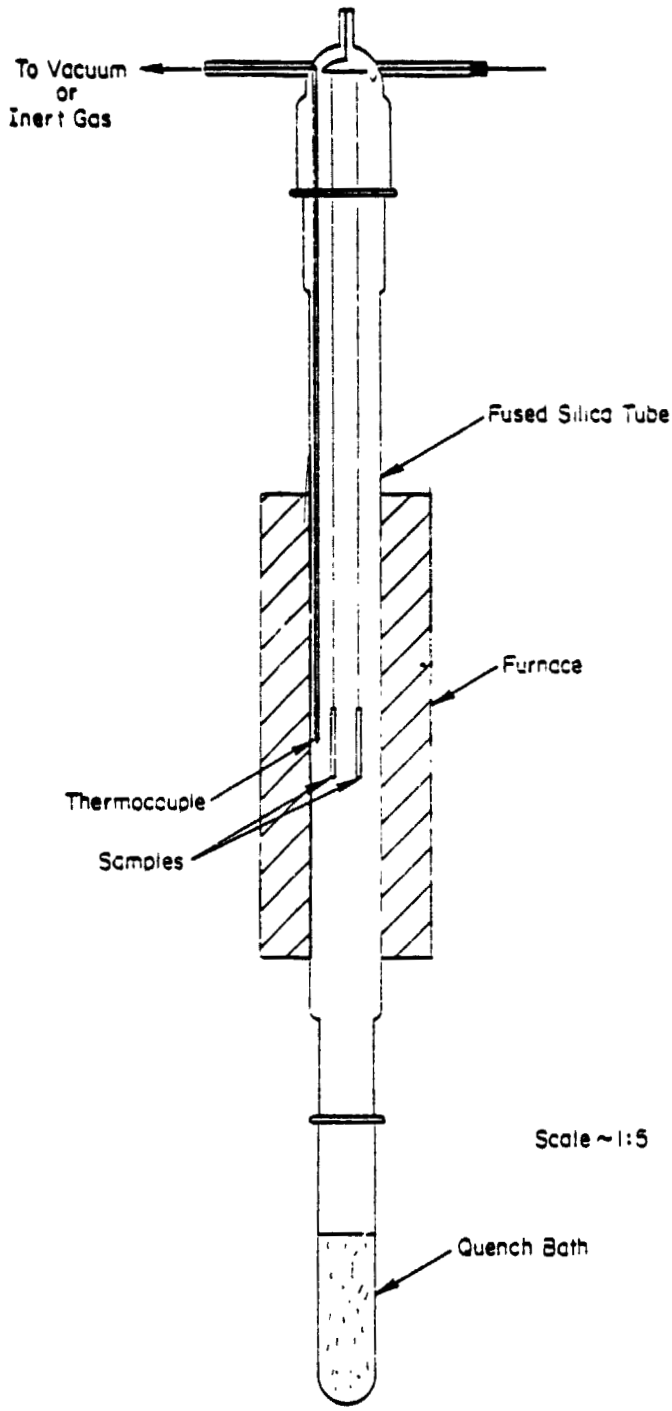

FIGURE 13. SCHEMATIC DRAWING OF APPARATUS USED IN LIQUID PHASE DIFFUSION EXPERIMENTS

while heating was continued to a temperature of 970 C. After the desired time at 970 C, the sample was dropped into a water-cooled siliconeoil quench bath where it was cooled to <20 C in ~ 1 second.

Table 6 summarizes some of the experimental parameters used in the two diffusion experiments. It should be noted that the calculated length of the diffusion couple at 979 C (~4.9 cm) is appreciably less than the 6 cm of original wire length because the wire diameter is somewhat smaller than the inside diameter of the capillary.

After the thermal treatment, the diffusion samples, while still in the Al_2O_3 capillaries, were metallographically polished down to the central longitudinal plane. Some difficulty was encountered in this procedure due to the presence of void regions and pull-out of portions of the specimen during polishing. Some macrostructural agglomeration was also observed which tends to complicate the composition analyses. Porosity and pull-out were so serious in Samples 1 and 2 that they were not analyzed.

The situation improved in the second experiment (DC 2), owing to a higher firing temperature (1200 versus 700 C) of the capillary and the maintenance of the vacuum environment to a higher temperature before introducing the inert gas. These procedures presumably allowed a greater proportion of the residual gases to be removed from the capillaries. Impregnation of the metallographic mounts with additional epoxy after the initial grinding was also found to be beneficial in retaining the bulk of the sample in the mount. However, even with these precautions, there were still some regions that suffered from pull-out. In addition, in the top portion of the specimen (the higher aluminum content portion) the metal only filled the capillary in isolated regions. The lack of complete filling is probably due to a combination of solidification shrinkage and the possible presence of gas bubbles.

Still another problem was encountered in the metallographic polishing of Samples 6 and 7. The presence of the alumina capillary tube interfered with the polishing of the appreciably softer metal and resulted in poorly prepared metallographic surfaces with the metal level substantially below the level of the ceramic.

TABLE 6. SUMMARY OF PARAMETERS USED IN Al-In LIQUID PHASE DIFFUSION EXPERIMENTS

Experiment No.	Sample No.	Diffusion Time (hr)	Wt. of In (gm)	Wt. of Al (gm)	L^{*}_{In} (cm)	L^{*}_{Al} (cm)
DC-1	1	4	0.1727	0.0603	2.401	2.349
	2	1	0.1827	0.0602	2.540	2.345
DC-2	6	1	0.1815	0.0584	2.523	2.275
	7	4	0.1830	0.0591	2.544	2.298
DC-3	8	1	0.1812	0.0636	2.519	2.477
	9	4	0.1769	0.0640	2.459	2.493

* L_{In} and L_{Al} are the lengths of In and Al at 970 C calculated on the assumption that the components fill the inside diameter of the capillary tube.

The preparation method described above was successfully applied to Samples 8 and 9. However, the polished sections revealed the presence of bubble-shaped void areas presumably due to gas bubbles.

The composition as a function of position in the diffusion couples was deduced for Samples 6, 7, 8, and 9 at 1.5 mm increments on an electron beam microprobe. The conditions used for these analyses are delineated in Table 7. Each of the diffusion couples was cut along its length into three approximately equal sections for these analyses. Pure aluminum and pure indium were used as standards. In a typical analysis of one of the section, the intensities from the aluminum and indium standards were first measured together with the background intensities determined on both sides of these peaks. The aluminum and indium peak and background intersities from positions along the diffusion couple section were then measured and finally a second set of intensity readings were taken on the aluminum and indium standards.

TABLE 7. PARAMETERS USED IN THE ELECTRON MICROPROBE ANALYSIS OF Al-In DIFFUSION COUPLES

Parameter	Sample 6	7	8	9
Approximate Spot Size, mm	0.13	0.13	0.4	0.4
Accelerating Potential, KV	25	25	15	15
Take-off Angle, deg.	20°	20°	20°	20°
Crystal	Mica	Mica	Mica	Mica
Al Line	Kα	Kα	Kα	Kα
In Line	Lα	Lα	Lα	Lα

The raw intensity data after background subtraction were converted to values of composition by means of MAGIC - Version 3[14], a computer program for quantitative electron microprobe analysis. This program calculates the values of $k = I_A/I_{A_0}$, the background subtracted intensity of the peak for element A in the sample divided by the corresponding peak intensity in the pure metal standard. The k values which represent a first approximation of the concentration of the element in the sample are then corrected for atomic number (Z), absorption (A), and fluorescence (F) effects to yield an independent aluminum and indium concentration for each position analyzed along the diffusion couple. The concentration-position relationships evaluated in the manner described above were used to determine the interdiffusion coefficients, D by the computer methods discussed below.

Computation of Interdiffusion Coefficients. A numerical procedure was constructed with which to determine the interdiffusion coefficients for liquid aluminum-indium alloys from the measured composition-distance data. A basic assumption of the analysis is that the spatial and time dependence of the concentration can be described by a solution of the one-dimensional, time-dependent diffusion equation, using an "effective" concentration-independent diffusion coefficient, and subject to the approximate initial and boundary conditions (see Equations 1 through 3). Since the experimental data were taken from solidified Al-In metal, account had to be taken of a number of factors, including shrinkage of the alumina container and net volume decrease of the Al-In liquid alloy upon cooling and solidification. An outline, in which the algorithm is summarized, is presented below.

Preliminary Steps.

A. Choose values for pertinent input parameters.
B. Choose an array of diffusion coefficients, relatively widely spaced, within which the "true" value is certain to be.
C. Read in experimental data for the weight-fraction of aluminum as a function of distance along the diffusion couple and the diffusion time. Convert the aluminum weight-fraction to indium weight fraction.

D. Compute the density of pure liquid aluminum and of pure liquid indium as well as the number of atoms per cubic centimeter in pure liquid indium, all corresponding to the temperature at which the diffusion experiment was performed.

E. Consider the liquid-metal system, which is shaped as a circular cylinder by the surrounding alumina crucible, to be divided (in a mathematical sense) into N "slices" (with N taken to be 100 in these computations), by "cutting" the cylindrical system along equally spaced planes perpendicular to the cylinder axis. This subdivision is assumed to represent the liquid metal at the diffusion temperature.

Computations.

A. Compute the thermal contraction upon cooling, of the inner cross-sectional area of the alumina cylinder, within which the liquid metal is contained.

B. For a given value of D and the diffusion time used in the experiment, compute the indium concentration at the center of each slice (assuming high-temperature conditions) using the solut of the diffusion equation (Equation 3).

It should be noted that the Barrer solution[8] involves evaluation of an infinite series; we retain up to some specified number (100) of terms in this series, but terminate the series before this point if the magnitude of the individual terms becomes very small.

C. Convert the concentration of indium calculated at the center of each slice to weight-fraction indium. This conversion not only makes the units of indium concentration the same as those for the experimental

data, but it also makes the calculated indium content of the slice invariant to the volume change undergone by the slice during cooling.

D. Compute the new thickness of each slice which exists after cooling from the test temperature (970 C) to room temperature.

1. Include the contribution due to contraction of alumina container.
2. Include also the volume contraction of the metal within each slice, calculated by simply summing the contractions that the constituent aluminum and indium would have undergone in the pure state. Assume that the net volume change of each slice is unaffected by interactions with any adjacent material (their slices or the container).
3. Note: the slices do not, in general, all have the same thickness after cooling, since the relative amounts of aluminum and indium that each slice contains varies from slice to slice.

E. Carry out a statistical analysis of the data.

1. Compute the sum of squares of the deviations of all values of indium concentration, measured on solidified material at room temperature, from the corresponding calculated indium concentrations. Each calculated value is obtained at the same spatial location as the corresponding data point. Each calculated value is determined by linear interpolation of values computed at midpoints of adjacent slices (with shrinkage due to cooling accounted for) such that spatial coordinate of the corresponding data point lies within the range of distance defined by these two midpoints.

2. Note: only data points lying within the spatial range from the midpoint of the first slice to the midpoint of the last slice are included in the analysis.

F. Repeat the previous computations for all diffusion coefficients in the "coarse" array chosen under B of "Preliminary Steps" described above.

G. From the results, determine the interdiffusion coefficient, D min, in the "coarse" array for which the calculated sum of square of deviations has the smallest value, and hence which constitutes the best estimate, obtained thus far at least, of the "true" diffusion coefficient.

H. Choose a more "finely" spaced array of diffusion coefficients about the value D_{min}

I. Repeat the previous computation with the "fine" array of diffusion coefficients. In this manner, a more refined estimate of D_{min}, and hence of the "true" interdiffusion coefficient, is obtained.

Graphics Programming.

A. Carry out all procedures necessary to plot the experimental data as well as the theoretical concentration curve corresponding to the refined estimate of D_{min}.

Results. As described earlier, difficulties have been encountered in obtaining accurate values of the interdiffusion coefficient in liquid Al-In alloys above the miscibility gap (970 C). These impediments can be delineated as follows:

(1) Difficulties in the metallographic preparation of the diffusion couples (Samples 6 and 7)

(2) Less than optimum selection of the parameters used in the electron microbeam probe analysis (Samples 6 and 7)

(3) Problems associated with gas-bubble formation in the capillaries. Static bubbles would be expected to affect mass transfer in the liquid whereas moving bubbles may cause fluid flows and a disturbance of the diffusion induced concentration gradients (Samples 8 and 9). The formation of gas bubbles may be due to improper out-gassing of the capillary tubes.

Four diffusion couples, Samples 6, 7, 8, and 9 were subjected to electron microprobe analysis including the MAGIC corrections. The results from Samples 8 and 9 appear to be reasonably self consistent in terms of the independent determinations of aluminum and indium concentrations. However, the results from Samples 6 and 7 were very inconsistent presumably due to the combination of the poor metallographic polish and the less than optimum selection of electron probe parameters. Further diffusion analysis of these latter specimens does not appear to be warranted at this time.

Through use of the computer code described above, the concentration-position data from Samples 8 and 9 were compared with the theoretical diffusion relations corrected for solidification shrinkage and thermal contraction and the value of D providing the best fit with the data was determined for each couple. These values are summarized in Table 8, and the experimental data points are compared with the "best fit" theoretical curves in Figures 14 and 15 for Samples 8 and 9 respectively.

In an independent study with a similar objective, Dr. Lewis Lacy of MSFC[15] has conducted in situ diffusion experiments by an X-radiographic technique on samples in the SPAR configuration. His observations on the interdiffusion of aluminum and indium in the weight proportion 30:70 at 920 C indicated a concentration difference between the top and bottom of the sample amounting to 10 atomic percent after 1.4 hours and 6 atomic percent after 2.2 hours. Calculations of the interdiffusion coefficients have been made based on these observations and on the assumption that compositional differences correspond to concentrations at the extreme top and bottom of the alloy.

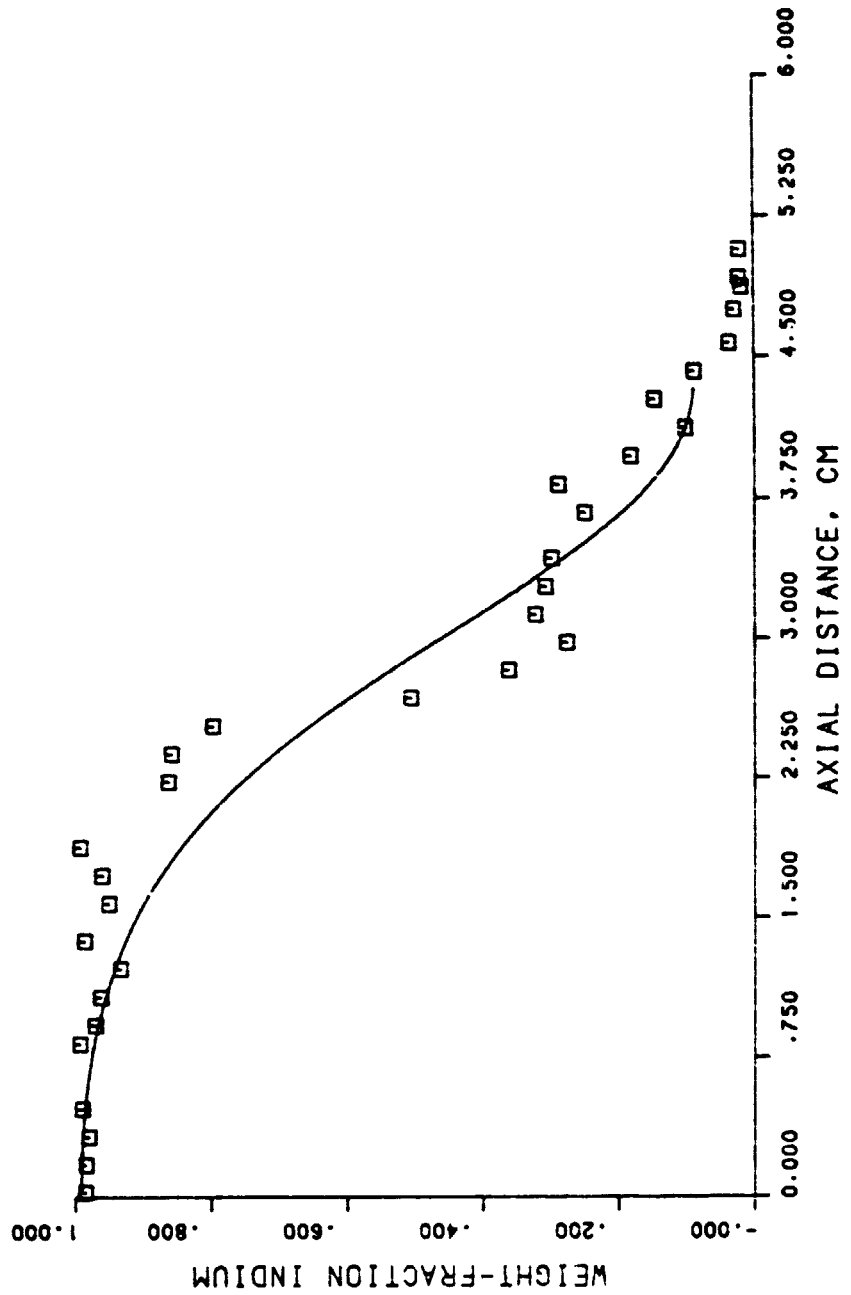

FIGURE 14. BEST LEAST SQUARE FIT OF THEORETICAL CONCENTRATION-DISTANCE CURVES WITH EXPERIMENTAL MEASUREMENTS.

Sample No. 8 - 1 hr at 970 C, D = 1.8×10^{-4} Cm^2/sec.

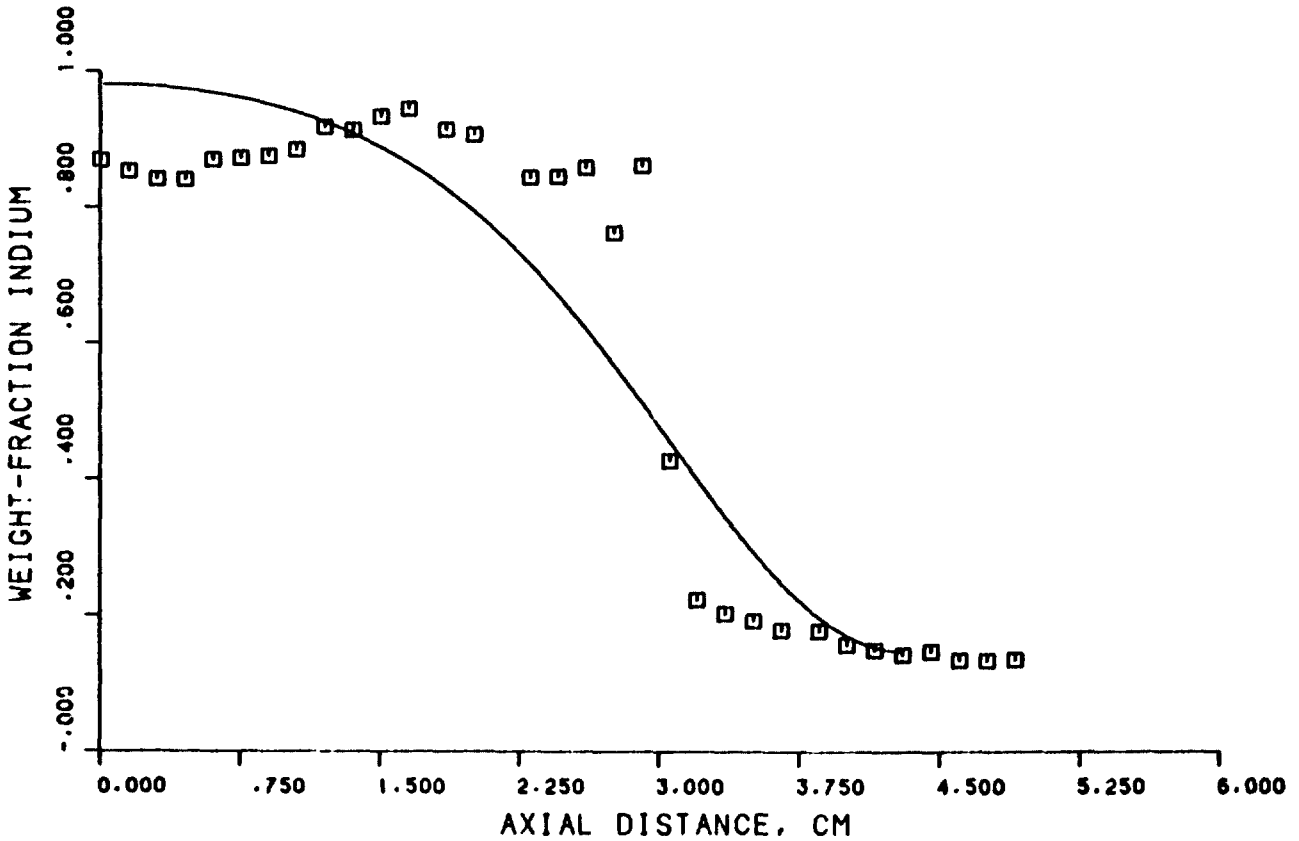

FIGURE 15. BEST LEAST SQUARE FIT OF THEORETICAL CONCENTRATION - DISTANCE CURVES WITH EXPERIMENTAL MEASUREMENTS

Sample No. 9 - 4 hrs at 970 C, D = 5.8×10^{-5} $cm^2/sec.$

TABLE 8. SUMMARY OF LEAST SQUARE DETERMINATION OF INTERDIFFUSION COEFFICIENTS

Sample No.	Diffusion Temp, C	Diffusion Time, Hour	D, cm^2/sec
8	970	1	1.8×10^{-4}
9	970	4	5.8×10^{-5}

Application of the solution of Fick's diffusion relations for the applicable boundary conditions (see Equation 3) provided a relationship between the concentration difference, ΔC, at the sample extremes and Dt. Table 9 lists the results of these calculations.

TABLE 9. CALCULATED DIFFUSION COEFFICIENT AS A FUNCTION OF COMPOSITIONAL DIFFERENCES AT THE SPECIMEN EXTREMES (a)

ΔC, Atomic percent	t, second	Dt, cm^2	D, $cm^2/second$
10.5	5040	0.25	5.0×10^{-5}
6	7920	0.30	3.8×10^{-5}

(a) SPAR configuration. Overall composition Al-70 weight percent In. Diffusion temperature 920 C.

Discussion and Conclusions. The technique utilized to evaluate diffusion in liquid Al-In alloys above the miscibility gap, in spite of the experimental difficulties which are expected t be eased with further development, has great potential as an experimental tool for characterizing liquid metal systems and their solid alloys. Two obvious attractions are as follows.

(1) The method allows the interdiffusion coefficient and its compositional variation to be determined by the same method (Matano-Boltzmann) as commonly used to characterize interdiffusion in the solid state.

(2) The technique produces a continuous series of rapidly cooled alloys whose microstructures can be related to composition. The method could also be applied to liquid phase miscibility gap systems cooled at slower rates but the processing would have to be conducted at low gravity to avoid segregation effects due to buoyancy.

An example of the metallographic potential of the technique is found in Figure 16, where the microstructure of a portion of Sample 7 is displayed. The photomicrograph shows that the separation process occurs extremely rapidly in this system as evidenced by the presence of well-developed droplets especially in the region of the critical composition. What is more, Figure 16a also shows a curious effect. In this low magnification photomicrograph, the size of the precipitating aluminum-rich droplets appears to vary in an almost continuous manner with composition. This effect will be discussed further in a later section dealing with interpretation of the SPAR V results.

The difficulties encountered with this method of determining the interdiffusion characteristics of liquids (electron probe analysis method, metallographic polishing technique, presence of gas bubbles) have largely been eliminated except for the presence of gas bubbles. These bubbles can probably be eliminated by outgassing the capillary tubes at high temperature and in high vacuum prior to filling. (The capillaries in the experiments to date have been baked in air rather than vacuum prior to the diffusion experiments.)

Two additional factors contributing to the uncertainty in the diffusion results to date are as follows:

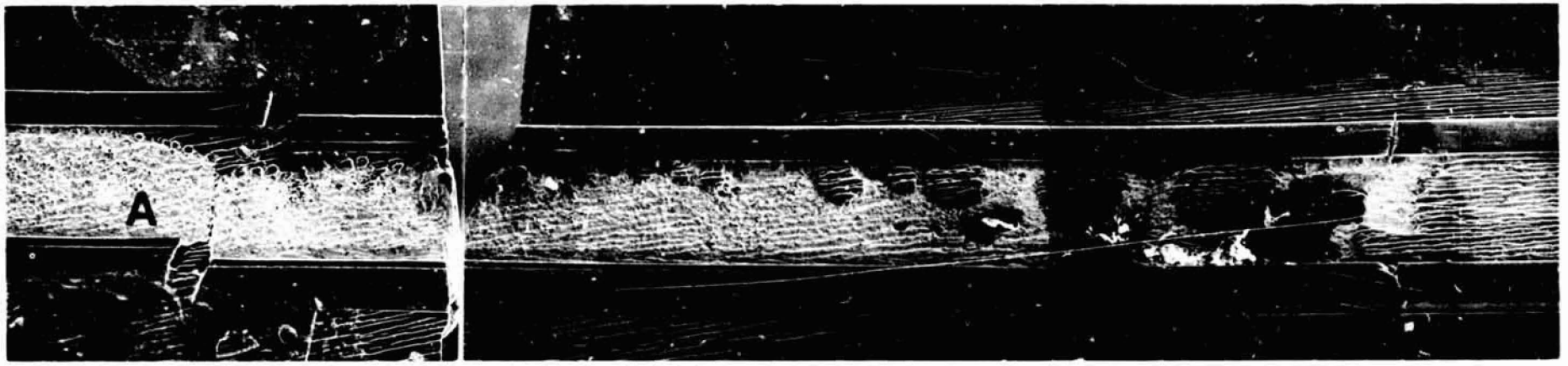

)

20X

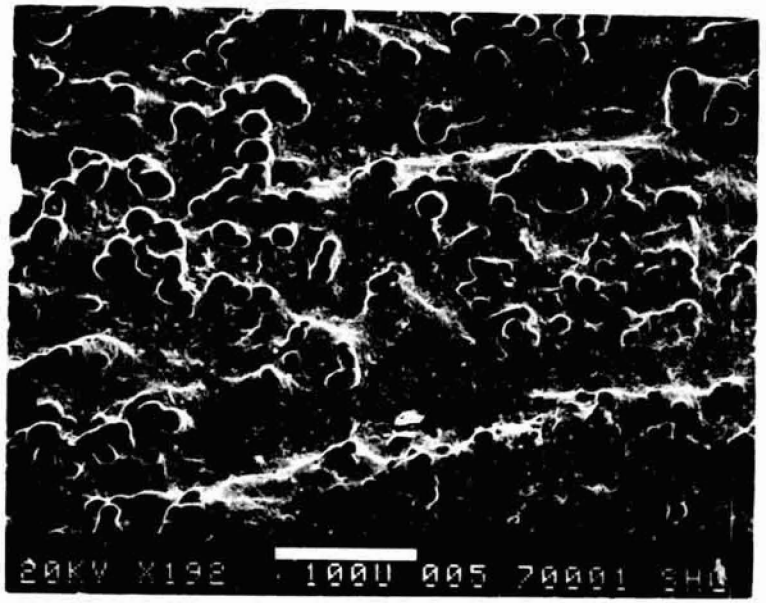

(b)

FIGURE 16. SEM PHOTOGRAPHS OF A PORTION OF SAMPLE 7, HEAT TREATED 4 HRS AT 970 C AND QUENCHED

(a) Macroview at 20X showing variation in size of aluminum-rich spheres, (b) higher magnification view of Area A in (a) showing finer Al-rich spheres.

(1) Diffusion occurring during the period of heating to the diffusion temperature

(2) The partial sinking of the solid aluminum wire into the molten indium at temperatures 155 C < T < 660 C.

Both of these factors lead to a deviation from the boundary conditions assumed in the solution of Fick's diffusion equation (Equations 1 and 2).

With regard to the diffusion occurring during the heat-up period, an estimate can be made for the contribution from this source by calculating a time-average interdiffusion coefficient that can be assigned to the period of heat-up from the monotectic temperature (640 C) to the desired diffusion temperature (970 C). This calculation assumes a value of 4.0 kCal/mole[16] for ΔH, the activation enthalpy which appears in the usual formulation describing the temperature dependence of interdiffusion coefficient:

$$D = D_o \exp [-\Delta H/RT] \qquad \text{Equation 4}$$

where

D_o is a constant
R is the gas constant
and T is the temperature in °K ;

and ignores the change in boundary conditions that occur in this temperature regime.

The temporal variation of temperature during the ∿ 38-minute heat-up period has been approximated by an analytical expression which closely fits the observed variation:

$$T = 913 + 427 \exp \{-9.82/t\} \qquad \text{Equation 5}$$

where

T is the temperature in °K
and t is the time in minutes

By combining Equations 4 and 5, an expression is obtained for the average value of the interdiffusion coefficient during heating.

$$\bar{D} = \frac{D_o}{t_H}\int_o^{t_h} \exp\{-4000/[(R)(913 + 427 \exp(-9.82/t)]\}\, dt \quad \text{Equation 6}$$

where

t_H is the heat-up time in minutes.

By numerical integration, it is then found that

$$\bar{D} = 0.179\ D_o\ , \quad \text{Equation 7}$$

The corrected value of interdiffusion coefficients, D_c at 970 C is then found by applying the following relationship:

$$D_{LSF}t_D = \bar{D}t_H + D_c t_D \quad \text{Equation 8}$$

where D_{LSF} is the least square fit value of interdiffusion coefficient calculated from the computer codes previously described and t_D is the diffusion time at 970 C.

The values of D_c are compared with the respective values of D_{LSF} in Table 10 and show the corrections accounting for diffusion during heat-up are small and certainly do not account for the major difference between the measurements.

TABLE 10. COMPARISON OF CORRECTED AND LEAST SQUARE FIT DIFFUSION COEFFICIENTS

Sample Number	Diffusion Temp, °C	Time at Diffusion Temp	D_{LSF} cm^2/sec	D_c cm^2/sec
8	970	1	1.8×10^{-4}	1.0×10^{-4}
9	970	4	5.6×10^{-5}	5.1×10^{-5}

The change in boundary conditions due to the partial sinking of the solid aluminum into the molten indium during the heat-up period at temperatures between 155 C and 640 C are probably rather small and due largely to the dissolution of the solid aluminum in the molten indium. It is anticipated that when the aluminum melts, a redistribution of the liquid phases will take place which will tend to restore the original boundary conditions. It is not clear whether any of the diffusion couples that have been run have actually encountered this problem. It would be rather easy for the solid aluminum wire to be held from moving down the capillary by friction. We intend to avoid this experimental complication in the future by crimping the aluminum wire to prevent its moving until it is molten.

Based on these preliminary measurements and those of Lacy corrected to 970 C, our best estimate of the interdiffusion coefficient in liquid Al-In alloys at 970 C is $6.4 \pm 3.1 \times 10^{-5} cm^2/second$. This value agrees quite well with the $8 \times 10^{-5} cm^2/second$ value which has been found to be consistent with the DTA measurements. The value of Dt = 0.5 calculated as necessary to homogenize the SPAR alloys (see Table 5) allows us to calculate a value of the necessary homogenization time as 2.2 hours.

These diffusion measurements indicate that the SPAR II alloys were not homogenized sufficiently assuming that there are no other processes involved except diffusion.

It is recommended that additional work be conducted to perfect this technique which is well on its way toward full development. An improved method should allow more precise determination of the diffusion coefficient and allow the variation of D with composition to be characterized.

SPAR V Flight Experiment 74-30

Objective

The realization that the experimental alloys processed on SPAR II may not have been completely homogenized at the start of the cool-down period and that this factor might have lead to the massive separation

observed on SPAR II prompted the decision to repeat the SPAR II experiment but with a longer hold time at the 970 C homogenization temperature. A hold time of 16 hours was chosen providing a safety factor of approximately 7. The large safety factor was selected in light of some uncertainty in the value of the interdiffusion coefficient in the liquid Al-In alloys.

The specific objective of the SPAR V experiment was to determine whether the concentration gradients probably present in the SPAR II samples at cool-down were the cause of the observed massive separation. A secondary objective which developed as a result of an opportunity to fly an additional two alloys was to determine whether alloy compositions in addition to those flown on SPAR II would also show the massive separation. One of the alloys had a high indium content and was also chosen in order to determine whether there is a tendency during cool-down for the precipitating phase (in this case aluminum) to separate preferentially at the crucible walls.

Alloy Composition

Four Al-In alloy compositions, 30, 40, 70, and 90 weight percent In were chosen for the SPAR V experiment. The 40 and 70 weight percent In alloys were the same compositions as processed in SPAR II. The 30 weight percent In alloy was chosen to determine the effect of a smaller concentration of indium droplets on the tendency toward massive separation. The 90 weight percent In alloy was selected for two reasons.

(1) This alloy should also produce a low concentration of precipitating phase and, in this respect, was chosen for the same reasons as the 30 weight percent In alloy.

(2) Aluminum droplets are expected to be the precipitating phase within the miscibility gap of this alloy. It is of interest to determine whether aluminum tends to precipitate preferentially at the crucible walls in a manner analagous to the precipitation of indium in the high aluminum concentration alloys.

Cartridge Design and Fabrication

The cartridges containing the components for the 40 and 70 weight percent In alloys were of the same design as used in the SPAR II flight and were fabricated in the same manner (see Figure 2). The capsules containing the components for the 30 and 90 weight percent In alloys were of similar design; the only changes being that no provision was made for an internal thermocouple to monitor the sample temperature and the aluminum components were fabricated from a different lot of 99.999 percent pure aluminum. The former change was prompted by a lack of capacity to accomodate another thermocouple whereas the latter change was due to the depletion of the original lot of aluminum. It was not expected that these changes would impact the experiment significantly. The cartridge containing the 30 and 90 weight percent In alloys had the 90 weight percent alloy positioned at the bottom of the cartridge (see Figure 17). In all cases, the indium components were positioned above the aluminum.

The fabrication of the cartridges containing these alloys was performed in the same manner as the SPAR II capsule [6,7] with the exception that the capsules without internal thermocouples did not undergo the brazing operation. A listing of the component weights for the flight and ground-samples is presented in Table 11.

Samples Processing

Flight Samples 74-30-36 containing the 40 and 70 weight percent In alloys and 74-30-48 containing the 30 and 90 weight percent In alloys were processed on September 11, 1978, aboard SPAR V. Capsule 74-30-36 was equipped with a thermocouple designed to measure the internal temperature of the 40 weight percent In alloy. Unfortunately, the thermocouple failed by fracturing at the base of the cartridge during preparation for the flight. As noted above, capsule 74-30-48 did not contain an internal thermocouple. Although the information obtainable from the internal thermocouple is of great value, a reasonable estimate of the thermal history of each of the cartridges is available based on the

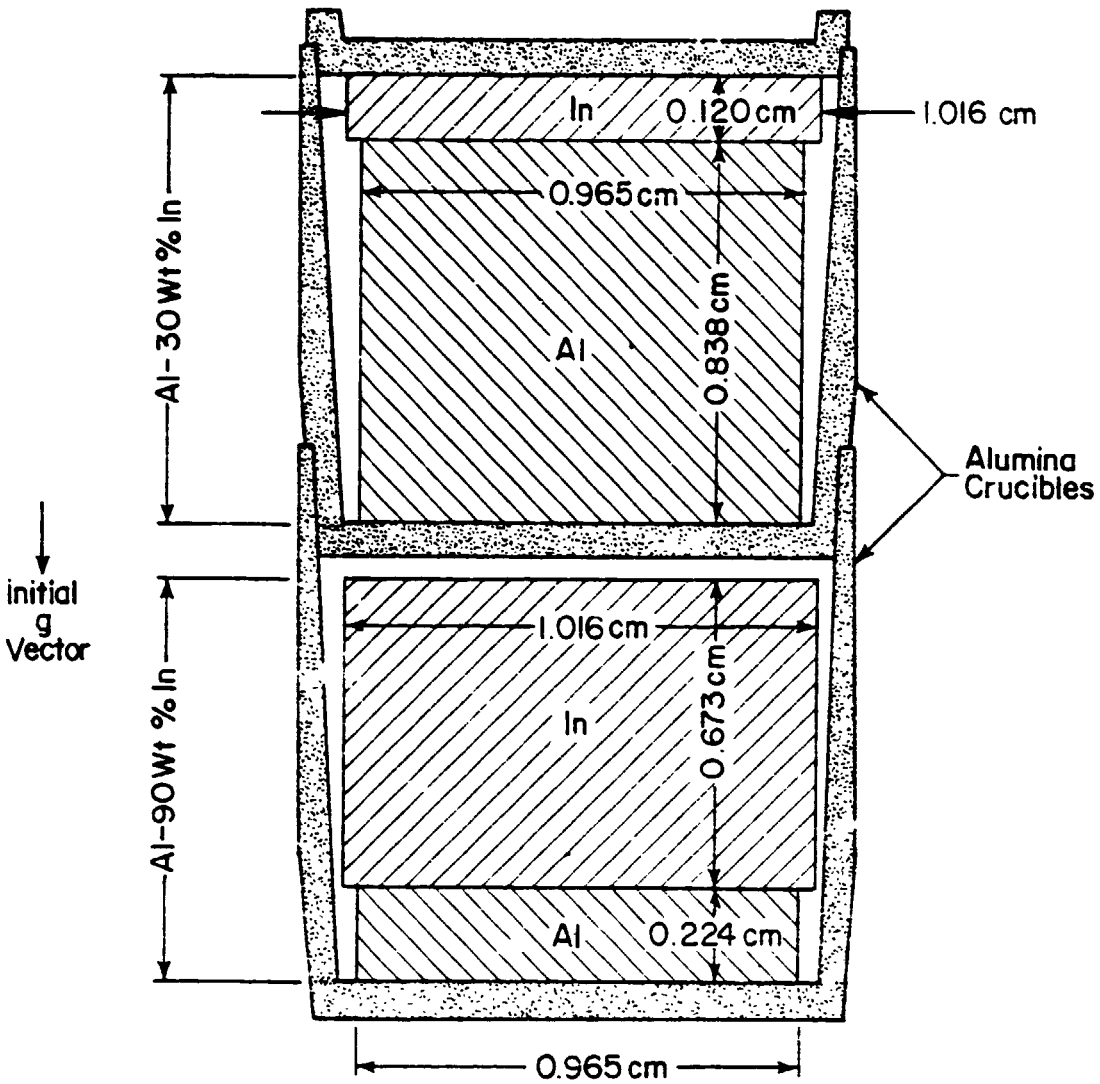

FIGURE 17. SCHEMATIC DIAGRAM SHOWING THE LAYOUT OF ALLOY COMPONENTS FOR Al-30 AND -90 WEIGHT PERCENT In ALLOYS FOR SPAR V EXPERIMENT CARTRIDGE (See Figure 2)

TABLE 11. WEIGHT AND COMPOSITION DATA FOR SPAR V FLIGHT AND GROUND BASE CARTRIDGES

Cartridge Number	Bottom Alloy			Top Alloy		
	Component Wt., gms		Composition	Component Wt., gms		Composition
	Al	In	Wt. Pct. In	Al	In	Wt. Pct. In
74-30-27GB	1.4234	0.9496	40.02	1.0083	2.3546	70.02
74-30-29GB	1.4264	0.9504	39.99	1.0078	2.3484	69.97
74-30-36FLT	1.4159	0.9439	40.00	0.9700	2.2635	70.00
74-30-38GB	1.3648	0.9104	40.01	0.9770	2.2805	70.01
74-30-48FLT	0.4024	3.6194	89.99	1.6027	0.6870	30.00
74-30-49GB	0.4140	3.7252	90.00	1.6190	0.6939	30.00

data from the furnace temperature thermocouple and past flight and ground base experiments. This data is summarized in Table 12.

In the SPAR V experiments, the samples were held at a temperature of ∿ 980 C (goal temperature of 970 C) for 16 hours on the ground before the flight. The rocket was launched after this hold period while the temperature was maintained at 980 C. Approximately 84 seconds after launch, the rocket entered a period of low g ($< 1 \times 10^{-3}$) and ∿ 76 seconds later the samples were rapidly cooled. Table 13 summarizes the sequence of events from the start of the hold period on the ground until the end of the low-g period. A plot of the furnace cavity temperatures and acceleration data as a function of time is shown in Figure 18.

It should be noted from Table 12 that the cooling rates experienced during SPAR V were somewhat lower than desired (∿10 C/second vs. the goal of 14 C/second). As may be seen from Table 12 and Figure 18, this factor has lead to the likelihood that the indium-rich phase was still liquid at the end of the low-g ($<1 \times 10^{-3}$g) period.[a] Although this factor is not expected to alter the general conclusions of the study, it does introduce some uncertainty in the results. The absence of a thermocouple internal to the melt adds further to the degree of uncertainty in the results. In other respects, the processing of the flight samples proceeded as planned.

Specimen Characterization - Method and Results

The two flight samples, 74-30-36 and 74-30-48, as well as two ground control samples, 74-30-29 and 74-30-49 were characterized by radiography and metallography. In addition, ground base sample 74-30-38 which had been held for 16 hours at 970 C and cooled through the miscibility gap at a rate of 3.5 C/second was examined metallographically and provided some understanding of the effect of cooling rate on the evolution of microstructure in the 40 and 70 weight percent In alloys.

(a) This conclusion is based on the assumption that when the furnace temperature reaches 120 C, the sample has completely solidified. The relationship between furnace temperature and specimens temperature is approximate and is based on previous comparisons of the two temperatures.

TABLE 12. FLIGHT AND GROUND CONTROL SAMPLE PROCESSING CONDITIONS

	Flight Sample 74-30-36	Flight Sample 74-30-48	Ground Base Sample 74-30-29	Ground Base Sample 74-30-49
Hold Temperature, C				
Furnace	1036	1040	1061	1060
Specimen	979[a]	980[b]	982	983[b]
Hold Time, hours	16	16	16	16
Cooling Rate,[c] C/sec				
Furnace	12	13.2	15.4	12.8
Specimen	10.0[a]	10.6[b]	10.0	10.4[b]

(a) Specimen thermocouple failed. Value is estimated.

(b) Specimen did not have an internal thermocouple. Value is estimated.

(c) Average cooling rate from hold temperature to monotectic temperature.

TABLE 13. SPAR V LAUNCH COUNTDOWN

Time	Event
T - ∿ 16 hours	Specimens at hold temperature
T = 0	Launch
T + 66 Sec	Nose tip eject
T + 68 Sec	Motor despin
T + 70 Sec	Payload separation and RCS enable
T + 71 Sec	RCS enable (Back-up)
T + 84 Sec	Estimated low-g period start
T + 160 Sec	Start of cooldown
T + 329 Sec	Estimated low-g period end (10^{-3} g)
T + 352 Sec	Estimated complete solidification in 74-30-48
T + 392 Sec	Estimated complete solidification in 74-30-36

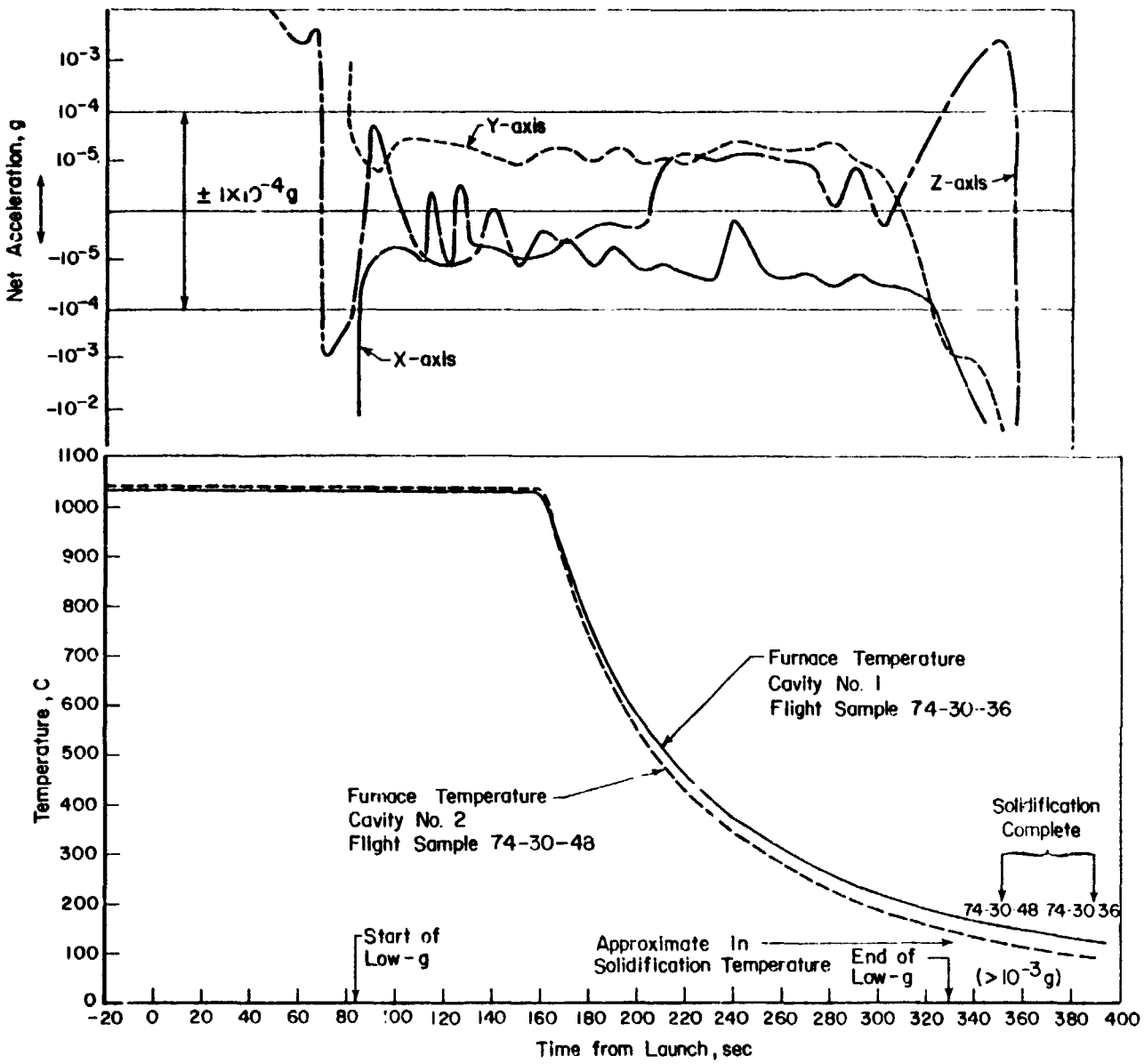

FIGURE 18. PLOT OF SPAR V ACCELEROMETER AND FURNACE CAVITY TEMPERATURE DATA VS TIME FROM LAUNCH

Radiography. Radiographs were taken of the two ground control samples and the two flight samples at kilovoltages ranging from 80 to 245 and at various sample orientations relative to the beam. The kilovoltage was varied in order to study various features of the sample. For example, 80 KV radiographs were utilized to examine the perfection of the alumina containers, whereas the higher kilovoltages were used to examine the macro-distribution of phases within the alloys. The highest kilovoltage (245 KV) was used in order to penetrate the alloy containing the highest indium content. The radiographs indicated that the samples were free of major flaws after thermal processing and demonstrated phase layering in the 1-g processed samples and massive separation in some of the flight samples. Some of the radiographs are presented in Figures 19 and 20 for the ground control and flight samples respectively.

Metallographic Examination. The two flight and two ground control samples after removal from the stainless steel container were sectioned along a longitudinal diametrical plane by first slitting the alumina crucibles with a diamond cut-off wheel and then carefully cutting through the alloys with a jeweler's saw. This technique avoids the usage of a SiC cut-off wheel and the associated problem of silicon carbide embedment in the soft alloy. After metallographic polishing, the samples were examined on both a macroscopic and microscopic level. Figures 21 through 28 show the macroviews as well as typical microstructures related to their positions in the macroview.

Aluminum-30 Weight Percent In Alloy. The macroviews and photomicrographs of this alloy processed at 1-g and in the microgravity environment are shown respectively in Figures 21 and 22. The macrograph of the 1-g processed alloy consists of a layered structure made up predominantly of the less dense aluminum-rich layer above a thin indium-rich layer. The settling of indium-rich droplets in the aluminum-rich layer is clearly observable in Figure 21 a-f. The top of this alloy is made up of an extremely fine distribution of indium droplets in the aluminum-rich matrix (Figure 21a-c) but as the interface between the aluminum-rich and indium-rich materials is approached, coarsening of the indium-rich droplets to

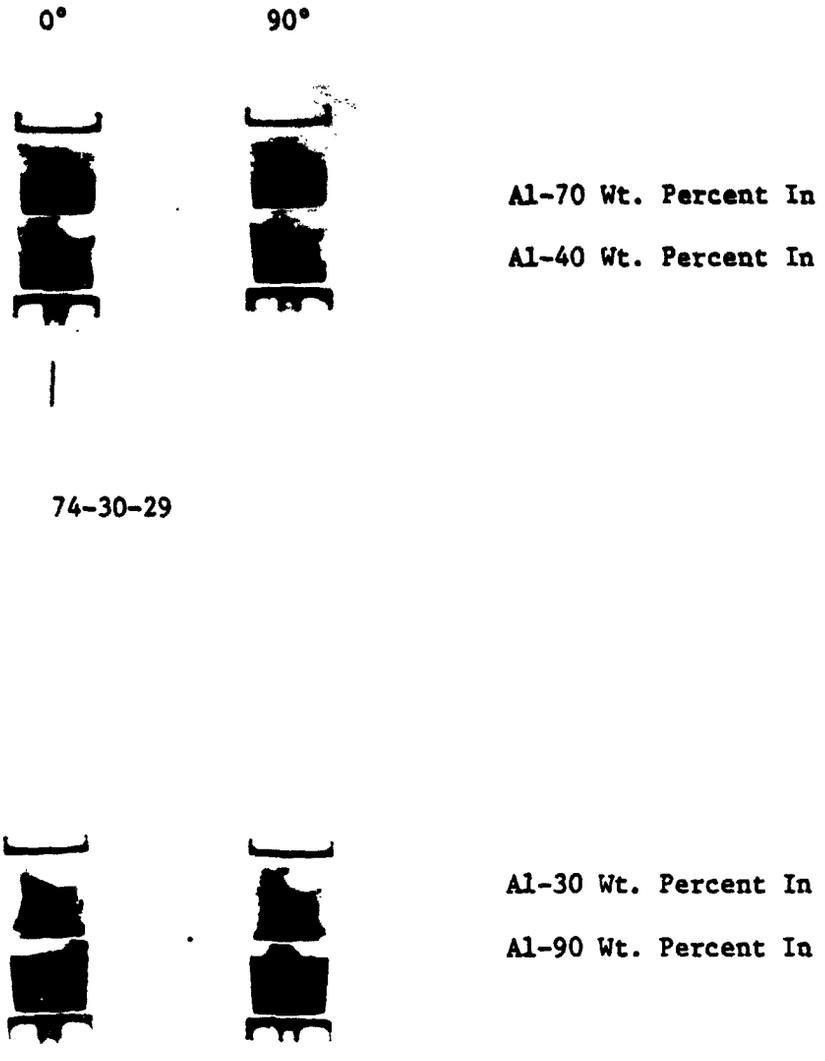

FIGURE 19. CONTACT PRINTS OF 200 KV RADIOGRAPHS OF GROUND CONTROL SAMPLES 74-30-29 AND 74-30-49

Al-70 Wt. Percent In

Al-40 Wt. Percent In

200 KV

Al-70 Wt. Percent In

245 KV

74-30-36

0° 120° 240°

Al-30 Wt. Percent In

Al-90 Wt. Percent In

200KV

Al-90 Wt. Percent In

245KV

74-30-48

FIGURE 20. CONTACT PRINTS OF RADIOGRAPHS OF FLIGHT SAMPLES 74-30-36 AND 74-30-48

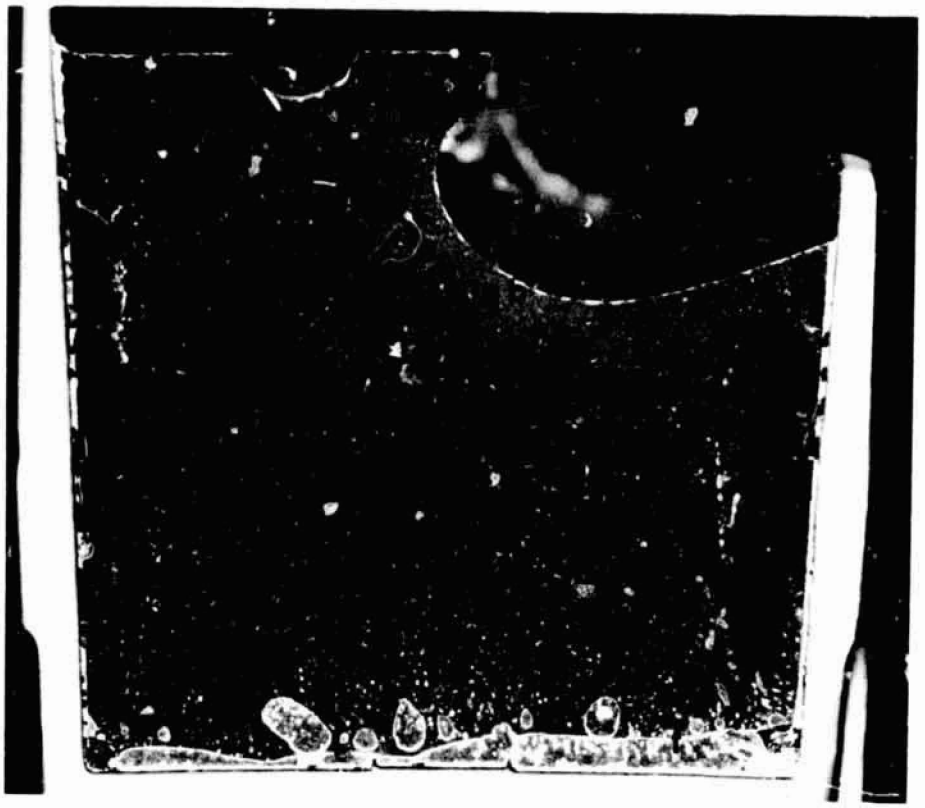

Darkfield 10X

7J664 (a) 100X 7J665 (b) 500X

FIGURE 21. MACROVIEW AND MICROSTRUCTURE OF Al-30 WEIGHT PERCENT In ALLOY FROM GROUND CONTROL CAPSULE 74-30-49

Note: Photomicrographs labelled (a) through (f) correspond to the regions similarly marked on macroview above.

7J666 (c) 100X

7J667 (d) 100X

7J669 (e) 100X

7J671 (f) 100X

FIGURE 21. (Continued)

Darkfield

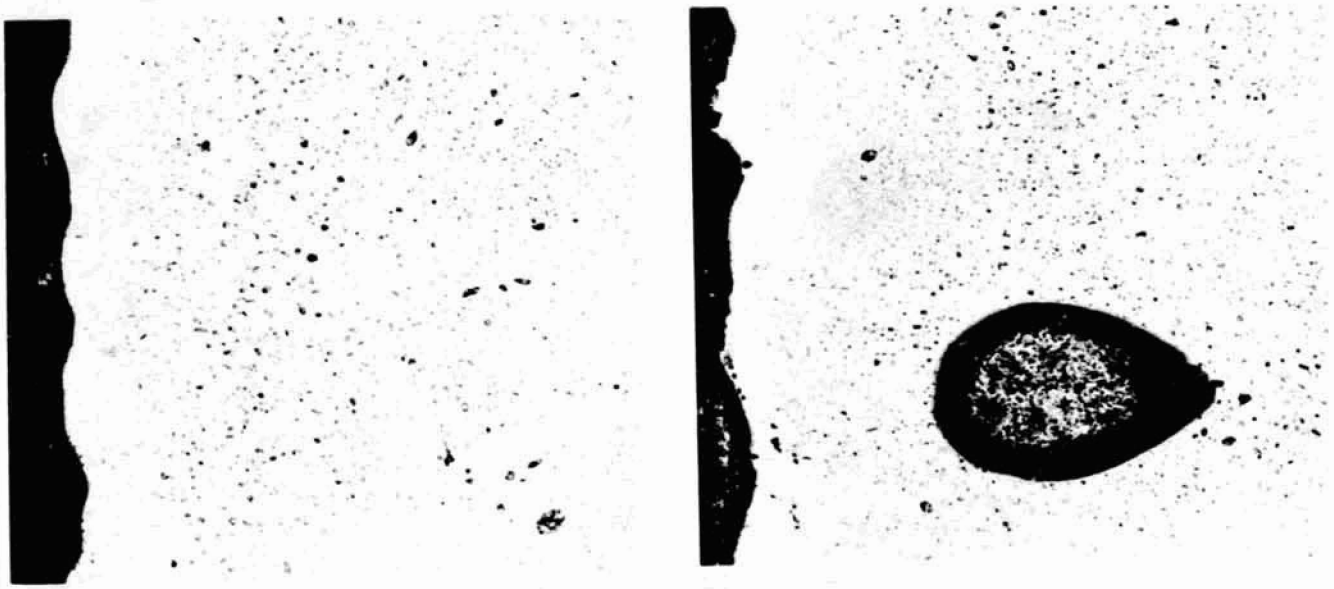

7J112 (a) 100X 7J111 (b) 100X

FIGURE 22. MACROVIEW AND MICROSTRUCTURE OF Al-30 WEIGHT PERCENT In ALLOY FROM FLIGHT SAMPLE 74-30-48

Note: Photomicrographs labelled (a) through (f) correspond to the regions similarly marked on mac· ›view above.

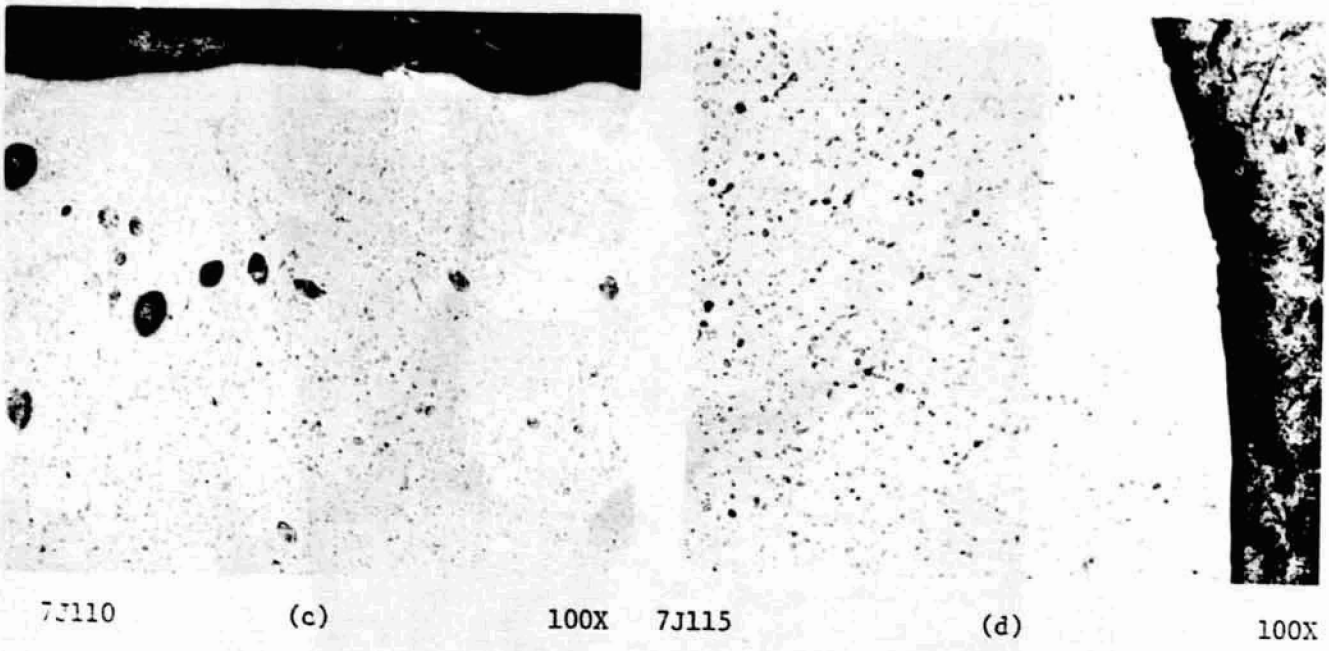

7J110 (c) 100X 7J115 (d) 100X

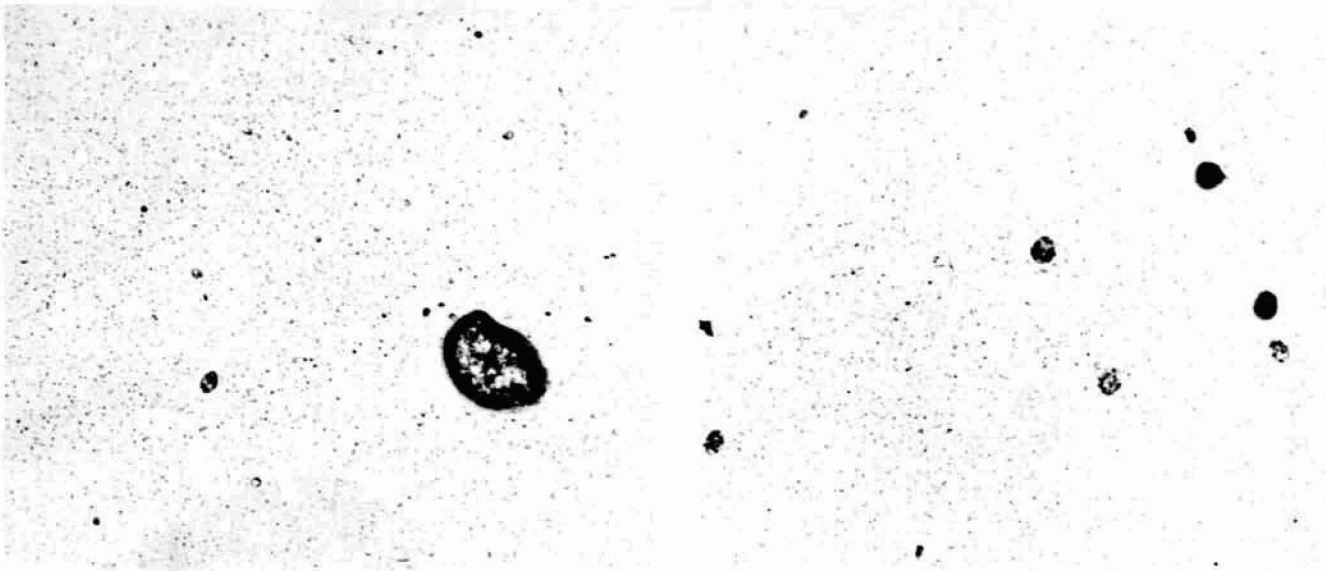

7J114 (e) 100X 7J113 (f) 100X

FIGURE 22. (continued)

sizes on the order of 1 mm is evident (Figures 21d-f). The structure of the indium-rich phase consists primarily of aluminum-rich dendrites in an indium-rich matrix. There is little evidence for the presence of aluminum-rich spheres as seen in alloys of this system with higher indium concentration.

The macroview of the 30 weight percent In flight sample shows a predominant aluminum-rich phase surounded by a very thin layer of indium-rich alloy (see Figures 22a-d). It should be noted that the interface between the aluminum-rich core and the surrounding indium-rich material is somewhat wavy. The aluminum-rich core contains in addition to a fine distribution of indium droplets, a distribution of coarse ($\leq$ 0.4 mm diameter) indium droplets which appears to be concentrated in the region extending from the upper left to the lower right of the macroview. The shrinkage cavity in the upper right portion of the macroview presumably is the last portion of the alloy to solidify because of the presence nearby of the low conductivity helium gas phase. The indium-rich phase surrounding the aluminum-rich core appears to be devoid of second phase aluminum.

Aluminum-40 Weight Percent In Alloy. The macroviews and microstructural features of the 40 weight percent In alloys processed on the ground and in the micro-gravity environment are shown respectively in Figures 23 and 24.

The macroview of the sample processed at 1-g possesses a layered structure typical of this type of alloy. The major differences between this alloy and 30 weight percent In alloy previously described are the relative thickness of the indium and aluminum-rich layers, the presence in the indium-rich layer of second phase aluminum-rich dendrites and droplets and the finer size of the indium-rich droplets settling within the aluminum-rich host.

The photomicrographs presented in Figures 23 a-d of the aluminum-rich portion of the alloy reveal a microstructure similar to that of the 30 weight percent In alloy. The photomicrographs of the indium-rich portion, Figure 23 d-f, show a relatively narrow region near the interface between the aluminum-rich and indium-rich portions of the alloy

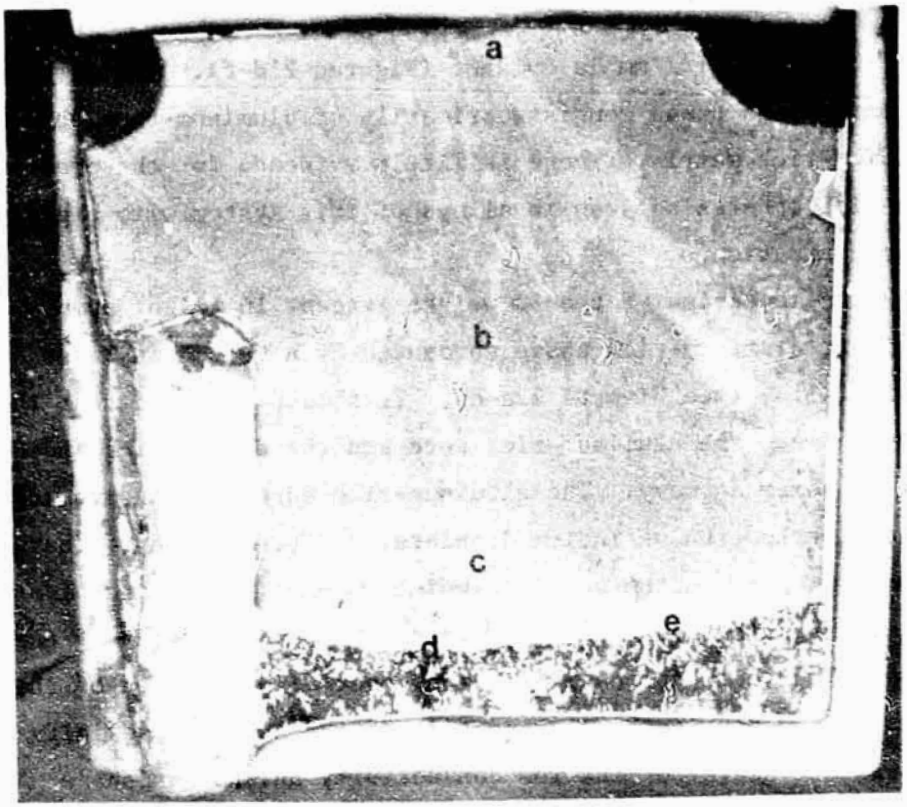

Darkfield 10X

7J657 (a) 100X 7J658 (b) 100X

FIGURE 23. MACROVIEW AND MICROSTRUCTURE OF Al-40 WEIGHT PERCENT In ALLOY FROM GROUND CONTROL CAPSULE 74-30-29

Note: Photomicrographs labelled (a) through (f) correspond to the regions similarly marked in the macroview shown at the top.

7J659 (c) 100X

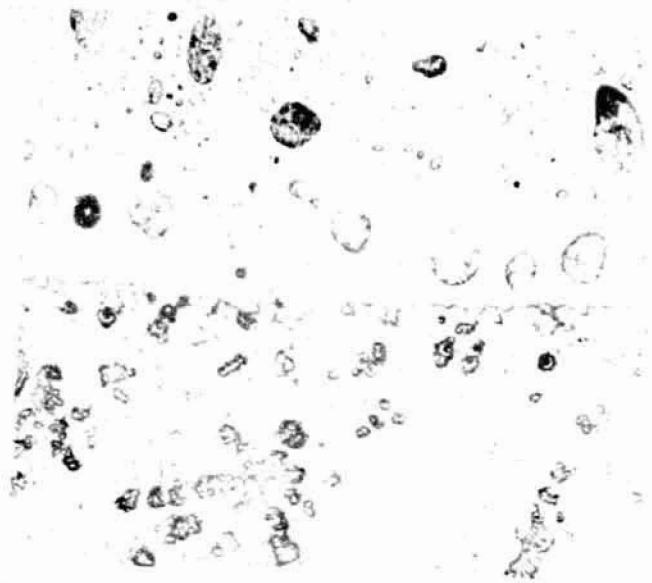

7J660 (d) 100X

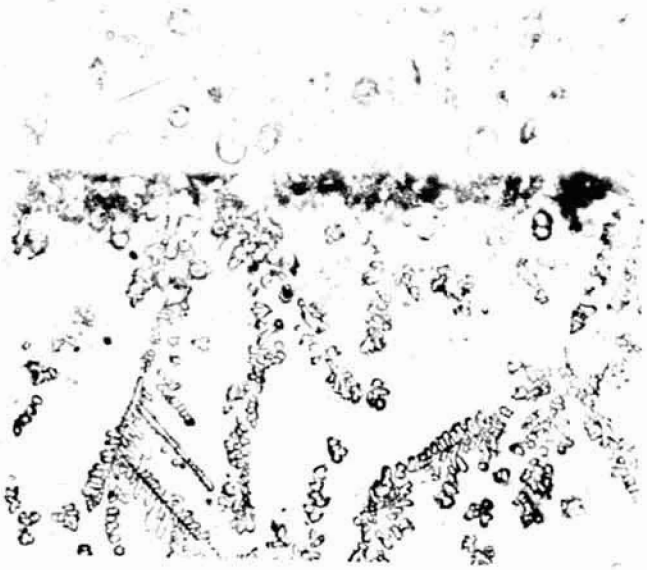

7J661 (e) 100X

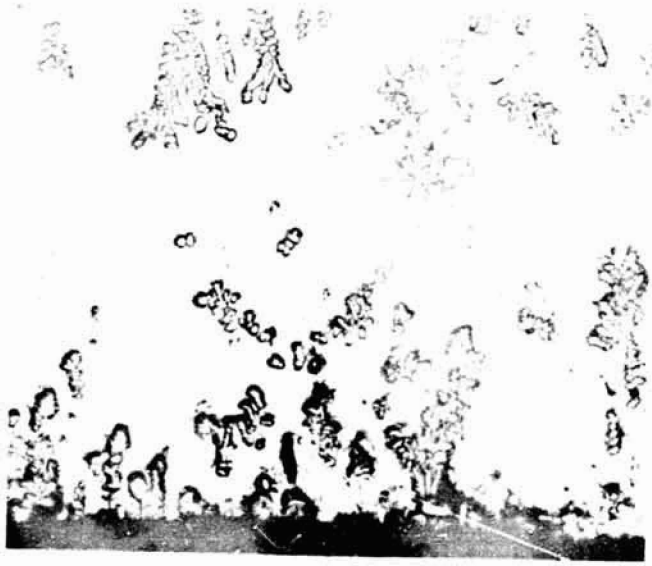

7J662 (f) 100X

FIGURE 23. (continued)

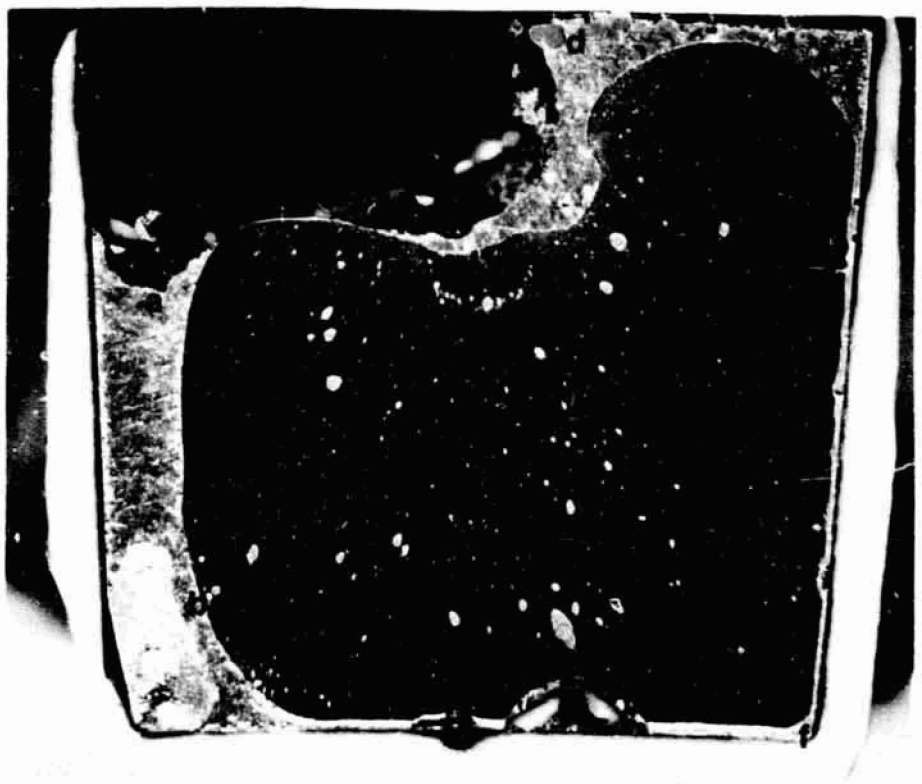

Darkfield

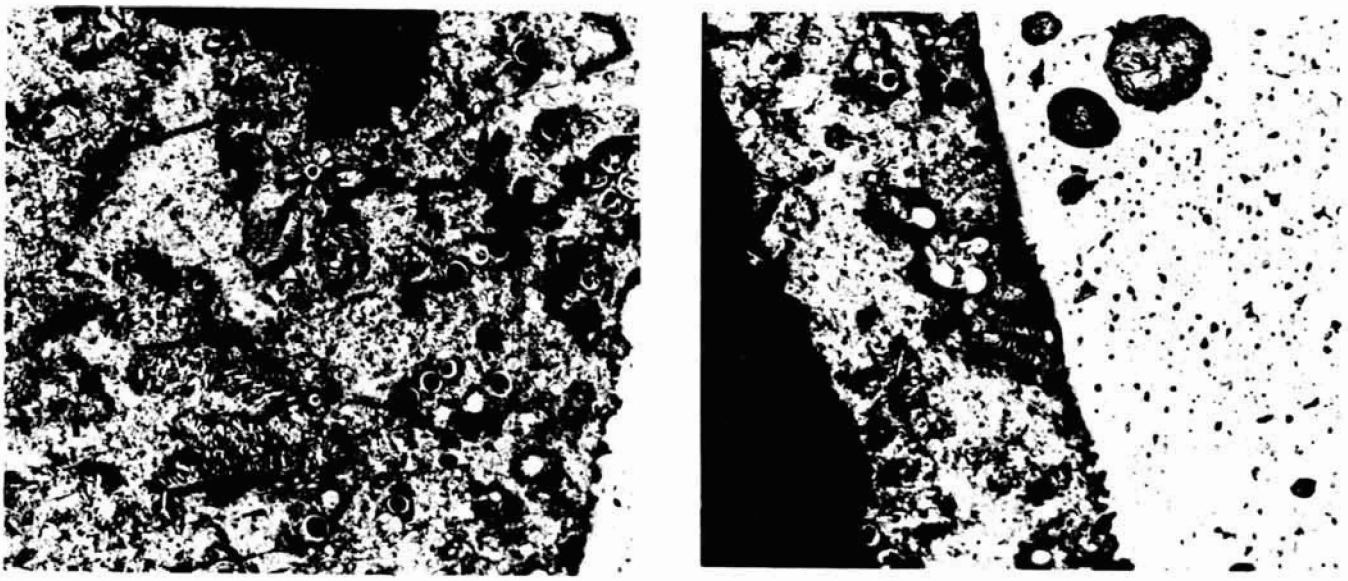

7J108 (a) 100X 7J104 (b) 100X

FIGURE 24. MACROVIEW AND MICROSTRUCTURE OF Al-40 WEIGHT PERCENT In ALLOY FROM FLIGHT SAMPLE 74-30-48

Note: Photomicrographs labelled (a) through (f) correspond to regions milarly designated in macroview above

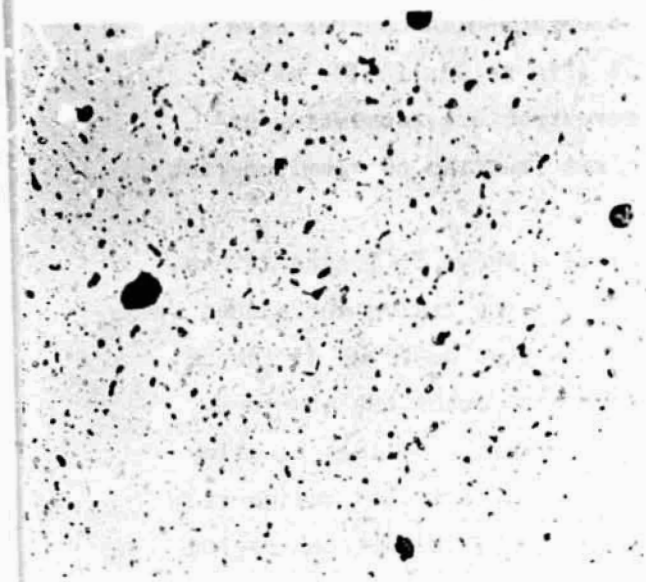

J102 (c) 100X

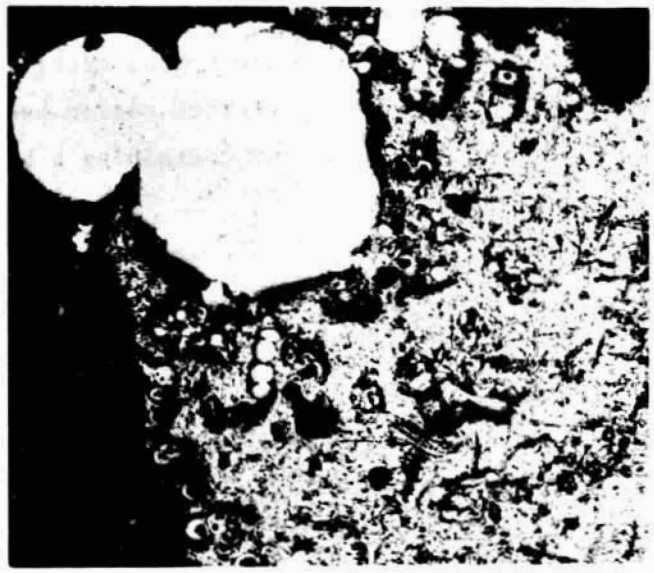

7J109 (d) 100X

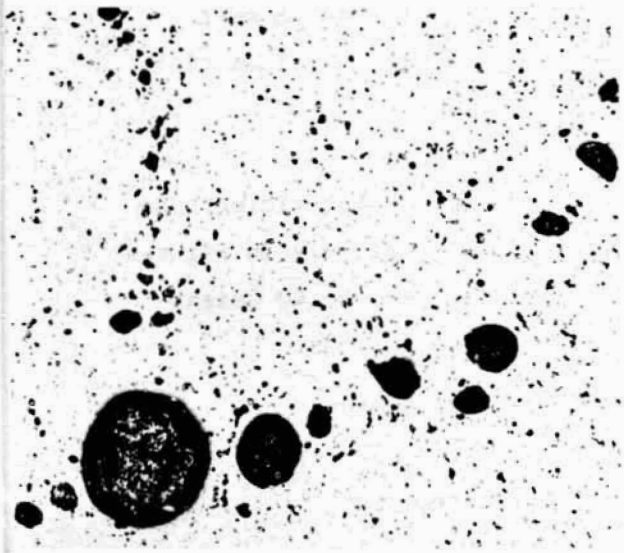

107 (e) 100X

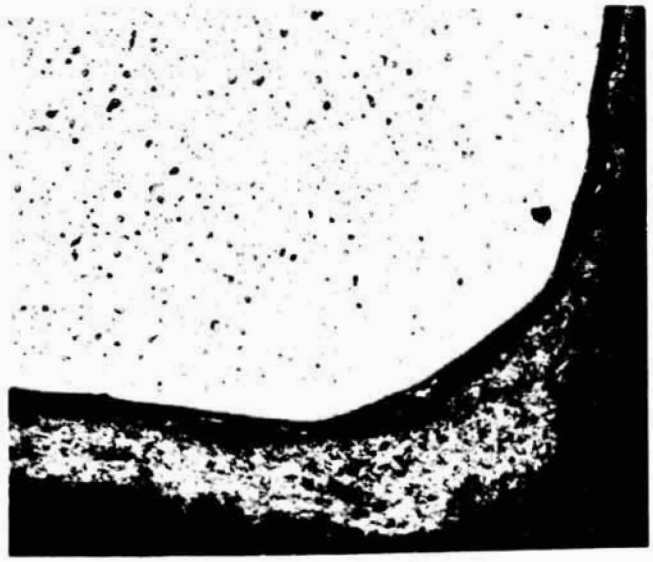

7J106 (f) 100X

FIGURE 24. (Continued)

that contain aluminum-rich spheres. Some aluminum-rich spheres have also been found at the bottom crucible wall (Figure 23f). The major portion of the indium-rich region has a microstructure consisting of an indium-rich matrix containing a high volume fraction of aluminum-rich dendrites.

The 40 weight percent In flight sample shown in Figure 24 has a macrostructure consisting of an aluminum-rich core region surrounded by an indium-rich region of much greater thickness than observed in the 30 weight percent In flight sample. The microstructures of the aluminum-rich regions are quite similar. However, the 40 weight percent In alloy appears to contain a somewhat more homogeneously distributed indium-rich phase. On the other hand, the microstructure of the indium-rich region differs significantly from its counter-part in the 30 weight percent In alloy in that aluminum-rich spheres and dendrites are present in this alloy and absent in the 30 weight percent In alloy. The aluminum-rich spheres appear to be concentrated near the aluminum-rich core in most cases. However, a region shown in Figure 24d shows larger aluminum-rich spheres surrounded by concentrations of smaller spheres.

Aluminum-70 Weight Percent In. Macroviews and photomicrographs of the ground control and flight samples are shown respectively in Figures 25 and 26. The ground control samples is very similar to the 40 weight percent In ground control sample with the following exceptions.

(1) The proportion of indium-rich to aluminum-rich material is larger.
(2) A larger number of aluminum-rich spheres are present along the interface between the indium-rich phase and alumina crucible (see Figure 25 f).
(3) A number of larger aluminum-rich spheres ($\sim$ 0.2-mm in diameter) are present at the interface between the aluminum-rich and indium-rich phases in addition to a concentration of relatively small spheres.

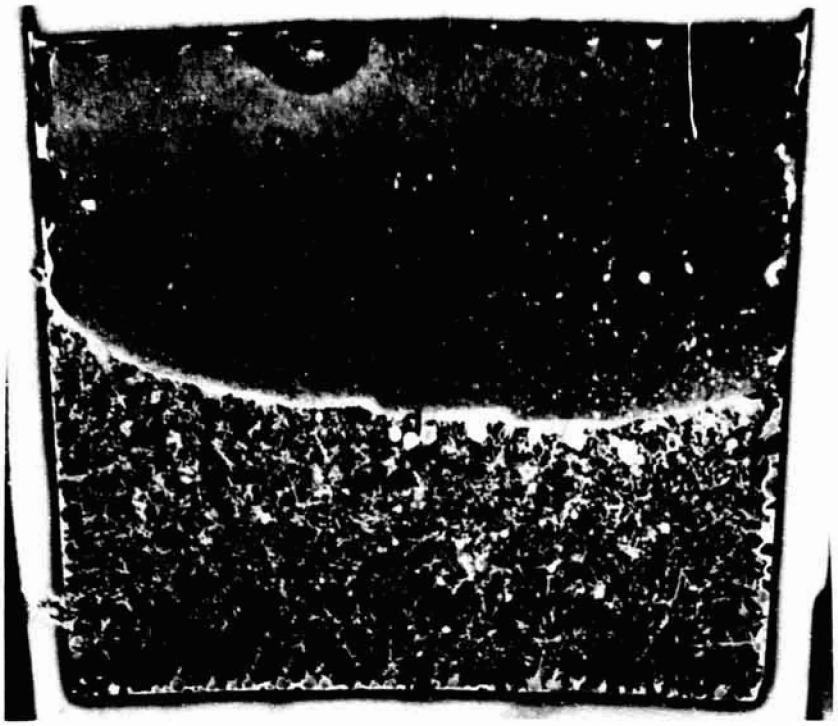

7J649 Darkfield 10X

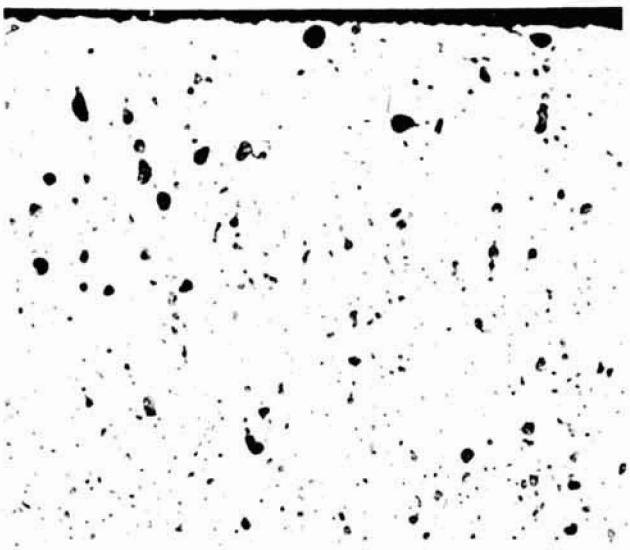

7J655 (a) 100X

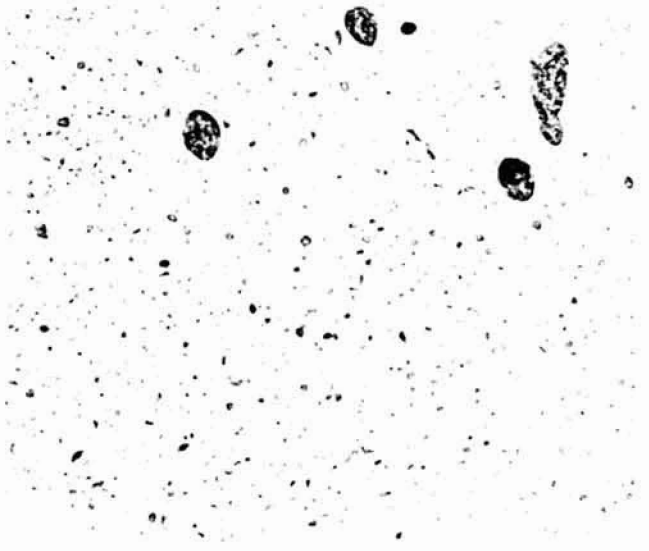

7J656 (b) 100X

FIGURE 25. MACROVIEW AND MICROSTRUCTURE OF Al-70 WEIGHT PERCENT In ALLOY FROM GROUND CONTROL CAPSULE 74-30-29

Note: Photomicrographs labelled (a) through (f) correspond to the regions similarly marked in the macroview shown at top

7J652 (c) 100X

7J654 (d) 100X

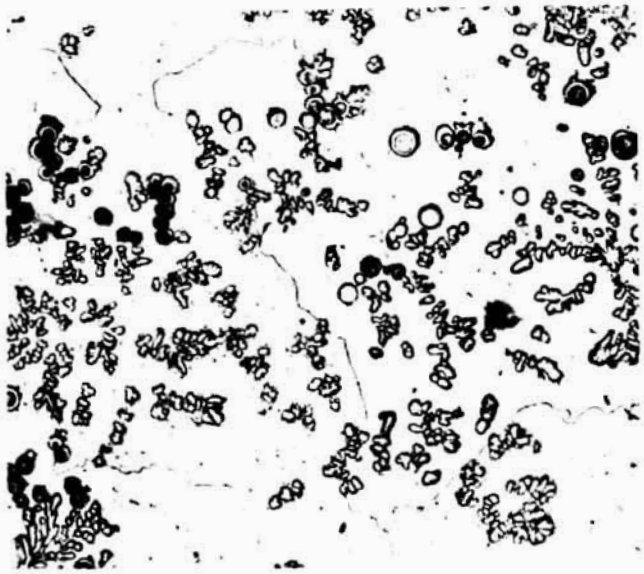

7J655 (e) 100X

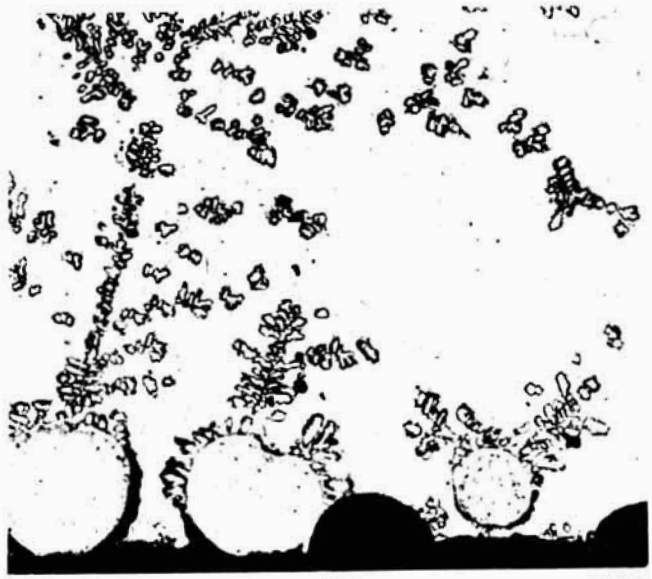

7J656 (f) 100X

FIGURE 25. (Continued)

Darkfield 10X

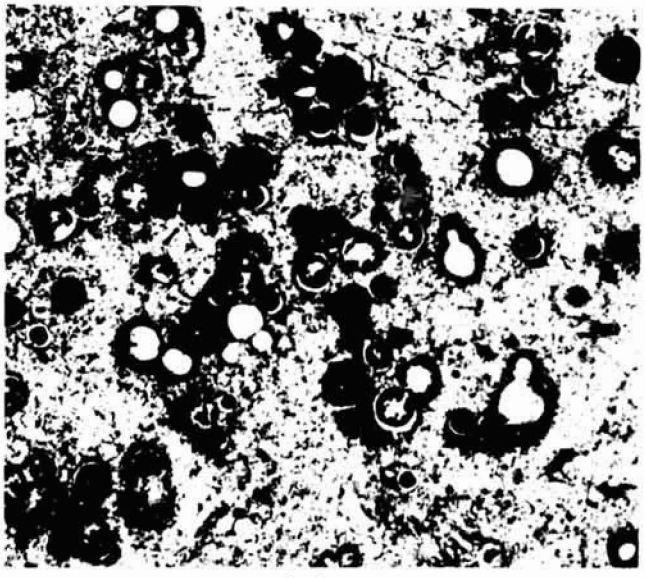

7J098 (a) 100X

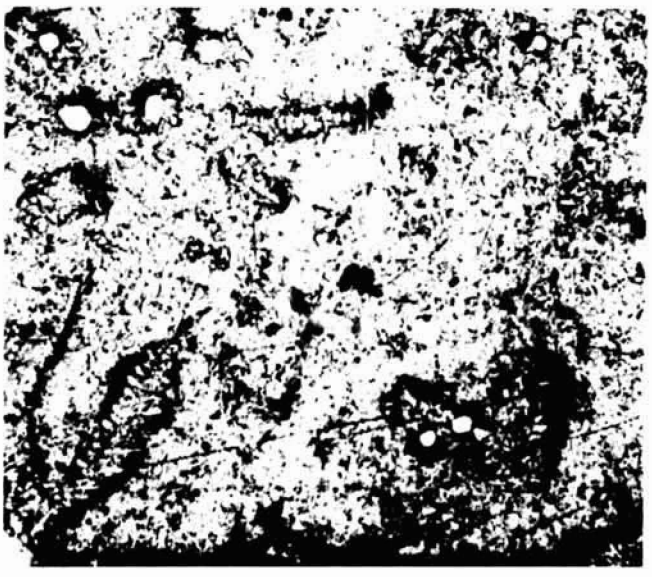

7J101 (b) 100X

FIGURE 26. MACROVIEW AND MICROSTRUCTURE OF Al-70 WEIGHT PERCENT In ALLOY FROM FLIGHT SAMPLE 74-30-36

Note: Photomicrographs labelled (a) through (f) correspond to regions similarly marked in the microviews shown at top

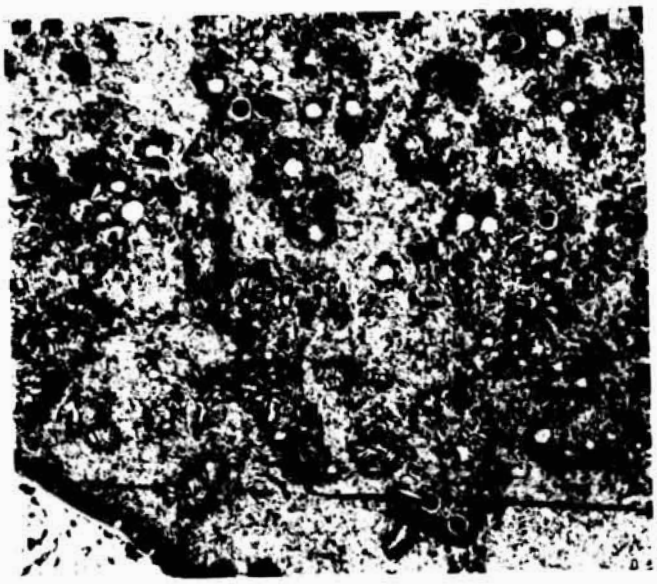

7J100 (c) 100X

7J097 (d) 100X

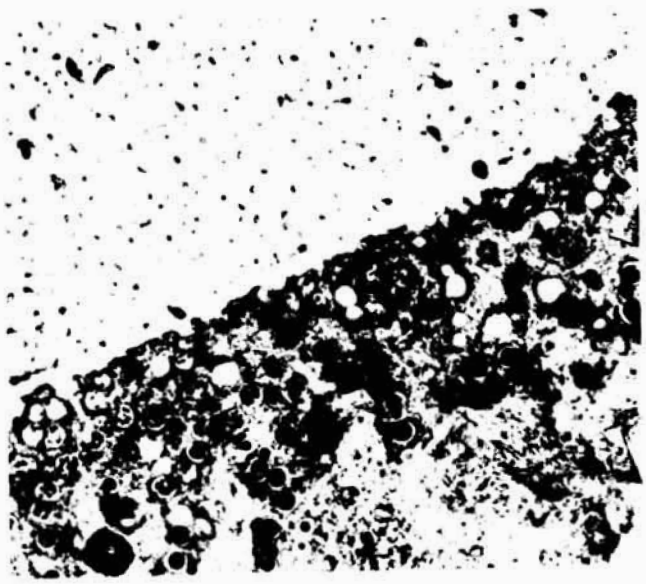

7J096 (e) 100X

7J099 (f) 100X

FIGURE 26. (Continued)

The 70 weight percent In alloy flight sample has a macrostructure very similar to that of its SPAR II counterpart. Since the volume of the aluminum-rich phase is now small enough not to be restricted by the crucible, this phase is able to assume a roughly spherical shape while being surrounded by the indium-rich metal. The indium-rich droplets contained within the aluminum-rich core appear to be of approximately the same size distribution as in the 70 weight percent In ground control sample and in the 40 weight percent In alloys and is much more homogeneously distributed than in the ground control samples.

As may be seen from photomacroviews shown in Figure 26 and the photomicrograph of Figure 26f, there is a great tendency for the aluminum-rich spheres in the indium-rich alloy to concentrate at the crucible walls. In addition, as may be seen in Figure 26e, there is adjacent to the aluminum-rich core a concentration of small aluminum-rich spheres which appear, in some cases, to be in the process of being absorbed at the periphery of the central core. Aluminum-rich spheres of somewhat larger size and, in some cases, seemingly frozen while in the process of coalescence were also found in isolated regions within the indium-rich region (see Figure 26a). As previously observed in the 40 weight percent In alloys and in the SPAR II samples, aluminum-rich dendrites have also formed in this sample.

Aluminum-90 Weight Percent In. Macroviews and photomicrographs of the 90 weight percent In ground control and flight samples are shown in Figures 27 and 28.

The ground control sample shows a layered structure consisting of a relatively small lenticular shaped aluminum-rich phase above the indium-rich layer (see macroview, Figure 27). The indium droplets are fairly uniformly distributed in the aluminum-rich host phase and appear to have a size distribution which is somewhat smaller than that observed in the previous alloys. The settling action of the indium droplets due to gravity is not evident in the macroview of Figure 27.

10X

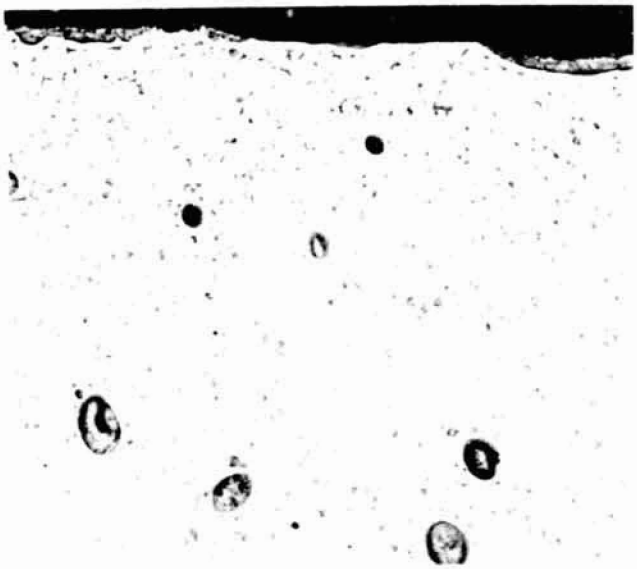

7J672 (a) 100X

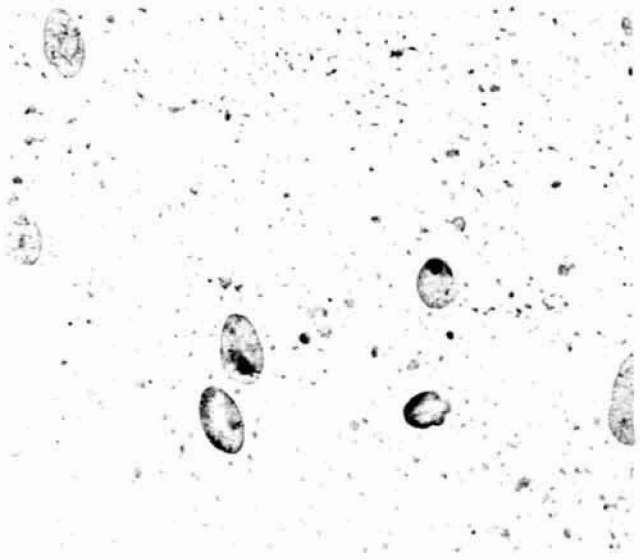

7J673 (b) 100X

FIGURE 27. MACROVIEW AND MICROSTRUCTURE OF Al-90 WEIGHT PERCENT In ALLOY FROM GROUND CONTROL CAPSULE 74-30-49

Note: Photomicrographs labelled (a) through (f) correspond to regions similarly marked on macroview above.

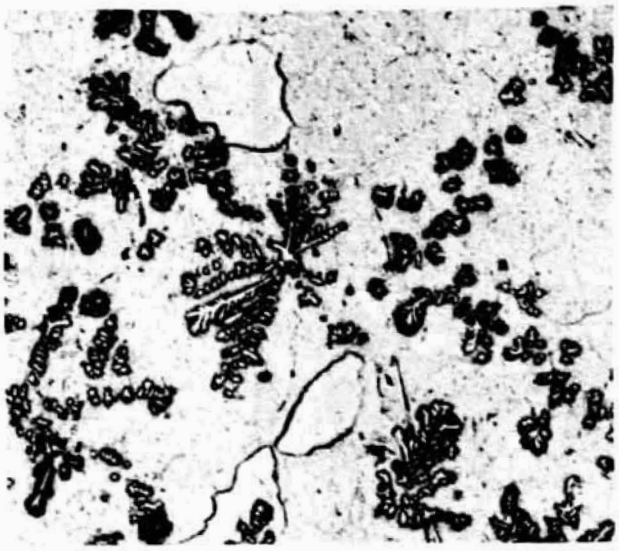

7J674 (c) 100X

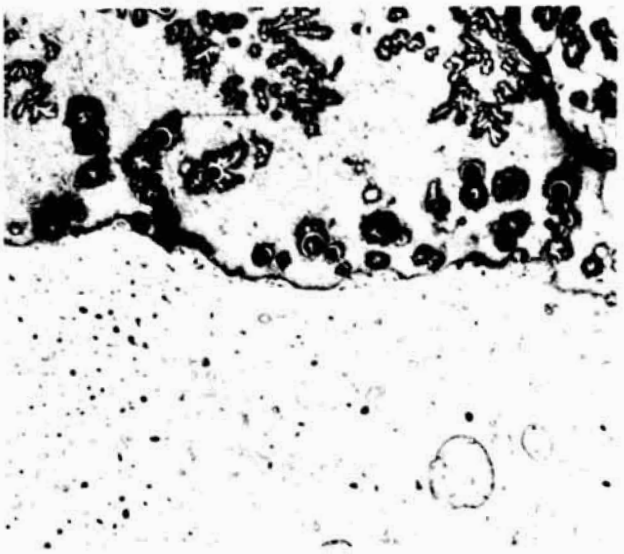

7J675 (d) 100X

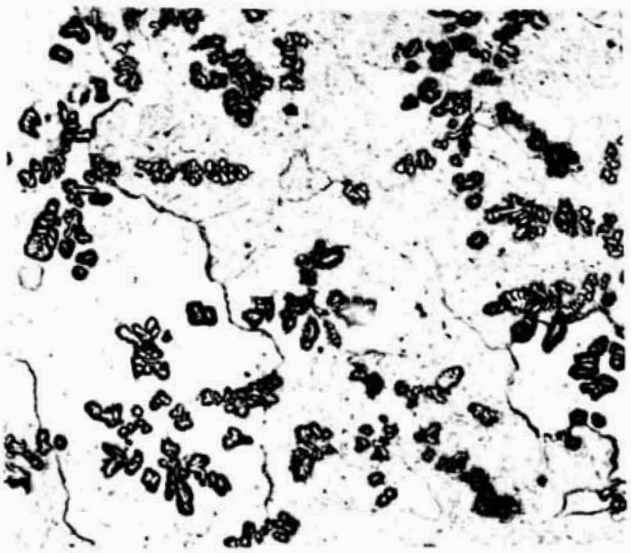

7J676 (e) 100X

7J677 (f) 100X

FIGURE 27. (Continued)

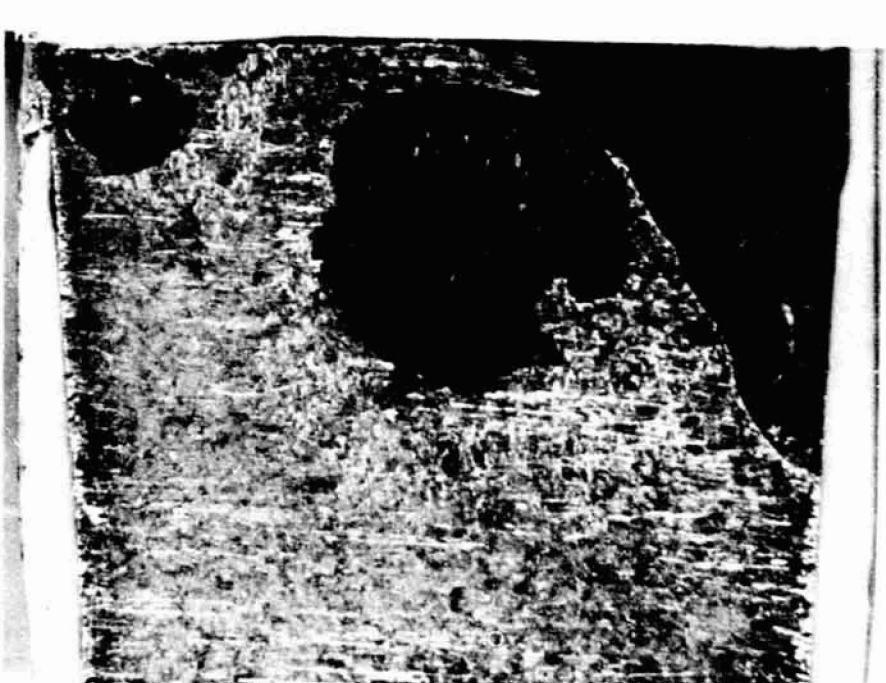

Darkfield 100X

7J116 (a) 100X 7J120 (b) 100X

FIGURE 28. MACROVIEW AND MICROSTRUCTURE OF Al-90 WEIGHT PERCENT In ALLOY FROM FLIGHT SAMPLE 74-30-36

Note: Photomicrographs labelled (a) through (f) correspond to the regions similarly marked on macroview above.

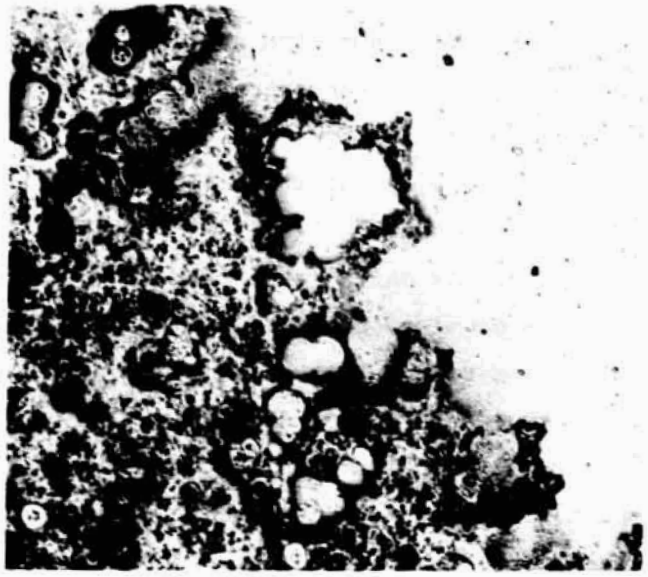

(c) 100X

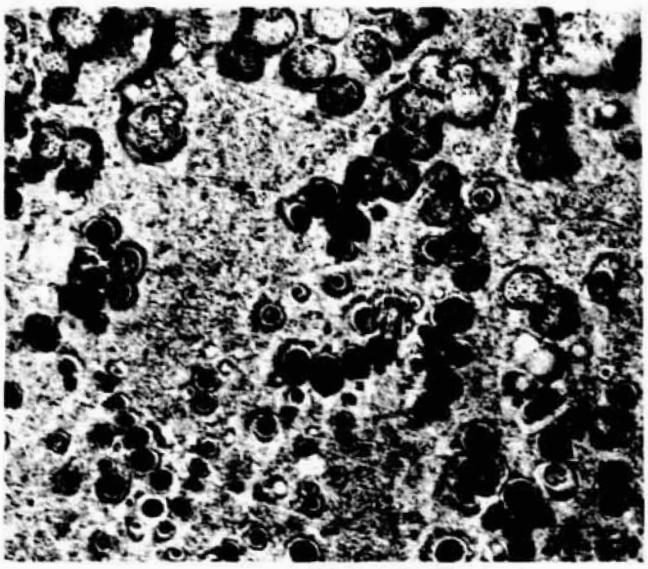

(d) 100X

7J123 (e) 100X

7J124 (f) 100X

FIGURE 28. (Continued)

The indium-rich portion of the 90 weight percent In ground base alloy consists of an indium-rich matrix containing a fairly uniform distribution of aluminum dendrites. The aluminum-rich spheres also present in this portion of the alloy appear to be concentrated along the crucible walls at the bottom of the sample and near the interface between the aluminum-rich and indium-rich portions of the alloy.

The 90 weight percent In flight alloy shown in Figure 28 was by far the most informative of the samples. As may be seen from the macroview shown in this figure, the structure consists of two aluminum rich regions (dark colored) surrounded by indium-rich metal. The aluminum-rich portion of the alloy shows features which are similar to those in the other alloys previously described (see Figure 28 a). The indium-rich portion, however, did reveal rather unusual macro- and microstructures. The region immediately surrounding the aluminum-rich phase (see macroview in Figure 28 and Figure 28b-d) contains a high concentration of aluminum spheres which appear to increase in size by a coalescence process as they approach the massive aluminum-rich phase. This process can be clearly seen in Figure 28c and 28d. (Note the macroscopic aluminum-rich phase is at the top right of Figure 28 and above Figure 2[illegible].) This annular region containing a high concentration of aluminum-rich spheres and surrounding the massively agglomerated aluminum-rich core is in itself surrounded by a region devoid of aluminum-rich spheres. The microstructure of this region, shown in Figure 28 consists of an indium-rich matrix containing aluminum dendrites. Aluminum-rich spheres are also found to be concentrated in the indium-rich region at the crucible bottom and walls (see macroview of Figure 28 and Figure 29).

Discussion of SPAR V Results

Comparison with the Results of Spar II

The major differences in the processing of SPAR II versus SPAR V samples were in the homogenization time (0.25 vs. 16 hours), cooling rate (17.9 C/second vs. 10.4 C/second for the ground control

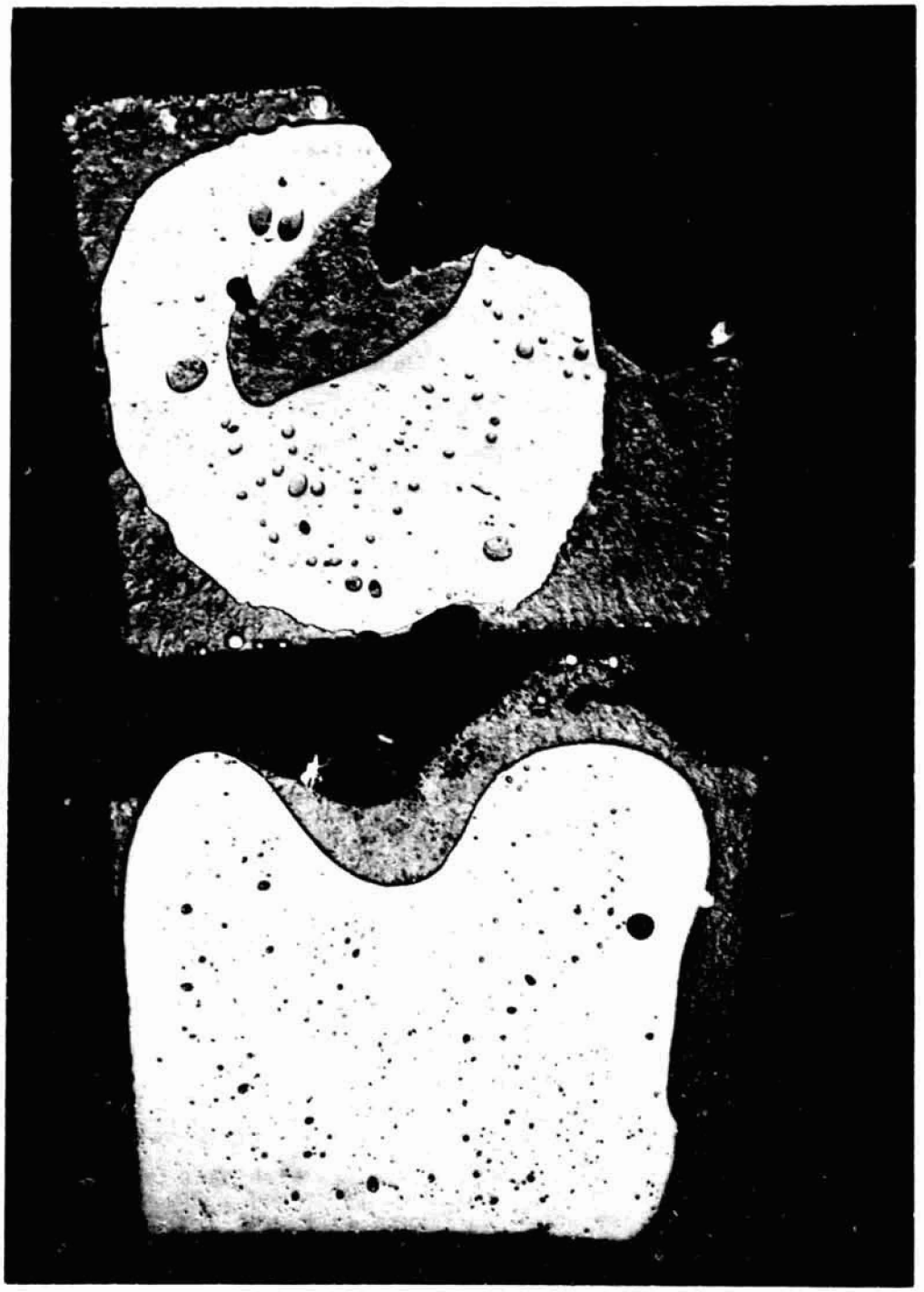

FIGURE 29. MACROVIEW OF CENTRAL POLISHED LONGITUDINAL SECTION FLIGHT SAMPLE 74-30-21 (SPAR II)

This section is the opposite half of that shown in Figure 3.

samples, 14.7 vs. 10.0 C/second for the flight samples) and the likelihood that the indium-rich portions of the SPAR V flight samples had not completely solidified while in the microgravity environment.

In spite of these seemingly large differences in processing conditions, the macro and microstructures of the 40 and 70 weight percent In ground control and flight samples from SPAR II and SPAR V were surprisingly similar. The only differences noted were rather subtle and can be attributed primarily to differences in cooling rate. Some of these microstructural variations are discussed below.

In the ground base 40 weight percent In alloys, the degree to which the indium-rich droplets have settled in the aluminum-rich host phase appears to be appreciably less in the SPAR II sample as evidenced by a wider band of coarse indium-rich droplets near the interface between the bulk phases. Likewise, the band containing aluminum-rich spheres appears to be wider in the SPAR II 70 weight percent In ground base sample than in its SPAR V counterpart. There are comparatively fewer aluminum-rich dendrites in both SPAR II ground base alloys. The wider extent of the indium-rich particles and aluminum-rich spheres in the SPAR II ground alloys may be attributed to the faster cooling rates and thus, the shorter times allowed for buoyancy forces to float or settle out the precipitated droplets. The more rapid cooling rate also restricts the time during which the aluminum dendrites can precipitate in the indium-rich phase of these samples.

The SPAR II and SPAR V flight samples were found to have very similar macro- and microstructures. There were some subtle differences seen however. For example, the indium-rich droplets in the aluminum-rich core of the SPAR II 70 weight percent In alloy appeared to be more highly coalesced. (Compare the macroview of Figure 26 with that of the SPAR II 70 weight percent In alloy shown in Figure 29.) These microstructural differences which may be in the realm of statistical variations cannot be readily interpreted at this time.

The close similarity between the structures of the SPAR II and SPAR V ground control and flight samples and the fact that most differences could be attributed to differences in cooling rates lead to the following possible conclusions.

(1) The SPAR II samples were more homogeneous at the start of cool-down than would be theoretically predicted based solely on diffusion considerations.

(2) The structures are insensitive to the degree of homogeneity, or

(3) Both the SPAR V samples were inhomogeneous at the start of cool-down.

On the basis of the diffusion experiments previously described, we would rule out the third possibility. The second possibility also does not appear viable since variations in structure associated with co. positional variations would be expected. For example, in the SPAR II 40 weight percent In alloys, hypomonotectic compositions ($C/Co < 0.07$ corresponding to compositions < 17 weight percent In) and structures would be expected at the top of the ground control sample (see Figure 11) and within the aluminum-rich portion of the flight sample. Since no evidence of hypomonotectic structures (primary aluminum plus monotectic) has been observed in the SPAR II 40 weight percent In samples, it would indicate that the first possibility is most probable and that convection currents appear to have played a substantial role in homogenizing the alloys. Since conventional convection is not expected to contribute significantly in this process owing to the compositionally stabilized configuration at 1-g, surface tension driven convection due to thermal or solutal gradients is suspected.

No differences in the macro- or microstructures between the SPAR II and SPAR V samples could be attributed to the likelihood that solidification of the indium-rich portions ofthe SPAR V alloys was not completed while in the micro-gravity environment. The 90 weight percent In alloy processed on SPAR V is the one expected to be most affected by this complication, but none of its structural features could be attributed to this effect. Further analysis, however, is necessary concerning the magnitude and direction of the acceleration present during the solidification of the indium-rich liquid. Some thermal analysis is also required to determine the extent of the solidification at the end of the low-g period. It should be noted that all of the aluminum-rich portion of this alloy had solidified under microgravity conditions.

Mechanisms of Massive Separation

As discussed in the review of the SPAR II experiment and delineated in Table 1, a number of mechanisms leading to fluid flow and droplet coalescence are possible. Additional observations made on SPAR V samples have added support for some of the suggested mechanisms.

Thermocapillary Convection. As previously discussed, the relatively large values for the Marangoni number, Ma, calculated on the basis of the thermal environment present during cool-down and the estimated variation of the liquid-vapor interfacial energy with temperature (-0.15 dynes/cm-deg C), has suggested that extensive fluid flows could result from this effect.

Since the time of the original analysis, here has been mounting evidence to suggest the presence of surface tension driven convection. In another NASA sponsored program[17], it has been calculated that the interfacial energy between the equilibrium aluminum-rich and indium-rich liquid phases has a variation with temperature of ~-0.2 dyne/cm-deg C, somewhat larger than the gas-liquid interfacial tension variation with temperature. Thus, it is expected that thermocapillary flows might originate at liquid-liquid interfaces. Moreover, it is likely that such surface tension drive fluid flows might develop as a result of solutal gradients in the region of liquid-liquid interfaces. The change in liquid-liquid interfacial energy with composition, $\frac{d\gamma_{12}}{dC}$, is expected to be relatively large in the Al-In system since the liquid-vapor surface energies for aluminum and indium are quite different (850 vs. 490 ergs/cm^2).[17] These considerations hold equally well for solutal capillary flows due to liquid-vapor interfaces. Further analyses are necessary to quantify these effects.

Additional evidence to support the supposition that surface tension drive convection significantly contributes to fluid flows in this system is delineated below.

(1) Wave-like structures at former liquid-liquid interfaces have often been observed in the Al-In system.

This effect is readily seen in the SPAR II 40 weight percent In flight sample and in the 70 weight percent In ground sample shown respectively in Figures 3 and 30. Such behavior has also been previously noted in the photomicrographs of Figures 22a and b.

(2) As noted in Figure 9, temperature oscillations occur in DTA samples during cooling from a single phase liquid field into the liquid-liquid miscibility gap. Such oscillations could be produced as a result of thermal or solutal surface tension driven convection cell formation. However, there is some evidence that they may be due to transformational volume changes.[12]

(3) The presence of convection currents induced by surface tension gradients can also explain the apparent homogeniety of the SPAR II alloys prior to cool-down in spite of the expectation to the contrary based purely on diffusional considerations.

Droplet and Particle Movement. We have found evidence in the 90 weight percent In flight sample (see Figures 28c and d) that there has been a movement of aluminum-rich liquid droplets in the indium-rich liquid host phase during the cool-down process. The fact that these droplets appear to have readily coalesced supports the hypothesis that they were molten at the time of migration. This observation precludes the possibility that this effect results from solid aluminum particles being pushed by an advancing indium-rich solidification front at ∿155 C.

The hypothesis that the aluminum-rich spheres were molten during their migration and the observation that migration appears to be toward the hottest portion of the melt indicate that these droplets have migrated as a result of thermocapillary forces.

A treatment of thermocapillary migration has been reported by Bewersdorff[9] for Al-In alloys. We repeat here his calculations, but with the introduction of some refined values for the applicable physical parameters.

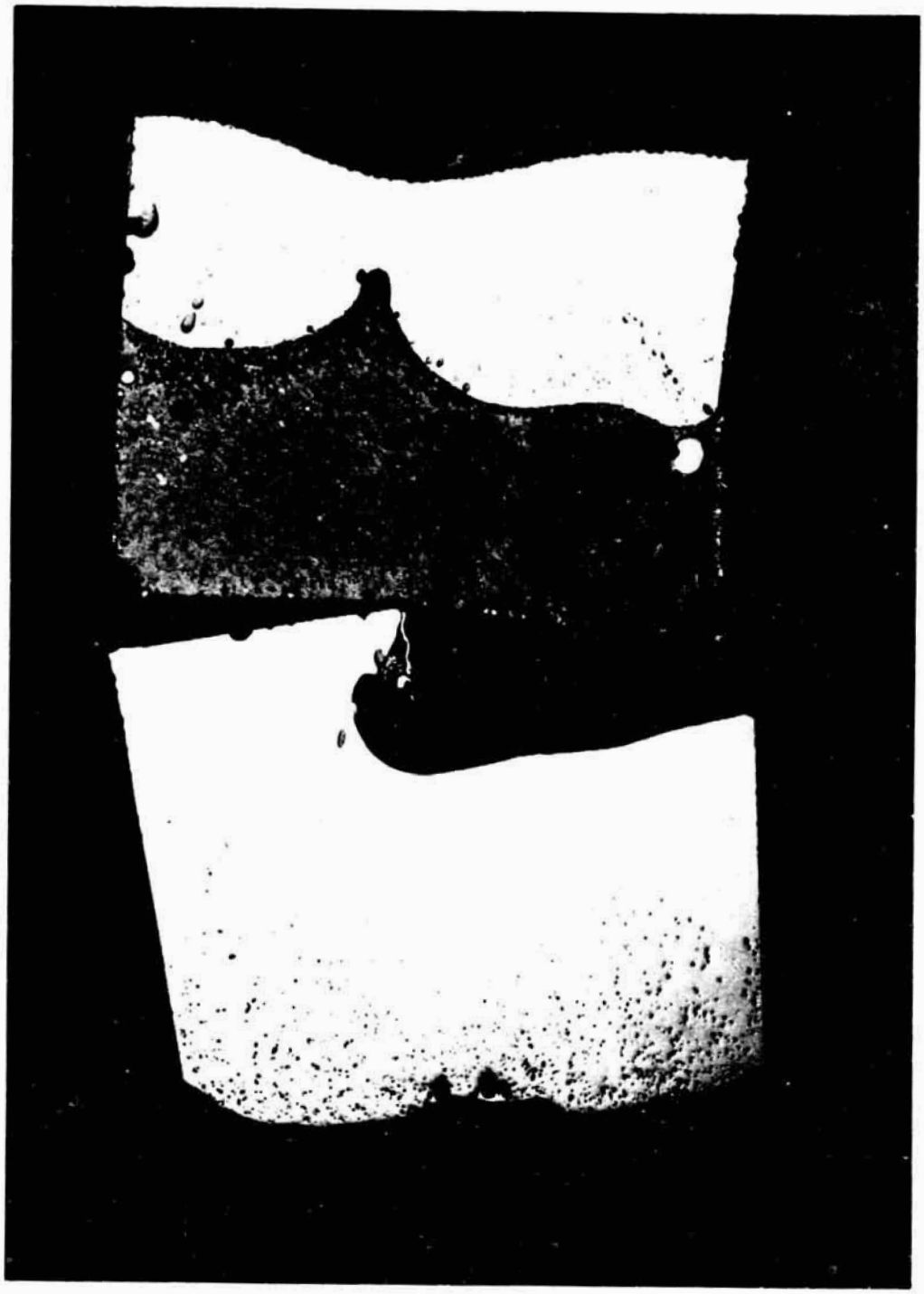

FIGURE 30. MACROVIEW OF SPAR II GROUND CONTROL SAMPLE 74-30-18

Note: Highly wavy interface between the aluminum-rich and indium-rich phases in the 70 weight percent In alloy.

The relationship for thermocapillary migration velocity, V has been formulated as follows:

$$V = \frac{-2R \frac{d\gamma_{12}}{dT} \frac{dT}{dx}}{3(2\mu_M + 3\mu_p)} \qquad \text{Equation 9}$$

where:

R is the droplet radius,

$d\gamma_{12}/dT$ is the change in interfacial energy with temperature,

$\frac{dT}{dx}$ is the temperature gradient, and

μ_M and μ_p are the kinematic viscosities of matrix and droplet fluids, respectively.

Values of these parameters are given in Table 14 assuming that the liquids are pure aluminum and pure indium at 800 C. The results of the calculation predict the following droplet migration velocities:

Indium Droplets in an Aluminum Matrix

V_{In} = 16.9 R/second, Equation 10

Aluminum Droplets in an Indium Matrix

V_{Al} = 19.1 R/second. Equation 11

On the basis of Equation 11, the extent of droplet migration in 10 seconds (corresponding to the approximate time in the miscibility gap for the SPAR V alloys) for different size droplets has been calculated and is summarized in Table 15.

The aluminum-rich droplets shown in Figure 28d have radii ranging in size from approximately 10μ to more than 50μ. The corresponding expected movements are respectively 0.19 and > 0.96 cm. From the macroview of Figure 28, it may be seen that the zone relatively free of aluminum-rich droplets is approximately 0.3μ wide, a value which is consistent with the proposed mechanism. Thus, it appears to be highly probably that thermocapillary migration of aluminum-rich droplets in an indium-rich host fluid has occurred during the SPAR V experiments. Controlled ground

TABLE 14. VALUES OF PHYSICAL PARAMETERS AT 800 C USED IN THERMOCAPILLARY DROPLET MIGRATION CALCULATIONS

μ_{Al}	1.1×10^{-2} Poise
μ_{In}	5.8×10^{-3} Poise
dT/dx (6)	7 C/CM
$d\gamma_{12}/dT$ (17)	-0.17 ergs/cm^2 - °C

TABLE 15. MIGRATION DISTANCE FOR VARIOUS SIZE ALUMINUM DROPLETS IN AN INDIUM HOST FLUID

Droplet Radius, μm	Movement in 10 seconds, cm
1	0.02
10	0.19
20	0.38
50	0.96
100	1.91

base experiments aimed at studying this effect in Al-In alloys will help to further elucidate this phenomenon.

It is interesting to note that although expected, there was little evidence to support the analagous movement of indium-rich droplets toward the warmer regions of the aluminum-rich host fluid. Localized precipitation accompanied by spreading of indium-rich fluid along the crucible walls may in part have interfered with indium-rich droplet migration.

Some of the macro- and microstructures of the SPAR II and SPAR V flight samples provided evidence that some of the agglomerates of aluminum-rich spheres may be the result of particle pushing by the advancing indium-rich solidification front. These particles would be solid at the solidification temperature of the indium-rich metal. Evidence for particle pushing is especially clear in the macroview of the 70 weight percent In alloy flight sample shown at the top of Figure 29. Concentrations of fine particles (marked A in Figure 29) may be seen in the indium-rich regions. In contrast to the coalesced agglomerates described earlier, these particles, although in close proximity, show much less tendency to coarsen (see Figure 26c and e). Controlled experiments on the pushing of solid aluminum-rich particles by an advancing solidification front and the subsequent coarsening process should shed additional light on this process.

Diffusional Growth of Liquid Droplets

At the suggestion of Dr. L. Lacy of MSFC, a calculation was made to determine the droplet size at the end of the diffusion growth period for aluminum-indium alloys of various compositions. Previous calculations have shown that the diffusional growth period is extremely short (on the order of 10^{-2} to 10^{-1} seconds, depending on the number of particles per unit volume).[6] Thus, diffusional growth is complete early in the phase separation process.

We have calculated the droplet radius of the precipitating phase for various Al-In alloys at the end of the diffusional growth period using a rather simple approach. The calculation starts with a

determination of the volume fraction of the precipitating phase at the monotectic temperature as a function of alloy composition on the basis of the phase rule and equilibrium diagram.[1] The calculation is completed by dividing the volume fraction by the number of particles per unit volume and converting the resultant average particle volume to an average particle radius. Results of this calculation for the alloys of interest in this study are presented in Table 16. The particle radius is based on an assumed concentration of 2×10^7 particles/cm^3. This latter figure has been obtained from measurements made on Figure 16b, a photomicrograph of a portion of an aluminum-indium diffusion couple which had been cooled at a rate of approximately 1000 C/second.

TABLE 16. EQUILIBRIUM PARTICLE SIZE AND SPACING RESULTING FROM DIFFUSIONAL GROWTH

Alloy Composition Weight Percent In	Volume Fraction of Droplets, percent	Particle Radius[a] μm	Interparticle Spacing[b]
30	7.5 In	9.6	1.95R
40	14.6 In	12.0	1.44R
70	45.8 In	17.6	0.35R
90	17.9 Al	12.9	1.21R

(a) Based on a droplet concentration of 2×10^7 droplets/cm^3

(b) Based on close packing of spherical drops

The distance between particles, d, is also listed in Table 16. This parameter has been calculated assuming that the centers of the droplets lie on a close-packed cubic grid of spacing a. It then follows that

$$d = \frac{a\sqrt{2}}{2} - 2\,r_p \qquad \text{Equation 12}$$

where

r_p is the droplet radius.

a and r are related to the volume fraction of droplets, V_f by the relation:

$$V_f = \frac{16r_p^3}{3a^3} \qquad \text{Equation 13}$$

By combining Equations 12 and 13 in such a way as to eliminate a, it follows that the ratio, d/r_p, is related to V_f by the equation:

$$\frac{d}{r_p} = \sqrt{\frac{2}{2}} \left(\frac{16\pi}{3V_f}\right)^{1/3} - 2. \qquad \text{Equation 14}$$

It should be noted that Equation 14 is independent of the number of droplets per unit volume.

The effect of composition may be clearly seen from Table 16. For a given assumed droplet density, and for the compositions treated, the particle radius at the end of the diffusional growth process is largest for the 70 weight percent In alloy. What is more important is that the spacing between droplets at this composition is extremely small being only 0.35 r_p. The small distance between droplets, especially if the droplets are very fine, can lead to gross instability of the droplet dispersion since only small movements are required for two droplets to collide and coalesce. Based on these consideration, it is not suprising that alloys of approximately this composition show massive separation even if they are in the miscibility gap for only a fraction of a second.

CONCLUSIONS

The following conclusions are based on our SPAR II and SPAR V flight studies and the supporting ground base experimentation:

(1) The results of SPAR V have established that the massive phase separation observed in both SPAR II and SPAR V was not caused by a lack of homogeneity in the molten liquid at the start of the cool-down portion of the experiments.

(2) It is highly probable that surface tension drive flows are active and significantly contribute to the observed structures in the SPAR II and SPAR V samples. This is evidenced by the presence of wavy interfaces between the aluminum-rich and indium-rich phases, the homogeneity of the SPAR II alloys at the start of cool-down and the presence of oscillatory flows in DTA experiments.

(3) It is highly likely that thermocapillary migration of aluminum-rich droplets has occurred in the indium-rich flight samples. The observation of particle coalescence distinguishes thermocapillary migration from particle pushing by an advancing liquid-solid interface. Some evidence is also presented for this latter mechanism, but it contributes little to the observed massive separation.

(4) The SPAR V flight samples had not completely solidified at the end of the low-g period ($< 10^{-3}$g). However, no macrostructural or microstructural features have been found that can be attributed to this effect.

(5) Ground-based experiments conducted on rapidly cooled aluminum-indium alloys have shown the phase separation to be extremely sensitive to composition with regions near the critical composition providing massively separated phases which nucleated and grew in much less than a second. A high volume fraction of second phase and the close proximity of neighboring droplets in this composition range has been used to explain the basic instability of these structures.

(6) We have found evidence to support the hypothesis that in the aluminum-rich region of the miscibility gap, the indium-rich phase nucleates at the crucible walls during cool-down and because of its wetting properties, spreads out along the walls. As the indium-rich content of the miscibility gap alloys increases, there is a greater tendency for aluminum-rich spheres to nucleate at the crucible walls.

(7) Additional work is required to corroborate and confirm some of the mechanisms thought to be important in the phase separation process. Additional analysis is also required to assess the possible role other mechanisms may play in the phase separation of the aluminum-indium alloys and other miscibility gap systems.

RECOMMENDATIONS FOR FUTURE WORK

Based on the results of our SPAR II and SPAR V ground base and flight experiments, we would recommend the following areas for futher investigation:

(1) Conduct confirming ground base work on the thermocapillary migration of aluminum droplets. This work should include thermocapillary migration experiments parallel and anti-parallel to gravity and studies aimed at providing an understanding of the role of liquid-liquid interfacial energy on this behavior. It will also be necessary to obtain measurements of these energies to compare with the theoretical calculations and for use in checking the thermocapillary migration predictions.

(2) Conduct further work on surface tension drive convecation currents induced either by temperature

gradients or concentration gradients. Analysis and measurement of the change of surface energy for both liquid-gas and liquid-liquid interfaces with temperature and composition are necessary. Direct observations of surface deformation and flow during the phase separation process should provide some insight into the presence of surface tension drive flows and/or spreading. A space experiment in which the gas-liquid interface is eliminated would provide information on the relative roles played by the gas-liquid vs. liquid-liquid interfaces on surface tension driven fluid flows.

(3) Perform research work on transparent miscibility gap systems having various interfacial energies and physical properties in order to directly observe fluid flow phenomena that might be leading to massive separation. Extensive ground base study should be conducted initially and then extended to the low gravity environment.

(4) Perform particle pushing experiments on aluminum-rich solid spheres in an indium-rich host liquid in order to confirm the interpretation of various aspects of the microstructure attributed to the interaction of the solid-liquid indium interface with the solid aluminum-rich spheres.

(5) Conduct experimental work on other metallic miscibility gap systems in order to obtain a range of physical parameters so as to provide insight into their effect on the phase separation process. Theoretical analyses on the interfacial behavior of these systems should be conducted to aid in their selection. Both ground base and flight studies will be necessary.

(6) Determine the influence of container-liquid interactions on the evolution of the final micro- and macrostructures. A containerless experiment will provide one extreme of behavior while other containers of various wetting characteristics will provide additional information.

(7) Continue the work on the diffusion behavior above the miscibility gap in order to both obtain accurate measurement of the diffusion coefficients in the aluminum-indium system as well as in other metallic miscibility gap systems. In addition, the close examination of the microstructures thus produced will provide insight into the initial stages of the phase separation for the different systems as a function of composition.

REFERENCES

1. B. Predel, "Beitrag Zur Konstitution und Thermodynamik von Entmischungssystemen", Zeitschrift fur Metallekunde, 56 (1965) 791.

2. J. L. Reger, "Study of Processing Immiscible Materials at Zero-G", Interim Report to NASA-MSFC, Contract NAS8-28267 (May, 1973).

3. A. J. Markworth, W. Oldfield, J. Duga, and S. H. Gelles, "Investigation of Immiscible Systems and Potential Applications", Final Report to NASA-MSFC, Contract NAS8-29748 (April, 1975).

4. S. H. Gelles, E. W. Collings, W. H. Abbott, and R. E. Maringer, "Analytical Study of Space Processing of Immiscible Materials for Superconductors and Electrical Contacts", Final Report to NASA-MSFC, Contract NAS8-31445, (September, 1976).

5. A. J. Markworth, S. H. Gelles, J. J. Duga, and W. Oldfield, "Immiscible Materials and Alloys", in Proceedings of the Third Space Processing Symposium, NASA Report No. 74-5, p. 1003 (June, 1974).

6. S. H. Gelles and A. J. Markworth, "Final Post Flight Report on SPAR II Experiment No. 74-30, Agglomeration in Immiscible Liquids", Report to NASA-MSFC, Contract NAS9-31543 (December, 1976).

7. S. H. Gelles and A. J. Markworth, "Microgravity Studies in Liquid Phase Immiscible System: Aluminum-Indium", AIAA Journal, 16 (1978) 431.

8. R. M. Barrer, Diffusion in and through Solids, University Press, Cambridge, 1951, p 14.

9. A. Bewersdorff, "A Mechanism for Macroscopic Phase Separation in Emulgated Liquid Systems" Paper VIII 2.2, COSPAR Meeting, 1978.

10. E. W. Otto, "Static and Dynamic Behavior of the Liquid-Vapor Interface during Weighlessness", Aerospace Chemical Engineering, 62 (1966) 158.

11. J. T. Neu and Robert J. Good, "Equilibrium Behavior of Fluids in Containers at Zero-Gravity", AIAA Journal, 1 (1963) 814.

12. C. Potard, "Directional Solidification of Aluminum-Indium Alloys at Microgravity: Results of Basic Preparatory Investigations", Presented at the 17th Aerospace Sciences Meeting AIAA held in New Orleans, January 15-17, 1979.

13. S. T. Zamarca, L. Ganovici, and I. Ganovici, "Self-Diffusion of Indium and Liquid Indium-Aluminum Alloys", Revue Roumaine de Chimie, 14 (1969) 35.

14. J. W. Colby, "MAGIC-Computer Program for Quantitative Electron Microprobe Analysis", Advances in X-Ray Analysis (J. B. Newkirk, G. R. Mallett, and H. G. Pfeiffer, Editors) Vol. II, Plenum Press, 1968, p 287.

15. L. Lacy, personal communications, 1978.

16. C. J. Smithells, Metals Reference Book 5th Edition, Buttersworth, London, 1976, p. 939.

17. "Experiments for Materials Processing in Space, Liquid Phase Miscibility Gap Materials, Eleventh Monthly Progress Report to NASA-MSFC, S. H. Gelles Associates, Contract NAS8-32952, March, 1979.

Grumman Research Department Report RE- 569

SPAR V TECHNICAL REPORT FOR EXPERIMENT 74-37 CONTAINED POLYCRYSTALLINE SOLIDIFICATION IN LOW-G

by

John M. Papazian
Research Department
Grumman Aerospace Corporation
Bethpage, New York 11714

and

Theodoulos F. Kattamis
Institute of Material Science
University of Connecticut
Storrs, Connecticut

Post-Flight Technical Report on Contract NAS 8-31530

for

George C. Marshall Space Flight Center
National Aeronautics and Space Administration
Marshall Space Flight Center, Alabama 35812

February 1979

Approved by: Richard A. Scheuing
Director of Research

ABSTRACT

The effect of gravity on the columnar-to-equiaxed microstructural transition was studied in small samples of NH_4Cl-H_2O. The behavior of the samples during laboratory (one-gravity) simulations was contrasted with their behavior during the SPAR V (low gravity) sounding rocket flight. In one gravity, the columnar zone accounted for 25 to 100% of the structure, depending on the superheat and orientation of the chill. Grain multiplication occurred by showering and by convection induced dendrite arm remelting. Convection was caused by both thermal gradients and solutal gradients. In low gravity, completely columnar structures were obtained; all grain multiplication mechanisms were entirely supressed. The absence of gravity also modified the thermal conditions and caused the liquid to cool more slowly. This resulted in a steeper temperature gradient in the liquid ahead of the solidification interface. The growth rate of the solid was not affected. A spring-loaded expansion piston jammed, causing "big bang" nucleation in two chambers and distributing nuclei throughout the liquid. Despite this occurrence, an equiaxed zone did not form, indicating that the most significant effect of low gravity on this experiment was the modification of the thermal conditions. This resulted in a situation in which the equiaxed grains could not grow and rendered the columnar-to-equiaxed transition impossible.

TABLE OF CONTENTS

LIST OF ILLUSTRATIONS

LIST OF ILLUSTRATIONS (contd)

INTRODUCTION

A zone of equiaxed (roughly spherical) grain structure will form in a casting only when nuclei for equiaxed grains are present in the melt and growth of the equiaxed grains is more rapid than growth of the columnar grains (Ref. 1). Both conditions are necessary and both steps can be influenced by gravitation.

Nuclei can appear in the melt in various ways. Inoculants may be present, making nucleation easy (Ref. 2). At low melt superheat, a large number of nuclei may form during pouring and be distributed through the liquid according to local fluid flow patterns ("big bang" nucleation (Ref. 3)). Convection, caused by thermal gradients, can induce remelting and break-off of dendrite arms from the growing dendritic interface. These arms are then transported to the center of the casting and act as nuclei for the formation of the equiaxed grains (Ref. 3). Convection may also be caused by the presence of composition gradients which arise from rejection of solute, even in a nonconvective thermal field. This process has been shown to be responsible for the formation of freckles, regions of fine equiaxed grains in a directionally solidified columnar grain structure (Refs. 4, 5). Also, Southin has demonstrated (Ref. 6) that fragments of dendrites can grow at the open surface of the solidifying ingot, "shower" down through the melt, settle on the advancing columnar interface, and form equiaxed grains. Finally, constitutional supercooling of the melt ahead of the interface can, in principle, cause nucleation (Ref. 7), although this is rarely observed.

All of the above mechanisms are influenced by gravitational acceleration. Reduced gravity will slow down or surpress those mechanisms that depend on density difference, namely thermal convections, solutal convection, and showering. In the case of heterogeneous nucleation reduced gravity could enhance nucleation by preserving a more uniform distribution of inoculants, because of reduction of the Stokes' settling or floating force. As for constitutional supercooling, reduced gravity may change the solutal and thermal gradients near the interface by altering thermal and mass transport in the melt. The precise effect of a reduction in gravity on each one of these gradients is not obvious; both might be expected to be steeper, with the thermal gradient being modified more than the solutal gradient

(Ref. 8). However, valid guidelines for a priori predictions of the effects of reduced gravity on these gradients at the solidification interface have not yet been developed.

Likewise, it is difficult to predict how reduced gravitational acceleration will affect growth of equiaxed relative to columnar grains. In the only model which directly considers growth, Burden and Hunt assume that the rate of growth of the columnar interface decreases continuously thereby causing the temperature at the growth interface to go through a maximum (Refs. 9,10). As the growth rate of the columnar grain continues to fall the interface temperature decreases, thereby increasing the rate of heat transport out of the melt and increasing the growth rate of equiaxed grains, causing the columnar-to-equiaxed transition (CET). They do not consider convective effects; and an increased temperature gradient can lead to an increased or decreased growth rate depending upon which side of the maximum in the growth rate versus interface temperature curve one is located.

In a clear cut low gravity experiment using NH_4Cl solutions, Johnston and Griner (Ref. 11) showed that dendrite arm remelting caused by thermal inversion driven convection did not occur, and a completely columnar structure was obtained. Other low gravity experiments have resulted in the formation of equiaxed structures instead of the expected columnar structures (Refs. 12, 13), but these observations remained largely unexplained. The significant effects of grain structure on some mechanical properties have prompted the current investigation. The main objective of this study was to directly observe the effect of a reduction in gravity on the CET (Ref. 14). It was thought that the experiment should be designed so that the occurrence of the CET varied in a systematic fashion in the ground base simulations; it was thus expected that the primary effect of reduced gravity on CET could be established.

EXPERIMENTAL PROCEDURE

This experiment was performed in a specially built apparatus which was designed for the payload of a Black Brandt sounding rocket. During the rocket flight, a free-fall interval of approximately 250s occurs in which all accelerations are less than $10^{-4}g_o$ (g_o = 980 cm/s^2). This "low-gravity" interval begins at approximately 80s after lift-off. The apparatus was programmed to perform a solidification experiment during that interval. The progress of the low-gravity experiment was recorded by a 35 mm camera which took 230 photographs at a rate of one frame per second. The apparatus has been described in detail elsewhere (Ref. 15), thus only a brief description will be given here. The heart of the apparatus is the solidificatio chamber, shown schematically in Fig. 1. It consists of a semicylindrical chill block, made of copper, brazed to a top plate of stainless steel. The front and rear faces are of plexiglass and are sealed with "O" rings. This geometry was chosen to provide radial heat extraction from the samples to simulate weld bead solidification and to allow direct observation of the experiment. Four such chambers are arranged symmetrically as shown in Fig. 2. All of the chill blocks were machined from a single piece of copper. The copper web which joins the four cells serves to transmit heat to and from the cells during prelaunch soaking and during the quench. Before launch the four-sample assembly is heated to and controlled at a uniform temperature of 80°C. At launch, power to the heaters is cut off and at 100s after lift off a timer opens a solenoid valve which allows liquid freon-12 to spray on the copper web, cooling the samples. Solidification takes place during the following 200s and is recorded by the camera. Simultaneously, readings are taken from thermistors which measure the temperature of the sample material in chamber I. The thermistors are located in the front and back plexiglass faces at equal intervals of 1/4 of the radius starting at the apex of the chamber. Two additional thermistors record the temperature of the chill block. Other details of the sample chambers are illustrated by the figures in the Results and Discussion section.

Two H_2O;NH_4Cl hypereutectic alloys were used; 325 grams of NH_4Cl per litre of solution (solution A) and 362.5 gm/litre, solution B. The NH_4Cl was reagent grade and the solutions were filtered after preparation. The liquidus temperatures

were 35 and 55°C, respectively. The solidus is given as -15°C by Copley, et al. (Ref. 5). The soak temperature was 80°C, thus the superheats were 45 and 25°C, respectively.

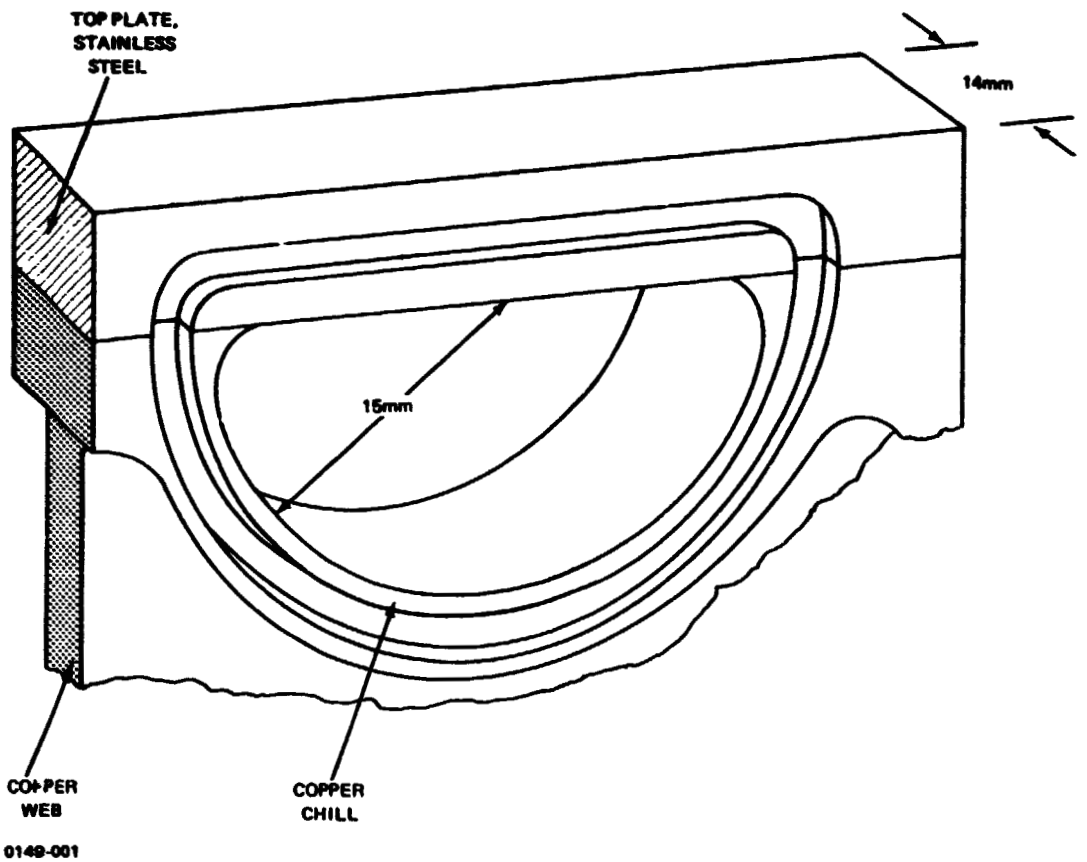

Fig. 1 Schematic Drawing of a Solidification Chamber

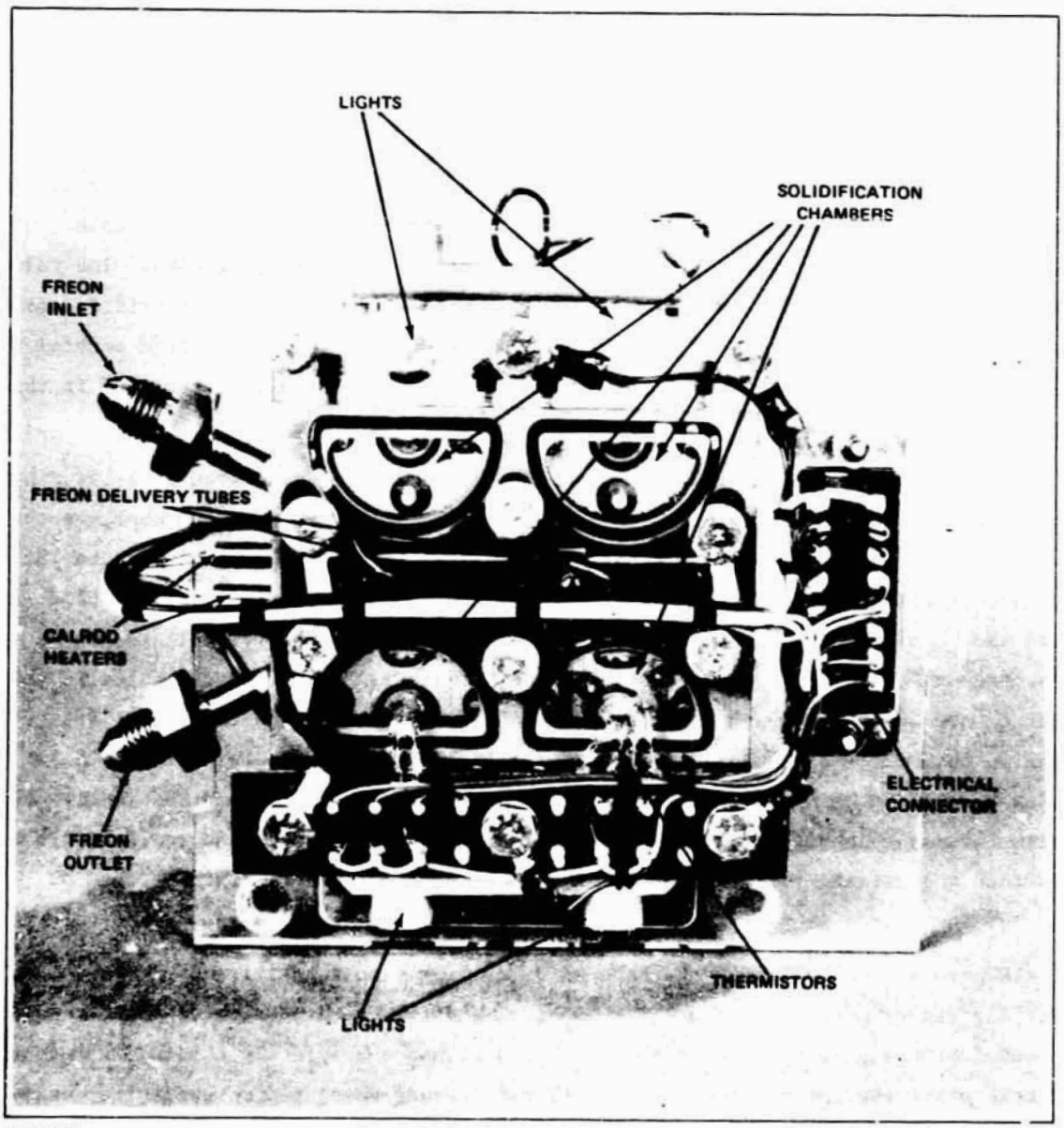

0149-002

Fig. 2 Overall View of the Flight-Ready Sample Holder Consisting of Four Solidification Chambers and Related Accessories

RESULTS AND DISCUSSION

LABORATORY (ONE-GRAVITY) EXPERIMENTS

Repeated laboratory simulations were performed with the flight apparatus in order to arrive at an optimum combination of the three experimentally variable parameters: solution concentrations, soak temperature, and cooling rate. The values finally chosen were such that, during one run, the solidified micro-structures varied from 25 to 100% columnar and three gravity-dependent grain multiplication mechanisms occurred. The results of these typical laboratory simulations are described in this section.

Figure 3 shows one of the lower chambers at 150s after simulated lift-off. No solid has formed yet. Since the semicylindrical wall of the sample chamber was the chill, a thermal inversion was present in this orientation. This gave rise to vigorous convection which was made visible by a simple Schlieren technique; a ruled grid had been installed on the rear face of each chamber. Also visible in Fig. 3 are three holes in the rear face of the sample chamber. The two small holes in the corners are for filling and emptying, and the larger hole communicates with the expansion chamber. The expansion chamber is a 12.5 mm diameter hole in the 12.5 mm thick plexiglass back plate. It contains a spring-loaded piston and was required to allow for expansion and contraction of the sample during heating and cooling. It provided a constant hydrostatic pressure in the sample chamber. Part of the "O" ring of the piston is visible as a black semicircular feature behind the hole.

Figure 4 shows all four chambers at 243s after simulated lift-off. White NH_4Cl crystals are present in each one. Chambers I and III contain solution A and chambers II and IV contain solution B. Chambers I and II had a completely columnar structure at this point whereas chambers III and IV had already developed a substantial equiaxed zone, in addition to the columnar growth which originated at the chill. As the experiment proceeded, columnar growth continued in II until solidification was complete whereas grain multiplication began in I and a substantial equiaxed zone formed. At the end of the experiment, columnar growth accounted for 40% of I, 100% of II, 25% of III and 50% of IV, with the remainders equiaxed. Grain multiplication occurred in III and IV via dendrite remelting caused by convection currents. The

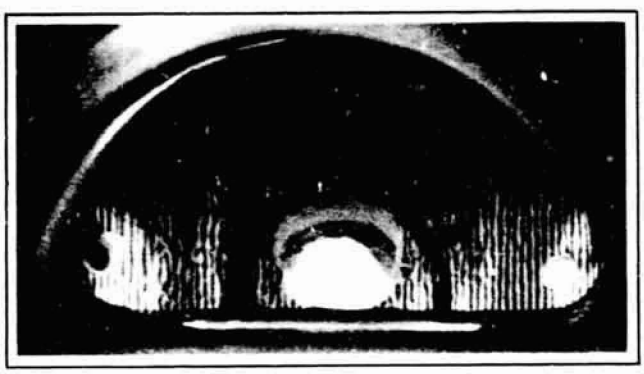

Fig. 3 Vigorous Thermal inversion Driven Convection in IV During a Laboratory Simulation, t = 150s

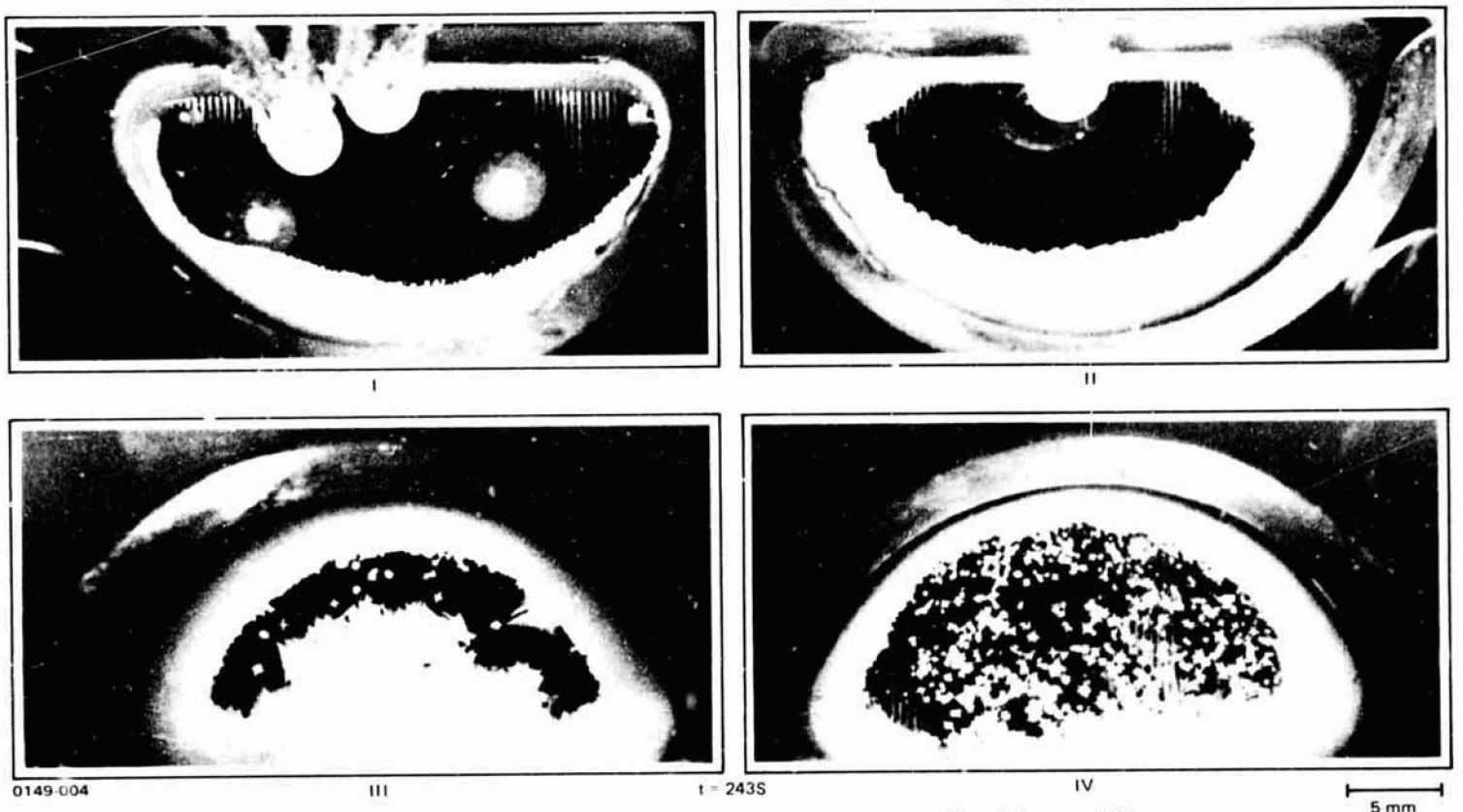

Fig. 4 Appearance of All Four Chambers During a Laboratory Simulation, t = 243s

convection currents were driven by thermal inversion induced density differences. The numerous crystals visible in III and IV were melted off the columnar interface by these convection currents and subsequently fell to the bottom of the chamber. In I, grain multiplication was mainly caused by showering and, to a limited extent, by convection induced dendrite arm remelting. Figure 5 shows a typical, small, grain multiplication convection cell in I. Since the chill in I was on the bottom there was no thermal inversion and thus this was a compositionally induced convection cell. As the NH_4Cl:H_2O solidifies in a columnar fashion, water is rejected in the interdendritic regions and the liquid therein becomes enriched in water and lighter than the liquid ahead of the dendrite tips. In the absence of complete mixing, this gives rise to a density inversion and hence, convection. The liquid which rises between the columnar dendrites accelerates dendrite arm remelting. Dendritic debris rises above the dendrite tips, leading to formation of equiaxed grains (Fig. 5). These results illustrate the effects of solute concentration and orientation of the chill (chill on top versus chill on bottom) on the extent of the columnar zone.

Figure 6 shows the results of a simulation in which the apparatus was rotated 90° so that the chill blocks were on the sides of the chambers. This orientation resulted in a highly nonuniform interface shape. Chambers II and IV were mainly columnar while I and III were mainly equiaxed. Grain multiplication occurred by convection and by showering.

LOW-GRAVITY EXPERIMENT, GENERAL OBSERVATIONS

The experiment was flown on NASA's sounding rocket flight, SPAR V. The apparatus successfully performed the experiment and the following data were obtained. Interpretation was facilitated by making the one frame per second flight film into a 16 mm cine film which could be projected at various rates. A copy of the cine film has been submitted to the program office at MSFC.

Figure 7 shows nucleation and initial growth of solid in IV.* Nine nuclei formed within seventeen seconds of each other at several locations along the chill. These crystals rapidly grew sidewise and eventually joined to form a macroscopically irregular solid-liquid interface. No evidence of Schlieren effects can be detected,

---

*All of the photographs taken during SPAR V have a pronounced scratch which was caused by a defect in the flight camera.

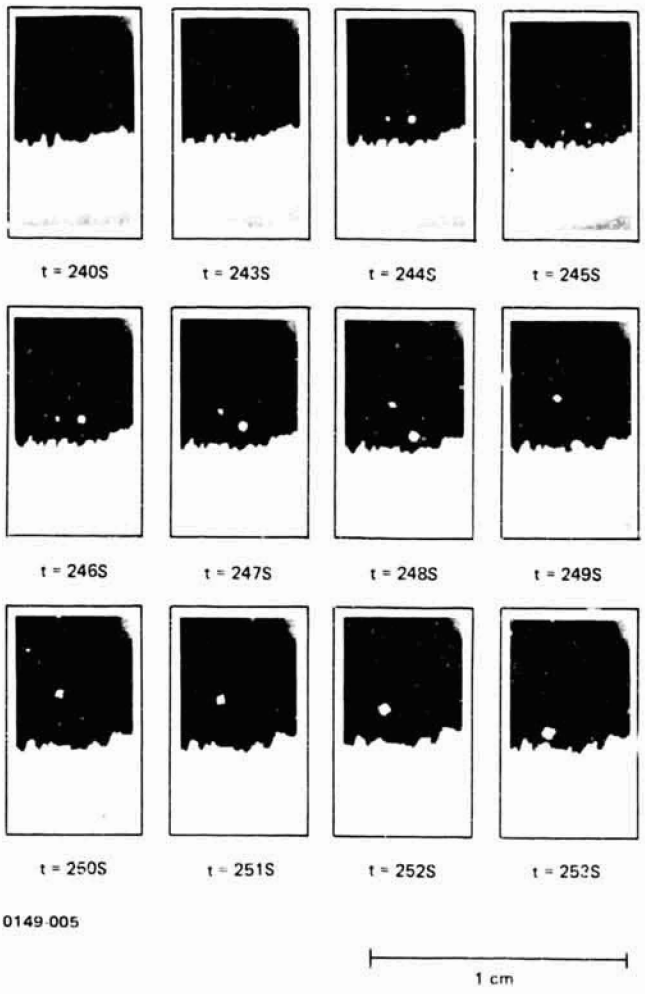

Fig. 5 Compositionally Induced Grain Multiplication Cell in Chamber I During a Laboratory Simulation

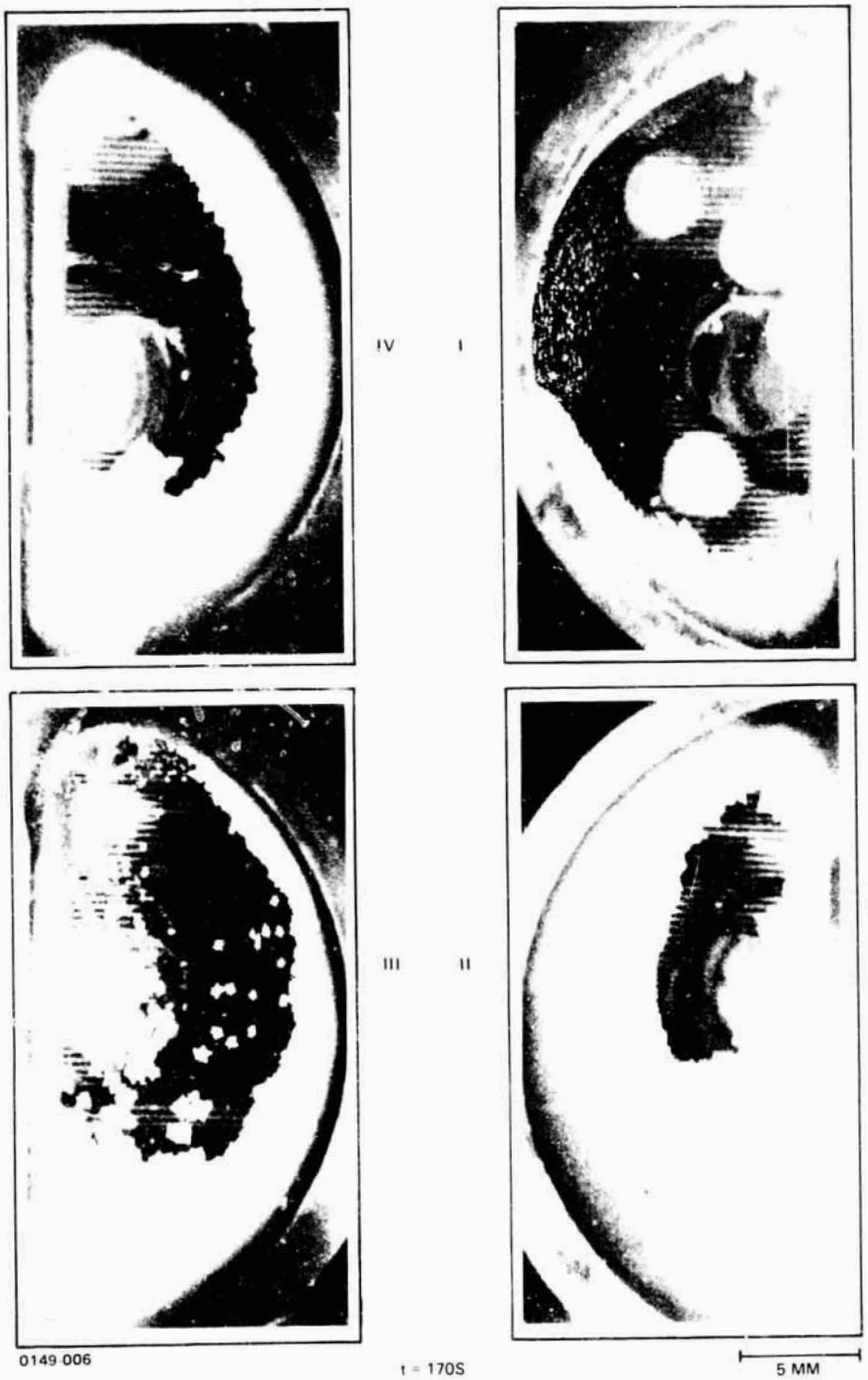

Fig. 6 Appearance of All Four Chambers During a Laboratory Simulation in Which Sample Holder was Rotated into a Vertical Orientation, t = 170s

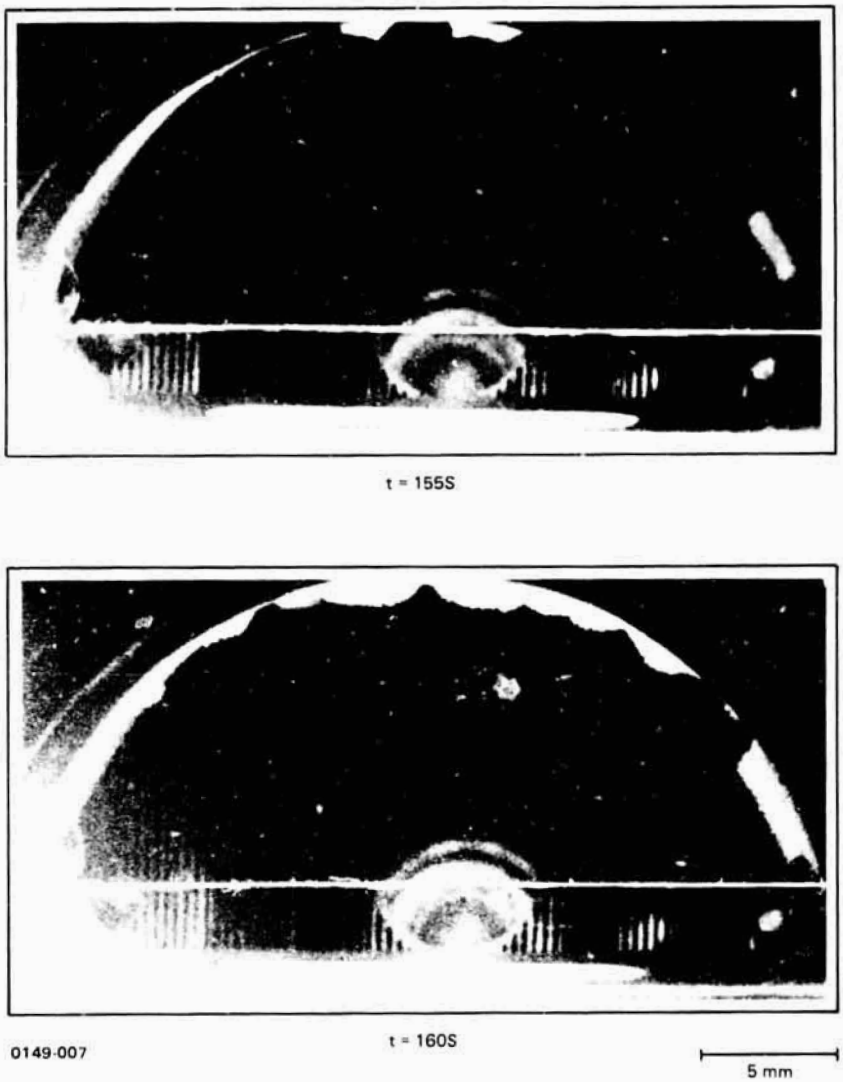

Fig. 7 Nucleation and Initial Growth in IV During Low-Gravity Experiment

thus, reduced gravity has supressed the vigorous convection observed in the laboratory simulation (Fig. 3), as expected. The irregular interface evened out as growth continued and, as seen in Fig. 8, a macroscopically smooth solid-liquid interface evolved. Comparison among Figs. 4, 6, and 8 shows the striking effect of gravitation on macroscopic interface shape. In Fig. 8 there is, of course, no difference between chill-up and chill-down positions, but, in addition, the solid-liquid interface faithfully reproduces the shape of the chill. The shape of the solid-liquid interface in the laboratory simulations (Figs. 4 and 6) was obviously influenced to a large extent by convection in the liquid. The primary dendrite spacing also appears to have been significantly more uniform in the low-gravity experiment (compare Figs. 4, 6, and 8).

Figure 9 shows the low-gravity experiment at 270s. Solidification in chambers II and IV is almost complete. All four samples solidified with a completely columnar microstructure, no columnar-to-equiaxed transition occurred, and no grain multiplication mechanisms were observed. No dendrites were observed to grow faster than the macroscopic interface, as had been reported in another low-gravity experiment (Ref. 11). Several peculiar events occurred which will be discussed in the final section. However, in order to facilitate interpretation, the thermal data will be presented now.

LOW-GRAVITY EXPERIMENT, THERMAL DATA

Thermistors had been installed in the plexiglass faces of chamber I such that their sensing elements were in intimate contact with the sample material. Two were located on the back face and two on the front, as illustrated in Fig. 4. Additional thermistors were in II and on the chill. A continuous record of the temperature as a function of time was telemetered to the tracking station during the rocket experiment. Figure 10 shows data from two of the thermistors for the flight experiment and for three different orientation ground base simulations. The chill cooled at practically the same rate in all four tests (data from the top chill test were perturbed by direct impingment of freon-12 on the chill-block thermistor), and the center of the samples cooled at almost identical rates in the three laboratory simulations. However, the center of the sample cooled at a significantly slower rate in the flight experiment. This behavior indicates that convection in the liquid accounts for a significant portion of the thermal transport in all of the laboratory simulations. This was true irrespective of the orientation of the chill. It is

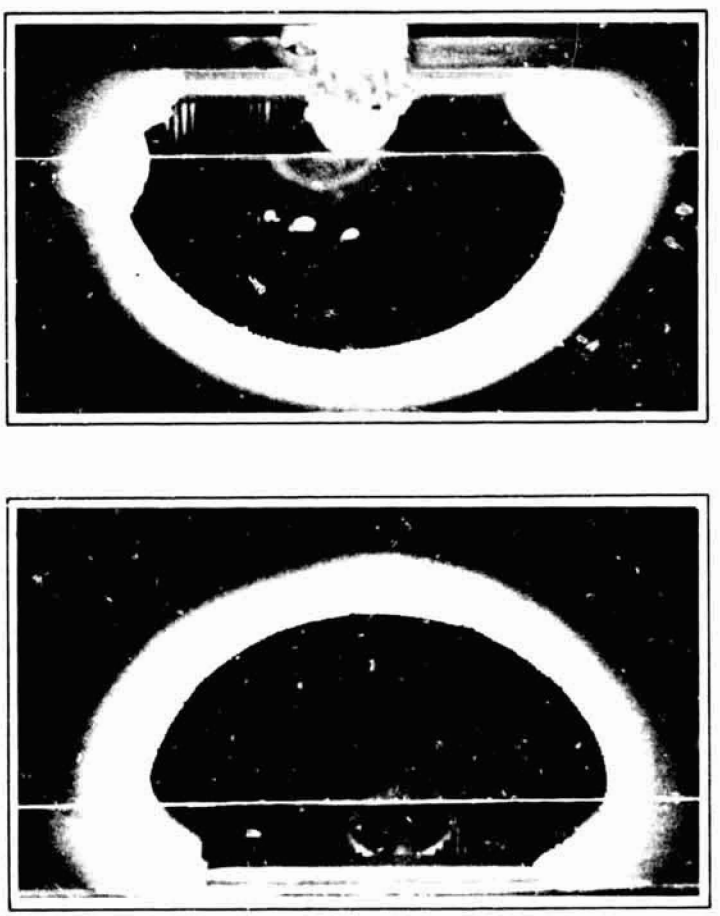

Fig. 8 Solidification in II and IV During Low-Gravity Experiment, t = 189s

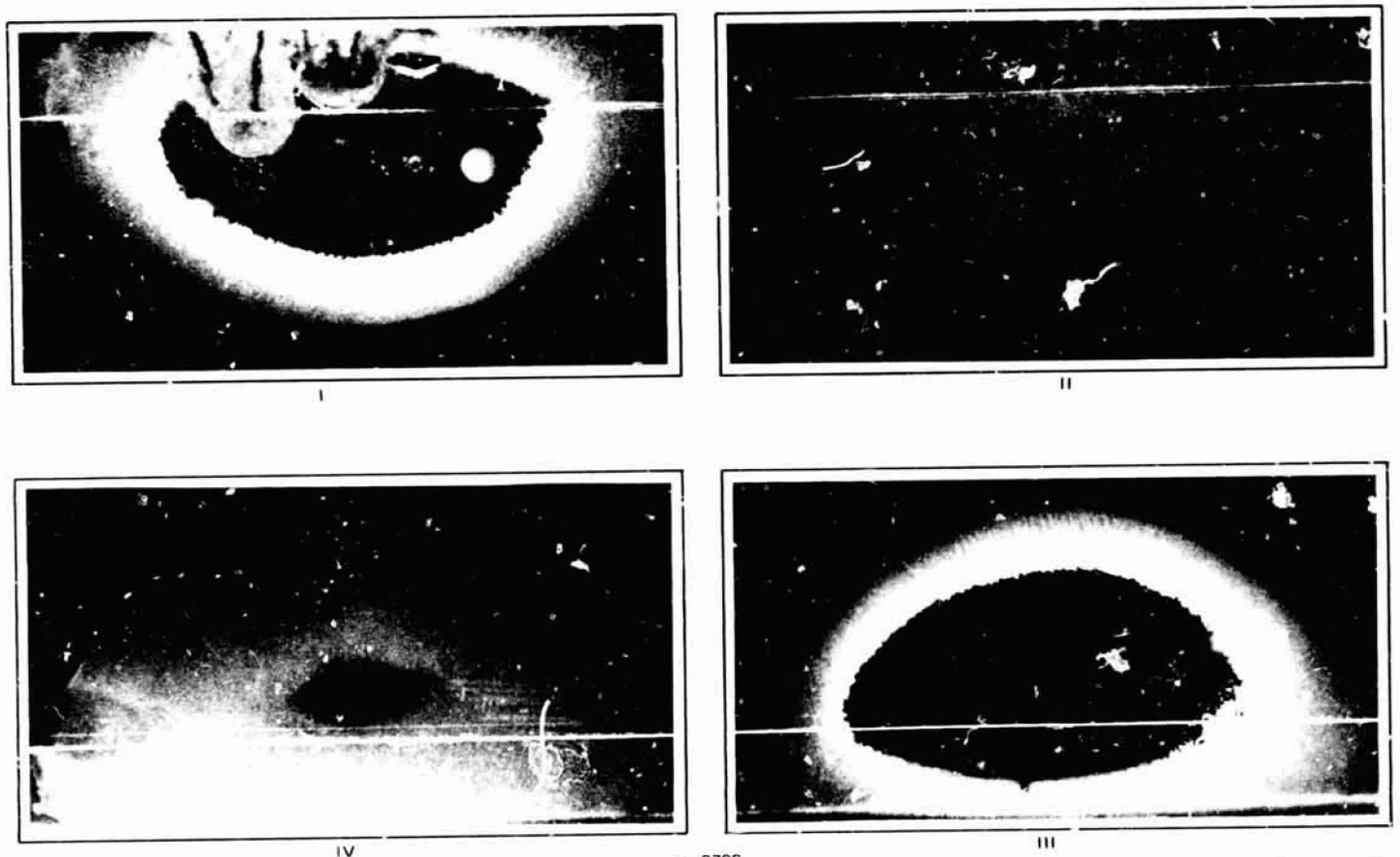

Fig. 9 Solidification in All Four Chambers During the Low-Gravity Experiment, t = 270s

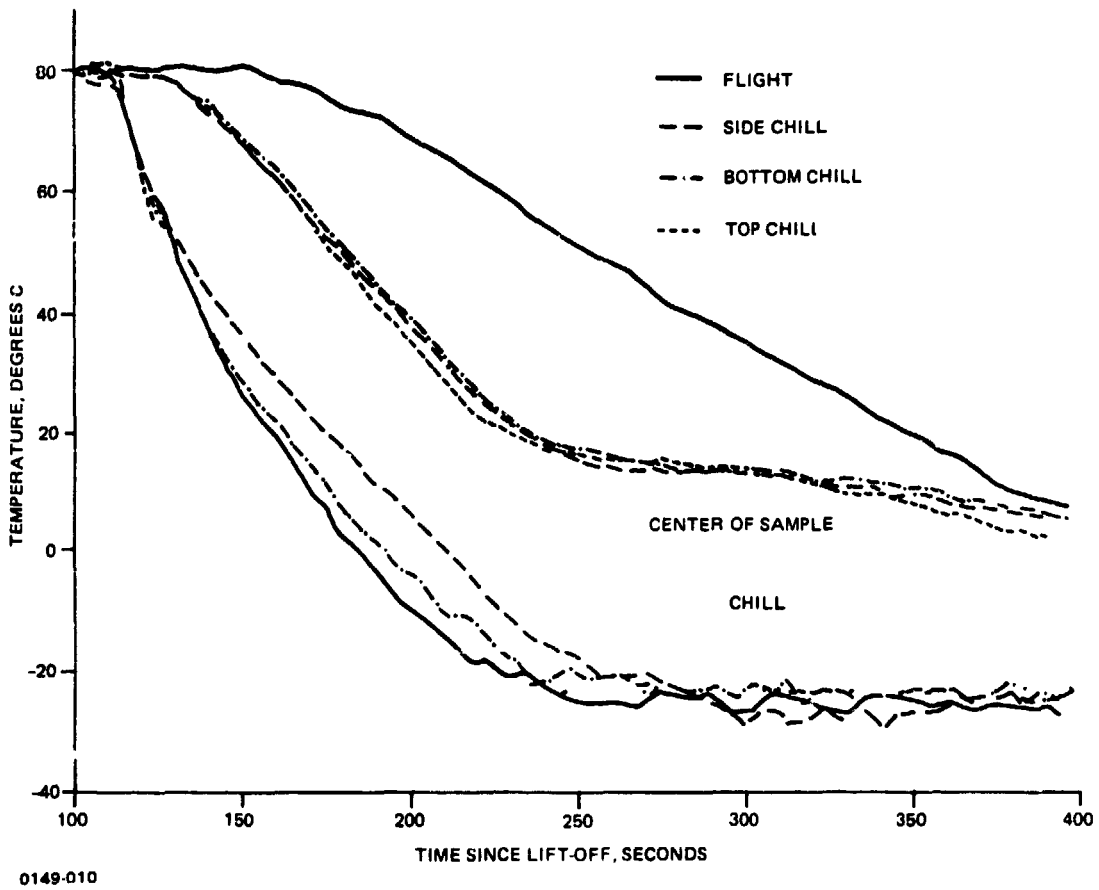

Fig. 10 Comparison of the Cooling Curves Measured at the Chill Block and Center of I During Flight and Laboratory Simulations. The Laboratory Simulations were Performed with the Sample Chamber in Three different Orientations.

thought that the semicylindrical shape of the chill was a contributory factor in this behavior; i.e., the density stratification was never purely horizontal, it was always conducive to natural convection.

The slower cooling of the center of the sample in low-gravity resulted in the presence of a steeper thermal gradient. This is illustrated in Fig. 11. It can be seen that, on a macro-scale, the thermal gradient ahead of the solid-liquid interface was significantly greater during the low-gravity experiment. It is thought that this behavior will be a general feature of low-gravity solidification operations in which the thermal gradient in the liquid is not imposed by the apparatus and heat extraction occurs through the solid.

The rate of growth of the solid was, however, not influenced by the gravity-free environment. Figure 12 shows the length of the solid measured along the center line of the front face of the sample chamber for solution A. Within experimental error all three samples grew at the same rate. The data from solution B led to a similar conclusion. Data from the side-chill experiments are not included because of the extremely nonuniform shape of the growth front. These results are to be expected since the rate of growth is controlled by thermal transport of the latent heat from the growth interface to the chill. This occurs through the solid NH_4Cl and is independent of gravitational effects.

It is the opinion of the authors that these thermal data are of particular importance in understanding the effects of gravitation on this experiment. In particular, the thermal data show that because of reduced convective transport of heat, the liquid portion of the sample was significantly warmer. This led to a steeper thermal gradient in the liquid, but more significantly, this did not allow for the growth of any equiaxed grains ahead of the columnar interface. No gravity driven convective mechanisms occurred to transport nuclei into the liquid, but this is thought to be of secondary significance. Even if nuclei had been present the thermal conditions would not have allowed them to grow. In order for an equiaxed zone to form, growth of the equiaxed grains must occur faster than growth of the columnar grains. This was not possible in the reduced gravity experiment. Support for this viewpoint can be found in several unexpected events which occurred during the flight experiment.

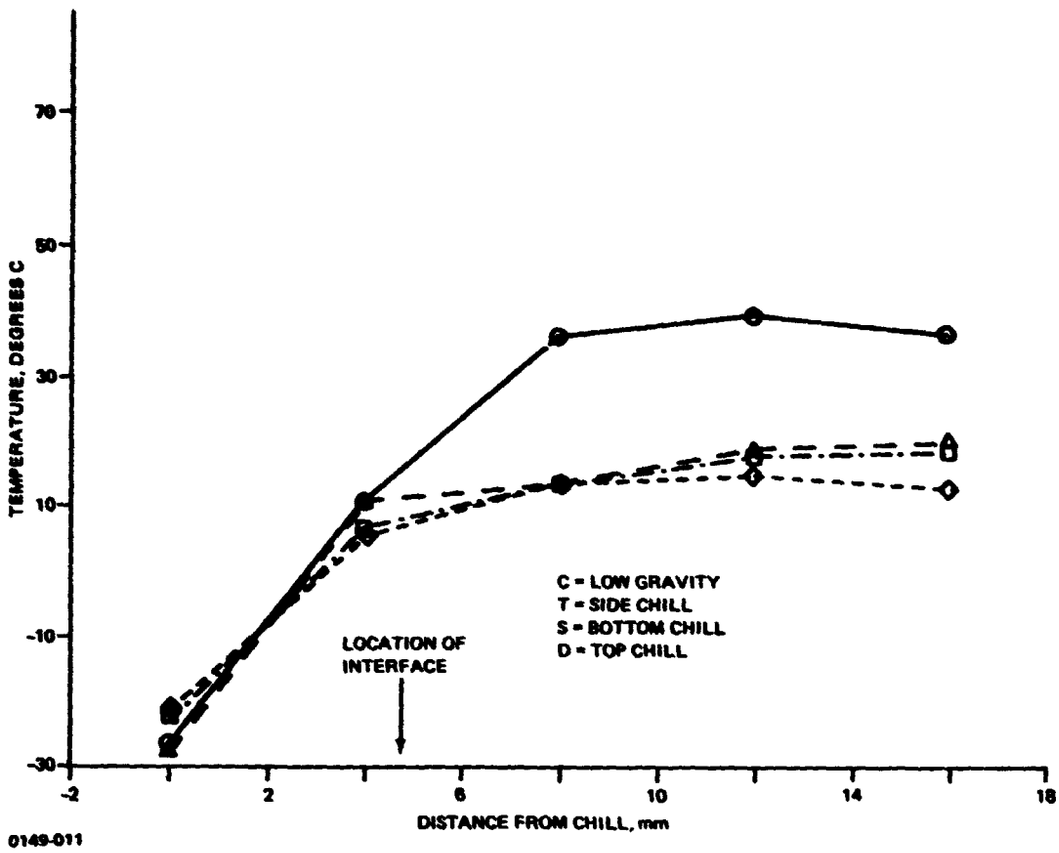

Fig. 11 The Thermal Gradient in I at t = 300s for the Flight Experiment and Three Laboratory Simulations. Location of the Solid-Liquid Interface is Marked with an Arrow.

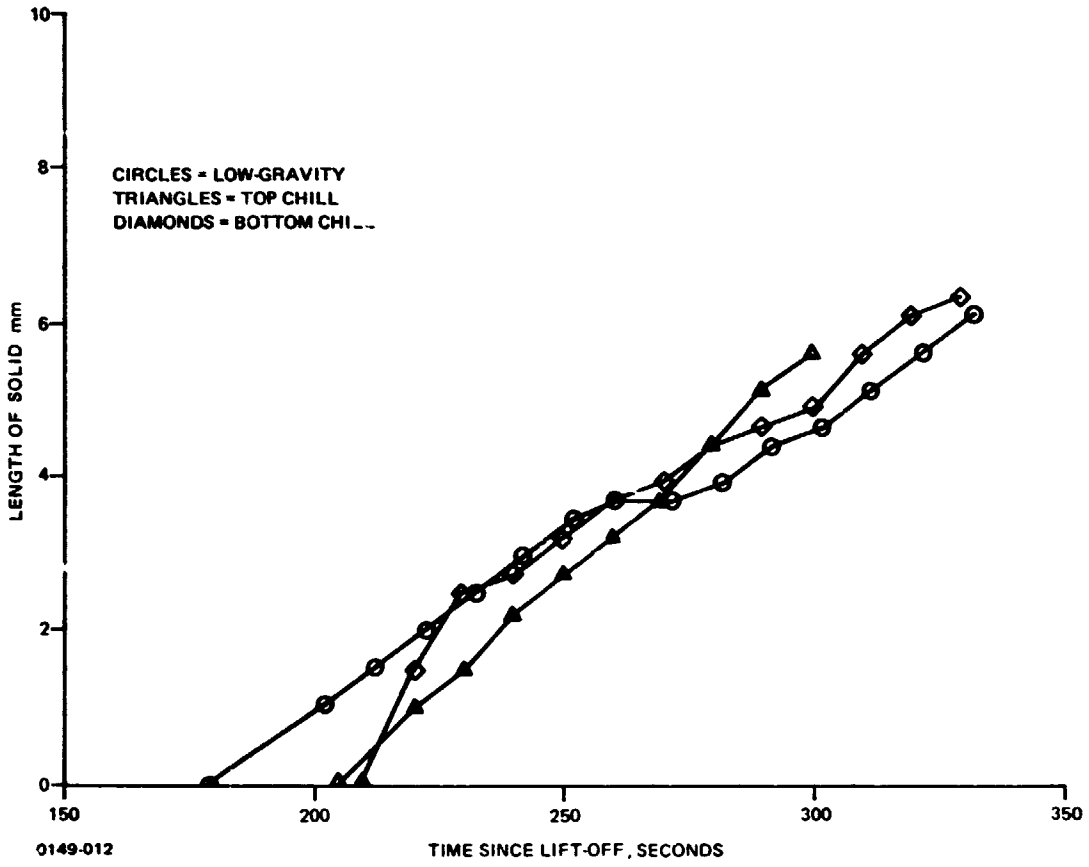

Fig. 12 Growth of NH_4Cl (Solution A) During the Flight Experiment and Two Laboratory Simulations

LOW-GRAVITY EXPERIMENT, PECULIAR EVENTS

An air bubble was present in chamber II. This bubble is presumed to have been caused by incomplete filling of the sample chamber. During solidification the bubble grew in size due to shrinkage, indicating that the expansion piston in cell II was not functioning properly. At 173s, NH_4Cl crystals appeared on the surface of the bubble. Figure 13 shows this event and subsequent growth. This seems to have been a nucleation event, but it is possible that solid simply grew along the rear surface of the bubble from existing solid. In either case, this indicates that the liquid near the surface of the bubble was cooler than liquid in the bulk. This thermal short circuit through the bubble must have been the result of an evaporation/condensation mechanism since simple gaseous conductivity should have been significantly less than the conductivity of the liquid or solid.

About 20 seconds later, another peculiar event occurred in II. Figure 14 shows this chamber at 195s and thereafter. At 195s bubbles were visible in the expansion chamber, they had been growing steadily in the 10 preceeding seconds. At 196s these bubbles disappeared and the hole in the rear face of the cell which communicates with the expansion chamber was filled with a cloud of small, opaque objects presumed to be NH_4Cl crystals. Subsequently these crystals grew slightly and were shot out into the center of the chamber. By 200s they had arranged themselves into a saddle-shaped configuration. From then on the crystals hardly grew and the overall shape of the feature changed only slightly if at all. As solidification continued the columnar growth front simply grew past the small crystals until the feature was obliterated at about 275s. At 196s, just after the bubbles in the expansion piston collapsed, a small bubble can be seen in the center of the NH_4Cl which had grown on the 4 mm bubble previously illustrated in Fig. 13. This feature is located at the top of the chamber in Fig. 14. Simultaneously, fragments of NH_4Cl appeared in the liquid just ahead of the NH_4Cl which had formed on the bubble surface. These observations, and repeated viewing of the cine film, led to the following reconstruction of the event.

It is presumed that the spring-loaded expansion piston was jammed, thereby allowing the pressure in the chamber to decrease and leading to bubble growth as solidification proceeded. Just after 195s the piston must have come unstuck, suddenly increasing the pressure in the chamber and causing the bubbles to collapse. Copious, shock induced, nucleation occurred in the expansion chamber and these nuclei were transported into the center of the chamber by fluid motion caused by

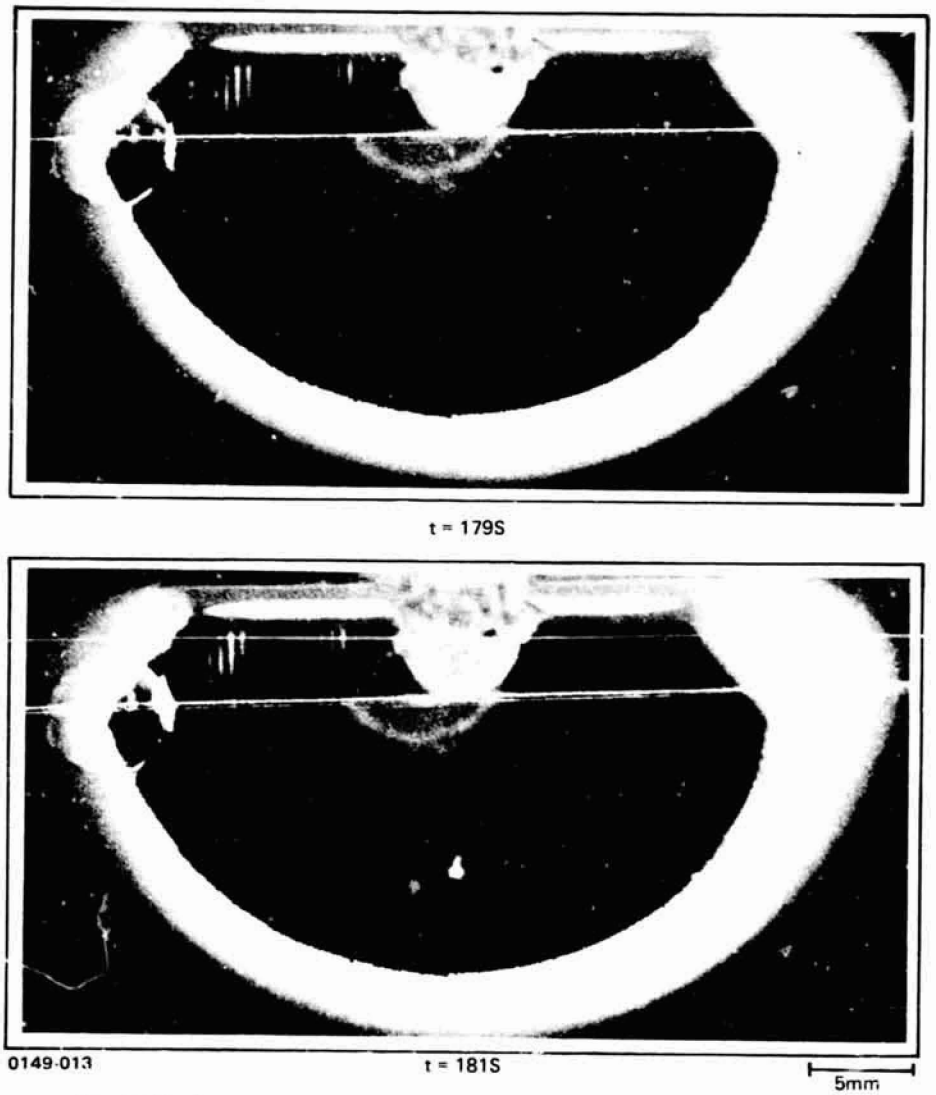

Fig. 13 Nucleation and Subsequent Growth of NH_4Cl on an Air Bubble in II During Flight Experiment

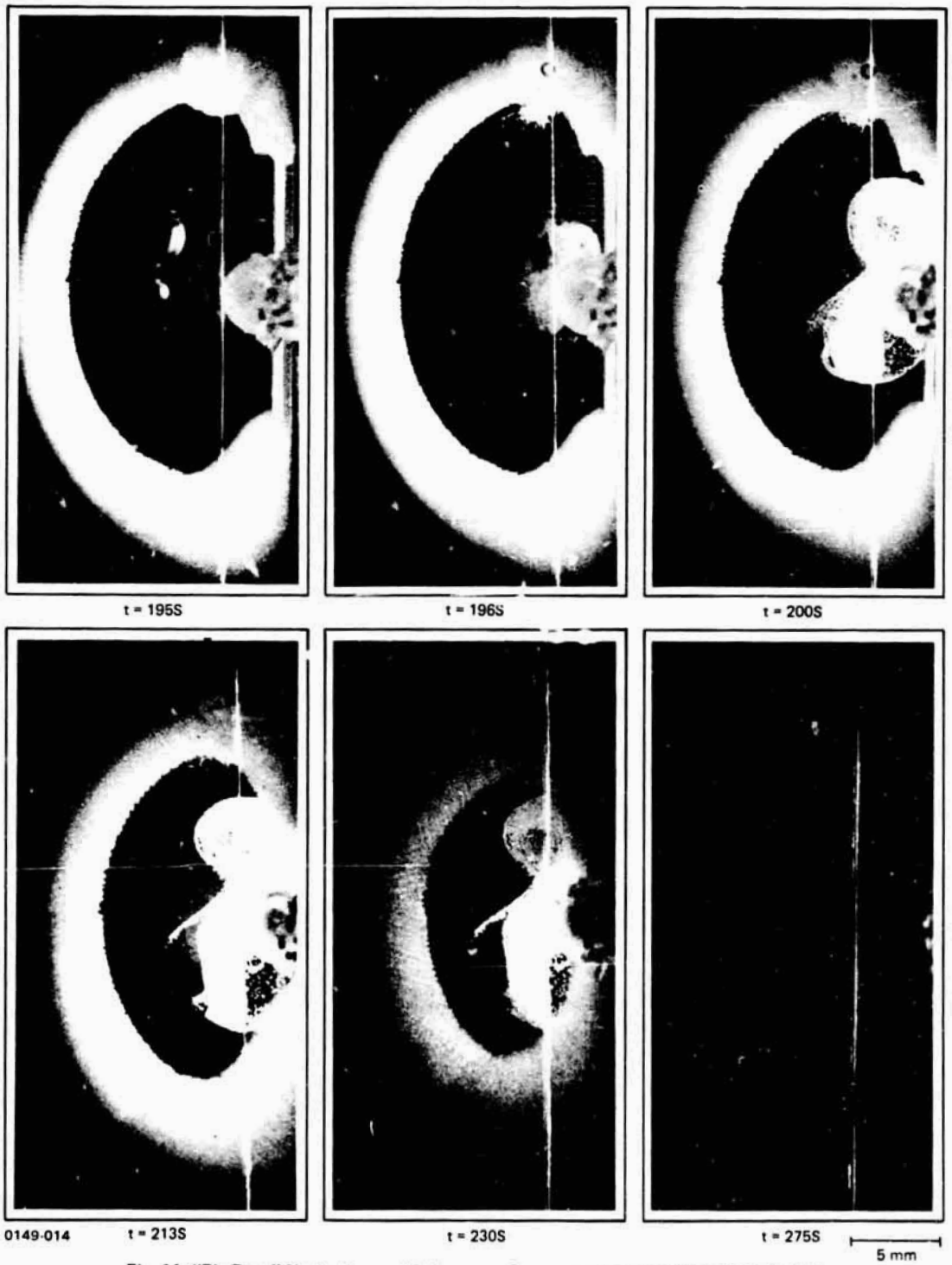

Fig. 14 "Big-Bang" Nucleation and Subsequent Growth in II During Flight Experiment

the motion of the expansion piston. The increased pressure reduced the size of the large bubble in the upper corner of the sample chamber from 4 to 0.7 mm. The reflected shock wave also punched out some NH_4Cl dendrites from the surface of the cavity which contained this bubble and pushed them into the liquid. The sequence of events at the expansion chamber can be aptly described as "big bang" nucleation. Crystals were nucleated by a shock and transported into the liquid by fluid flow. For this experiment, however, the most important aspect of this event is the observation that although copious nuclei were formed and transported into the center of the chamber, a substantial equiaxed zone never formed. The equiaxed nuclei did not grow and did not halt the advance of the columnar interface. The columnar grains simply grew past the equiaxed ones and entrapped them. It is thought that this growth was a result of the thermal conditions existing in the low-gravity environment. This observation supports the hypothesis that, for this experiment, the primary effect of the low-gravity environment was not the supression of gravity related grain-multiplication mechanisms but, rather, the alteration of the thermal conditions by the elimination of convective thermal transport in the liquid.

Figure 15 shows a similar sequence of events which occurred in chamber I. At 214s bubbles were present in the expansion chamber. Prior frames show that they had been growing steadily. At 215s the bubbles had collapsed and a filmy, indistinct feature had appeared at the bottom of the chamber. One second later the filmy feature was more distinct; subsequent frames show that it consisted of small NH_4Cl crystals which grew slightly. In addition, some small NH_4Cl crystals which nucleated in the expansion chamber drifted out into the center of the solidification chamber (215-240s) They also grew only slightly, and even seem to have been shrinking at later times (275s). Their spatial arrangement did not change, again illustrating the absence of a Stokes settling force and of convection. The explanation for this sequence is thought to be similar to that postulated for chamber II; a jammed expansion piston suddenly released, causing a pressure pulse and a small amount of circulation of the melt. The pressure pulse either caused nucleation in an apparently featureless region of the melt ahead of the solidification interface or simply transported some very small dendrite fragments from the interface into the melt. Again, the most important aspect of this observation is the inability of the small equiaxed nuclei to grow, and to halt the growth of the columnar interface. The low-gravity induced modification of the thermal conditions rendered a columnar-to-equiaxed transition impossible.

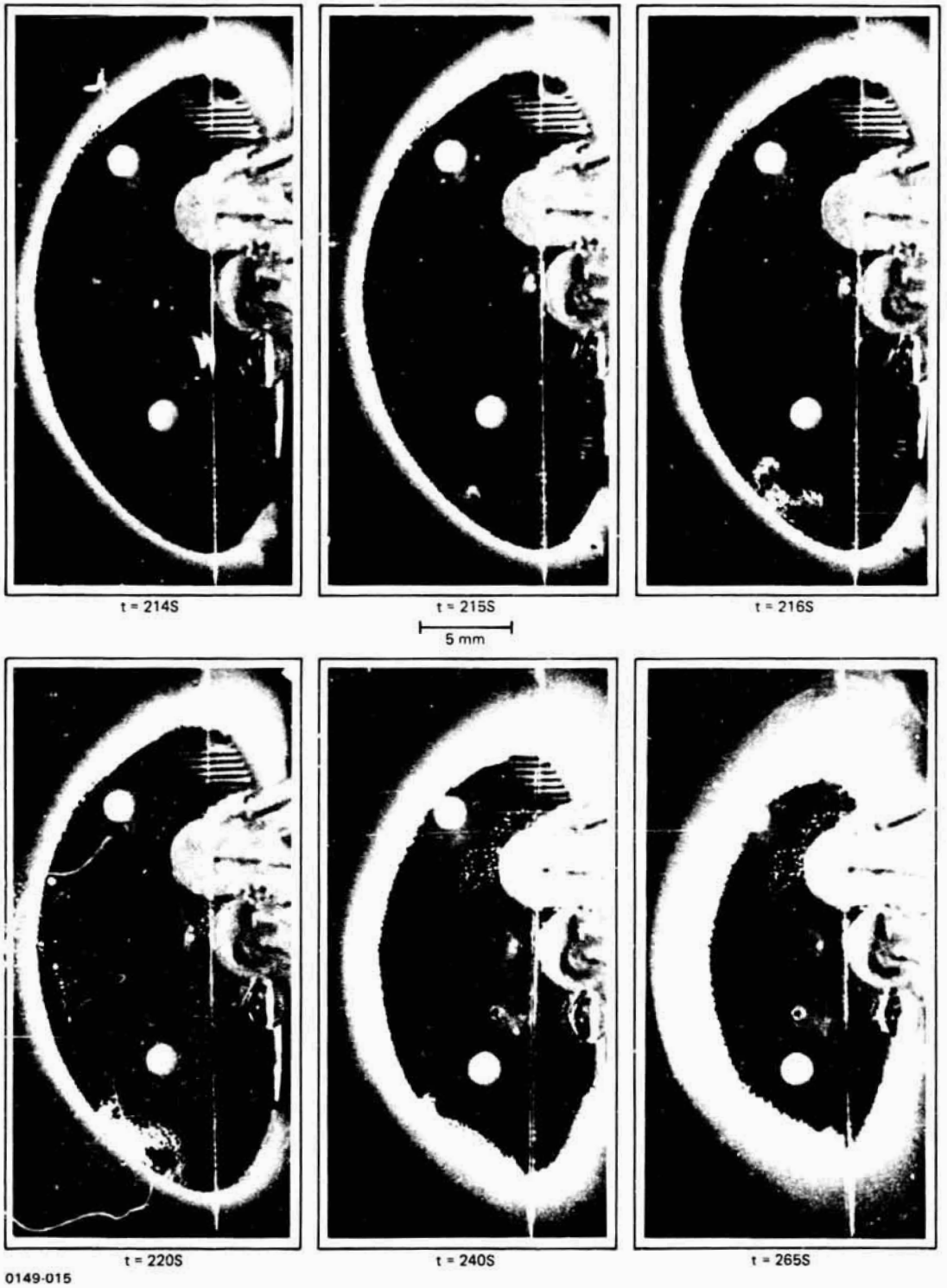

Fig. 15 Shock Induced Nucleation and Subsequent Growth in I During Flight Experiment

The last peculiar observation is shown in Fig. 16. This occurred in chamber III and involved the appearance of small crystals in an apparently featureless region of the melt (t=181), the appearance of bubbles (t=189), some small motion of bubbles, and the growth of the columnar interface past the bubbles with no apparent interaction. No complete explanation for these events is immediately obvious, but the growth of the columnar interface past these features is identical to the observations discussed previously (Figs. 14 and 15), and the lack of interaction between the dendritic interface and the bubbles is similar to previously reported low-gravity observations (Ref. 16).

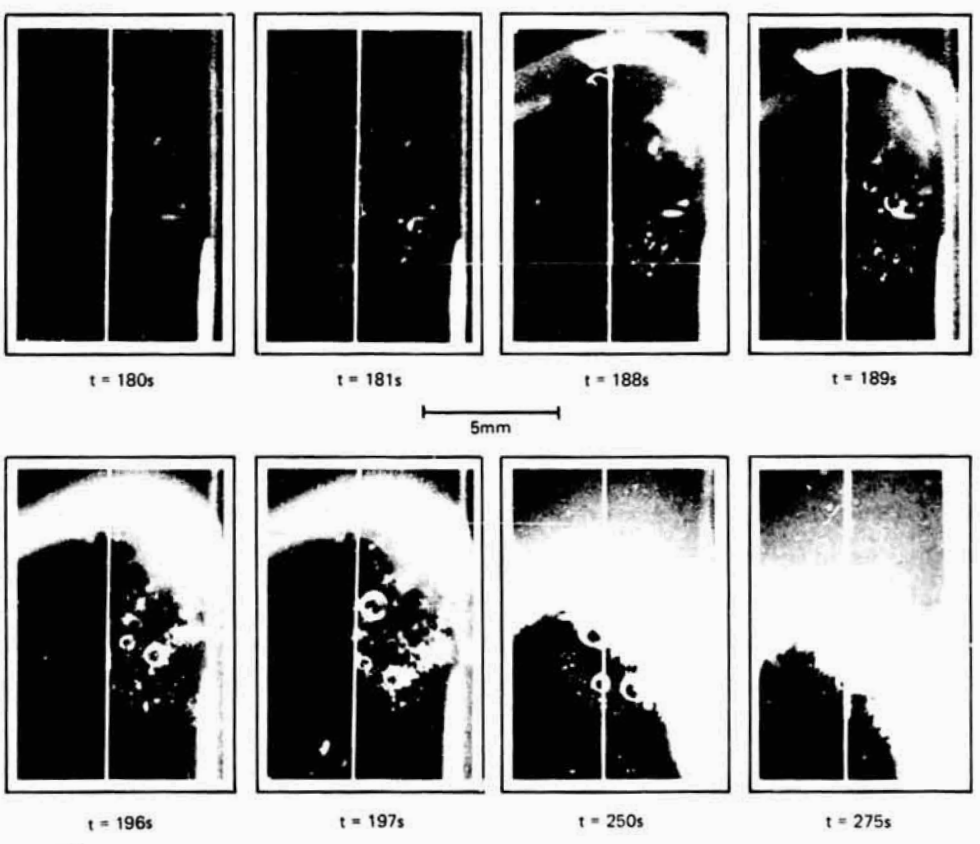

Fig. 16 Appearance and Growth of Small Bubbles in III During Flight Experiment

SUMMARY

An experimental study of the effect of a reduced gravity environment on the columnar-to-equiaxed transition in samples of 325 and 362.5 gm/litre NH_4Cl in H_2O has shown that in reduced gravity:

- Vigorous thermal inversion driven convection is absent
- No grain multiplication by showering occurs
- No thermal inversion driven grain multiplication cells occur
- No compositional inversion driven grain multiplication cells occur
- Completely columnar structures are obtained
- The liquid cools significantly slower than in one-gravity
- The thermal gradient in the liquid is steeper than in one-gravity
- The growth rate of the solid is not changed
- A bubble can act as a thermal short circuit
- Induced big bang nucleation did not give rise to an equiaxed structure
- Bubbles were not pushed by the dendritic interface

It is thought that the most significant effect of the reduced gravity environment on this experiment was the modification of the thermal conditions in the melt. The lack of convective thermal transport in the liquid resulted in conditions under which equiaxed grains could not grow and could not halt the growth of the columnar interface. The columnar-to-equiaxed transition was rendered impossible despite the presence of sufficient nuclei.

ACKNOWLEDGMENTS

It is a pleasure to acknowledge the extensive contribution of M. Kesselman, the project engineer, who was responsible for the successful operation of the apparatus. Thanks are also due to J. Mulholland and Grumman Aerospace Presentation Services fo. photographic assistance, to J. Drauch for experimental assistance, to R. DeIasi, D. Larson, and R. Pirich for technical discussions, and t· P. N. Adler for technical guidance and encouragement.

REFERENCES

1. H. Fredriksson, and M. Hillert, "On the Formation of the Central Equiaxed Zone in Ingots," Met. Trans. Vol. 3, 565 (1972).

2. G.S. Cole, K.W. Casey, and G.F. Bolling, "A Practical Method for Identifying Inoculants," Met. Trans. Vol. 5, 407 (1974).

3. K.A. Jackson, J.D. Hunt, D.R. Uhlman, and T.P. Seward, "On the Origin of the Equiaxed Zone in Castings," Trans. TMS-AIME, Vol. 236, 149 (1966)

4. A.F. Giamei and B.H. Kear, "On the Nature of Freckles in Nickel Base Superalloys," Met. Trans., Vol. 1, 2185 (1970).

5. S.M. Copley, A.F. Giamei, S.M. Johnson and M.P. Hornbecker, "The Origin of Freckles in Unidirectionally Solidified Castings," Met. Trans., Vol. 1, 2193 (1970).

6. R.T. Southin, "Nucleation of the Equiaxed Zone in Cast Melts," Trans. TMS-AIME, Vol. 239, 220 (1967).

7. W.C. Winegard and B. Chalmers, "Supercooling and Dendritic Freezing in Alloys," Trans. ASM, Vol. 46, 214 (1954).

8. H. Fredriksson, "Possible Dendrite Growth and Segregation Phenomena During Solidification of Alloys in Space," ESA Special Publication no. 114.

9. M.H. Burden and J.D. Hunt, "A Mechanism for the Columnar-to-Equiaxed Transition in Castings or Ingots," Met. Trans. Vol. 6A, 240 (1975).

10. R.D. Doherty, P.D. Cooper, M.H. Bradbury, and F.J. Honey, "On the Columnar-to-Equiaxed Transition in Small Ingots," Met. Trans. Vol. 8A, 397 (1977).

11. M.H. Johnston and C.S. Griner, "The Direct Observation of Solidification as a Function of Gravity Level," Met. Trans. Vol. 8A, 77 (1977).

12. E.C. McKannan, "M551 Metals Melting," Proceedings Third Space Processing Symposium, Skylab Results, p. 85, M-74-5 Marshall Space Flight Center, Alabama, June 1974.

13. J.M. Papazian and T.Z. Kattamis, "Contained Polycrystalline Solidification in Low Gravity," Flight I Technical Report NASA TM X-3458, p. VIII-1 (1976).

14. J.M. Papazian and T.Z. Kattamis, "Technical Proposal for Contained Polycrystalline Solidification in Low Gravity," RP-546 File no. 74-128 NAS. February 1975.

15. J.M. Papazian, M. Kesselman, and T.Z. Kattamis, "Flight IV Technical Report for Experiment 74-37 Contained Polycrystalline Solidification in Low-G," Grumman Research Department Memorandum RM-645, December 1977.

16. J.M. Papazian and W.R. Wilcox, "Interaction of Bubbles with Solidification Interfaces," AIAA J. Vol. 16, no. 5, p. 447, May 1978

Grumman Research Department Report RE-569

Addendum to
SPAR V TECHNICAL REPORT FOR EXPERIMENT 74-37 CONTAINED POLYCRYSTALLINE SOLIDIFICATION IN LOW-G

by

John M. Papazian
Research Department
Grumman Aerospace Corporation
Bethpage, New York 11714

and

Theodoulos Z. Kattamis
Institute of Material Science
University of Connecticut
Storrs, Connecticut

Post-Flight Technical Report on Contract NAS 8-31530

for

George C. Marshall Space Flight Center
National Aeronautics and Space Administration
Marshall Space Flight Center, Alabama 35812

May 1979

Approved by: Richard A. Scheuing
Richard A. Scheuing
Director of Research

The results of this experiment showed that the reduced gravity environment of SPAR V significantly modified the thermal conditions in the liquid portion of the samples. This was presumed to be due to the elimination of natural convection as a heat transport mechanism. Simple calculations can be made which support this view, as follows. The proportion of heat transported by convection is expressed as the Nusselt number

$$Nu = \frac{Q_{cond.} + Q_{conv.}}{Q_{cond.}} \qquad (1)$$

where $Q_{cond.}$ is the amount of heat transported by conduction and $Q_{conv.}$ is the amount of heat transported by convection.

In Fig. 4 of Ref. 1, Cole presents a correlation between the Nusselt number and the Raleigh number, Ra, for heat transfer in horizontal cylinders. Using this correlation as a rough guide we can estimate the Nusselt number for the conditions that existed at the beginning of our experiment. Values of the Raleigh number for the solidification chamber were first calculated from the expression

$$Ra = g\ \rho\ \beta\ \Delta T\ H^3/\mu\alpha \qquad (2)$$

where g is the acceleration of gravity, ρ is the liquid density, β is the thermal coefficient of volume expansion, ΔT the temperature difference, H the height, μ the viscosity, and α the thermal diffusivity. Typical values of the experimental parameters were taken as H = 15mm and ΔT = 45K, (Ref. 2). The Raleigh numbers and the corresponding Nusselt numbers so obtained are given in the Table for $g = g_o$ (9.8 m/s^2), and for $g = 10^{-4}\ g_o$. The Raleigh number is directly proportional to g, thus values for $g = 10^{-4}\ g_o$ are not listed. Also shown in the Table are values of these numbers for four other materials: succinonitrile ($C_4H_4N_2$), iron, lead and copper. Finally, the Prandtl numbers for each liquid are listed in the same Table. It can be seen that for water or succinonitrile, in the sample configuration of this experiment, the Nusselt number is reduced by almost a factor of ten when going

PRECEDING PAGE missing (V-32).

from normal gravity to 10^{-4} g_o. Since $Q_{cond.}$ is the same in both one-gravity and low-gravity, this result is consistent with our observations of significantly reduced heat transport in the low gravity experiment.

DIMENSIONLESS NUMBERS FOR FIVE MATERIALS

	H_2O	$C_4H_4N_2$	Fe	Pb	Cu
$Ra(g=g_o)$	3×10^6	4×10^6	2×10^4	3×10^4	3×10^3
$Nu(g=g_o)$	25	25	3	3	1.3
$Nu(g=10^{-4}g_o)$	3	3	1	1	1
Pr	7	23	0.07	0.003	0.003

This behavior is expected to be typical of other high Prandtl number liquids. Metals, which typically have much lower Prandtl numbers, behave in a qualitatively similar manner, i.e., their Nusselt numbers are reduced, but the differences between one gravity and reduced gravity are must less pronounced. The Nusselt numbers in iron and lead would drop by a factor of three; but in copper, the heat transport would be practically unchanged by the elimination of convection. Thus, an experiment similar to this one, but using copper as the sample material, might yield significantly different results.

The substantial reduction in heat transport in high Prandtl number fluids observed in the low gravity experiment and illustrated by the above calculation suggests an explanation for the results of our SPAR I experiment (Ref. 2). In that experiment a quartz cuvette containing cyclohexanol was solidified by cooling the bottom of the cuvette. Solidification in one-gravity always proceeded in an aligned columnar manner; but in the low-gravity experiment, repeated nucleation ahead of the interface was observed and an equiaxed structure resulted. The Raleigh number for that geometry was roughly 10^6 in one-gravity, thus the Nusselt

number changed from about 22 in one-gravity to 2.5 in low-gravity. This reduction of thermal transport in the liquid in low-gravity resulted in a situation in which the thermal transport in the quartz wall of the cuvette (K = 1.3 W/mK) was greater than that of the cyclohexanol, liquid or solid, (K = 0.1 W/mK). Thus, the wall became a preferred path for conduction of heat out of the solution, cooling the liquid near the wall of the cuvette ahead of the solid-liquid interface to below its liquidus and causing nucleation. In this case, therefore, the reduced heat transport in low-gravity caused the aligned, columnar, one-gravity structure to change to an equiaxed structure in low-gravity. This is exactly the opposite of the SPAR V result; but both changes in microstructure appear to have been caused by the gravity related reduction in thermal transport in the liquid. The contrasting results emphasize the importance attached to detailed consideration of the experimental conditions and reinforce the conclusion that modification of the thermal conditions in the liquid was the most important effect of reduced gravity on this experiment.

A comparable, equiaxed, result appears to have been obtained in the SPAR V flight of experiment 74-21 in which an NH_4Cl:H_2O solution was solidified in a quartz cuvette assembly that was very similar to that of our SPAR I experiment (Ref. 3).